UNIVERSITÀ DI SIENA 1240

Dipartimento di Biotecnologie, Chimica e Farmacia

Dottorato in Chemical and Pharmaceutical Sciences

38° Ciclo

Coordinatore: Prof. Maurizio Taddei

DEVELOPMENT OF PROTEIN MODULATORS WITH THERAPEUTIC POTENTIAL IN NEUROINFLAMMATORY-BASED DISEASES, NEUROLOGICAL DISORDERS, AND PANCREATIC CANCER

Settore scientifico disciplinare: CHEM-07A

Candidato

Nicola Tardiolo

Sede di attività Dipartimento di Biotecnologie, Chimica e Farmacia, Università degli Studi di Siena

Firma digitale del candidato

NICOLA
TARDIOLO
30.03.2026
23:53:56
GMT+02:00

Supervisore

Prof.ssa Stefania Butini

Ente di appartenenza: Università degli Studi di Siena

Anno accademico di conseguimento del titolo di Dottore di ricerca

2024/25

Università degli Studi di Siena

Dottorato in Chemical and Pharmaceutical Sciences

38° Ciclo

Data dell'esame finale

15/04/2026

Commissione giudicatrice

Prof.ssa Laura Scalvini

Dr. Filippo Samperi

Prof. Gabriele Carullo

______

______

Supplenti

Prof.ssa Stephanie Federico

______

Abstract

Il progresso nel campo medico-farmaceutico ha fortemente impattato sulla società, diminuendo significativamente il tasso di mortalità dovuto alle malattie infettive di natura batterica, virale o parassitaria. Conseguentemente, patologie relative all'invecchiamento, come il cancro e le malattie su base neuroinfiammatoria, hanno gradualmente acquisito molta rilevanza. Allo stesso modo, le nuove conoscenze scientifiche hanno permesso di definire più precisamente dei disturbi neurologici fino ad oggi annoverati sotto etichette errate e quindi trattate inadeguatamente, come alcune forme rare di epilessia. Tutte queste condizioni patologiche sono accomunate da un'eziologia poco nota ed un quadro clinico complesso, in cui sono coinvolti sia fattori genetici che epigenetici, nonché un intrigato network di neurotrasmissione e neuromodulazione. Lo sviluppo di strategie terapeutiche basate su approcci polifarmacologici o di letalità sintetica promettono di colpire efficacemente queste malattie multifattoriali.

Lo sviluppo di ligandi capaci di modulare contemporaneamente più bersagli molecolari rappresenta un approccio olistico nel quale una molecola può contemporaneamente modulare più sistemi biologici, aumentando l'efficacia terapeutica e riducendo gli effetti collaterali dovuti alle interazioni farmaco-farmaco. In tale contesto, grande importanza ha assunto il sistema endocannabinoide (ECS), la cui attivazione da parte dei due più importanti ligandi endogeni, anandamide (AEA) e 2-arachidonoilglicerolo (2-AG), deprime la neurotrasmissione glutammatergica, promuove i processi neuroprotettivi e regola la risposta infiammatoria periferica e centrale. Ciò risulta essere di estrema rilevanza nell'ambito di patologie con base neuroinfiammatoria o in disturbi neurologici, come l'epilessia. Visto che l'agonismo diretto dei recettori cannabinoidi 1 e 2 (CB_1R e CB_2R) è connesso a desensibilizzazione degli stessi, nonché ad effetti psicotropici dovuti alla sovrastimolazione dei CB_1R, la modulazione dei processi biosintetici e catabolici

dell'AEA o del 2-AG è una strategia che mantiene i benefici dovuti alla attivazione dell'ECS, limitando gli effetti avversi. Questo progetto di dottorato si è concentrato sullo sviluppo di nuovi strumenti polifarmacologici che hanno la capacità di modulare i principali enzimi catabolici di AEA e 2-AG, rispettivamente l'idrolasi delle ammidi degli acidi grassi (FAAH) e la lipasi dei monoacilgliceroli (MGL), per lo sviluppo quindi di agonisti indiretti dell'ECS. Abbiamo però pensato di espandere la nostra ricerca attraverso l'integrazione di un'attività antagonista del sistema istaminergico, precisamente verso il sottotipo autorecettoriale H_3 (H_3R), o inibitoria verso modulatori epigenetici, nella fattispecie l'isoforma 6 dell'istone deacetilasi (HDAC6). I composti inibitori degli enzimi FAAH e MGL ed antagonisti del H_3R hanno dimostrato un'interessante attività neuroprotettiva in un modello murino *ex-vivo* di neuroinfiammazione. Allo stesso tempo, sono efficaci nel promuovere la differenziazione dei precursori degli oligodendrociti umani nelle corrispondenti cellule gliali mature, suggerendo una loro possibile applicazione nell'ambito del trattamento di patologie demielinizzanti come la sclerosi multipla. D'altro canto, i composti ibridi HDAC6/MGL hanno dimostrato una bilanciata attività inibitoria su entrambe le proteine target, così come un'assenza di tossicità sugli astrociti 1321N1, indicando un loro potenziale utilizzo nelle terapie di patologie su base neuroinfiammatoria, da verificare con successivi saggi farmacologici. Un ulteriore approccio ha previsto lo sviluppo di composti capaci di ostacolare la produzione di 2-AG mediante il blocco di entrambe le isoforme α e β della lipasi dei diacilgliceroli (DGLα and DGLβ). Sulla base di saggi farmacologici precedenti, l'intrigante profilo enzimatico dei derivati costruiti sui target biologici suggerisce un loro potenziale utilizzo nel trattamento farmacologico dell'epilessia con assenze in pazienti pediatrici, da corroborare con ulteriori esperimenti *in vitro* ed *in vivo*.

D’altro canto, le mutazioni genetiche assumono un’estrema rilevanza in ambito oncologico, favorendo la cancerogenesi ed il successivo progresso della massa tumorale. Recentemente, l’approccio di letalità sintetica (SL) ha attratto molto interesse per via della sua elevata selettività ed efficacia. Questo concetto si basa sull’interazione funzionale tra due elementi cellulari, che siano geni o le corrispondenti proteine codificate, in cui la perdita o l’inibizione di uno solo di essi non compromette la vitalità cellulare, mentre la simultanea alterazione di entrambi risulta essere letale. Ciò permette di sviluppare delle terapie personalizzate caratterizzate da una elevata specificità per le cellule neoplastiche recanti una determinata mutazione genetica, mentre le cellule sane che non presentino tale isoforma genetica sarebbero risparmiate. Un’applicazione emblematica di questo approccio è rappresentata dall’inibizione della poli ADP-ribosio polimerasi (PARP) in cellule tumorali recanti mutazioni dei geni 1 e 2 del tumore al seno (*BRCA1/2*), la quale comprometterebbe la capacità della cellula di riparare i danni al DNA. Tuttavia, l’insorgenza di meccanismi di compensazione da parte delle cellule neoplastiche associata a tale approccio ha reso necessaria una indagine approfondita su questi meccanismi di resistenza, in modo da ristabilire l’efficacia terapeutica di questa strategia. In questo contesto, la proteina sensibile alle radiazioni 52 (RAD52) è emersa come un potenziale bersaglio da colpire allo scopo di ostruire completamente la riparazione dei danni al singolo e doppio filamento del DNA in cellule BRCA-deficienti trattate con inibitori di PARP, provocando un effetto letale. Tenendo in considerazione le informazioni provenienti dallo sviluppo dell’aptamero F79, questo lavoro di dottorato si è focalizzato sullo sviluppo di nuove molecole di natura peptidica o peptico-mimetica potenzialmente in grado di modulare l’attività di RAD52 andando ad ostacolare le interazioni protomero-protomero, impedendo l’assemblaggio della proteina target ed inducendo la morte delle cellule neoplastiche.

Abstract

The progress in the medical and pharmaceutical fields has profoundly impacted modern society, leading to a significant decrease in mortality caused by bacterial, viral, and parasitic infectious diseases. Consequently, age-related pathologies, such as cancer and neuroinflammatory-based diseases, have gained increasing prominence. Likewise, advances in scientific knowledge have allowed a more precise classification of neurological disorders that were previously misdiagnosed and inadequately treated, as for some rare forms of epilepsy. All these pathological conditions share a cryptic aetiology and a complex clinical frame, involving both genetic and epigenetic factors, as well as an intricate network of neurotransmitter and neuromodulatory pathways. The development of therapeutic strategies based on polypharmacological or synthetic lethality approaches hold promise for targeting multifactorial diseases.

The design of multitarget-directed ligands (MTDLs) represents a holistic approach in which a single molecule can simultaneously modulate multiple biological systems, thus enhancing the therapeutic efficacy while reducing side effects correlated to drug–drug interactions. Within this framework, the endocannabinoid system (ECS) has gained considerable importance, as its activation by the two main endogenous ligands, anandamide (AEA) and 2-arachidonoylglycerol (2-AG), can suppress glutamatergic neurotransmission, promote neuroprotective processes, and regulate both peripheral and central inflammatory responses. These effects are particularly relevant in the context of neuroinflammatory-based diseases and neurological disorders such as epilepsy. Since direct agonism of cannabinoid receptors 1 and 2 (CB$_1$R and CB$_2$R) is associated with receptor desensitisation, while psychotropic effects can come from CB$_1$R overstimulation, the modulation of AEA or 2-AG biosynthetic and catabolic pathways represents a valuable strategy to obtain the same benefits while minimizing adverse

effects. In this frame, this PhD project focused on the development of novel polypharmacological tools able to arrest the activity of AEA or 2-AG catabolic enzymes, namely fatty acid amide hydrolase (FAAH) and monoacylglycerol lipase (MGL) respectively, whilst integrating either antagonism toward the histaminergic system, particularly the H_3 autoreceptor subtype, inhibiting epigenetic modulators, such as histone deacetylase 6 (HDAC6). The constructed compounds simultaneously inhibiting FAAH and MGL enzymes while antagonising H_3R showed interesting neuroprotective activity in an *ex vivo* murine model of neuroinflammation. Similarly, they can promote the differentiation of human oligodendrocyte precursor cells into the corresponding mature glial cells, suggesting a potential application in the treatment of demyelinating diseases, such as multiple sclerosis. On the other hand, HDAC6/MGL hybrids displayed balanced inhibitory activity on both target proteins, as well as an absence of toxicity in 1321N1 astrocytes, indicating their potential use in therapies for neuroinflammatory-based disorders, to be further probed through more in-depth pharmacological assays. Another approach involved the development of compounds able to hinder the production of 2-AG by blocking both the α and β isoforms of diacylglycerol lipase (DGLα and DGLβ). Based on previous pharmacological assays, the intriguing enzymatic profiles of the constructed derivatives on the biological targets suggest their potential use in the pharmacological treatment of absence epilepsy in paediatric patients, to be corroborated with additional *in vivo* experiments.

On the other hand, genetic mutations play a crucial role in oncogenesis and during tumour growth. Recently, the synthetic lethality (SL) approach has attracted considerable interest due to its high selectivity and efficacy. This concept is based on the functional interaction between two cellular components, whether genes or their encoded proteins, where the loss or inhibition of either alone does not compromise cell viability, but the simultaneous alteration of both leads to cell death. This approach enables the development of personalised therapies characterised by a high specificity toward neoplastic cells harbouring peculiar genetic mutants, while sparing healthy cells lacking the altered genotype. A perfect example of this strategy is the inhibition of poly(ADP-ribose) polymerase (PARP) in tumour cells bearing mutated breast cancer genes 1 and 2 (*BRCA1/2*), which impairs the cellular ability to repair DNA damage. Nonetheless, compensatory mechanisms acquire by neoplastic cells has limited the therapeutic efficacy of this approach, hence the molecular basis of such resistance has been deep investigated to restore treatment effectiveness. In this context, the radiation-sensitive protein 52 (RAD52) has emerged as a promising target to hinder both single- and double-strand DNA repair in BRCA-deficient cells treated with PARP inhibitors, thereby inducing a lethal effect. Building on the insights gained from F79 aptamer, this PhD work embarked in the development of novel small peptide and peptidomimetic molecules modulating RAD52 activity by interfering with protomer–protomer interactions, thus preventing the assembly of the target protein and inducing neoplastic cell death.

Table of contents

Preface: New world, new diseases

The history of ancient medicine could be tracked back to prehistorical era, when humans tried to understand the correlation between the healing process and the use of certain plants, later known as medicinal herbs.[1] This empirical approach was followed for millennia, leading to the development of several traditional medical treatments influenced by religious beliefs and autochthone medicinal flora. The Industrial Revolution of the 18th century represents the milestone from which modern medicine emerged. Indeed, industrialisation boosted technological and scientific progress, fostering the application of the scientific method to medicine while providing innovative therapeutic tools to treat many pathological conditions. On the other hand, overurbanisation provoked a decrease in hygienic standards whilst air pollution increased the rate of respiratory diseases, like asthma.[2] Nevertheless, the rapid advancement in medicine brought to an extended life expectancy, posing new health challenges in modern society.

According to the World Health Organization (WHO), the top 10 leading causes of death account for over 57% of worldwide deaths. Among chronic diseases, neurodegenerative diseases (NDs), such as Alzheimer's disease (AD) and Parkinson's disease (PD), significantly raised their incidence during the last two decades.[3] This effect is tightly entwined with the increased life span, since aging prompts neurodegenerative processes thus representing one of the major causes of NDs. A major component accounting for neurodegenerative processes is neuroinflammation, which can culminate in an excessive immune response of neuronal tissues towards exogenous and endogenous stimuli, promoting cell death. Another age-related group of pathological affections gaining high relevance in worldwide deaths is cancer. Oncogenic diseases caused nearly 10 million deaths in 2020, with an overall steadily increment in tumour incidence mainly in elderly people.[4] As predicted, the socioeconomic factors robustly impact cancer and NDs rates, as the population in higher-income countries benefits of longer life expectancy. Indeed, they represent the fourth, fifth and seventh causes of death within this group.

Although apparently diverse, NDs and neoplastic diseases may share some common pathological pathways (**Figure 1**), such as cell cycle disruption caused by genetic mutations or altered protein isoforms, suggesting a tight link between these two classes of diseases.[5,6]

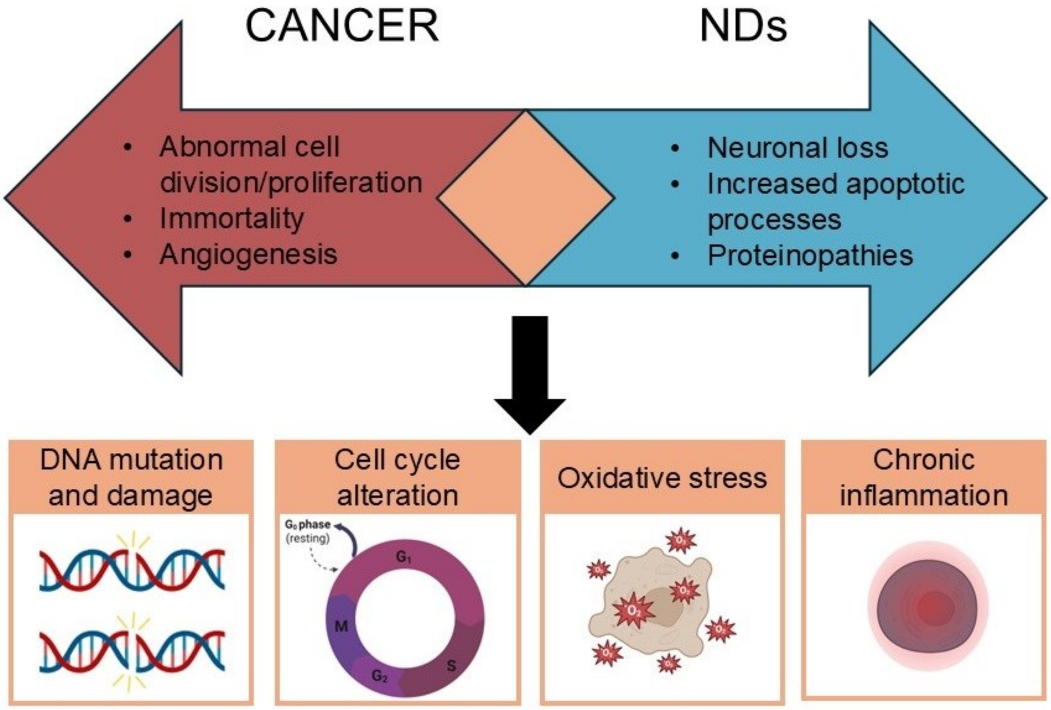

Figure 1. Schematic representation of specific and common biological pathways in cancer and neurodegenerative diseases.

Similarly, neurological disorders represent a heavy burden in global health. Particularly, epilepsy is one of the top 3 leading cause of disability-adjusted life years in older children and adolescence (5-19 years).[7] Due their multifactorial nature and cryptic etiopathology, the current pharmacological treatments are only partially able to manage the symptoms without addressing the underlying pathological processes. Therefore, the development of novel pharmacological agents, as well as integrative therapeutic strategies, are utterly needed in order to counteract both neuroinflammatory-based diseases, NDs, neurological disorders, and cancer.

Chapter 1: development of polypharmacological approaches engaging ECS for tackling neuroinflammatory-based diseases, and neurological disorders

1.1 Neurodegenerative diseases

Neurodegenerative diseases are a heterogeneous group of pathological conditions typified by progressive loss of neurons' functionality in central nervous system (CNS) or peripheral nervous system, eventually leading to extensive cell death. This induces cognitive impairments, such dementia and amnesia, and motor dysfunctionalities, like ipo- or iperkinesia, worsening patient lifestyle.[8]

The most common NDs are AD, PD, Huntington's disease (HD), and amyotrophic lateral sclerosis (ALS). Despite their veiled aetiology, NDs show clear biological hallmarks contributing to neuronal damage, that could be broadly divided in four categories: modified proteostasis, promoting the accumulation of misfolded protein aggregates; oxidative and endoplasmic reticulum stress, generating dangerous reactive oxygen species (ROS); metabolic dysfunctions, accelerating cells aging; neuroimmune overstimulation, triggering chronic neuroinflammation associated with overproduction of proinflammatory chemokines and cytokines.[9] Furthermore, an increased amount of scientific reports correlated NDs with altered epigenetic modulation. Epigenetic regulation encompasses the comprehensive cellular pathways able to tune gene expression without affecting DNA sequence. Direct addition of chemical groups to the

DNA bases, such as methylation, or chromatin remodelling, for example through histones modification, robustly influences neuronal growth and survival, representing pivotal machinery underlying the neurodegenerative processes.[10,11]

Within this framework, multiple sclerosis (MS) stands out as a unique pathological condition, in which neurodegeneration represents one of a multitude of traits of its multifaceted nature.

1.2 Multiple sclerosis

Multiple sclerosis is a chronic disease characterised by the progressive loss of myelin, leading to motor disability and paralysis. Since patients exhibit a broad spectrum of symptoms and different prognosis, only in 2018 a general standardised classification system was proposed.[12] Nonetheless, the aetiology underlying MS is yet to be unravelled, but a mixture of environmental and genetic factors is thought to drive MS clinical symptoms (**Figure 2**).[13]

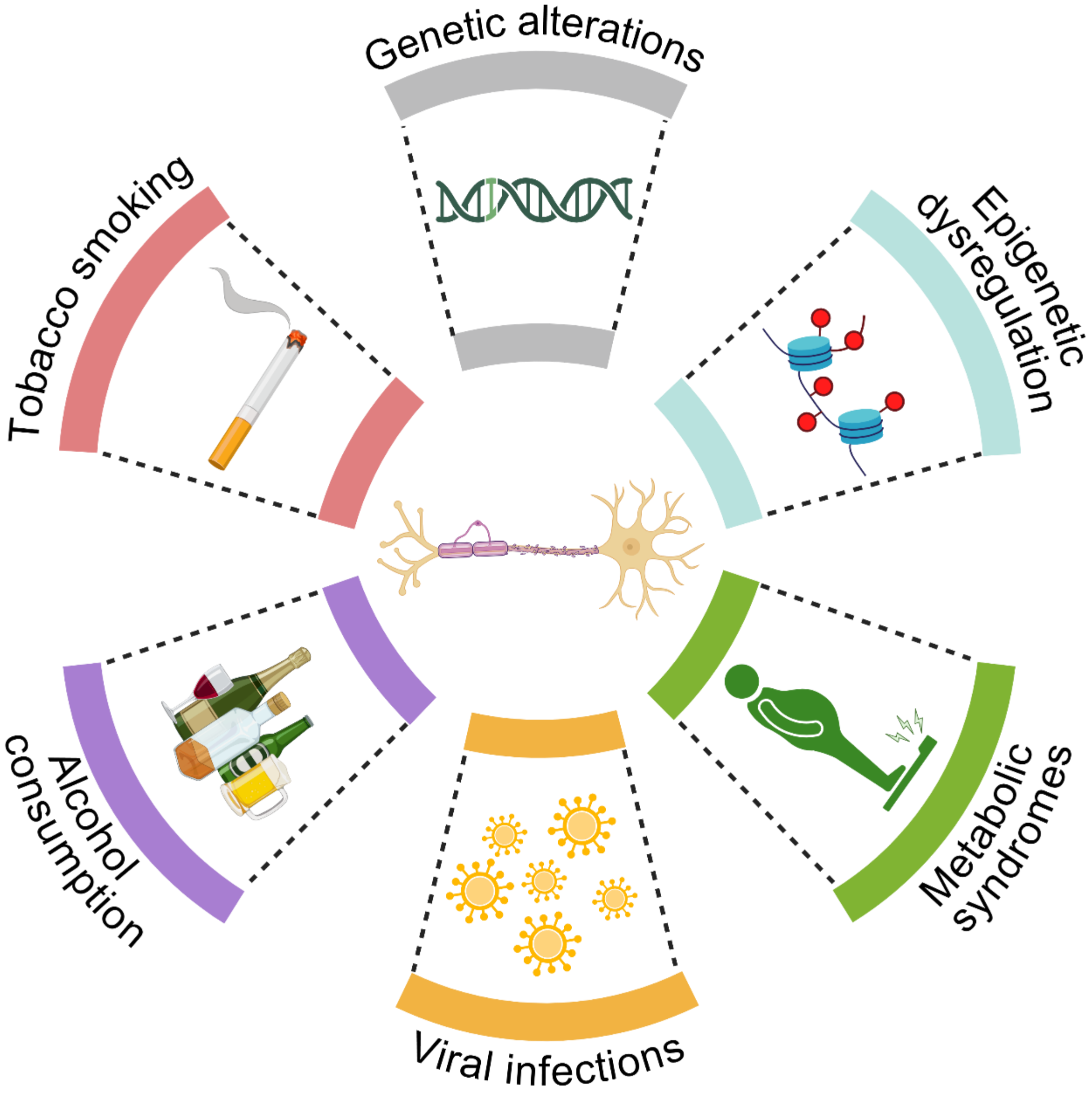

Figure 2. Schematic representation of environmental and genetic factors potentially triggering MS.

Notably, neurodegenerative processes play a minimal role in the onset of MS, but they can gradually exacerbate demyelination as the disease progresses. On the other hand, the initial stage seems to be triggered by a combination of autoimmune responses and neuroinflammation. Both adaptive and innate immune systems are overactivated, and their dysregulation provides great neuronal insults in CNS. Particularly, $CD4^+$ and $CD8^+$ T lymphocytes release proinflammatory cytokines, like tumour necrosis factor α (TNF-α), and interleukins 1β and 6 (IL-1β and IL-6, respectively), creating a persistent neuroinflammatory environment that is responsible for depleting myelin thus fostering neurodegeneration.[14] These negative outcomes are tightly intertwined with oligodendrocyte activity, pivotal for myelin production. Particularly, recent evidence showed that the recruitment of oligodendrocyte precursors cells (OPCs) is robustly impaired in MS lesions. This brings to poor differentiation of OPCs into mature oligodendrocyte, creating demyelinating areas known as MS lesions.[15] OPCs are also central in the inflammatory damage occurring in MS plaque. Indeed, OPCs isolated from post-mortem patients' samples exhibit high levels of Wingless/Integrated (Wnt) signalling, a marker of neuroinflammation. This condition was replicated using a well-established MS rodent model, experimental autoimmune encephalitis (EAE)-induced mice. Notably, EAE clinical manifestations were exacerbated in brain and spinal cord, due to enhanced T-cell and cytotoxic infiltration in MS lesions, suggesting that OPCs control a complex immune network operating early demyelination.[16]

As for NDs, the development of an effective therapeutic approach is still unmet; nevertheless, reducing the risk factors and acting on clinical manifestations effectively prevent disease progression, supporting symptoms management. Through the years, several FDA-approved immunomodulators were employed to control MS relapses, comprising both natural products (interferons β-1a and β-1b), small molecules (glatiramer acetate and fingolimod), and humanised monoclonal antibodies (natalizumab and alemtuzumab).[17,18] However, monotherapies based on these compounds posed significant safety concerns.[19] Combination therapies employing different class of immunoregulators were also proposed to increase clinical efficacy, but the extended immunosuppression might trigger more negative outcomes.[20]

On the other hand, polypharmacological strategies in which multiple different biological targets and pathways, involved in neuroinflammatory and neurodegenerative processes, are simultaneously targeted emerged as promising therapeutic approaches to overcome these issues.[21,22]

1.3 Epilepsy

Epilepsy is a group of chronic neurological disorders typified by at least two epileptic seizures in more than 24 h. According to WHO, epilepsy is one of the oldest registered pathologies in history, and 50 million of people are affected by this pathological condition.[23] The first general classification of different epileptic syndromes, as well as their definition and clinical manifestations, has been proposed by the International League Against Epilepsy in 1989, and it has been updated since then. On this ground, epilepsy is the predisposition of an individual to undergo unprovoked epileptic seizures, which are briefly episodes of abnormal or extremely synchronous neuronal activity within the CNS. This produces several neurobiological, psychological, and cognitive impairments in patients. Epileptic episodes can occur in specific region of one brain hemisphere (focal) or, starting from one point, engaging both hemispheres (generalised). Further, when the data are too low to define a clear classification as focal or generalised, epileptic syndromes are categorised as "unknown", whereas whether it is extremely difficult to characterise the seizures, they are called "unclassified". The main clinical manifestations consist of involuntary movements resulting from the excessive firing of excitatory neurotransmitter on neurons, inducing either clonic or tonic motor states, or a cyclical alternation between the two. In some cases, the patient's symptomatology could be exacerbated by additional pathological features.[24] Among these latter, the impaired consciousness status assumes a critical role in a peculiar type of epileptic episodes, absence epilepsy (AE). This neurological disorder comprises a series of pathological conditions typified by unresponsiveness to high-orders tasks, loss of awareness towards the external world, and transient lack of memories during the seizures. AE predominantly affect among children (CAE), or juveniles (JAE), presenting specific ictal activity, >3s, and spike-wave discharges (SWDs), around 3-4.5 Hz. The loss of consciousness presumably stems from an intricate neurological signalling network, involving the basal ganglia, the thalamus, the striatum, and other subcortical districts.[25,26] Further, both environmental and genetic factors, recapitulated in **Figure 3**, has been indicated as possible initiators of AE onset.[27,28]

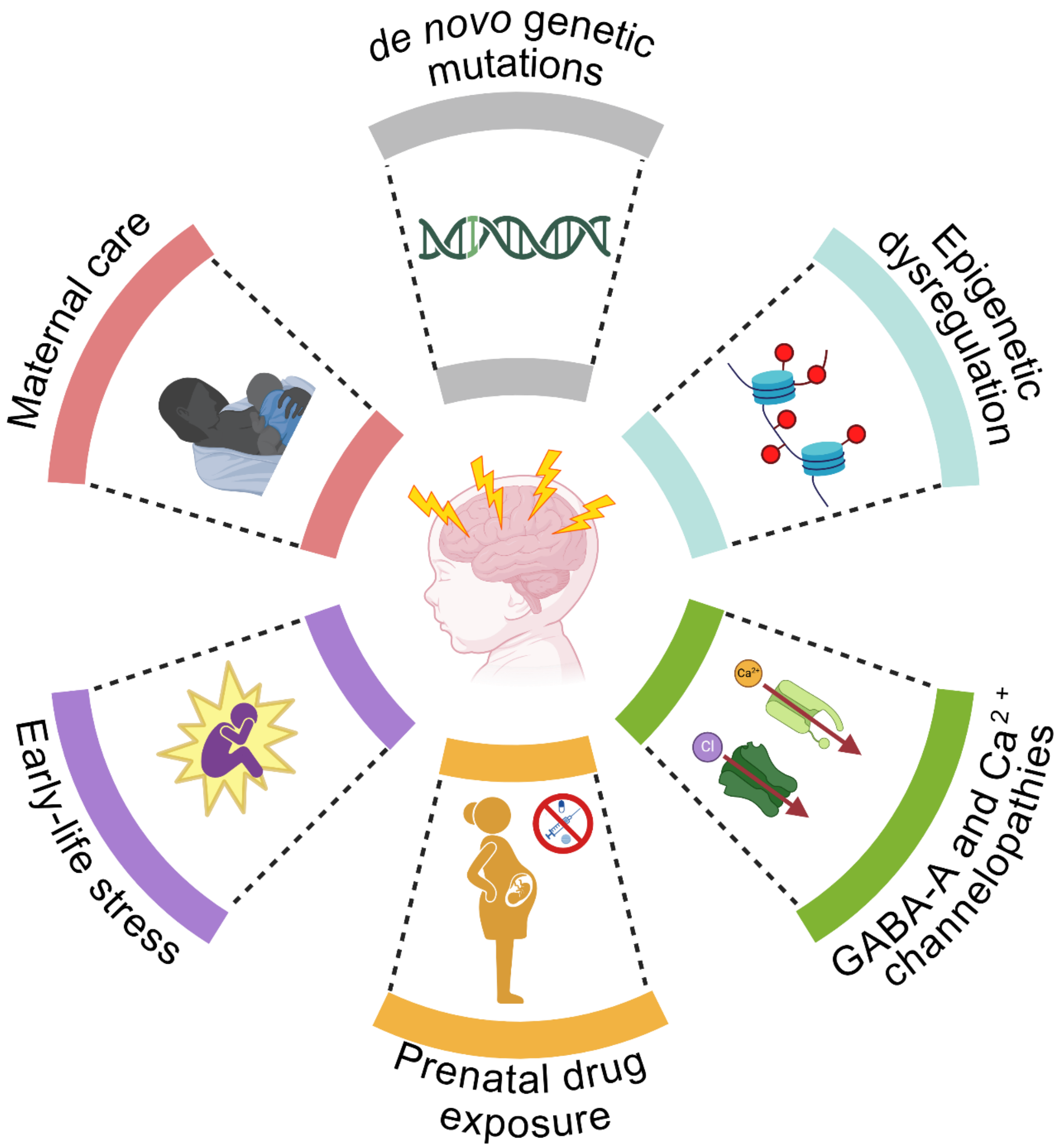

Figure 3. Schematic representation of the environmental and genetic factors potentially triggering absence epilepsy.

Despite having a benign course, the unawareness towards the external world occurring in AE patients strongly increased the potential for accidental injuries and may account for cognitive dysfunctions, such as attention-deficit/hyperactivity disorder. This condition is also associated with academic underachievement, social challenges, anxiety, and depression.[29]

The current medical treatments addressing AE include low dose pharmacological therapy based on three classical antiseizure drugs (**Figure 4**), ethosuximide (**1**), which is considered the first line therapeutic tool in treating AE, valproic acid (**2**), and lamotrigine (**3**).

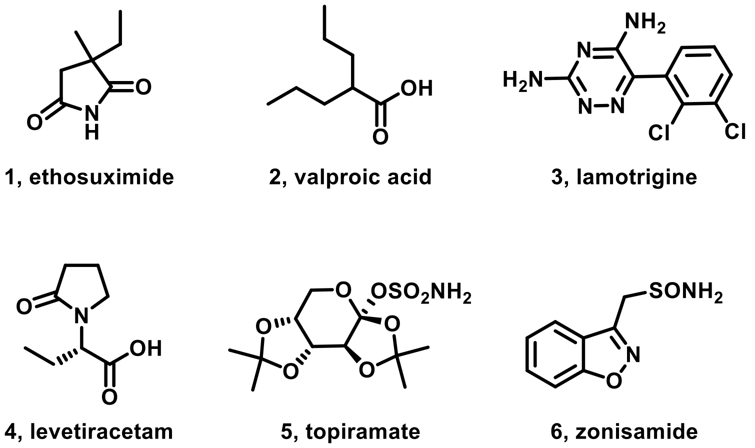

Figure 4. Chemical structures of drugs currently approved for first-line or alternative pharmacological treatments in absence epilepsy.

Despite their satisfactory activity, 30% of paediatric patients present innate resistance to monotherapies based on these drugs. Moreover, their chronic administration is correlated with several side effects, particularly in polytherapy. Therefore, second-line therapeutic options, such as levetiracetam (**4**., **Figure 4**), topiramate (**5**, **Figure 4**), and zonisamide (**6**, **Figure 4**), as well as innovative pharmacological tools, specifically targeting cortical T-type Ca^{2+} channel or potentiating thalamic $GABA_A$ neurotransmission, have been proposed to overcome this issue.[26,30]

1.4 Multitarget-directed ligands

Multitarget-directed ligands (MTDLs) are chemical compounds able to concurrently interact with multiple biological targets, involved in the same or in different pathological pathways. The development of MTDLs followed the principles of polypharmacological approach, which holds promise in fulfilling the compelling call for ameliorated therapeutic strategies. Polypharmacological agents benefit of limited drug-drug interactions, better pharmacokinetic properties, and improved patient compliance compared to active compounds based on single-drug strategies and polytherapy.[31] In this context, drug promiscuity, which is a critical feature for MTDLs, should be strategically guided to avoid the interaction with potential off- and anti-targets, hence thwarting the eventual side effects, whilst engaging the complex networks driving the pathogenesis of multifactorial diseases.[32]

The identification of suitable candidates for designing MTDLs could rely on clinical observations, phenotypic screenings or in silico approaches regarding mono or combination therapies. Further, off-target effects of traditional treatments could also suggest possible repurposing or repositioning of polypharmacological agents. Once the targets are selected, a new molecular architecture should be constructed. This latter should comprise all the pharmacophoric elements useful to obtain the desired multiple activities against the biological targets. To achieve this, it is possible to joint different pharmacophores following three different routes (**Figure 5**):

- Linking: multiple individual pharmacophores are connected by simple degradable or stable linkers.
- Fusion: a cleavable or non-cleavable bond allows the fusion between the single pharmacophores.

- Merging: the essential features to achieve effective activity over the selected targets are hybridised to generate a novel scaffold. In this case, a certain grade of overlapping in the individual pharmacophores of each target is crucial.[33]

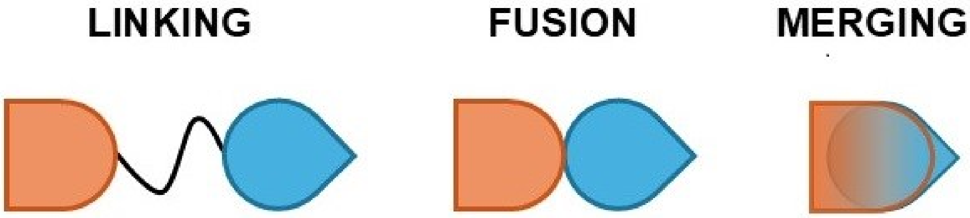

Figure 5. Different design strategies to develop MTLDs.

In recent years, scientists have gained interest in exploiting polypharmacology to treat multifaceted diseases, such as cancer, neurological disorders, and NDs.[22,34]

In this framework, the neuroprotective and anti-inflammatory properties of the endocannabinoid system (ECS) appear as an excellent candidate for the development of novel polypharmacological strategies.

1.5 Endocannabinoid system

Cannabis Sativa is a widespread plant with a long history of use in several countries. Its captivating curative abilities, e.g. in eye diseases treatment, as well as its psychotropic effects, employed during religious ceremony, were described in ancient Chinese and Egyptian Empires. Nonetheless, *Cannabis Sativa* was pharmacologically intensively studied starting from the 19th century, when Scheslinger isolated the first active extract from the hemp.[35] Only in the '60, Mechoulam *et al.* reported the resolved structures of the main *Cannabis* active principles: the psychoactive partial agonist Δ^9-tetrahydrocannabidinol (THC, 7, **Figure 6**) and the non-psychoactive negative CB_1R agonist and CB_2R partial agonist cannabidiol (CBD, **8**, **Figure 6**).

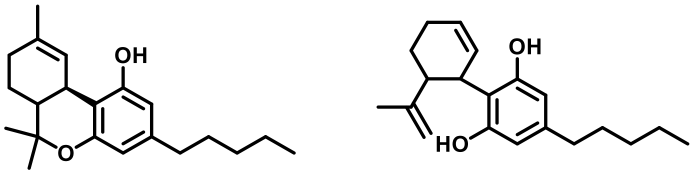

7, THC
K_i *h*CB_1R = 40.7 nM
K_i *h*CB_2R = 36 nM

8, CBD
K_i *h*CB_1R = 4350 nM
K_i *h*CB_2R = 2860 nM

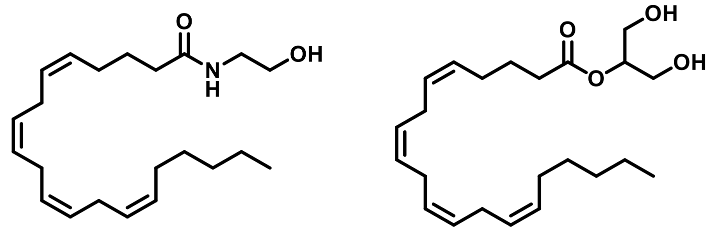

9, anandamide
K_i *h*CB_1R = 252 nM
K_i *h*CB_2R = 581 nM

10, 2-AG
K_i *h*CB_1R = 472 nM
K_i *h*CB_2R = 1400 nM

Figure 6. Chemical structures and IC_{50} values for *h*BC_1R and *h*CB_2R of the main exogenous and endogenous cannabinoids.

Still, the activity of these compounds remained to be ascertained for another 30 years. In 1990 and 1993 the cannabinoid receptors 1 and 2 (CB_1R and CB_2R) were cloned, opening the gate of an unexplored network now called endocannabinoid system (**Figure 7**).[36]

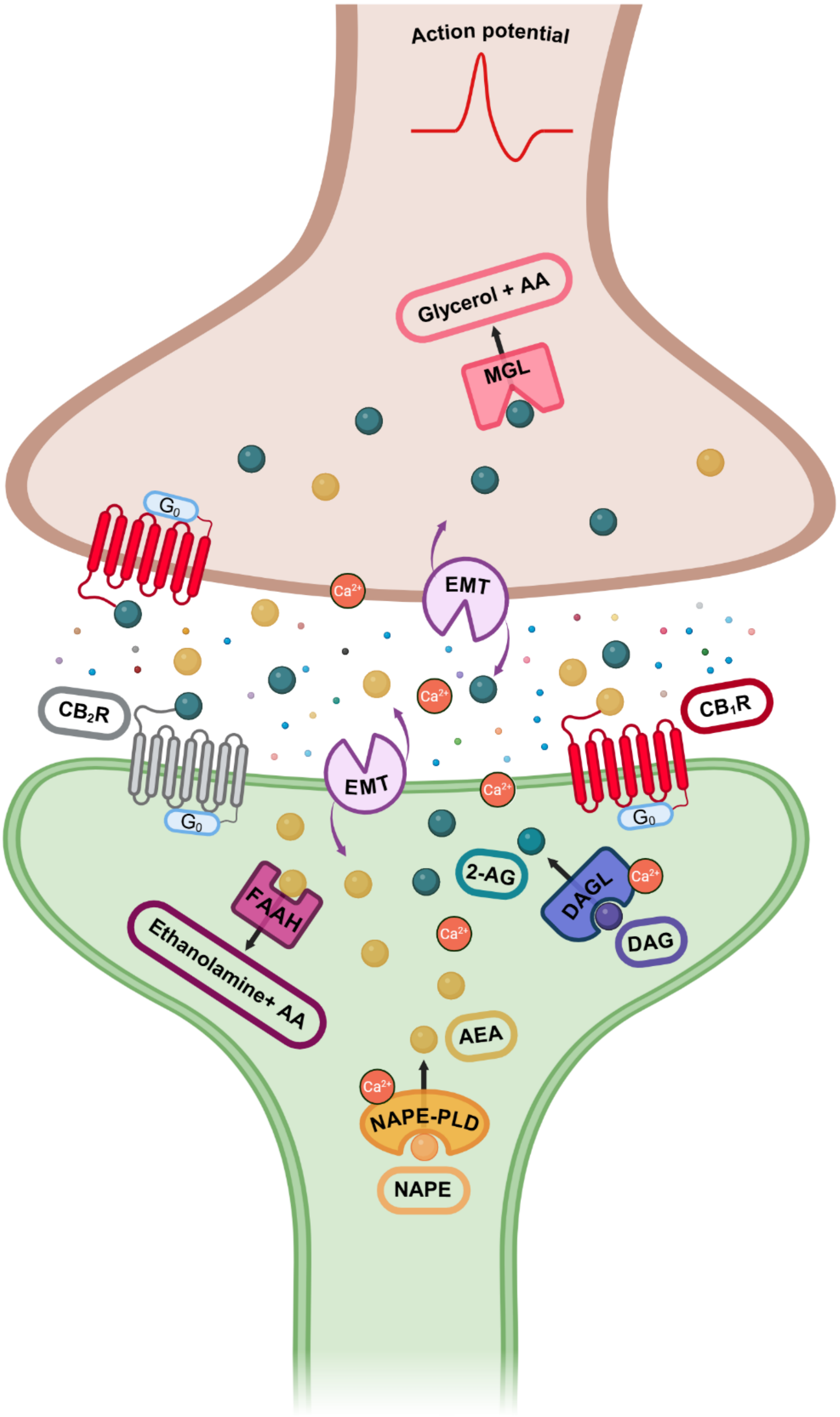

Figure 7. Schematic representation of ECS synapsis. 2-AG: 2-arachidonoylglycerol; AEA: anandamide; AA: arachidonic acid; CB_1R: cannabinoid receptor 1; CB_2R: cannabinoid receptor 2; DAG: diacylglycerol; DAGL: diacylglycerol lipase; EMT: endocannabinoid membrane transporter; FAAH: fatty acid amide hydrolase; MGL: monoacylglycerol lipase; NAPE: *N*-acyl phosphatidylethanolamine; NAPE: *N*-acyl phosphatidylethanolamine phospholipase D.

CBRs are 7-loop transmembrane proteins predominantly coupled to inhibitory G proteins ($G_{i/o}$). CB_1R is mainly concentrated in CNS pre-synaptic neurons, regulating the tones of excitatory (glutamate) or inhibitory (GABA) neurotransmitters. It is also responsible for the altered state of consciousness triggered by THC. On the other hand, CB_2R is also expressed in peripheral tissues and some immunocompetent cells, like macrophages and microglia, suggesting a possible role in regulating the inflammatory cascade.[37]

Following CBRs identification, two main endogenous ligands were discovered, anandamide (AEA, **9**, **Figure 6**) and 2-arachidonoyl glycerol (2-AG, **10**, **Figure 6**). Both of them are synthesised on demand from arachidonic acid (AA) metabolites in postsynaptic bottoms, and they are secreted in response to increased Ca^{2+}-intracellular levels, migrating out of the neurons through specific endocannabinoid membrane transporter. In CNS, they act as retrograde messengers within the synaptic cleft, engaging pre-synaptic CB_1R and CB_2R in neurons, but they could also trigger CB_2R superficially expressed by immunocompetent CNS cells, such as microglia.[38] In competition assays performed in COS cells transfected with either CB_1R or CB_2R, 2-AG demonstrated to fully agonise CB_1R (K_i = 472 nM) and CB_2R (K_i = 1400 nM) but displayed lower affinity compared to AEA (K_i values of 252 and 581 nM for CB_1R and CB_2R, respectively), which act as a partial agonist.[39] Besides CBRs, both AEA and 2-AG can interact with other biological targets, such as peroxisome proliferator-activated receptors (PPARs), deorphanised G protein-coupled receptors, like GPR55, and ion channels, particularly the vanilloid-sensible transient receptors.[40]

The biosynthesis of these two molecules follows two different routes, requiring a sequence of different enzymes that convert membrane phospholipids, like phosphatidylethanolamine (PE), phosphatidyl-cholines (PCs) and phosphatidylinositol 4,5-phosphate (PI 4,5-phosphate), into the endocannabinoids (**Figure 7**). The most common and straightforward biosynthetic pathway affording AEA starts with *N*-acyl phosphatidylethanolamine, which is obtained through acylation of PE mediated by specific Ca^{2+}-dependent or independent acyltransferase. Then, this intermediate is hydrolysed in a one-step process by *N*-acyl phosphatidylethanolamine phospholipase D (NAPE-PLD), providing AEA. On the other hand, 2-AG derived from the catabolism of PCs or PI 4,5-biphosphate, which furnishes diacylglycerol species. These latter are subsequently metabolised by diacylglycerol lipase α and β (DAGLα and DAGLβ), leading to 2-AG. Alternative biosynthetic routes to obtain both AEA and 2-AG have also been described in literature.[41]

As above mentioned, AEA and 2-AG stimulate CBRs, thus playing pivotal roles in interconnected physiological and pathological signalling pathways. Direct agonism elicited by exogenous and endogenous ligands proved to exert interesting activity in neurological and neurodegenerative diseases. Phytocannabinoids (**7** and **8**), and synthetic CBRs agonists are well-known to possess antinociceptive, anti-inflammatory, anticancer, and anxiolytic properties.[42] However, many CB_1R ligands demonstrated to induce depression and suicidal thoughts (inverse agonist), or hallucination and altered state of consciousness (agonists). Moreover, chronic use of THC seems to foster psychosis. These effects are correlated with promiscuous CB_1R signalling, which could recruit different G proteins ($G_{s/q}$), under specific circumstances.[43] Therefore, the interference with noradrenergic and dopaminergic networks as well as its role in reward system might explain the arising side effects caused by acute and chronic CB_1Rs overstimulation. The development of allosteric agonists and orthosteric biased ligands hold promise in overcoming these issues. However, research in these fields is still poor, and overwhelming problems, like drug promiscuity, hinder their systematic application.[42–44]

An alternative way to stimulate ECS is blocking the hydrolytic processes operated by endocannabinoids' catabolic enzymes. This would augment the levels of AEA and 2-AG, indirectly activating CBRs and their neuromodulatory pathways. AEA and 2-AG catabolism is extremely complex, and it can proceed through various mechanisms. Oxidative metabolism, mainly conducted by cyclooxygenase-2 and lipoxygenases, produces several compounds, whose biological activity appears to be unique and should be further investigated.[45] The more extensive hydrolytic catabolism relies on fatty acid amide hydrolase (FAAH), breaking-down AEA, and monoacylglycerol lipase (MGL), metabolizing 2-AG, though FAAH and alpha/beta-hydrolase domain containing 6 and 12 (ABDH6 and ABDH12) are also involved in this process. Impairing FAAH and MGL catalytic activities proved to exert all the beneficial outcomes associated with ECS stimulation, limiting CB_1R-related side effects thanks to their localized action only in overstimulated area and the lower in intensity but prolonged CBRs activation compared to direct agonists.[46]

1.6 Monoacylglycerol lipase

MGL is a 33 kDa homodimeric protein belonging to the α/β serine hydrolase superfamily and located on the surface of cell membrane. It accounts for 85% of 2-AG catabolism, which forms AA and glycerol, and its distribution is mostly concentrated in adipose tissues and CNS, particularly in astrocytes and presynaptic neurons expressing CB_1R.[47] Three-dimensional structure of MGL was resolved through X-ray diffraction, highlighting the critical features of this enzyme (**Figure 8**).[48]

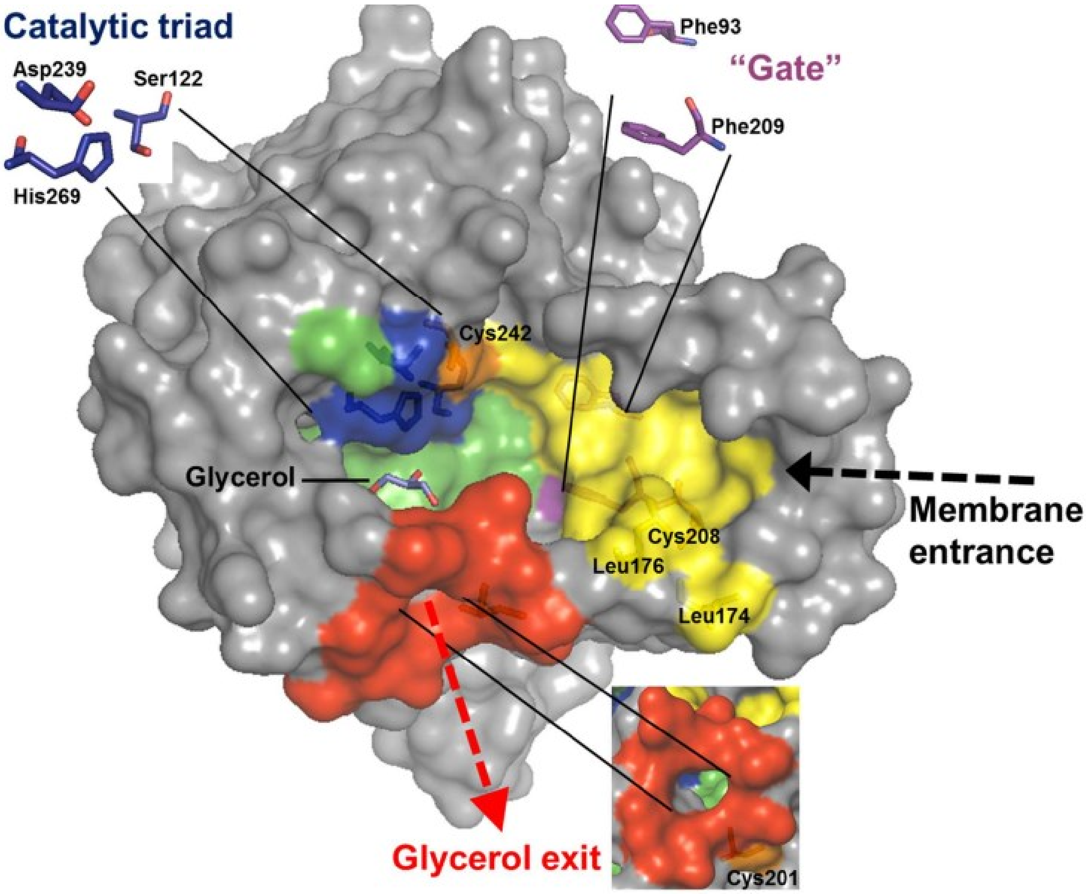

Figure 8. Key structural features in MGL enzyme.[49]

Six α-helices surround a central β-sheet, composed of seven parallel and one antiparallel strands. Above this latter, a cap domain, acting as a lid, allows MGL to switch from an open to a closed conformation. At one end, the flexible α_4 helice and the loop connecting this feature to α_5 helice, comprising Leu 174 and Leu 176, assume a U-shape conformation, providing a wide access site to the active site. A bipartite hydrophobic tunnel linking the MGL's catalytic site with cell membrane accommodates the flexible acyl chain of 2-AG. In this channel, Phe93 and Phe209 are thought to play gating roles in driving ligands' conformation during catalysis.[50] The hydrolytic machinery is constituted by a classical Ser-His-Asp catalytic triad, particularly Ser122, His269, and Asp239. Ser122 is placed in the nucleophilic elbow between α_3 and α_5, near to the oxyanion hole, a highly conserved region delineated by Ala51 and Met123 stabilising the tetrahedral intermediate generated during the catalytic process. Alongside the active site, an additive hydrophilic cavity accommodates 2-AG polar head, facilitating glycerol to migrate out the enzyme.[48,50] Furthermore, three pivotal cysteine residues help preserving the functional conformation of the ligands, hence contributing in tuning MGL's activity.[51]

The hydrolytic process metabolizing 2-AG occurs in 5 steps, involving a sequence of nucleophilic attacks and structural rearrangements, ultimately leading to the regeneration of the catalytic triad and the exit of AA and glycerol (**Figure 9**).

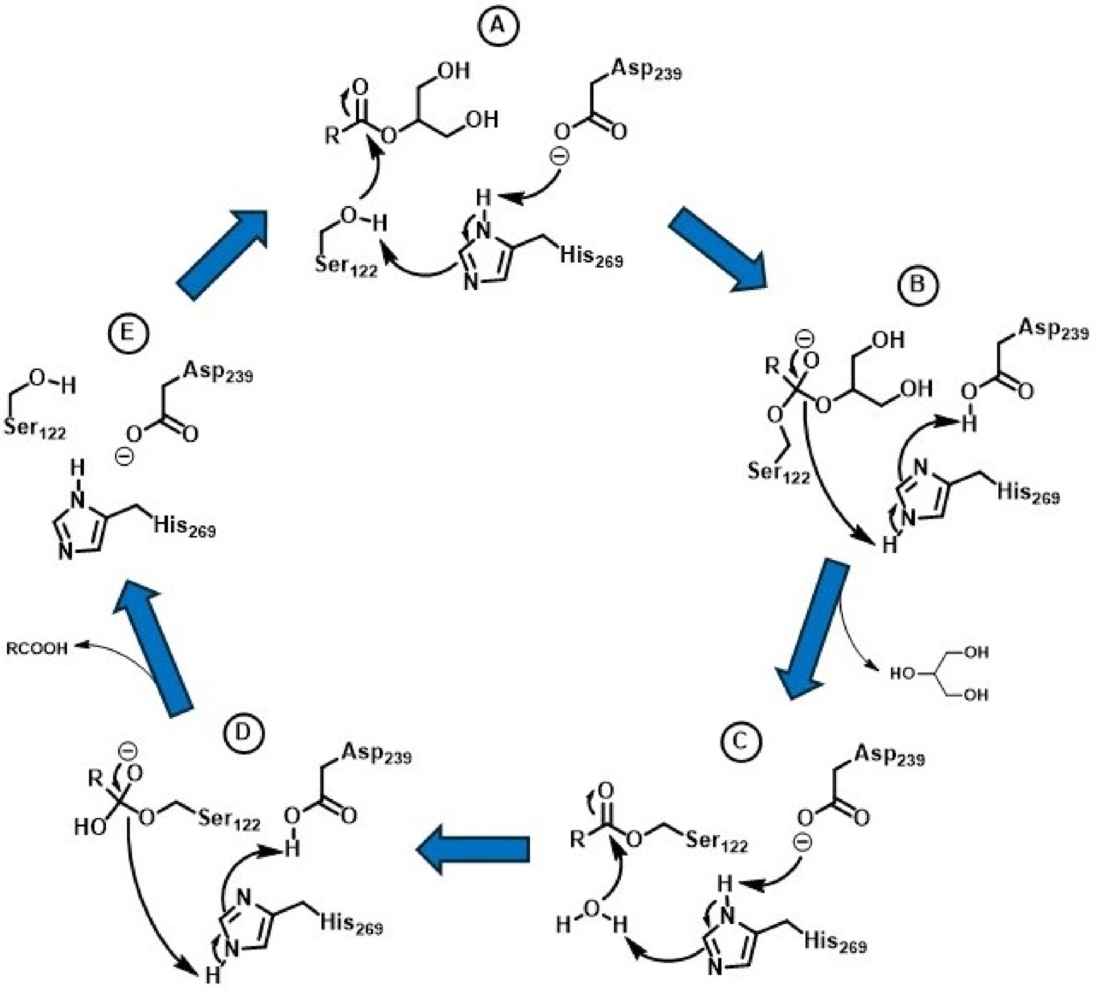

Figure 9. Schematic representation of MGL catalytic cycle. A) Following the deprotonation of its hydroxylic moiety, catalytic Ser122 attacks the carbonylic centre, forming a tetrahedral intermediate. B) Electronic rearrangements allow the exit of glycerol, leading to Ser122 esterification. C) Upon its activation, a molecule of water, present in the hydrolytic site attaches the carbonylic centre, forming another tetrahedral intermediate. D) Electronic rearrangements allow the exit of the appropriate carboxylic acid, regenerating all the catalytic residues of MGL (E).

To date, several irreversible and reversible MGL inhibitors have been developed, constituting a wide library of pharmacological tools exerting positive effects for the potential treatment various pathological conditions.[52]

1.6.1 Monoacylglycerol lipase inhibitors

MGL inhibitors (MGLis) could covalently or non-covalently bind specific critical amino acidic residues of the target enzyme. Moreover, these compounds irreversibly or reversibly inhibit the target protein, depending on which essential electrophilic moiety, also called warhead, is embedded inside their scaffold. Therefore, MGLis could be clustered based on these fragments' chemical structures, reflecting their mode of action.

Irreversible inhibitors

The first series of irreversible MGLis targeted the cysteine thiol residues near the active site, impairing MGL's activity. Rational optimisation of maleimides and sulfhydryl-containing scaffolds led to octhilinone (**11**, **Figure 10**) and CK16 (**12**, **Figure 10**), displaying nanomolar potencies in MGL enzyme inhibition. Notably, the enzymatic inhibition does not occur through a Michael reaction between the electrophilic warhead and the Cys thiol residues, but via a disulfide bond adduct formation.[51,53] **12** also showed excellent selectivity over MGL cognates, particularly more than 2800-fold over FAAH. Despite this, the potential off-target interactions of these derivatives arose that could generate many health issues thus halting their future development.

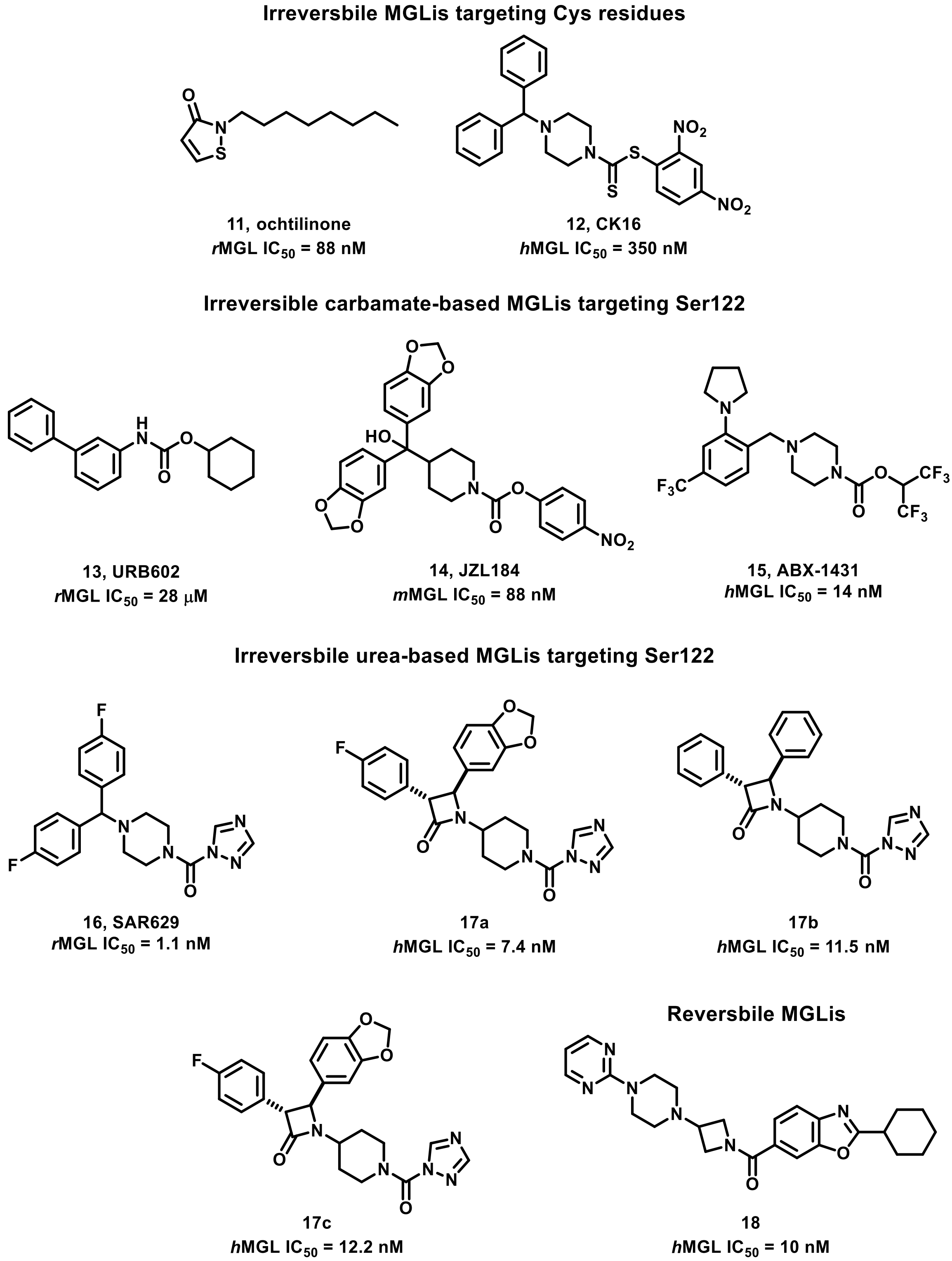

Figure 10. Chemical structures and IC_{50} values for *r*MGL, *m*MGL, or *h*MGL of the most relevant irreversible and reversible MGLis.

On the other side, targeting Ser122 appeared to be a more feasible way to interfere with MGL hydrolytic activity. The selected MGLi should enter inside the active site, and it should undergo a nucleophilic attack by Ser122. Following this, a fragment of the MGLi, titled leaving group (LG), should exit from the hydrolytic site, thus allowing Ser122 irreversible acylation, and subsequently arresting the catalytic cycle. Molecules featuring a carbamate as an electrophilic centre, such as URB602 (**13**, **Figure 10**), exhibited modest to good inhibitory potency for MGL but lacks selectivity over FAAH. The first groundbreaking pharmacological tool was JZL184 (**14**, **Figure 10**), embedding a Y-shaped aromatic region that abolishes off-target activity over the FAAH enzyme (6 μM). In the quest for reducing the potential harmful effects, the 4-nitrophenyloxy motif of **14** was replaced with a hexafluoroisopropyloxy, N-hydroxysuccinimidyl, or trifluoromethyl glycol carbamates, providing a second generation of MGLis.[52] One of them, ABX-1431 (**15**, **Figure 10**), exhibited optimal inhibitory potency and selectivity, oral availability, and BBB permeability.[54] Nonetheless, it failed to control tics in Tourette Syndrome patients during a phase 2 clinical trial, despite promising preliminary results.[55]

In parallel, Sanofi-Aventis identified urea-based compounds as a suitable alternative to carbamates. Among them, SAR629 (**16**, **Figure 10**) unravelled the mechanism of action of Y-shaped ureas-based MGLis, confirming the formation of a tetrahedral anionic intermediate with Ser122 via X-ray structure determination.[56] Its biphenyl methane region perfectly fits inside two lipophilic binding pockets, entailing MGL selectivity over FAAH. Notably, one of these hydrophobic cavities ends with a polar region, suggesting possible additive contacts. The rigid piperidine linker confers the appropriate conformation to the molecule, whereas it establishes Van der Waals interactions within the lipophilic channel. Further, the urea oxygen forms a crucial hydrogen bond with Met123, placed in the oxyanion hole. The pivotal feature in **16** is the triazole ring, whose corresponding "acid" possess a pKa value around 10. Indeed, Aaltonen *et al.* reported that the pKa of the leaving group correlates with its ability to be displaced under the nucleophilic attack by Ser122, and it should ideally be between 8 and 11.[57] This peculiar characteristic explained the low nanomolar inhibitory potency of compound **16**.

The research group where I have performed my PhD internship previously contributed to this field by rationally designing and synthesising a series of *β*-lactam based MGLis. The new compounds typified by compound **17a** (**Figure 10**) challenged the Y-shape diphenylmethane-based structure of the MGLis developed so far by exploiting the drug-like azetidinone scaffold as a valid support for projecting (via a dihedral angle geometry) the hindering aromatic moieties into two pockets of the MGL enzyme. This allowed the identification of potent and selective compounds over FAAH enzyme and other serine hydrolases of the CNS. The hit compound of the series was selected as a promising tool for further exploration of its therapeutic potential in MS. In fact, **17a** displayed a promising activity in the experimental autoimmune encephalitic (EAE) mice. Bottom-up proteomic analysis confirmed the tetrahedral intermediate between Ser122 and **17a**, whilst rapid dilution assays proved that it blocks MGL in a time-dependent irreversible fashion. These results prompted the development of a second generation of 2-azetidone-based analogues.[58] Among the new analogues the crystal structure of compound **17b** (**Figure 10**) inside MGL was determined and it substantially overlapped with the one of **10**. These data were used for elucidating the mechanism of inhibition of this new class of compounds and confirmed their hypothesised binding pose. Moreover, **17c** (**Figure 10**) displayed an excellent IC_{50} value for MGL, with low-to negligible inhibition potency for FAAH, and improved distomer/eutomer ratio compared to **17a** (900 vs 9.6, respectively).[59]

Reversible inhibitors

Another strategy for tackling MGL activity is the reversibly binding to some characteristic features, temporarily inhibiting the enzyme, and increasing 2-AG levels. To date, various scaffolds were reported to act as reversible MGLis, potentially reducing the side effects elicited by an overstimulation of CBRs. The archetypes of these compounds are piperazine azetidine amide-based derivatives, like **18** (**Figure 10**), patented by Janhsenn Pharmaceuticals. X-ray diffraction demonstrated that this ligand could effectively interact with MGL's cap domain, promoting its closed conformation. This opened the quest for new amide-based compounds acting as reversible MGLis.[60] However, research in this field is still limited by the unsatisfactory MGL inhibitory potency of the currently developed pharmacological tools.

1.7 Fatty acid amide hydrolase

FAAH is a 66 kDa membrane-bound enzyme possessing both esterase and amidase functions. It predominantly accounts for AEA metabolism, generating AA and ethanolamine, but it can also degrade 2-AG, and other bioactive N-acylated lipids, amines and amino acids.[61] Two *h*FAAH isoforms, namely *h*FAAH-1 and *h*FAAH-2, were isolated, showing marked homology between their structure with distinct tissues distribution. Both isoforms are expressed in peripheral tissues, like lungs, kidneys, liver, and prostate. *h*FAAH-2 and not *h*FAAH-1 was found in heart, while *h*FAAH-1, but not *h*FAAH-2, could be detected in the CNS.[62] Particularly, immunohistochemical assays performed in mouse brain highlighted a wide distribution of FAAH throughout the CNS. Furthermore, this study underlined an intricate neuromodulatory tuning of CB_1Rs, occurring through either postsynaptic modulation or via proximal regulation. Notably, not only neurons but also oligodendrocytes constitutively express high levels of FAAH.[63]

Unfortunately, biochemical issues, such as instability in the medium as well as aggregation phenomena, impede to gain structural information on *h*FAAH, thus a humanised rat (*h/r*)-FAAH enzyme was generated applying site-directed mutagenesis technique.[64] This engineered protein shares ≈82% sequence identity with *r*FAAH, displaying the same characteristics features, recapitulated in **Figure 11**.

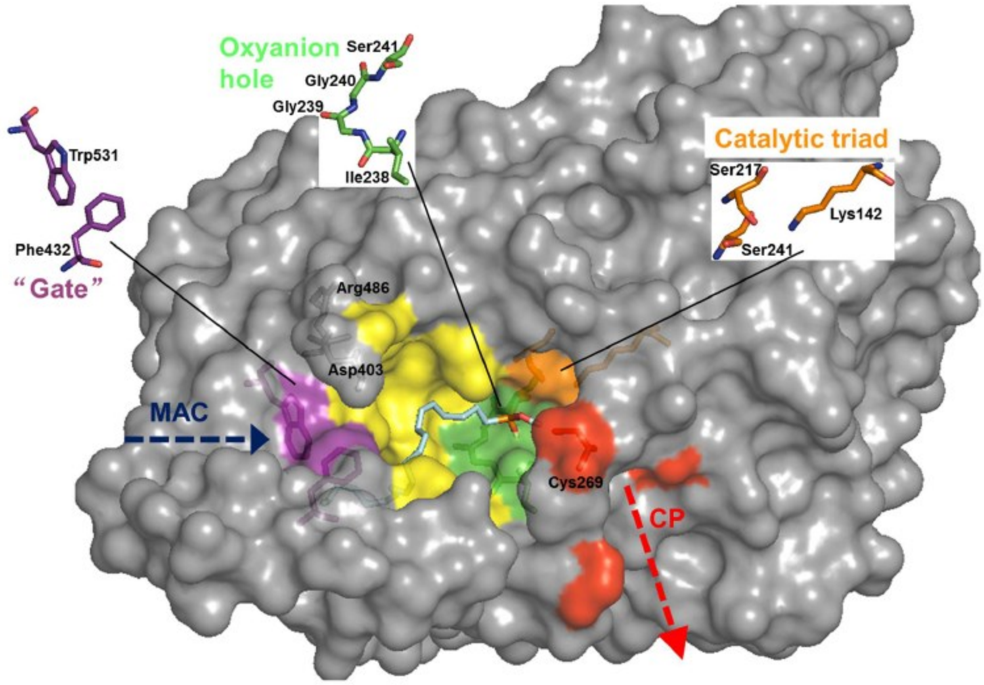

Figure 11. Key structural features in FAAH enzyme.[49]

All the evidence gained highlight that FAAH appears as a homodimer comprising a tangled protein core, made of 11 β-sheets, surrounded by 24 α-helices. The broad plethora of substrates reflected the presence of multiple binding pockets in FAAH architecture. A long tunnel, titled membrane access channel (MAC), links the membrane to the active side. Its amphiphilic walls are almost completely covered with hydrophobic amino acid, permitting to accommodate the acyl chain of the endogenous ligands. The remaining rim is constituted by Arg486 and Asp403, that interacts with the substrates polar head, forcing them to assume the correct binding conformation. Nearby the catalytic site, two additional binding pockets could be detected. The lipophilic tail of the substrates is well fitted inside the acyl-chain binding pocket (ABP), due to its hydrophobic nature. On the other hand, the cytosolic port (CP), covered with hydrophilic amino acids, represents a good exit route for polar metabolites, such as ethanolamine and AA. FAAH enzyme embeds a unique Ser-Ser-Lys catalytic triad (Ser241-Ser217-Lys142), as well as a peculiar circular oxyanion hole.[65]

The hydrolytic machinery processes FAAH substrates in five steps, leaving the corresponding carboxylic acids and ethanolamines (**Figure 12**).

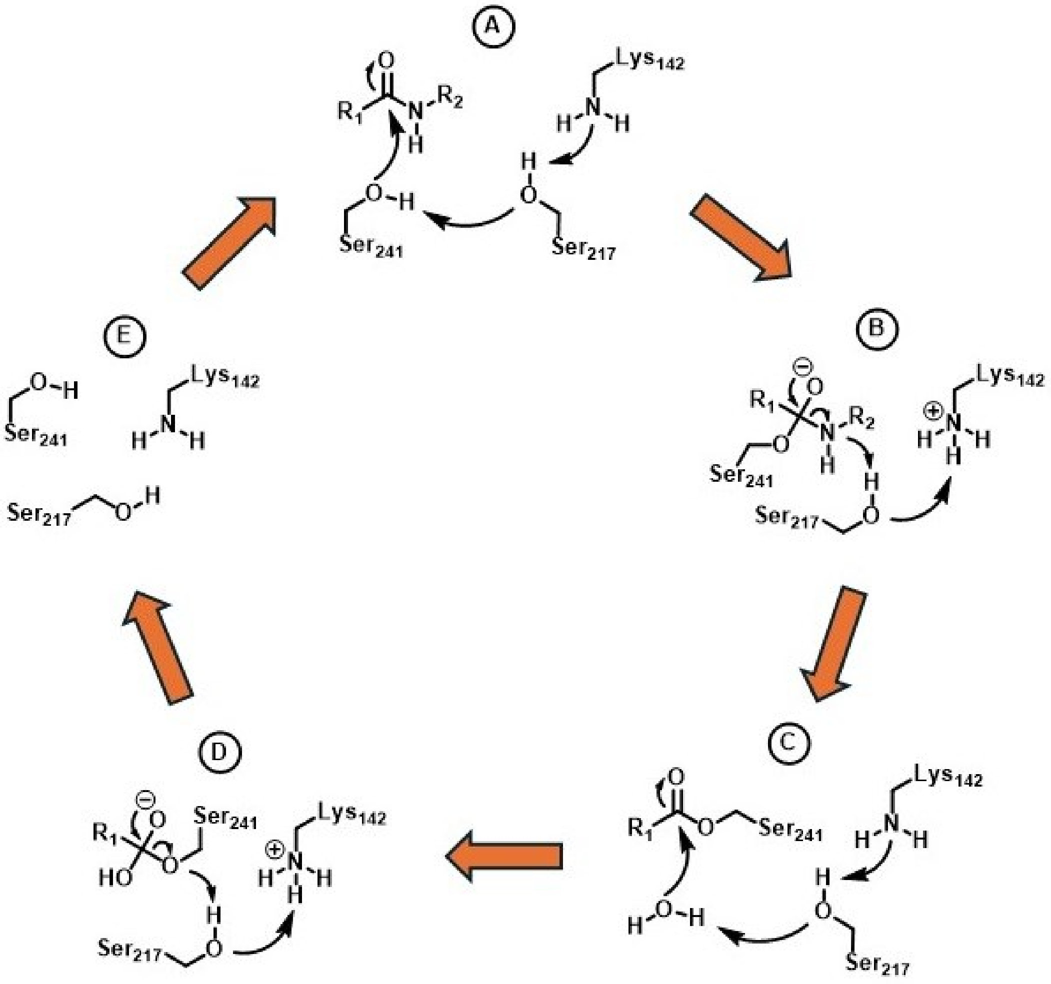

Figure 12. Schematic representation of FAAH catalytic cycle. A) Following the deprotonation of its hydroxylic moiety, catalytic Ser241 attaches the carbonylic centre, forming a tetrahedral intermediate. B) Electronic rearrangements allow the exit of the appropriate ethanolamine, leading to Ser241 esterification. C) Upon its activation, a molecule of water, present in the hydrolytic site, attaches the carbonylic centre, forming another tetrahedral intermediate. E) Electronic rearrangements allow the exit of the appropriate carboxylic acid, regenerating all the catalytic residues of MGL (E).

Likewise, both reversible and irreversible FAAH inhibitors (FAAHis) of this target have been descripted so far, emphasising its relevance in tackling several pathological conditions.[66]

1.7.1 Fatty acid amide hydrolase inhibitors

A plethora of diverse scaffolds were reported to reversibly or irreversibly inhibit FAAH, providing many pharmacological tools to indirectly modulate AEA levels. As for MGL, they displayed electrophilic warheads able to covalently or non-covalently interact with FAAH's peculiar feature. These compounds could be classified based on their structural architecture, ultimately influencing their inhibitory mechanism of action towards FAAH.

Reversible inhibitors

Among the first series of FAAHis, ketone-based compounds stood out as the most relevant pharmacological agents to be further develop. They embed a long unsaturated carbon tail, mimicking the one present in fatty acid derivatives, and harbour an activated carbon, a ketone moiety. Among them, the trifluoromethyl ketone **19** (**Figure 13**) emerged as a potent reversible inhibitor of FAAH enzyme. Although this class exhibited poor selectivity over relevant off-targets, SAR analysis identified some critical features. First, kinetic studies demonstrated that more electrophilic warheads positively correlate with inhibitory potency. Then, a phenylhexyl chain was identified as a suitable bioisosteric motif to replace the long fatty acid-inspired carbonous chain.[67]

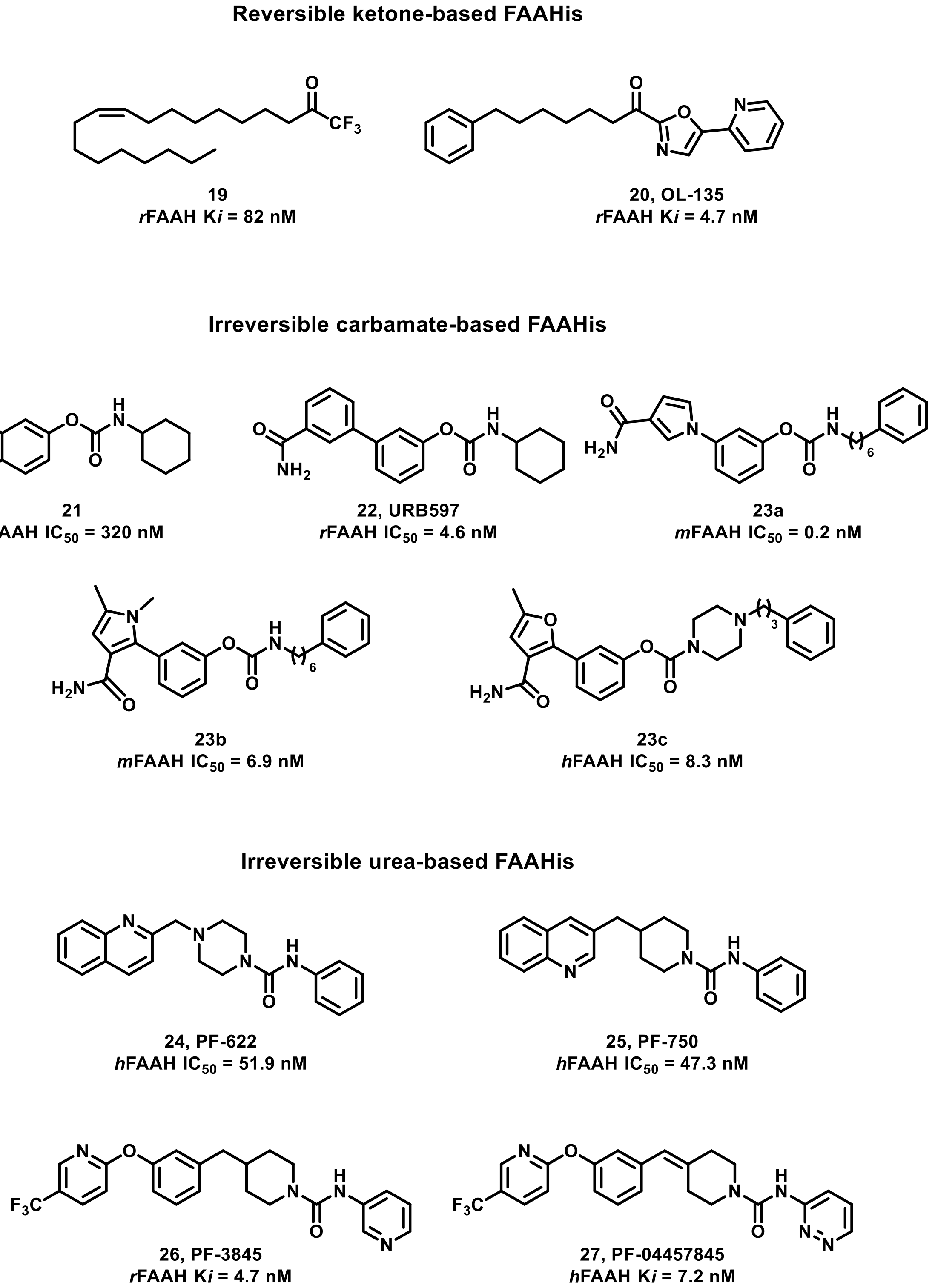

Figure 13. Chemical structure, K_i and IC_{50} values for *r*FAAH, *m*FAAH or *h*FAAH of the most relevant reversible and irreversible FAAHis.

All this information were translated in the following class of compounds, namely the α-ketoheterocycles. These latter showed high inhibition potency for the target protein associated with good selectivity over FAAH cognates. Particularly, crystal structure of

OL-135 (**20**, **Figure 13**) within the FAAH binding pocket confirmed that α-ketoheterocycles act as covalent reversible inhibitors, forming a hemiketal adduct with the catalytic Ser241, mimicking the tetrahedral intermediate generated during substrates' degradation.[65] Further exploration led to the development of non-covalent reversible inhibitors, like arylisoxaloyl-amides, aryloxyacetamides, and pyrimidine-based derivatives.[66]

Irreversible inhibitors

Huge scientific efforts were made to develop irreversible FAAHis, ensuring prolonged *in vivo* activity compared to reversible ones. Although the potential promiscuity could be a potential threat to their use, structural modifications demonstrated ability in managing some off-target effects. The research in this field stemmed from the rational structural modification of a known acetylcholinesterase inhibitor (**21**, **Figure 13**), that embeds a carbamate moiety. This molecule captivated the scientists' interests as a suitable candidate to achieve effective FAAH inhibition.[68] Extensive SAR analysis aiming at introducing few point modifications ultimately provided a potent and selective FAAHi, URB597 (**22**, **Figure 13**). This latter became a standard reference molecule for future research. **22** was pivotal for proving that the carbamate moiety could efficiently undergo nucleophilic attack by Ser241, subsequently carbamylating this pivotal residue, hence halting AEA hydrolysis.[69] Inspired by this evidence, the research team where I have performed my PhD internship previously developed several carbamate-based FAAHis inspired to **22**. Some of the new FAAHis were potent and selective inhibitors and were used as new tools for different pathological conditions.[70–72] All these compounds present a lipophilic chain joint through a carbamate group with a biarylic system, constituted of a *m*-disubstituted phenyl group connected to a five-member heterocycle. Initially, compound **23a** (**Figure 13**) was identified as a potent and selective FAAHi.[70] The electrophilic warhead undergoing Ser241 nucleophilic attack is constituted by a carbamate unit, which connects the phenylhexyl tail to a phenyl-carboxyamidopyrrole system. Structural modifications of both the biarylic system, using different five membered heterocycles, and the hydrophobic linker, introducing rigid *N*-containing aliphatic ring, improved the PK and PD properties, furnishing two interesting new pharmacological tools, **23b** (**Figure 13**) and **23c** (**Figure 13**), exhibiting interesting activity in epilepsy and neuroinflammatory conditions.[71,72]

In parallel, many urea-based scaffolds were largely exploited as alternative warheads to target Ser241. Although previous efforts identified promising derivatives, the first groundbreaking compounds were described by Pfizer in 2007. These latter embed piperazine, as shown in PF-622 (**24**, **Figure 13**), or piperidine, like in PF-750 (**25**, **Figure 13**), moieties connected through a urea moiety to an aniline fragment, bestowing excellent inhibitory potency for FAAH and selective profile over relevant off-targets. Moreover, the covalent irreversible inhibition of the target occurs through Ser241 acylation following aniline displacement, and it was proved via radioactive labelling studies, MS spectrometry, and X-ray diffraction.[64,73] In the quest for new FAAHis with improved PK and PD profiles, several analogues were synthesised. Among them, PF-3845 (**26**, **Figure 13**) displayed interesting anti-inflammatory properties in mice. Furthermore, crystal structure analysis underlined that **26** positioned the reactive urea moiety next to catalytic Ser241, facilitating its carbamylation and the following displacement of the 3-aminopyridine leaving group. As for **19**, the remaining part of the molecule occupies the ABP, engaging Phe192 with its phenyl group while establishing several Van der Waals interactions with the hydrophobic amino acids covering this region. Notably, compound **26** binding to FAAH induces structural rearrangements of Phe432 and Met436, modifying both ABP and MAC sizes thereby favouring inhibitor accommodation.[74] Further scientific efforts brought to the discovery of PF-04457845 (**27**, **Figure 13**), a potent, selective and druggable FAAHi. Despite not showing any analgesic effects in patients affected by knee osteoarthritis, it exhibited promising activity in cannabis withdrawal treatment during a phase IIa clinical trial, and it is currently being evaluated for other therapeutic use.[66] Therefore, scientific efforts were fuelled by this encouraging data, and the quest for next-generation FAAHis based on carbamate or urea scaffolds is still compelling.

1.7.2 MGLis and FAAHis as potential pharmacological tools in neuroinflammatory-based conditions

Due to their wide distribution throughout the body, and since the ECS is highly interconnected with multiple modulatory and neurotransmitter systems, MGLis and FAAHis may counteract several pathological conditions, affecting both peripheral, and central tissues.[75] Particularly, the central roles played by CBRs modulation in regulating neuroinflammatory, neurodegenerative, and immune processes attracted scientific interests. CB_2R activation lowers the levels of crucial proinflammatory cytokines, like TNF-α, IL-1β, and IL-6, in AD, PD, and HD as well as in MS, whereas CB_1R reduces glutamate and NMDA-excitotoxicity, whereas. Furthermore, mainly CB_2R but also CB_1R contribute to diminish the recruitment of immune cells, such as leukocytes, and stabilises BBB structure, thus suggesting a potential control over MS dysregulated autoimmunity.[76] In this framework, both selective MGLis and FAAHis showed intriguing activity in neuroinflammatory-based conditions, including NDs and MS treatments.

In AD mice models, derivative **14** attenuates neuroinflammation by impairing IL-1β and TNF-α release, whilst suppressing microglial, and astrocytes activation. Moreover, it also mitigates tauopathies and amyloid-β sedimentation, whilst enhancing synaptic plasticity.[77–79] Compound **14** administration could revert neurotoxicity induced by MPP^+

in mice and human cellular models of PD, fostering the secretion of neuroprotective and anti-inflammatory mediators, like TGF-β and GDNF.[80–82] Lastly, it also alleviates AMPA-excitotoxicity in oligodendrocyte, preventing myelin depletion in MS.[83] Our *β*-lactam based MGLis perfectly fits in this framework, as it was effective in alleviating the clinical symptoms in EAE mice.[58]

On the other hand, compound **22** was proposed as adjuvant strategy to dwindle *L*-DOPA behavioural side effects in MPP$^+$-exposed monkey models of PD, while in MPP$^+$-treated mice it exerted relevant neuroprotective effects, likely due to downregulation of NMDA receptors and antioxidant properties.[84,85] Moreover, **22** proved to concurrently shift BV2 microglia cells into M2 anti-inflammatory phenotype, and promote the removal of amyloid β aggregates via autophagy in AD rodent models.[86,87] Within this context, the previous contributions of my research team expanded the pharmacological tools able to counteract neurodegenerative and neuroinflammatory-based conditions, such MS.[72,88,89]

1.8 Diacylglicerol lipases

DGL enzyme is a α/β hydrolase which acts as the main character in 2-AG biosynthetic pathway, present in two different isoforms in the human body, DGLβ (≈70 kDa) and DGLα (≈120 kDa). DGLα is highly distributed throughout the CNS, whereas DGLβ is mainly located in peripheral immuno-competent cells, but also in hippocampal region and microglia.[90]

No crystal structures of *h*DGLα or *h*DGLβ have been published yet. Nevertheless, sequence and structure-based methodologies based on *Drosophila* DGL allow to elucidate human DGLα and DGLβ architectures. Both enzymes display 4 transmembrane helices and a canonical catalytic domain, with 8 β-sheets strands as core structure. A highly conserved catalytic triad, constituted of a Ser-His-Asp sequence, is responsible for the physiological activity. Further, structural analysis of the crystal structure of fungal DGL suggests that the catalytic site region is covered by an extensive loop motif, switching from a closed to an open conformation, thus regulating substrates' accessibility to the active site. The major difference between DGL isoforms is the presence of a long C-terminal tail in DGLα but not in DGLβ, involved in protein recognition.[90,91]

The catalytic cycle of these enzymes has not been deciphered yet. Nevertheless, it is thought that the catalytic Ser residue would attack the ester functionalities of DAG, breaking them down, thus liberating a monoacylglycerol, including 2-AG, and a free fatty acid, depending on the specific DAG structure. Since DGLα and DGLβ can hydrolyse a wide plethora of DAGs, including arachidonoyl-containing ones, the modulation of their activity might lead to several beneficial effects in many pathological conditions. DGLα inhibition has been associated with promising activity in obesity and alcoholism pharmacological treatments,[92,93] contrasting body weight gaining and ethanol consumption, whilst blocking DGLβ activity resulted in antiallodynic effects both in inflammatory and neuropathic pain mouse models.[94,95]

1.8.1 Diacylglicerol lipases inhibitors

Through the years, several classes of compounds exhibited interesting activity as selective DGLα or DGLβ inhibitors (DGLαis or DLGβis), as well as promiscuous inhibition of both isoforms (**Figure 14**).

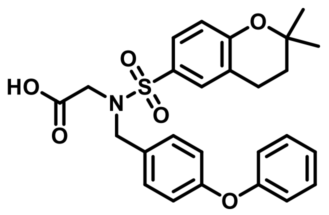

28, LEI106
***m*DGLα IC_{50} = 631 nM**

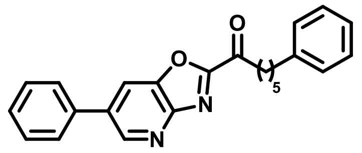

29, LEI105
***m*DGLα IC_{50} = 13 nM**

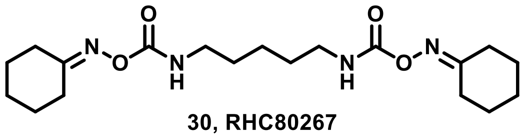

30, RHC80267
***m*DGLα IC_{50} = 5.01 μM**

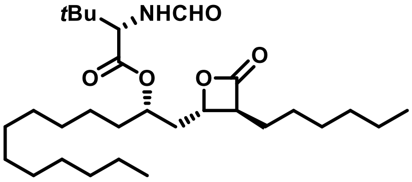

31, THL
***m*DGLα IC_{50} = 1.0 μM**
***m*DGLβ IC_{50} = 100 nM**

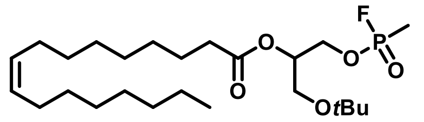

32, OL-5596
***m*DGLα IC_{50} = 100 nM**

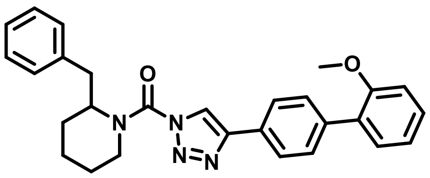

33, KT172
***m*DGLβ IC_{50} = 79 nM**

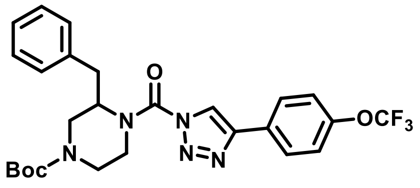

34, DH376
***m*DGLα IC_{50} = 6.3 nM**
***m*DGLβ IC_{50} = 2.51 nM**

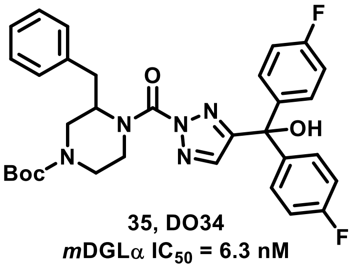

35, DO34
***m*DGLα IC_{50} = 6.3 nM**
***m*DGLβ IC_{50} = 7.9 nM**

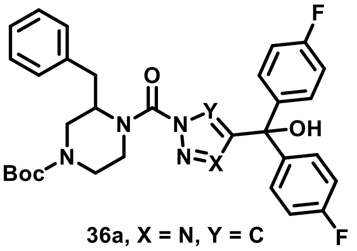

36a, X = N, Y = C
***m*DGLα IC_{50} = 3.0 nM**
***m*DGLα K_i = 10 nM**

36b, X = C, Y = N
***m*DGLα IC_{50} = 6.3 nM**
***m*DGLα K_i = 339 nM**

Figure 14. Chemical structure, K_i and IC_{50} values for DGLα and DGLβ of the most relevant reversible and irreversible DGLαis and DGLβis.

These derivatives can reversibly or irreversibly inhibit DGL, thus providing several pharmacological tools endowed with different mechanisms of action. Completely reversible DGLα/βis, as LEI106 (**28**, **Figure 14**), embed a glycine sulphonamide warhead that enables good potency for the target enzymes, but they can also engage several DGL cognates. Following the same strategy, LEI105 (**29**, **Figure 14**), belonging to a class of α-keto heterocycles, has been described as reversible, potent and selective DGLβi, with promising activity in decreasing hippocampal transmission. However, *in vivo* efficacy of **29** has not been assessed, due to its low activity on DGLα, which is the most abundant isoform in the CNS. On the other hand, bis-oximino-carbamates, like RHC80267 (**30**, **Figure 14**), together with β-lactones, typified by THL (**31**, **Figure 14**), act as irreversible DGLα/βis, but lacking selectivity over other relevant serine hydrolases. Fluorophosphonates, such as OL-5596 (**32**, **Figure 14**), represents a first pitfall in the quest for potent and selective DGLα/βis. Nevertheless, they encompass a potentially harmful warhead, hindering their further progression in clinic.[96] The very groundbreaking compounds in irreversible DGLis context are 1,2,3-triazole ureas. KT172 (**33**, **Figure 14**), a selective DGLβ inhibitor, promotes a profound reorganisation of lipidic metabolism, decreasing 2-AG levels in macrophages, while concurrently mitigating LPS-induced production of TNF-α. This evidence opened the way for developing structural analogues which can overcome **33**'s major limitation, that is the restricted peripheral activity.[97] These efforts culminated in the identification of two equipotent DGLα/βis, DH376 (**34**, **Figure 14**) and DO34 (**35**, **Figure 14**), serving as chemical probes to induce pathological conditions typified by DGL inhibited phenotypes, as well as potential treatments in obesity and NDs.[96,98] Notably, compound **36a** (**Figure 14**), an analogue of **35** missing the O-propargyl moiety on the chiral piperidine ring, integrates optimal DGLα activity and robustly prevent fast-inducing refeeding in mice.[99] Further, **36a** and its analogue **36b** (**Figure 14**), presenting a *N*1-substituted azole motif, underlined that the position of the nitrogen in the heterocyclic leaving group and not its pKa value is essential for substrates' binding.[100] The same warhead core was employed to develop a series of chiral disubstituted piperidinyl ureas, acting as dual ABDH6/DGL inhibitors.[101] Aside from these compounds, no other MTDLs involving DGL enzymes have been reported so far, despite the involvement of these enzymes in critical physiological pathways.

1.9 Aim of the PhD work

Since life expectancy and median survival are continuously growing, the incidence of neurodegenerative and neuroinflammatory-based diseases as well as neurological disorders are continuously increasing. Due to the complex network underlying these diseases, the quest for effective therapies with suitable therapeutic index is still unmet. This goal could be achieved by modulating different biological pathways playing critical roles in the pathological processes, thus applying polypharmacological principles. This PhD work perfectly fits in this framework, providing the development of MTDLs able to modulate the ECS, particularly via the inhibition of its catabolic enzymes, while concurrently tuning different neurotransmitters' networks, like histaminergic system, epigenetic modulators, such histone remodelling protein, or the anabolic enzymes involved in 2-AG biosynthetic pathways. Pursuing these objectives, three distinct class of derivatives were developed, acting as new pharmacological tools either holding promise in fighting neurodegenerative and neuroinflammatory-based diseases, or potentially counteracting neurological disorders.

In this context, I synthesised two novel FAAHis endowed with H3R antagonistic activity, I optimised the synthetic pathway affording the most promising compound of the series employing a flow-chemistry approach, and I contributed in the preliminary pharmacokinetic profile assessment of four selected derivatives. Moreover, I developed the synthetic pathways to afford 16 MGL inhibitors with potential histone deacetylase 6 (HDAC6) inhibitory activity. Lastly, I synthesised two compounds showing dual DAGLα/β-FAAH inhibitory profile.

1.10 Development of dual FAAH/MGL inhibitors integrating H3R antagonism

1.10.1 Background

As previously discussed, both AEA and 2-AG elicit a broad spectrum of therapeutic activity, exhibiting significant overlap between their clinical benefits. Therefore, several polypharmacological agents have been reported to regulate endocannabinoids' tone by simultaneously inhibiting FAAH and MGL enzymes. [102–104] In this context, JZL195 (**37**, **Figure 15**), featuring a 4-nitro-phenyl carbamate, represents the milestone for dual irreversible inhibition of endocannabinoids' catabolic enzyme. Notably, compound **37** not only proved to exert anti-inflammatory and neuroprotective effects in AD mice, but it also showed improved anti-allodynic properties compared to **14** and **22** in a murine neuropathic pain model.[105,106] My research group previously contributed to this field describing the specific structural features to achieve dual FAAH/MGL inhibition within a series of pyrroloquinoxaline-based compounds, exemplified by **38** (**Figure 15**). In this context, the hybrid activity of the constructed molecules was strongly influenced by the spatial configuration imposed by the linker unit, as well as the correct choice of an appropriate leaving group.[107]

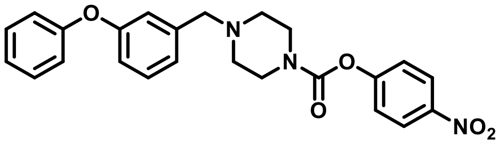

37, JZL195
***m*FAAH = 2 nM**
***m*MGL = 4 nM**

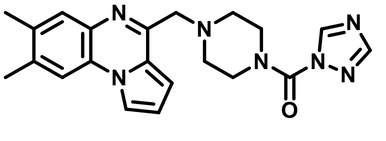

38
***r*FAAH = 32.4 nM**
***r*MGL = 133 nM**

Figure 15. Chemical structures of the most relevant dual FAAH/MGL inhibitors.

Furthermore, the extensive neuro-connectivity of ECS offers a compelling avenue for association with many biological targets through a polypharmacological strategy. Therefore, the pharmacophoric elements useful to attain FAAH inhibition were hybridised with the structural determinants of other relevant enzymatic or neurotransmitter pathways, in order to obtain hybrid molecules potentially addressing CNS diseases.[21,66] In this context, my research team previously embarked in the development of hybrid FAAH/dopamine receptors 2 and 3 (D_2 and D_3, respectively) ligands and dual FAAH/HDAC6 inhibitors, exhibiting significant anti-inflammatory and antioxidant properties.[88,89] On the other hand, the same approach is poorly explored for MGL enzyme, and there is no evidence reporting its application in CNS affections.[21,108] Seeking this approach, during my PhD internship I developed a novel class of dual FAAH/MGL inhibitors integrating antagonistic activity towards histamine H_3 receptor (H_3R).

H_3R is a $G_{i/0}$ coupled receptor organised in 7 transmembrane loops (TMs1-7), linked through three extracellular loops (ECLs1–3) and three intracellular loops (ICLs1–3) with an amphipathic helix.[109] It is highly concentrated on neurons, but it is also moderately expressed in oligodendrocytes and minimally in astrocytes, glial, and Schwann cells.[110] Due to its predominant pre-synaptic localisation in CNS neurons, it acts as auto and heteroreceptor, regulating the levels of histamine and other relevant neurotransmitters, like dopamine, acetylcholine, noradrenaline. This multi-modulating ability is attracting of interests for contrasting many pathological conditions, particularly via H_3R antagonism, that potentiate histamine and other neurotransmitters' release from the pre-synaptic end.[111]

To date, several H_3R antagonists were reported in the literature, classified in imidazole- and non-imidazole containing compounds. These synthetic efforts delineate a general pharmacophore, comprising the structural determinants to achieve effective H_3R antagonism. This encompasses a tertiary basic amine, an aliphatic linear linker, a central aromatic core, and highly variable arbitrary zone (**Figure 16A**).[112]

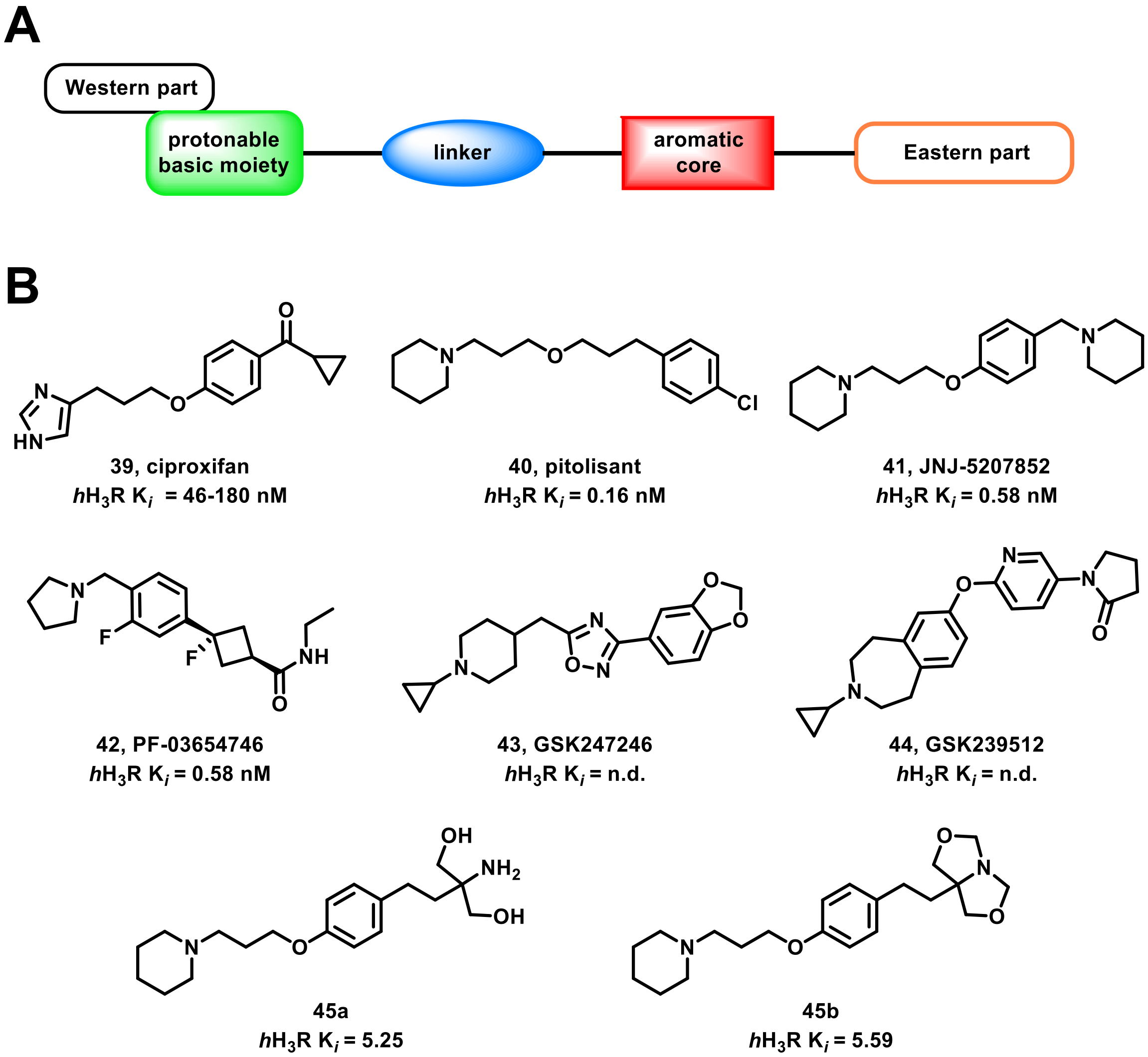

39, ciproxifan
$hH_3R\ K_i$ = 46-180 nM

40, pitolisant
$hH_3R\ K_i$ = 0.16 nM

41, JNJ-5207852
$hH_3R\ K_i$ = 0.58 nM

42, PF-03654746
$hH_3R\ K_i$ = 0.58 nM

43, GSK247246
$hH_3R\ K_i$ = n.d.

44, GSK239512
$hH_3R\ K_i$ = n.d.

45a
$hH_3R\ K_i$ = 5.25

45b
$hH_3R\ K_i$ = 5.59

Figure 16. A) General scaffold of H_3R antagonists. B) Chemical structures and K*i* values on *h*H_3R of the most relevant imidazole and non-imidazole based H_3R antagonists.

Imidazole-based derivatives, typified by ciproxifan (**39**, **Figure 16B**), showed good affinity for H_3R but is plagued by bad PK and PD properties, such as low BBB permeability and lack of selectivity over histamine H_4 receptor (H_4R). Moreover, imidazole ring poses many concerns for its mutagenic potential, limiting further development. Therefore, several series of non-imidazole embedding H_3R antagonists were subsequently developed, bringing to the identification of highly potent and selective compounds, like pitolisant (**40**, **Figure 16B**), JNJ-5207852 (**41**, **Figure 16B**), and PF-03654746 (**42**, **Figure 16B**).[113]

The crystal structure of the H_3R with **42** and the subsequent docking studies performed with other H_3R antagonists, including **40** and **41**, showed that these molecules shared substantial overlap of their binding pose within H_3R. Particularly, the protonable tertiary amine residue, always present in these classes of compounds, forms a salt bridge with the key Asp114, pivotal for the antagonistic activity. Although the binding site is quite shallow, an extended binding pocket (EBP) protrudes towards the extracellular side, allowing additional interactions (π-π stackings or Van der Waals) involving Tyr91, and Tyr189. Moreover, an aromatic cage, constituted by Tyr115, Tyr374, Phe398, and Trp402 and located at the bottom of the orthosteric site, completely embrace the aliphatic ring encompassing the positive-charged amino group, establishing relevant hydrophobic interactions.[109] Moreover, a propyloxy linker, as in **40** and **41**, seems to correctly distance the aromatic region from the basic moiety, while the oxygen atom could engage Tyr374 in a hydrogen bond.[114]

H_3R antagonists possess extremely relevant waking-up promoting activity, with compound **40** being approved by FDA in narcolepsy, but they also hold promise in contrasting neuroinflammatory and neurodegenerative processes.[115–117] Furthermore, the high adaptability of H_3R pharmacophore led to the development of many MTDLs, integrating the modulation of other neurotransmitter systems, like cholinergic, adenosine and serotoninergic networks, as potential neuroprotective agents in NDs.[118–120] Moreover, two H_3R antagonists, GSK247246 (**43**, **Figure 16B**) and GSK239512 (**44**, **Figure 16B**) proved to dwindle micro- and astroglia reactivity, whereas they foster OPCs differentiation in animal models both *in vitro* and *in vivo*.[110,121] Similar results were detected in a phase II clinical trial involving patients with relapsing-remitting MS, in which **44** exhibited interesting activity on remyelinating hallmarks, though it did not ameliorate clinical symptoms.[122] Since a polypharmacological approach could help improving therapeutic efficacy, a series of dual S1P agonist and H_3R antagonist, exemplified by **45a** (**Figure 16B**) and **45b** (**Figure 16B**), has been recently published, displaying potential neuroprotective activity in EAE mice.[123]

Taking all this evidence into account, the development of MTDLs concurrently inhibiting FAAH and MGL enzymes while antagonising H_3R might bring to synergistic beneficial effects improving therapeutic efficacy in counteracting demyelination processes occurring in MS.

1.10.2 Rational design

During my PhD work, I was involved in the design, synthesis, and characterisation of a series of polypharmacological agents able to modulate both the ECS and the histaminergic system. Together with Prof. Holger Stark at Heinrich-Heine University in Düsseldorf, a collaborative project development led to the identification of 12 novel MTDLs displaying different pharmacological profiles across the target proteins (compounds **46a-l**, **Figure 17**, and **Table 1**). In the frame of this research topic, the work done during my PhD internship capitalised the results gained thanks to a project where I was involved during my master thesis studies. Indeed, my master thesis work was in part developed in the same medicinal chemistry laboratories at the University of Siena, and part in six months stay in the laboratories of Prof. Holger Stark at Heinrich-Heine University.

Particularly, during my PhD I have synthesised, and characterised two derivatives, **46k,l**, needed for completing the SARs to be explored within this class of compounds. The elaboration of this project also gave me the chance of learning a new technique for optimising the synthetic pathway yielding to hit compound **46f**. Indeed, a flow-chemistry approach was set up, in collaboration with Prof. Antimo Gioiello at the University of Perugia. As a further endeavour of my PhD work, I was involved in an extensive preliminary analysis of the solubility, chemical stability, and lipophilic profiles of the most interesting molecules.

The rational design that brought to the development of this set of molecules modulating both the ECS and the histaminergic system, particularly endowed with FAAH and MGL inhibition profile, and H_3R antagonism, are summarised in the flow chart reported in **Figure 17**.

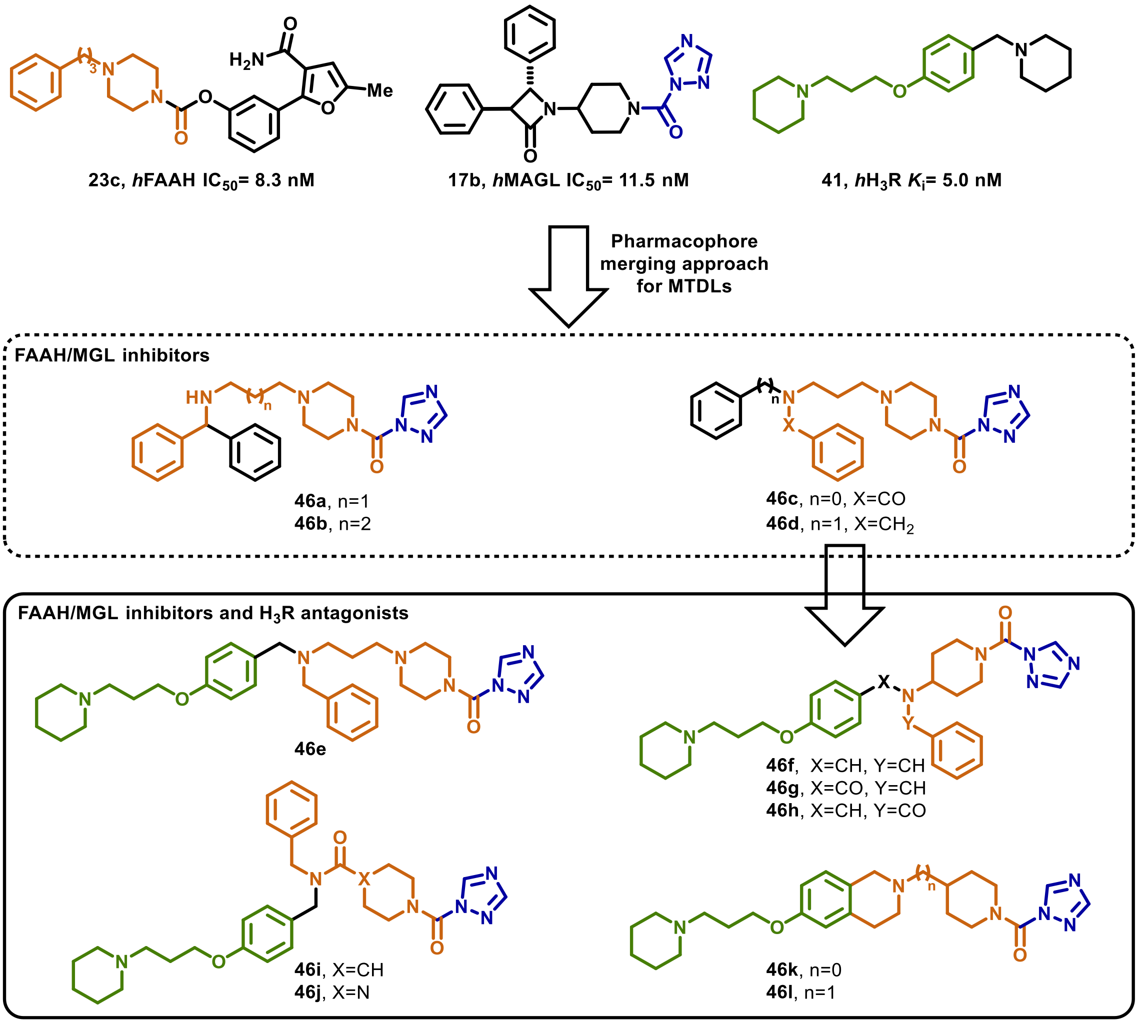

Figure 17. Flow-chart of the rational design for MTLDs modulating both the endocannabinoid and histaminergic system. Different colours highlight the key pharmacophoric elements of the reference compounds (**23c**, **17b**, and **41**), which are incorporated into the structure of the title compounds (**46a-l**).

A systematic sequential strategy was applied, initially the critical features required for effective FAAH and MGL inhibition, were selected exploiting our previously reported structural templates **23c** and **17b**, respectively. The key pharmacophoric elements were merged to afford four dual FAAH/MGL hybrids (**46a**-**d**). Further, the SARs were also explored focusing on changing the nature of the linker (length, basicity, and flexibility) to achieve the optimal scaffold for concurrent FAAH/MGL inhibition, ultimately leading to the identification of **46d**. The essential features for H_3R antagonism, typified by **41**, was consequently incorporated in **46d**'s scaffold. Indeed, the partial overlap between the pharmacophores of H_3R antagonists and endocannabinoids' catabolic enzymes inhibitors favoured the construction of a novel molecular architecture tuning both these neuromodulatory systems. Structural modifications of the linker unit, including rigidification and linearisation, enabled a detailed SARs investigation (**46e-l**). This underlined how smooth changes in the molecular backbone differently drive the activity towards the target proteins, providing three distinctive class of compounds: trial-acting FAAH/MGL/H_3R polypharmacological agents (**46e,f**), dual MGL/H_3R ligands (**46g-j**), and FAAH/H_3R hybrids (**46k,l**).

Table 1. Chemical structures, IC_{50} values for *h*FAAH and *h*MGL, and K_i values for *h*H_3R of compounds **46a-l**.

Cmpd	**Structure**	***h*FAAH IC_{50} (nM)^a**	***h*MGL IC_{50} (nM)^a**	***h*H_3R K_i (nM)^b**
46a	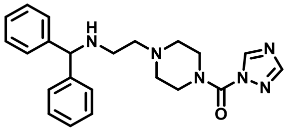	64	32	11397
46b	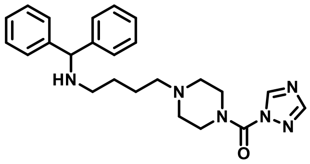	24	13	9006
46c	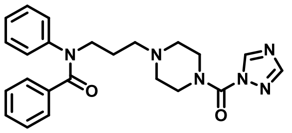	207	3.83	19278
46d	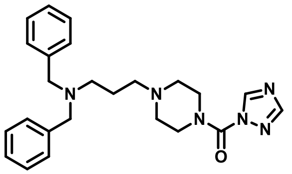	27	2.02	8360
46e	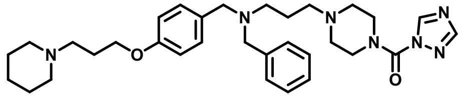	164	54	23
46f	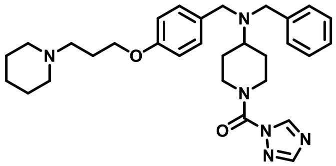	17	46	1.40
46g	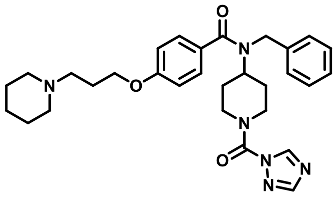	5339	110	1.02
46h	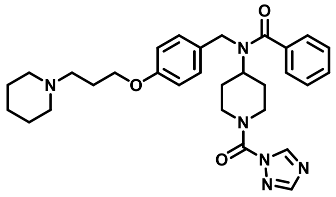	>10000 (12%)	6.55	7.81
46i	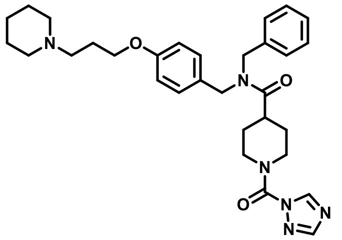	972	2293	4.57
46j	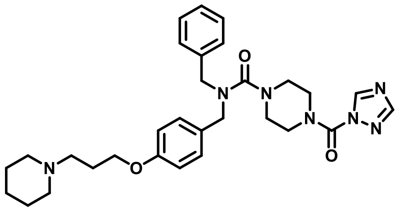	2075	477	1.84

46k	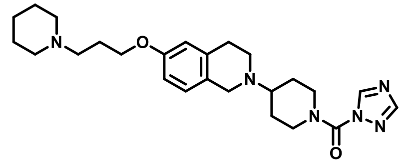	142	>10000 (24%)	3.04
46l	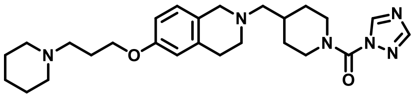	39	>10000 (23%)	4.28
23c[72]	-	8.3	-	-
17b[59]	-	-	11.5	-
41[124]	-	-	-	9.2

[a] Data are expressed as mean of three independent experiments performed in triplicate. All SDs are within 10%. Data in parentheses indicates inhibition at the 10 μM concentration. Incubation time = 30 min; [b] K_i values were determined by radioligand displacement assays, using $[^3H]$Nα-methylhistamine (2 nM) as radiolabelled probe. Experiments were conducted on membrane fractions of HEK-293 cells expressing *h*H$_3$R. Values are expressed as mean of three independent experiments in duplicate. All SDs are within 10%.

1.10.3 Chemistry

1.10.3.1 Synthesis of compounds 46k,l

The synthetic pathways affording derivatives **46k,l** are described in **Scheme 1**.

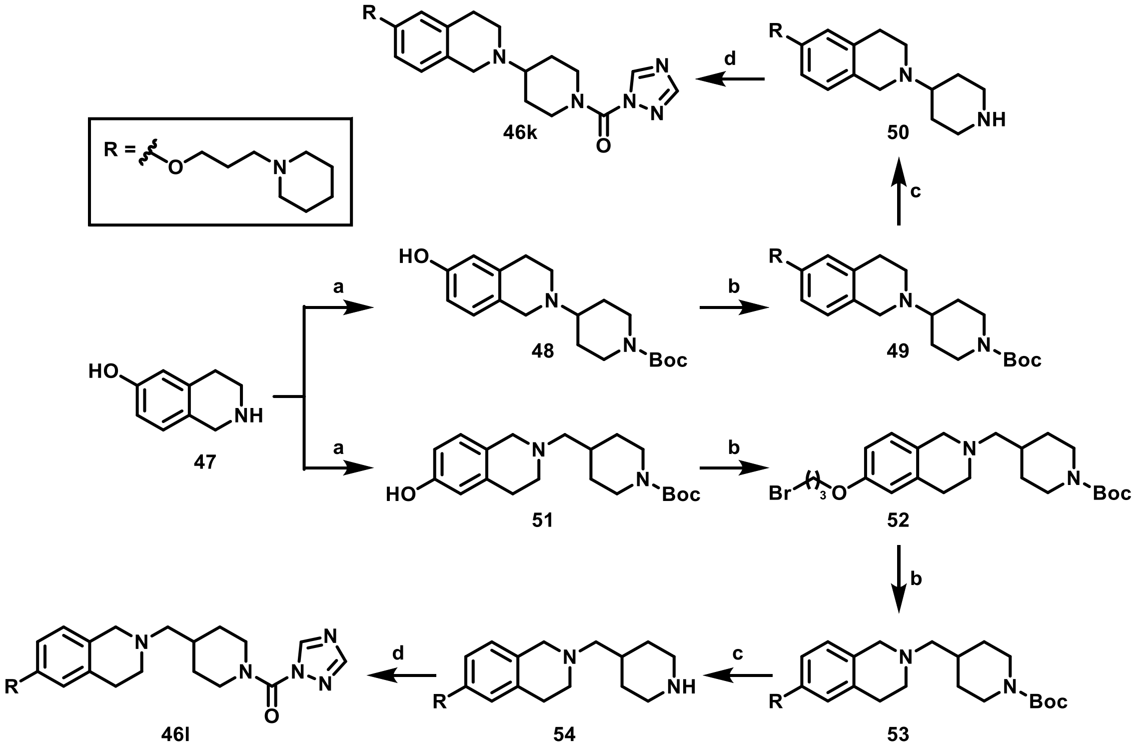

Scheme 1. Reagents and conditions: a) i. (1-Boc-4-piperidone for **48**, 1-Boc-piperidine-4-carboxaldehyde for **51**), AcOH, EtOH, 82 °C, 2 h; ii. $NaBH_3CN$, MeOH, 0 °C to 25 °C, 12 h, 38-55%; b) (1-(3-chloropropyl)piperidin-1-ium for **49**, 1,3-dibromopropane for **52**, and piperidine for **53**), K_2CO_3, MeCN, 85 °C, 12 h, 20-47%; c) 1 N HCl in MeOH, MeOH, 40 °C, 1 h, 99%; d) CDT, DCM, 25 °C, 12 h, 58-61%.

Compounds **46k** and **46l** were obtained according to **Scheme 1**. The synthesis of **46k** started with 1,2,3,4-tetrahydroisoquinolin-6-ol (**47**), which underwent reductive amination with 1-Boc piperidone to obtain intermediate **48**. This latter was alkylated by means of 1-(3-chloropropyl)piperidin-1-ium, synthesised as previously reported,[125] furnishing compound **49**. Boc deprotection (**50**) and subsequent coupling with 1,1′-carbonyl-di-(1,2,4-triazole) (CDT) gave compound **46k**. Similarly, a reductive amination protocol involving **47** and 1-Boc-piperidine-4-carboxaldehyde led to intermediate **51**.

This was alkylated by means of 1,3-dibromopropane, generating bromo-derivative **52**. Intermediate **52** was employed to alkylate piperidine, obtaining compound **53**. Boc deprotection (**54**) and subsequent coupling with CDT afforded compound **46l**.

1.10.3.2 Optimisation of the synthetic pathway affording hit compound 46f

During my master thesis, the most promising compound, **46f**, was obtained in batch following the synthetic route recapitulated in **Figure 18**.

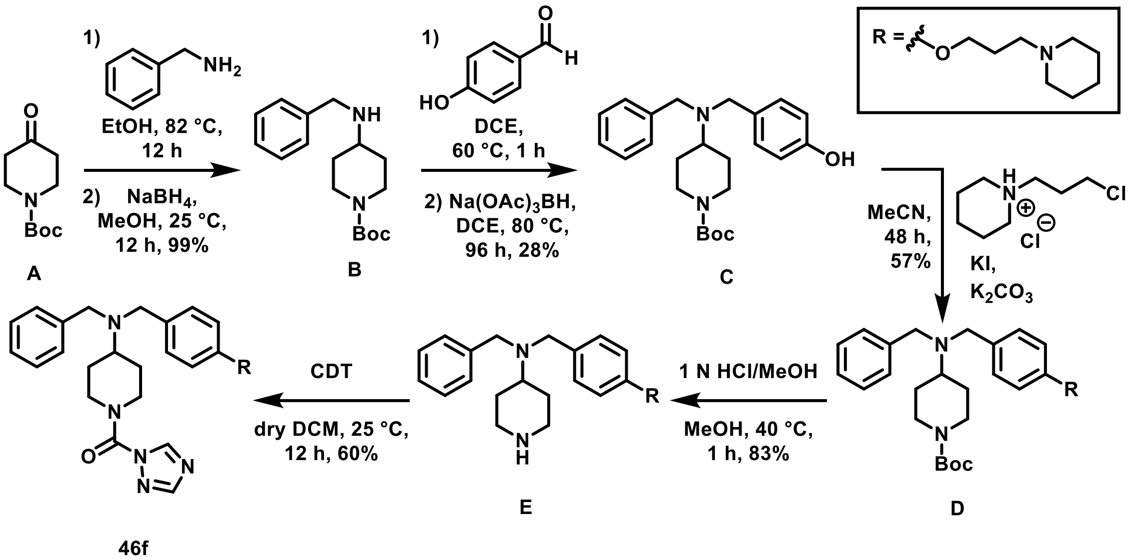

Figure 18. Schematic representation of batch synthetic route affording compound **46f**.

Pursuing the optimisation of the synthetic protocol, I focused my attention on the two critical points in this pathway majorly impacting the overall yield, which are the conversion of amine E in title compound **46f**, and the two steps protocol affording intermediate D starting from secondary amine B. The first one has already displayed satisfactory yield, but it needs long time for attaining the title compound **46f**, whereas the conversion of secondary amine B into tertiary amine D showed very poor yield over two steps (16%). This is likely due to the high steric hindrance between the reactants, hindering the transition from the reagents to the products. As a first approach, I implemented a microfluidic flow synthetic strategy aiming at overcoming these issues, ameliorating reactions' yield, and decreasing environmental footprint according to the green chemistry principles. In the case of **46f**, this approach significantly reduced the reaction time, but it did not affect the conversion rate. On the other hand, the same microfluidic apparatus could not be employed for obtaining D following this synthetic pathway, as the use of 1-(3-chloropropyl)piperidin-1-ium may clog the microfluidic chip. Therefore, before applying the microfluidic flow chemistry approach, I deeply analysed this rate-limiting reaction from a retrosynthetic point of view, to find alternative pathways leading to intermediate D (**Figure 19**).

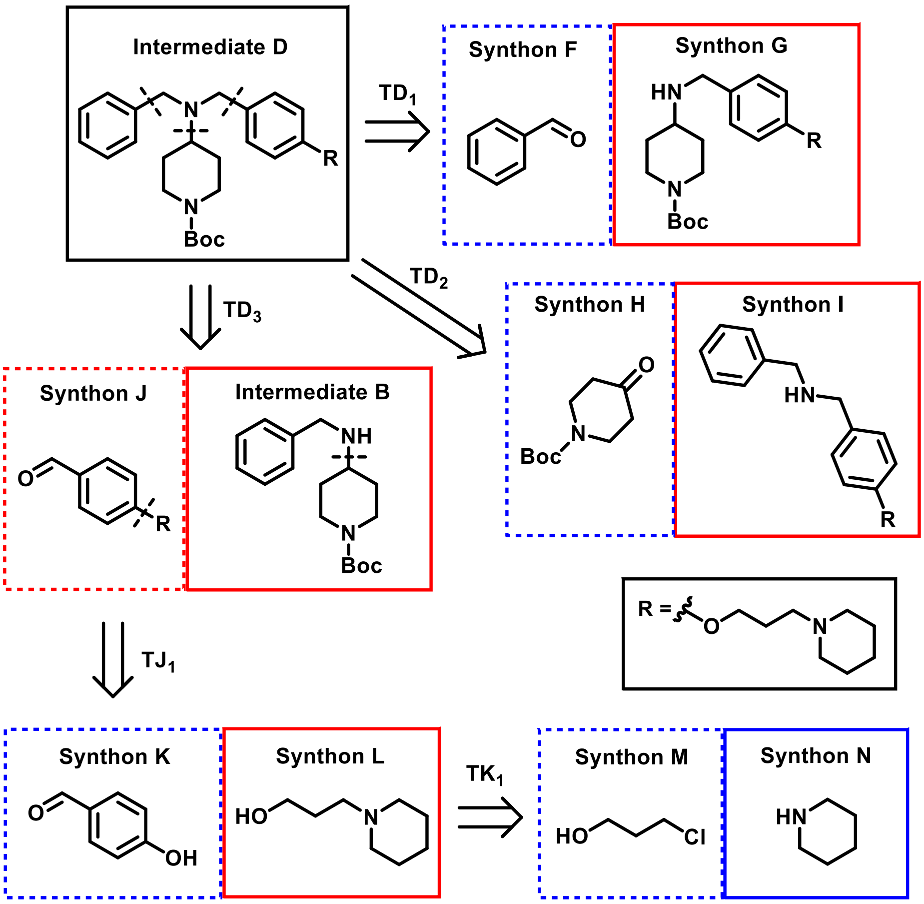

Figure 19. Proposed retrosynthetic planning for obtaining intermediate D. Blue squares highlights commercially available synthons, while red squares show not-commercially available compounds.

Retrosynthetic disconnection underlined that three reductive amination protocols, involving different reactants, could be applied for constructing intermediate D. TD_1 and

TD$_2$ includes two commercially available synthons (F and H), but they also exhibit more hindered secondary amines compared to TD$_3$, hence they are presumed to be less synthetic feasible. TD$_3$ required intermediate B, that was successfully obtained as described in **Figure 19**, and synthon J. This latter could be achieved applying a Mitsunobu reaction between synthons K and L. This strategy represents an alternative option to avoid the potential chip clogging associated with the use of 1-(3-chloropropyl)piperidin-1-ium. Synthon L can be easily achieved in batch reacting synthons M and N, as previously reported. The application of microfluidic flow chemistry approach allowed to quickly obtain synthon J, while it successfully enabled the reductive amination protocol involving intermediate B and synthon J, which previously failed to afford intermediate D in batch. On this ground, a synthetic route for obtaining **46f** combining both batch and microfluidic flow chemistry approaches has been proposed (**Scheme 2**).

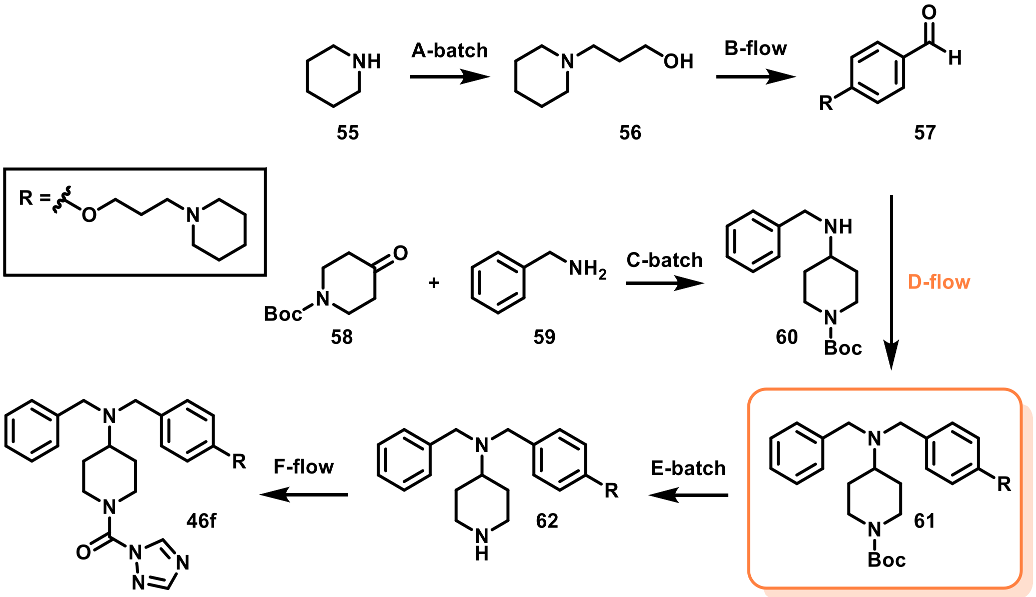

Scheme 2. Reagents and conditions; A-Batch) 3-chloropropan-1-ol, KI, K_2CO_3, acetone, 65 °C, 96 h, 84%; B-Flow) 4-hydroxybenzaldehyde, DEAD, PPh_3, THF, 60 °C, 1 min, 56%; C-Batch) i. benzylamine, EtOH, 82 °C, 2 h; ii. $NaBH_4$, MeOH, 0 °C to 25 °C, 12 h, 85%; D-Flow) AcOH, TEOF, $NaBH_3CN$, EtOH, 75 °C, 2.5 min, 44%; E-Batch) 1 N HCl in MeOH, MeOH, 40 °C, 1 h, 83%; F-Flow) CDT, THF, 40 °C, 3 min, 59%.

This synthetic pathway allowed to reduce time reactions whilst increasing overall yield. Further, not harmful reagents and green solvents were used, when possible, pursuing a synthetic strategy with lower environmental impact. Nonetheless, microfluidic chips allow to load low volume of the reactants' solutions, thus it cannot be used in industrial applications. To enable efficient large-scale production, I optimised the synthesis of **46f** exploiting a flow chemistry approach, in collaboration with Prof. Gioiello's research group at University of Perugia. Particularly, I focused my attention on the bottle-neck reaction converting aldehyde **57** in tertiary amine **61** via reductive amination in the presence of intermediate **60**. This occurs in two step (**Figure 20**):

1) Iminium/enamine formation: the nucleophilic nitrogen attaches the carbonylic aldehyde group, providing an unstable hemiaminal. Following structural rearrangements led to the loss of a molecule of water, pushing the equilibrium towards the iminium ion, which may undergo rapidly interconversion with its tautomer, enamine. Generally, this step requires to be performed under acidic conditions, since the initial protonation of the aldehyde fosters the condensation with the secondary amine.
2) Iminium/enamine reduction: the use of a hydrogen donor allows to reduce the double bond of the iminium intermediate, yielding to the corresponding tertiary amine. The hydrogen donor is generally a hydride source, like borohydride or aluminium hydride salts.

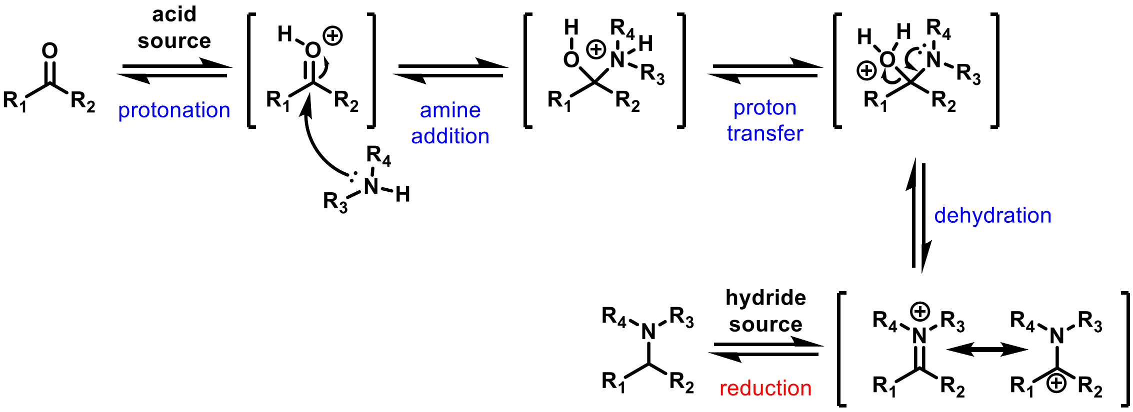

Figure 20. Schematic representation of a reductive amination occurring between a carbonyl group and a secondary amine.

Considering this mechanism, I applied a two steps protocol employing a meso-fluidic flow-chemistry reactor to afford compound **46f**. The general flow set-up is recapitulated in **Figure 21**.

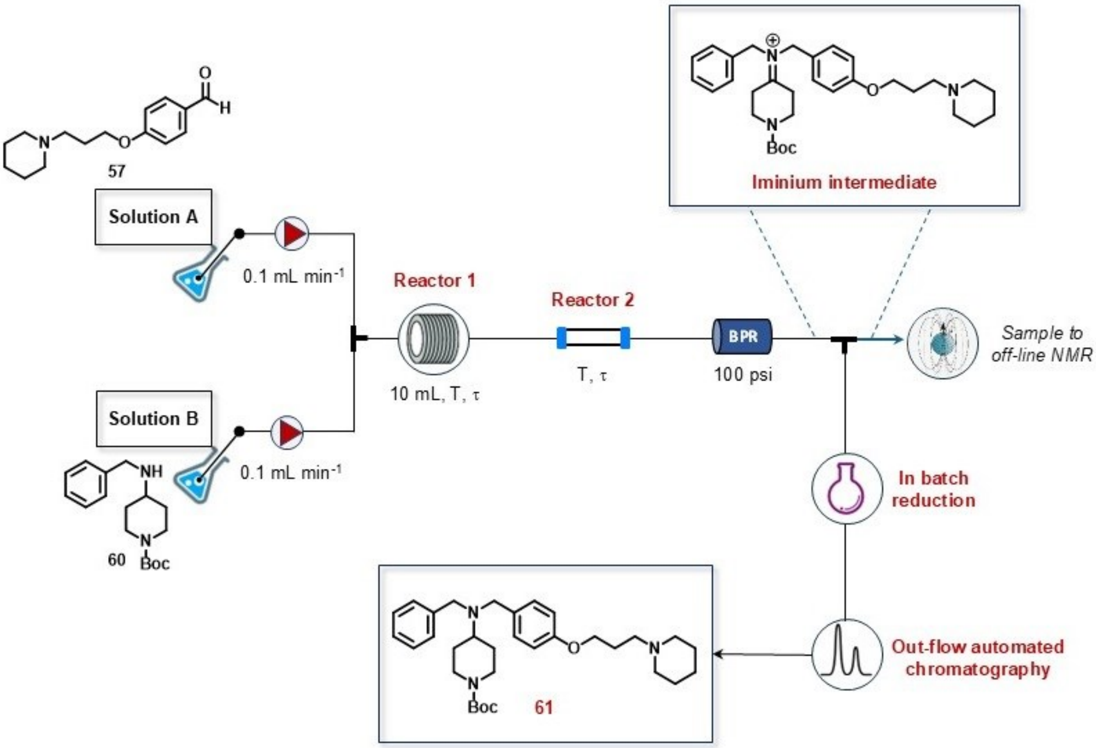

Figure 21. Flow + batch apparatus general set up. T = temperature; τ = time residence.

In this framework, I systematically changed the acid catalyst, the dehydrating agents, the reducing hydride sources, the temperature, and the time residence inside the flow-chemistry apparatus to find the optimal conditions providing **61**. In the quest for the optimal conditions to employed in the flow apparatus, I used triethyl orthoformate (TEOF) as an inexpensive, mild, and ethanol-compatible dehydrating agent, reported to be extremely effective both in solid and liquid phase synthesis.[126] Since the hydride source was very slightly soluble in EtOH, I also switched from a continuous flow-chemistry strategy to a mixed flow+batch approach, forming the iminium/enamine intermediate in a flow apparatus, and subsequently performing the reduction step inside a round-bottom flask. **Table 2** summarises the conditions used in the most representative attempts to obtain **61**.

Table 2. Most representative reductive amination protocols applied for obtaining compound **50**.

Entry	Solution A in EtOH	Solution B in EtOH	Reactor 1 conditions	Reactor 2 conditions	Batch reduction conditions	Yield
1	**57** (1 eq., 0.2 M) **60** (1 eq., 0.2 M) TEOF (2 eq., 0.4 M)	$Na(OAc)_3BH$ (1.5 eq., 0.3 M)	Coil (10 mL) T = 75 °C τ = 10 min	-	-	0%
2	**57** (1 eq., 0.2 M) **60** (1 eq., 0.2 M) TEOF (2 eq., 0.4 M) AcOH (2 eq., 0.4 M)	$NaBH_3CN$ (1.5 eq., 0.3 M)	Coil (10 mL) T = 90 °C τ = 50 min	-	-	0%
3	**57** (1 eq., 0.2 M) TEOF (1 eq., 0.2 M) AcOH (1 eq., 0.2 M)	**60** (1 eq., 0.2 M) TEOF (1 eq., 0.2 M) AcOH (1 eq., 0.2 M)	Coil (10 mL) T = 90 °C τ = 50 min	-	$NaBH_3CN$ (10 eq., 0.8 M suspension in EtOH) T = 25 °C τ = 3 h	0%
4	**57** (1 eq., 0.2 M) AcOH (1 eq., 0.2 M)	**60** (1 eq., 0.2 M) TEOF (1 eq., 0.2 M)	Coil (10 mL) T = 90 °C τ = 50 min	Column (1 g $MgSO_4$ + 1 g Al_2O_3) T = 50 °C, τ = 20 min	$LiBH_4$ (5 eq., 0.4 M suspension in EtOH) T = 40 °C τ = 1 h	0%
5	**57** (1 eq., 0.2 M) $Yb(OTf)_3$ (0.2 eq., 0.04 M)	**60** (1 eq., 0.2 M)	Coil (10 mL) T = 90 °C τ = 50 min	Column (1 g $MgSO_4$ + 1 g Al_2O_3) T = 50 °C, τ = 20 min	$Na(Oac)_3BH$ (2.5 eq., 0.4 M, suspension in EtOH) T = 25 °C τ = 4 h	0%
6	**57** (1 eq., 0.2 M) $Yb(OTf)_3$ (0.2 eq., 0.04 M)	**60** (1.2 eq., 0.24 M)	Coil (10 mL) T = 90 °C τ = 50 min	Column (7 g $MgSO_4$ + 7 g Al_2O_3) T = 50 °C, τ = 20 min	$LiBH_4$ (2 eq., 0.4 M suspension in EtOH) T = 25 °C τ = 4 h	48%
7	**57** (1 eq., 0.2 M) $Yb(OTf)_3$ (0.2 eq., 0.04 M)	**60** (1.2 eq., 0.24 M)	Coil (10 mL) T = 90 °C τ = 50 min	Column (2.5 g $MgSO_4$) T = 50 °C = 20 min	$NaBH_3CN$ (2 eq., 0.4 M suspension in EtOH) T = 82 °C τ =1 h	62%

Among the tested conditions, entry 7 displayed the best performance in terms of overall yield. The conditions used as well as a schematic description of the flow-apparatus are reported in **Figure 22**.

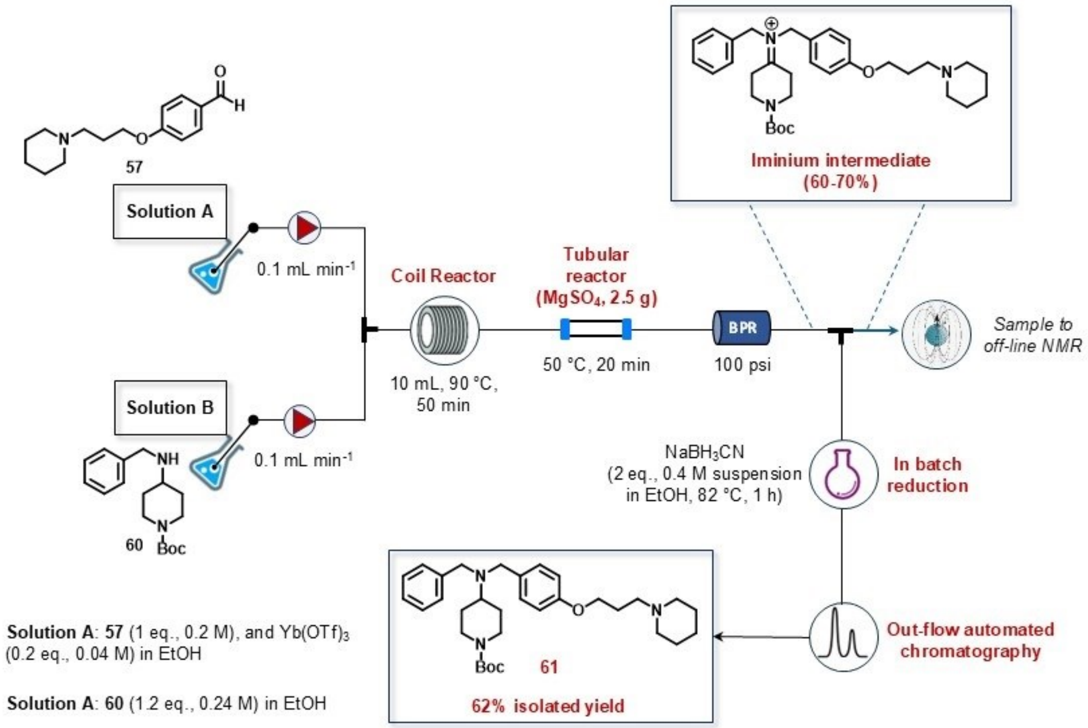

Figure 22. Schematic representation of the flow + batch apparatus, and the conditions employed to afford intermediate **61**.

In the first step, enamine intermediate was obtained by mixing aldehyde **57** and secondary amine **60** in the presence of ytterbium-triflate ($YbOTf_3$) inside a coil reactor and subsequently flushing the corresponding mixture in a tubular column packed with magnesium sulphate ($MgSO_4$). Previous works reported that $YbOAc_3$ could catalyse asymmetric reductive amination of a series of chiral ketones, though a stochiometric amount of $YbOAc_3$ was needed. On this ground, here I employed $YbOTf_3$, characterised by relative low-cost, high water-compatibility, and reusability,[127] as an efficient Lewis acid to catalyse the iminium intermediate formation, while $MgSO_4$ acts as an excellent dehydrating agent. The resulting iminium ion was dropped into a flask containing a suspension of $NaBH_3CN$ in EtOH, yielding tertiary amine **61** with a 62% of the overall yield, increased of 18% compared to the older synthetic approach.

1.10.4 SAR analysis and docking studies

The rational strategy applied for the development of this series of MTDLs was validated by the biological evaluation, revealing distinct SAR patterns across all target proteins (**Table 1**). Strategical variations in the linker unit were introduced to explore the SARs, while maintaining a Y-shape throughout all the designed compounds. In particular, the electrophilic warhead is represented by a urea moiety supporting a 1,2,4-triazole ring, acting as a good leaving group for the carbamylation of the catalytic Ser residues of both FAAH and MGL enzymes. On the other side, a nitrogen-containing linker connects the electrophilic centre to the hydrophobic region, which is constituted by two phenyl groups. As expected, compounds **46a-d** demonstrated potent dual FAAH/MGL inhibition, lacking *h*H_3R affinity (K_i values >8 μM), due to the absence of the H_3R pharmacophore. Among them, linker flexibility appears tightly intertwined with the inhibitory potency for the target enzymes. The analogues **46a** and **46b** showed similar inhibitory profile on FAAH and MGL in the low nanomolar range (IC_{50} values of 64 and 24 nM for *h*FAAH, 32 and 13.1 nM for *h*MGL, respectively), whereas compound **46c** exhibited a slight preferential activity on *h*MGL (IC_{50} = 3.83 nM) compared to *h*FAAH (IC_{50} = 207 nM). This latter data likely stems from the increased rigidity of this derivative. Indeed, the introduction of an amide bond nearby the aromatic region might hinder the binding pose within FAAH, decreasing the IC_{50}. The high flexibility given by the introduction of two benzyl groups confers to compound **46d** an excellent potency for both *h*FAAH (IC_{50} = 27 nM) and *h*MGL (IC_{50} = 2.02 nM) enzymes, electing it as the most promising dual FAAH/MGL inhibitor.

The juxtaposition of a piperidinyl-propyloxy feature on one of the phenyl groups of **46d** enabled potent H_3R antagonism. Indeed, compounds **46e** and **46f** successfully achieved this goal, keeping good inhibitory potency for both FAAH and MGL enzymes (IC_{50} values of 164 and 17 nM for *h*FAAH, 54 and 46 nM for *h*MGL, respectively) whilst exhibiting high *h*H_3R affinity (K_i values of 23 and 1.40 nM, respectively).

Systematic modification of the linker unit, including rigidification or linearisation, provided interesting patterns in the activity across the targets, tuning endocannabinoids' catabolic enzyme without affecting H_3R antagonism (**46g-j**). Compounds **46g** and **46h**, containing an amide group with the nitrogen directly attached to the nitrogen-containing cycle, act as dual potent and selective MGL/H_3R hybrids (IC_{50} values of 110 and 6.55 nM for *h*MGL, K_i values of 1.02 and 7.81 nM for *h*H_3R, respectively), displaying low affinity for *h*FAAH (IC_{50} > 5 μM). On the other hand, compounds **46i** and **46j**, embedding either amide or urea moieties immediately after the aliphatic cyclic linker, maintain potent *h*H_3R antagonistic activity (K_i values of 4.57 and 1.84 nM for *h*H_3R), but moderate to poor inhibition of both endocannabinoids' catabolic enzymes (IC_{50} values of 972 and 2075 nM for *h*FAAH, IC_{50} values of 2293 and 477 nM for *h*MGL), indicating that such rigid connections in this position are detrimental for protein recognition. This evidence confirms specific stereoelectronic requirements needed to efficiently inhibit the FAAH enzyme, due to its narrower binding site compared to MGL, reflecting a minor tolerance to fit rigid and hindering Y-shaped lateral chains.[50,58]

Conversely, the replacement of the classical Y-shaped backbone with a linear tetrahydroisoquinoline system in **46k** and **46l** dramatically lowers the inhibition potency for *h*MGL (IC_{50} >10 μM), shifting the activity towards FAAH/H_3R selective compounds (IC_{50} values of 142 and 39 nM for *h*FAAH, K_i values of 3.04 and 4.28 nM for *h*H_3R). This data aligns with previous literature reports suggesting that reduced MGL inhibition is observed in the absence of Y-shaped backbone,[58] whereas FAAH enzyme proved to accommodate diverse ligand geometries, including conformationally restricted scaffolds.[66,67]

The SAR exploration brought to four structurally interconnected but distinct classes of active polypharmacological molecules: dual FAAH/MGL inhibitors (**46a-d**), MGL/H_3R (**46g-j**) and FAAH/H_3R ligands (**46k-l**), and FAAH/MGL/H_3R triple-acting hybrids (**46e,f**).

Based on these data, compound **46f** emerged as the best-in-class compound, exhibiting optimal balanced activity across all three biological targets (*h*FAAH IC_{50} = 16.9 nM, *h*MGL IC_{50} = 46 nM, *h*H_3R K_i = 1.40 nM). The compound's superior profile is achieved by preserving three vital structural components: a Y-shaped scaffold, pivotal for MGL recognition; a benzylamino-based linker region, maintaining good flexibility for FAAH inhibition; a piperidinyl-propyloxy motif, delivering effective H_3R antagonism. The relevance of these features was further corroborated through docking studies performed for all the engaged proteins (F**igure 23A**-**C**).

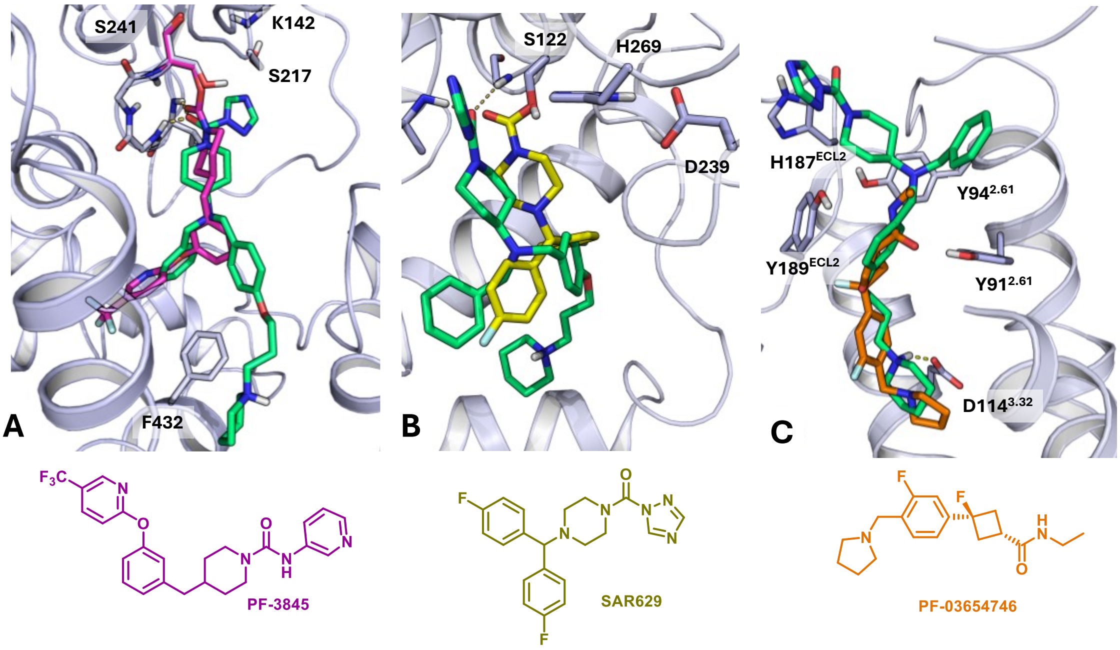

Figure 23. Docking models for compounds **46f** (green carbon atoms) within FAAH (panel A), MGL (panel B) and H_3R (panel C). The structure of the co-crystalised ligand is reported for each considered molecular target, namely PF-3845 (pink carbon atoms), SAR629 (yellow carbon atoms), PF-03654746 (orange carbon atoms). In the case of FAAH and MGL, pyridine-3-amine and triazole substituents are not present in the X-ray structure as they acted as leaving group in the carbamylation of Ser241 (FAAH) and Ser122 (MGL), respectively.

In FAAH (**Figure 23A**), compound **46f** places its carbamoyl triazole portion close to the nucleophilic Ser241 as for the co-crystallised inhibitor PF-3845, while the remaining Y-shaped portion of the molecule occupies the two narrow membrane access channels present in FAAH. Similarly, **46f** well approaches the nucleophilic residue Ser122 in MGL (**Figure 23B**), while its *N*,*N*-disubstituted piperidin-4-amine scaffold perfectly fills the same lipophilic channel occupied by the co-crystallised inhibitor SAR629. Docked inside H_3R (**Figure 23C**), the binding pose of **46f** shows significant overlap with the one of PF-03654746 (co-crystallised in H_3R), with its piperidine tertiary amino group engaging the key Asp114 in a salt bridge.

1.10.5 Preliminary PK properties

Determination of pseudothermodynamyc solubility, chemical stability, and logP values

Selected pharmacokinetic parameters were evaluated for the most promising compounds in the series using suitable HPLC methodologies (**Experimental section**).

Pseuodthermodynamic solubility for the four hybrids **46f**, **46g**, **46h**, and **46l** at both pH = 3.0 and physiological pH = 7.4 after 24 h was determined (**Table 3**). As predicted, all of them exhibited high solubility at pH = 3.0 and pH = 7.4, due to the presence of several basic centres, that facilitate protonation and consequently enhance solubility in aqueous media.

Furthermore, lipophilicity profiles were quantified by determining log*P* values via HPLC-based protocol at pH 10.75 (**Table 3**), ensuring the tested compounds to be available as not-protonated free bases. As expected, the constitutional isomers **46g** and **46h** showed neglectable difference in their log*P* values. Moreover, the incorporation of a polar amide moiety considerably lowers their hydrophobic profiles compared to **46f** and **46l**. These latter lacks one benzyl group compared to **46f**, augmenting its hydrophilic nature. Therefore, **46f** possess the highest log*P* value among the tested molecules, which is a crucial feature for CNS-acting compounds because it reflects the ability to permeate through the blood brain barrier.

For lead compound **46f**, chemical stability in water solution at pH = 3.0 and pH = 7.4 was also assessed (**Table 3**). Despite the presence of an easily cleavable leaving group, this compound demonstrated high chemical stability (>95%) after 24 h at 25 °C under both acid and neutral conditions.

Table 3. Determination of pseudothermodynamic solubility, chemical stability, and log*P* values of selected compounds **46f-h,l** via HPLC.

Cmpd	**Solubility (μM after 24 h)**[a]		**Chemical stability (% after 24 h)**[a]		**Log*P*[b]**
	pH 3.0	**pH 7.4**	**pH 3.0**	**pH 7.4**	
46f	263	227	98.0%	95.9%	5.49
46g	255	206	-	-	2.92
46h	246	229	-	-	2.71
46l	233	256	-	-	3.63

[a] Data are expressed as mean of three independent experiments performed in triplicate. All SDs are within 10%. [b] Data are expressed as mean of three independent experiments performed in duplicate. All SDs are within 10%.

Assessment of metabolic stability

Compounds **46f**, **46h**, and **46l** were also selected for metabolic stability testing (**Table 4**), evaluated by measuring their half-life ($t_{1/2}$) and intrinsic clearance (CL_{int}) in mouse liver microsomes, utilizing **40** as a reference approved drug. All these novel compounds proved to possess improved metabolic stability compared to **40**, suggesting potentially higher bioavailability. **46l** demonstrated the highest metabolic stability among the subset, followed by **46h** and **46f**. This data might correlate with increased structural hinderance, impairing the accessibility to cytochromes and decreasing the metabolic hot spots.

Table 4. Determination of metabolic stability in mouse liver cells for compounds **46f,h,l,** and reference compound **40**.

Compound	**$t_{1/2}$ [min]**[a]	**CL_{int} [μL/min/mg]**[a]
40	10.0	693.7
46f	64.4	107.7
46h	93.6	74.2
46l	227.3	30.5

[a] Data are expressed as mean of three independent experiments performed in triplicate. All SDs are within 10%.

1.10.6 Pharmacological data

Selectivity assays for H_3R-related GPCRs, CB_1R, and CB_2R

The most promising compounds (**46f-h,l**) were evaluated for their selectivity against *h*CB_1R and *h*CB_2R, as well as H_3R-related GPCRs, including human histamine receptors 1 and 4 (*h*H_1R, *h*H_4R), and human dopamine receptors 2 and 3 (*h*D_2R, *h*D_3R), which are known to form heterodimers with histamine receptors (**Table 5**). All the compounds show no affinity for CB_1R, CB_2R, and H_4R (>10 μM) at the tested concentration. Among the remaining H_3R-related GPCRs, the selected derivatives display low to moderate affinity for *h*H_1R (>0.9 μM), *h*D_2R (>1.2 μM), and *h*D_3R (>1.9 μM). This evidence confirm that all the tested compounds retain appropriate selective profiles over CBRs and H_3R-related GPCRs, with compound **46f** exhibiting slightly broader multi-receptor activity for *h*H_1R (IC_{50} = 1821 nM), *h*D_2R (IC_{50} = 1283 nM), and *h*D_3R (IC_{50} = 1996 nM), though its potent H_3R affinity still ensures favourable selectivity ratios.

Table 5. Selectivity data for selected compounds **46f-h,l** against CB_1R, CB_2R and H_3R-related GPCRs, histamine receptors H_1R and H_4R, and dopamine receptors D_2R and D_3R (expressed as K_i nM).

Cmpd	hH_1R^a	hH_4R^b	hD_2R^c	hD_3R^c	hCB_1R^d	hCB_2R^d
46f	1821	>10000	1213	1996	>10000 (5%)	>10000 (7%)
46g	4301	>10000	>10000	>10000	>10000 (3%)	>10000 (1%)
46h	4971	>10000	5844	>10000	>10000 (11%)	>10000 (6%)
46l	926	>10000	5122	>10000	>10000 (9%)	>10000 (14%)

[a] K_i values were determined by radioligand displacement assays, using [^{3}H]pyrilamine (1 nM) as radiolabelled probe. Experiments were conducted on membrane fractions of CHO-K1 cells expressing hH_1R. Values represent affinity as mean of three independent experiments performed in duplicate. All SDs are within 10%. [b] K_i values were determined by radioligand displacement assays, using [^{3}H]histamine (10 nM) as radiolabelled probe. Experiments were conducted on membrane fractions of HEK-293T-SF-hH_4R-His6-CRE-Luc cells. Values represent affinity as mean of three independent experiments performed in duplicate. All SDs are within 10%. [c] K_i values were determined by radioligand displacement assays, using [^{3}H]spiperone (0.2 nM) as radiolabelled probe. Experiments were conducted on membrane fractions of CHO-K1 cells expressing $hD_{2,short}R$, or CHO-K1 cells expressing hD_3R Values represent affinity as mean of three independent experiments performed in duplicate. All SDs are within 10%. [d] K_i values were determined by radioligand displacement assays, using [^{3}H]-CP 55,940 (0.5 nM) as radiolabelled probe. Experiments were conducted on membrane fractions of CHO cells expressing *h*CBR1 or *h*CBR2. Values represent affinity as mean of three independent experiments performed in triplicate. In parentheses the percentage of inhibition at the 10 μM concentration is indicated. All SDs are within 10%.

Toxicity assessment in SH-SY5Y cells

Cytotoxicity of the constructed derivatives (**Figure 24**) were evaluated in SH-SY5Y neuroblastoma cells, a widely employed cell lines which can be induced to differentiate from a neuroblast state into a mature human neurons-like phenotype, establishing a suitable *in vitro* model for assessing neurotoxicity.[128] Cell viability was preserved above 90% at 10 μM following a 24 h exposure period, indicating favourable safety profiles.

Notably, lead compound **46f** showed only minimal effects on cell viability (>90%), supporting its suitability for further development as a MTDL.

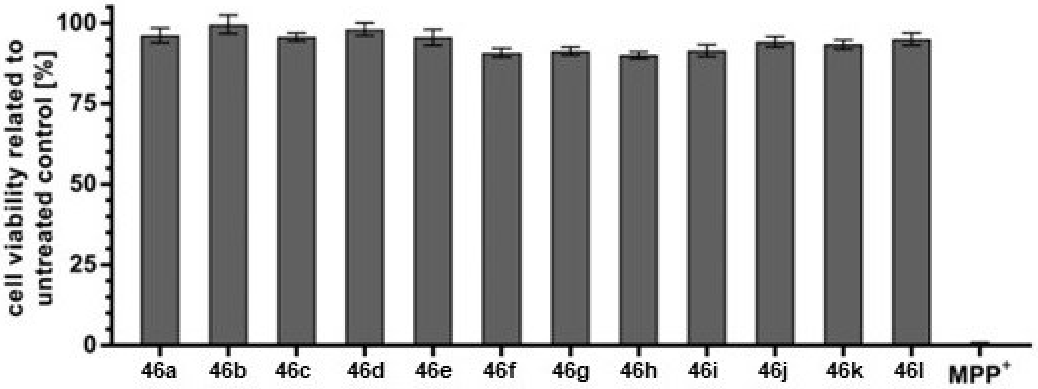

Figure 24. Remaining SH-SY5Y cell viability after 24 hours of treatment.

Neuroprotective effects against inflammation-induced neurodegeneration in rat organotypic explants

Neuroprotective properties of the most promising compounds (**46f-h,l**) and reference compound **40** were studied in *ex vivo* cultures of rat hippocampal explants exposed to LPS + interferon-γ (IFN-γ) neuroinflammatory insult assessing cell death through propidium iodide staining, as previously described (**Figure 25**).[72] Although some differences in enzymatic kinetic profile, sensitivity to inhibitors, and pharmacology have been reported in literature, both FAAH and MGL enzymes are highly conserved across rat and human species.[129,130] Therefore, organotypic hippocampal slice cultures (OHSC) of post-natal rat are considered a valuable translational platform for studying neuroinflammatory processes and drug responses in a physiologically relevant *ex vivo* system. Indeed, OHSC preserves the cytoarchitecture and synaptic connectivity of the human hippocampus, which is usually less employed due to several limitations, including ethical considerations for embryonic samples or post-mortem delay, affecting the success of the culture.[131,132] Compound **40** (0.3-3 nM) was used to evaluate the contribution of H_3R antagonism alone in the model, displaying no ability to counteract cell death. On the other hand, the presence of **46f** (0.3-30 nM), **46g** (0.3-3 nM), **46h** (0.3-30 nM), and **46l** (0.3-3 nM) in the incubation media differently affected neurons viability, as they exhibited a dose-dependent, moderate to high neuroprotective abilities in this model. Among them, **46l** proved to be the best performing compound in contrasting the inflammatory damage in CA1 hippocampal organotypic cultures induced by administration of LPS + IFN-γ. The employed organoid model of neuroinflammation is very similar to the one that occurs in MS: The activity of the compound was displayed at a low nanomolar concentration (3 nM), highlighting its potential in NDs and MS treatment.

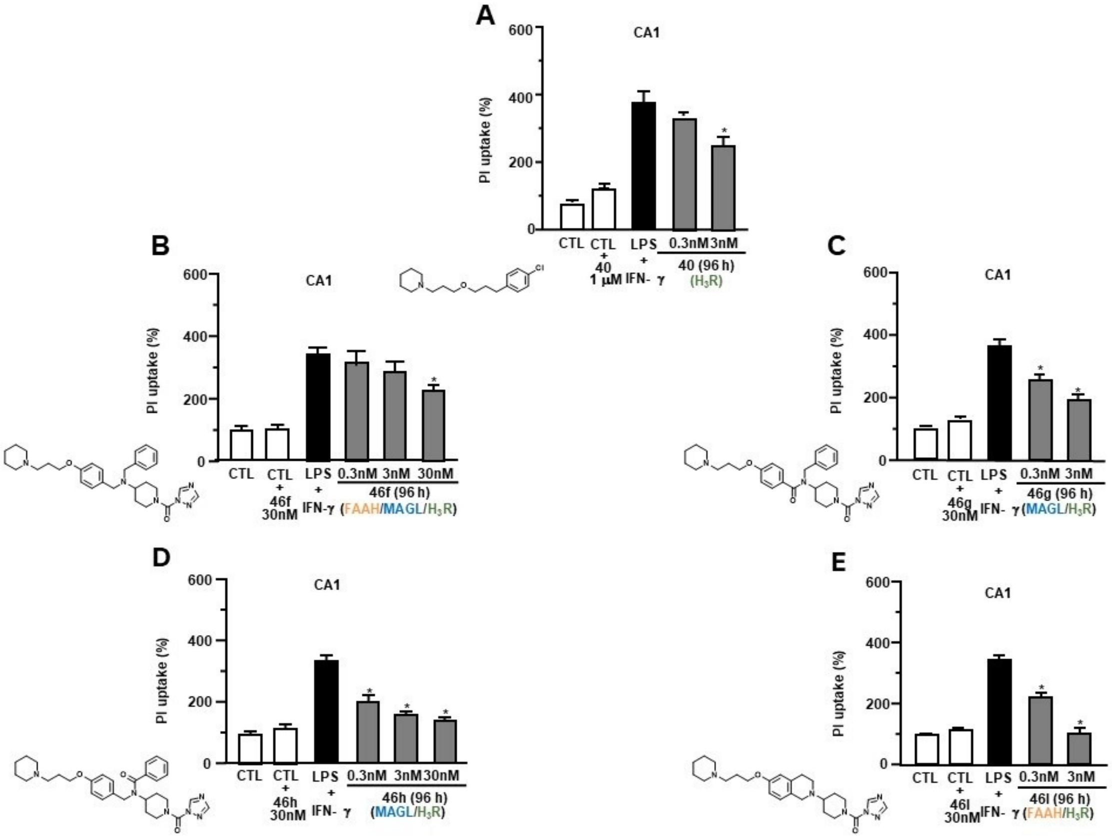

Figure 25. Effects of selected compounds **40**, **46f-h,l** against LPS + IFN-γ-induced inflammatory damage in CA1 hippocampal organotypic cultures. A–E; PI uptake observed in hippocampal organotypic slices under control conditions (A-E) and following 96 h of LPS + IFN-γ-exposure in the absence of drug exposure (A-E) or in the presence of 0.3 nM–3 nM **40** (A); 0.3 nM–30 nM **46f** (B); 0.3 nM–3 nM **46g** (C); 0.3 μM–30 nM **46h** (D); 0.3 nM-3 nM **46l**. Scale bars in A-E: 600 μm. *$p < 0.05$ versus LPS + IFN-γ.

Remyelinating abilities evaluation in human OPCs

The ability to thwart demyelinating processes was assessed by exposing *h*MO3.13 cells, a human OPC line commonly used to evaluate oligodendrocyte (dys)functionalities,[133] to the selected compounds **46f** (30 nM), **46h** (30 nM), **46l** (3 nM), and reference compound **40**. The transcription levels of myelin basic protein (MBP), a well-established MS marker, was registered to analyse the impact of the tested molecules in this *in-vitro* MS model (**Figure 26**).[134] Compound **40** (3 nM) was employed for establishing the role of H_3R alone in this model, ultimately failing in achieving the fixed goal. Notably, all the tested compounds enhanced MBP transcripts. Notably, compound **46f** stood out for efficiently promoting oligodendrocyte maturation at a dose of 30 nM. This effect was comparable to the differentiating agent PMA and significantly higher of all the other tested molecules, underlining that polypharmacological triple-acting compounds finely tuning both endocannabinoid and histaminergic systems hold promise in tackling MS.

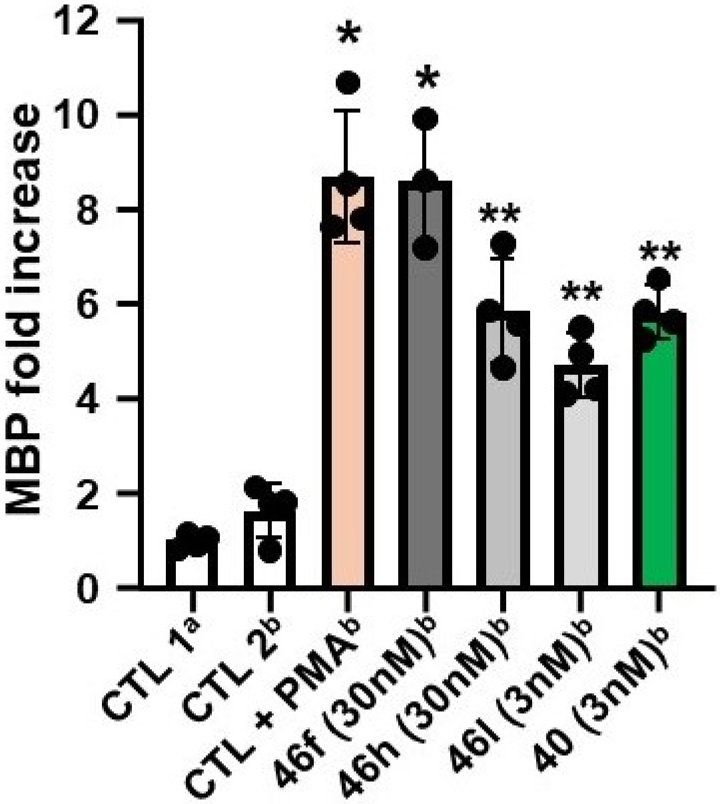

Figure 26. Effect of selected compounds **40**, **46f,h,l** on MBP transcripts in *h*MO3.13 cells. Cells were harvested after 24 h (a) or 96 h (b). The values represent the means ± S.E.M. (n=3-4). One-way analysis of variance (ANOVA) followed by Bonferroni post hoc analysis. * p< 0.05 versus CTL1, CTL2, **46h**, **46l**, and **40**; ** p< 0.05 versus CTL1 and CTL2.

1.11 First-in-class pyrazole-based MGLis integrating HDAC6 inhibition

1.11.1 Background

Epigenetic modulators are a class of factors which can regulate gene expression by altering the chromatin state. Based on their functions, these proteins could be classified in four distinct categories:

- “remodellers”, that directly act on chromatin localisation and its three-dimensional structure;
- “writers”, adding specific groups (methyl, acetyl, etc.) on DNA, RNA or histones;
- “readers”, recruiting key proteins contributing to gene expression nearby the flagged region;
- “erasers”, which removes the epigenetic marks.

Epigenetic regulation is key to many physiological pathways, as it tunes cell division, replication, and survival. In this context, dysfunctional histone acetylation status emerged as a dynamic mechanism exhibited in various pathological processes. Therefore, finely tuning of histone deacetylase (HDACs) activity attracts lots of scientific interests.[135]

HDACs family encompasses 18 isoforms, clustered in 4 classes according to their phylogenetic similarity with yeast enzymes. They are specialised in catalysing deacetylation of ε-N-acetyl lysine on histones, leading to reduce accessibility to chromatin thus hampering gene transcription. Notably, some isoforms could also operate on non-histone substrates, suggesting the existence of a complex post-translational regulatory machinery. Class I comprehends isoforms 1, 2, 3, and 8, broadly expressed throughout the body in cell nucleus and predominantly targeting histones. Class II is further divided into IIA (isoforms 4, 5, 7, and 9) and IIB (isoforms 6 and 10), performing tissue-specific activity. Class IV is constituted of only one isoform, HDAC11, showing high similarity with the catalytic site of class I and II, whilst class III resembles yeast sirtuin protein 2, hence these seven isoforms are called sirtuins (SIRT1-7). The catalytic activity of HDACs belonging to class I, II, and IV relies on the presence of a central Zn^{2+} ion, while sirtuins are NAD^+-dependent enzymes.[136]

Among this protein family, HDAC6 stands out as an interesting biological target due to its peculiar features. First, its cellular location is in the cytoplasm, facilitating the efficient delivery of candidate drugs compared to the nucleus-located isoforms. It also possesses an exquisite molecular architecture, displaying two catalytic binding domains (CD1 and CD2), with a unique zinc-finger ubiquitin binding domain (ZnF-UBP) at the C-terminal, allowing HDAC6 to bind mono- or poly-ubiquitinated proteins. CD2 acts on a wide group of substrates, while CD1 seems to be highly specific for ligands presenting a C-terminal acetylated lysine. In 2016, crystal structure of *h*HDAC6 CD2 in complex with trichostatin A (TSA, **63**, **Figure 27**), a known natural HDAC6 inhibitor (HDACi), elucidated the catalytic mechanism of action of this enzyme, involving the catalytic Zn^{2+} ion, a molecule of water, and several key amino acid residues (His573, Asp610, Asp612, His614, and Asp705).[137]

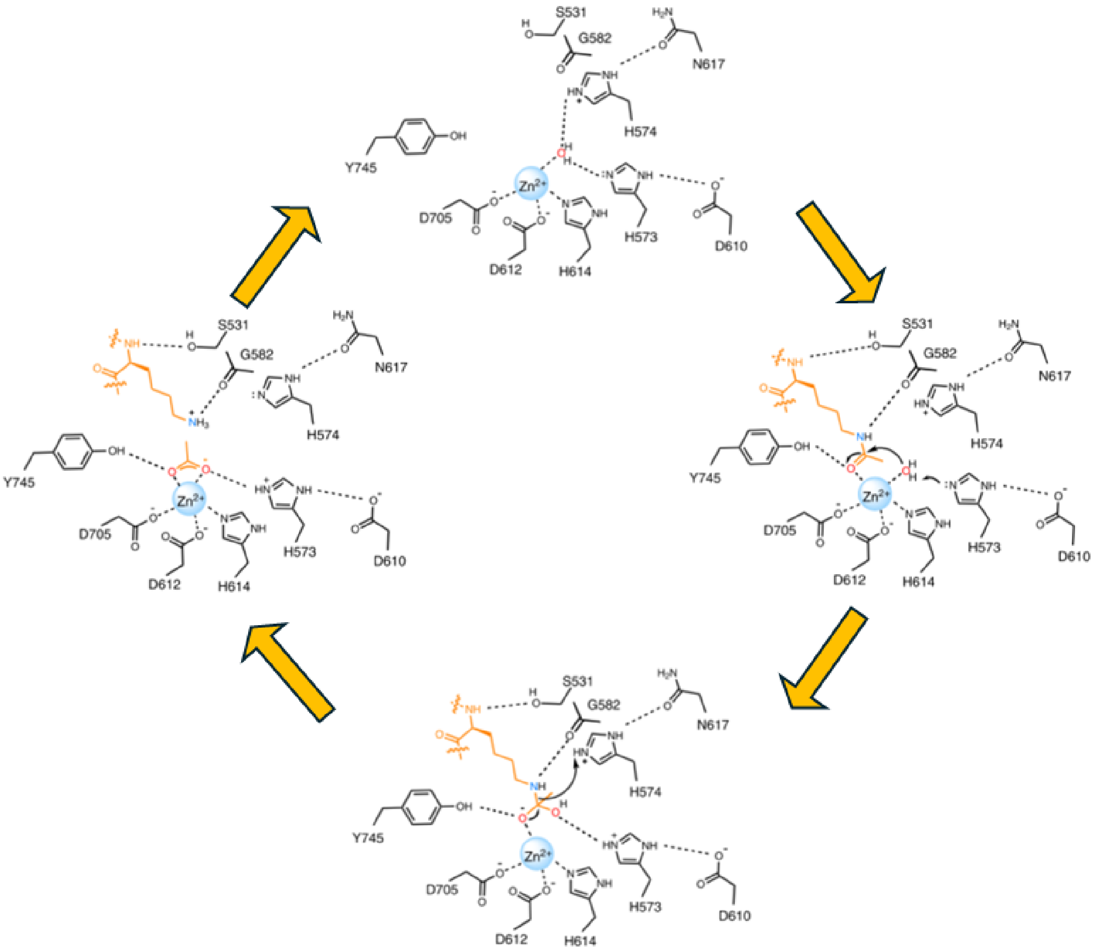

Figure 27. Schematic representation of HDAC6 catalytic cycle. A) In the active site of unliganded *zf*CD2, a molecule of water is coordinated by the catalytic Zn^{2+} ion, His573, and His574. B) The oxygen atom of the carbonyl group of **63** is coordinated by the Zn^{2+} ion, getting closer the scissile acetyl moiety to the catalytic molecule of water. Substrate's binding fosters His573 deprotonation by means of Asp610, consequently leading to hydroxide ion formation. This latter attaches the acetyl group of **63** forming a tetrahedral compound. C) Structural rearrangements bring to the collapse of this unstable intermediate, prompting the deacetylation of the substrate. D) Ser531 and Gly582 residues facilitate the exit of deacetylated **63**, whilst the acetate group remains coordinated within the active site. Lastly, a molecule of water displaces the acetyl group, restoring the initial conditions.

HDAC6 primarily interacts with non-histone substrates involved in cell signalling and motility (GSK3β and α-tubulin), protein degradation (Hsp90), and inflammation (NF-κB), also via PPIs (ubiquitin and τ proteins).[138] Interestingly, HDAC6 seems to contact dynein, forming a heteroduplex machinery deputy to NLRP3 inflammasome transport to the microtubule-organizing centre and its subsequent activation.[139] Several reports highlighted the relevance of a hyperacetylated status of these HDAC6 ligands in many pathological conditions. Therefore, HDAC6 inhibition appears as a suitable strategy for contrasting a plethora of diseases, including cancer, rare diseases, such as idiopathic pulmonary fibrosis (IPF) and retinitis pigmentosa (RP), and various NDs.[138,140,141]

The information gained from the X-ray structure analysis of *zf*HDAC6 CD2-TSA complex as well as docking studies performed with other HDACis allowed to identify the structural requirements crucial to achieve potent and selective HDAC6 inhibition.[137] Consequently, a general scaffold for HDAC6is was defined, comprising three essential structural frames:

1. Zing binding group (ZBG): this moiety should be able to efficiently chelate the catalytic Zn^{2+} ion inside HDAC6 binding pocket, interfering with the deacetylating process. Commonly, a hydroxamic acid motif is the golden standard bidentate ZBG, but it is also associated with potential safety concerns, as it could generate genotoxic species following the Lossen rearrangement. Several alternative ZBGs have been reported so far, including mercaptoacetamide and hydrazide.[142,143] More recently, 2-(difluoromethyl)-1,3,4-oxadiazole (DFMO) was identified as an intriguing ZBG for selective HDAC6 inhibition. Following an enzyme-catalysed ring-opening reaction, the active form, represented by a deprotonated difluoroacetyl hydrazide, is released, available for coordinating the catalytic Zn^{2+} ion of HDAC6.[143] The correct choice of the ZBG and its positioning in respect of the "cap" robustly influence the selectivity among HDAC isoforms.[144]
2. Linker unit: serving as an aliphatic or aromatic-based spacer tethering the ZBG and the "cap", this fragment displays high variability among HDAC6is. It occupies a hydrophobic channel connecting the outer membrane to the active site, featuring many aromatic amino acids, potentially able to establish additional π-π interactions.

Generally, it embeds a *p*-disubstituted aromatic motif, ensuring the correct conformational geometry within HDAC6. Linker optimisation in terms of length and lipophilicity can impact potency for the target protein.

3. Cap domain: it establishes hydrophobic interactions with amino acids located on the surface of the target. It plays a crucial role in isoforms selectivity, as class I HDACs present narrower access to the catalytic site compared to HDAC6. Therefore, introducing lipophilic, bifurcated, and bulky groups in this region should led to increase the selective profile over HDAC6 cognates.[145]

To date, the only compounds able to inhibit HDAC6 that are employed in the clinic are four pan-inhibitors. They have been approved as anticancer drugs against T-cell lymphoma (**Figure 28**): vorinostat (**64**), rodimepsin (**65**), belinostat (**66**), and panabinostat (**67**).[146]

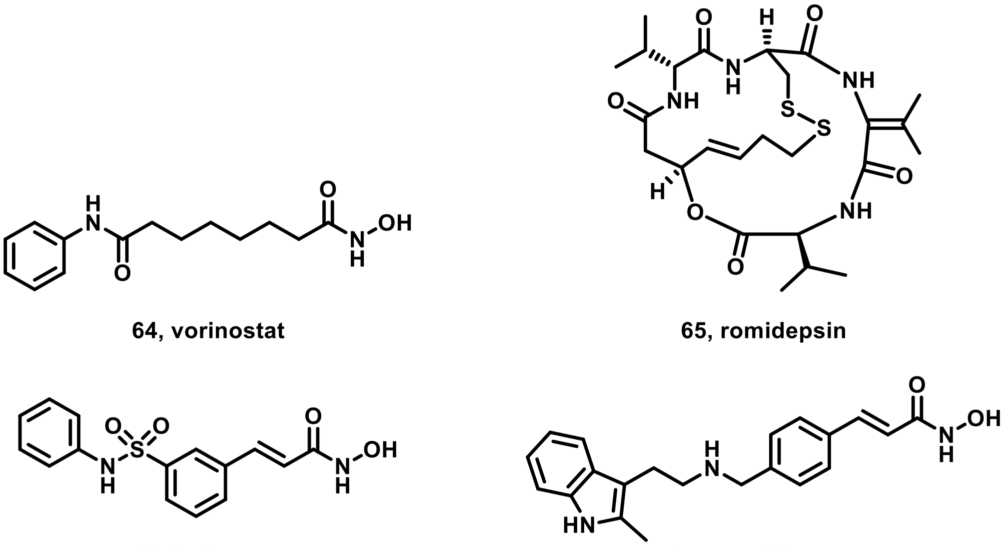

64, vorinostat

65, romidepsin

66, belinostat

67, panabinostat

Figure 28. Chemical structures of the FDA-approved pan HDAC inhibitors.

Nonetheless, their lack of selectivity over several HDAC isoforms promotes mild to severe side effects, such as asthenia, vomit, diarrhoea, but also thrombocytopenia, sepsis and pulmonary embolism.[147] Therefore, scientific efforts were focused on developing potent and selective HDAC6is for contrasting various pathological conditions, including AD,[148] MS,[149,150] PD,[151,152] ALS and HD.[153]

Among the plethora of distinct HDAC6is reported so far, seven of them underwent clinical evaluation as mono- or polytherapy in cancer, arthritis rheumatoid, HD, and rare diseases, such as Charcot-Marie Tooth.[154] In this quest, my research group previously reported the discovery of several HDAC6is as novel pharmacological tools for cancer, RP, and IPF therapies.[59,155–158] Among them, compound **68** (**Figure 29A**), recently developed by the research group where I performed my PhD internship, emerged as a potent and selective HDAC6i, typified by low geno/cyto/cardio toxicity. Crystal structure with *zf*HDAC6 (**Figure 29B**) and docking studies performed on *h*HDAC6 and *h*HDAC1 corroborated its captivating inhibitory profile, while more in-depth pharmacological studies confirmed that it could revert lung fibrogenesis.[156]

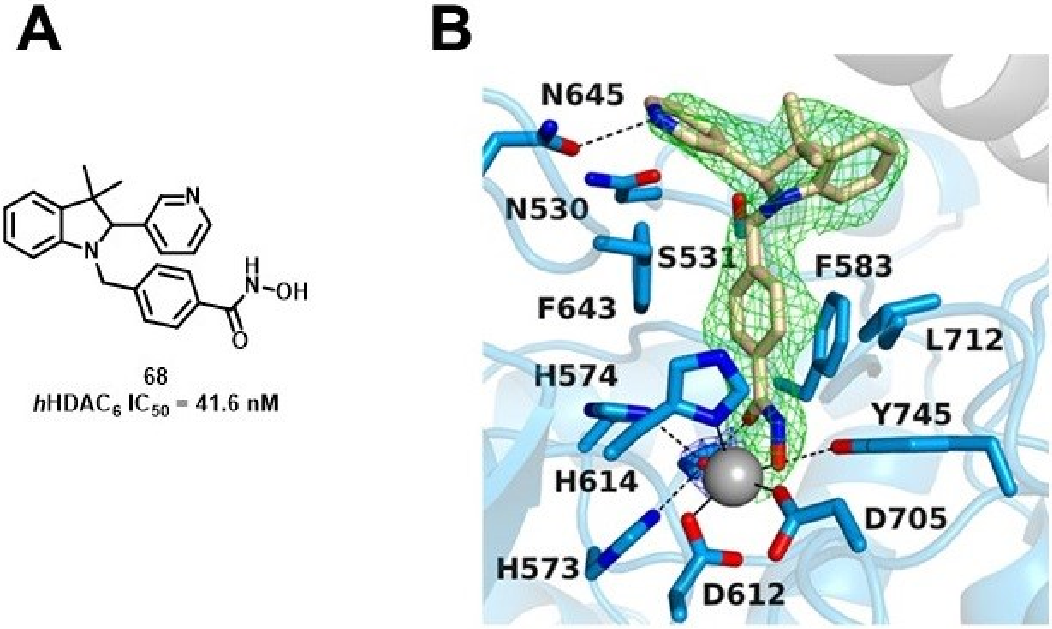

Figure 29. A) Chemical structure and IC_{50} value for *h*HDAC6 of compound **68**. B) Stereo view of a Polder omit map of the *zf*HDAC6/(*S*)-**68** complex (PDB 6V79; contoured at 2.5 σ).

Moreover, the general scaffold of HDAC6is proved to be a versatile platform for the rational design and synthesis of MTDLs tackling AD, owing to its high structural compatibility with a range of pharmacophores underlying this condition.[141,148] As previously discussed, my research group contributed to this field developing a series of dual FAAH and HDACs inhibitors, endowed with interesting antioxidant and neuroprotective properties.[89]

The success of this class of compounds prompted further exploration of polypharmacological approaches addressing the concurrent modulation of HDAC6 and the ECS. In this context, MGL appears as an appealing biological target for MTDLs development, due to its little employment in this field so far. Furthermore, the essential features to achieve effective MGL inhibition nicely overlap with the structural requirements for HDAC6 inhibition. Therefore, the rational design and synthesis of MTDLs simultaneously inhibiting both MGL and HDAC6 enzymes might represent cutting-edge polypharmacological tools harnessing neurodegenerative and neuroinflammatory based diseases.

1.11.2 Rational design

Taking inspiration from the abovementioned approach, I developed a novel class of compounds for exploring the chemical space around MGL inhibition through systematic variation of the leaving group. Then, HDAC6 activity was integrated on the identified scaffolds, furnishing hybrid molecules as dual HDAC6/MGL inhibitors. Hence, my synthetic efforts led to the development of 16 compounds, namely **69a-p** (**Figure 30, Table 6**). The newly developed compounds can be clustered in two sets, namely Set A (**69a-l**) and Set B (**69m-p**), based on different design strategies.

In particular, the compounds of Set A were conceived with the aim of exploring the possibility to substitute the triazole moiety, present also in **17b**, with some bioisosteric features. Therefore, starting from the known inhibitor AKU-005 (**69a**),[57] herein resynthesised for comparing its MGL inhibition potency with our compounds, the triazole ring was systematically replaced with several pyrazole-based moieties (**69b-h**). The remaining Y-shaped biphenyl methane unit tethered to a piperazine-based urea moiety was maintained unchanged. Particularly, the installation of several electron-withdrawing groups (EWG) at position 4 of the pyrazole ring allowed investigating the role of this feature in driving the targeting of the catalytic Ser122 residue of the MGL enzyme. Among these EWGs, the incorporation of a hydroxamic acid group, that is key for HDAC 6 inhibition, not only maintained good inhibition potency for MGL, but also ensured good inhibitory activity for HDAC6. Indeed, the structural requirements for MGL inhibition show substantial overlap with those elements needed for HDAC6 inhibition, as exemplified in compound **68**. The hydrophobic region required for MGL recognition acts as bulky cap motif within HDAC6, whilst the aromatic-based spacer, optimal for HDAC6 inhibition, can be well integrated in the scaffolds of the MGLis. Therefore, a merging approach appears as a suitable strategy to afford HDAC6/MGL hybrids. On this ground, SARs were explored focusing on structural modifications of the aliphatic linker and the aromatic region (**69i-l**). Changing on this latter altered the molecular shape, identifying linear dual MGL/HDAC6 hybrids (**69k,l**).

Starting from the linear scaffold of compound **69l (Table 6)**, the critical features for the effective MGL and HDAC6 inhibition were rearranged, constructing another set of derivatives, titled Set B (**69m-p**). Particularly, these molecules show a *p*-disubstituted benzyl group supporting the ZBG. On the other side, a piperidine-based urea linked the aromatic centre with the azole leaving group. While the same linker unit was kept throughout this set of molecules, SARs were explored by modifying the ZBG and the azole leaving group, leading to intriguing insight in the modulation of both targets.

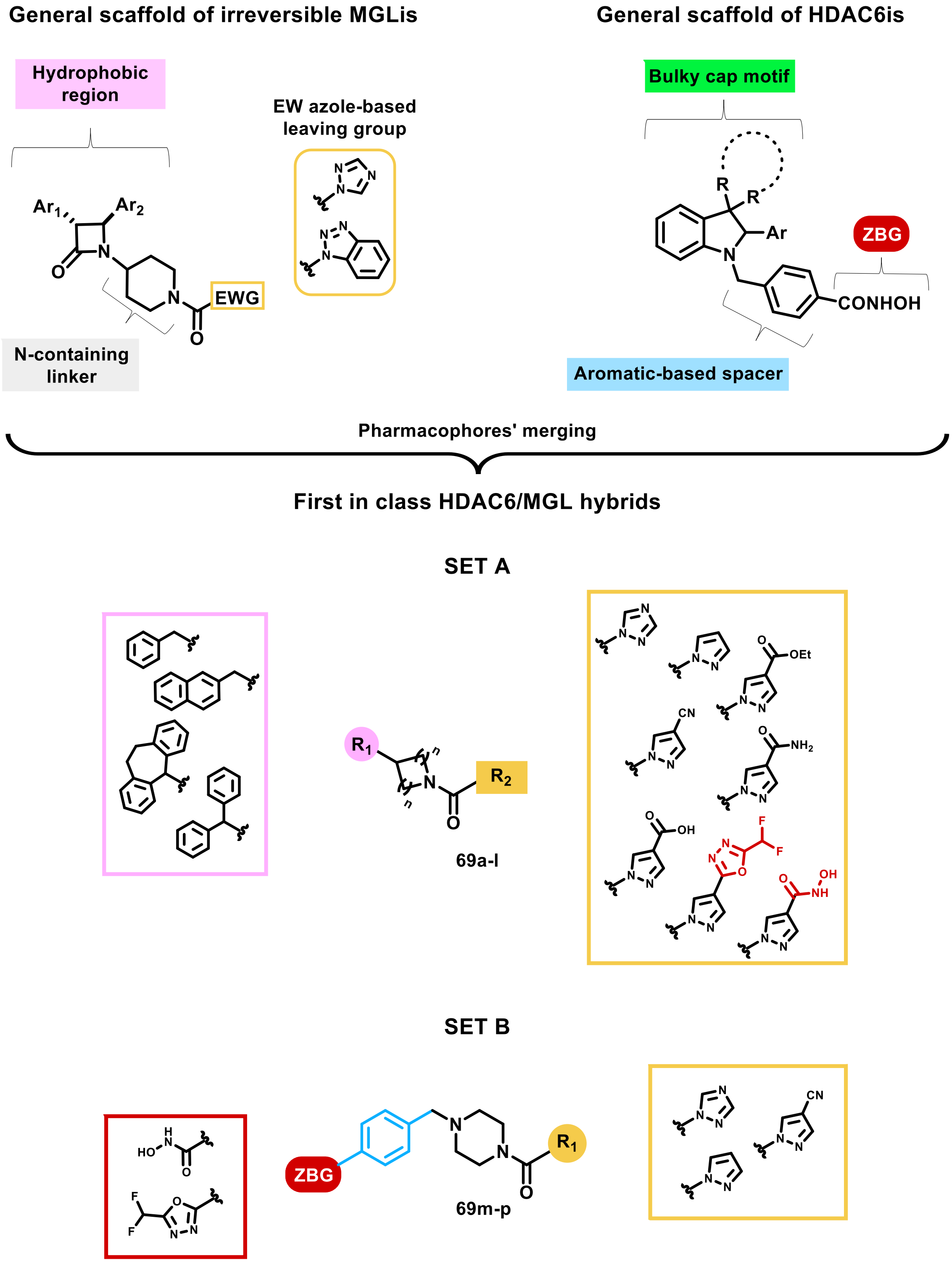

Figure 30. Flow-chart of the rational design for MGL/HDAC6 hybrids. Different colours highlight the key pharmacophoric elements for the inhibition of both targets, which are incorporated into the structure of the title compounds (**69a-p**).

Table 6. Chemical structures and IC_{50} values for *h*MGL and *h*HDAC6 of novel MGLis **69a-p**.

Cmpd	Structure	*h*MGL IC_{50} (nM)^{a}	*h*HDAC6 IC_{50} (nM)^{b}
69a AKU-005	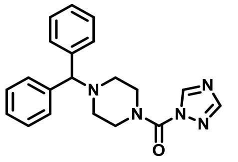	0.82	>10000 (7%)
69b	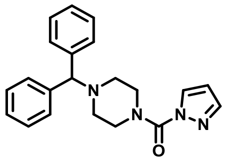	12.6	>10000 (4%)
69c	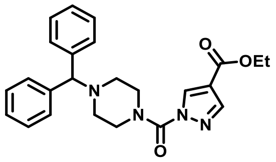	4.30	>10000 (12%)
69d	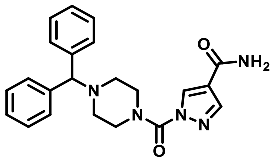	0.34	>10000 (3%)
69e	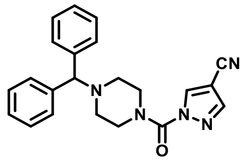	0.24	>10000 (1%)
69f	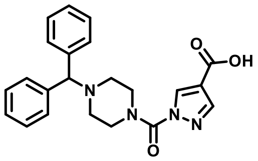	45.3	>10000 (22%)
69g	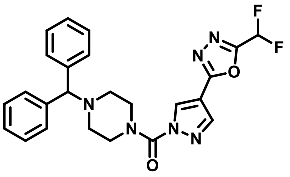	3.97	>10000 (13%)
69h	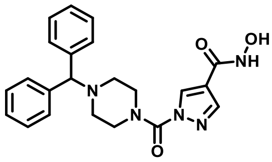	2.96	238
69i	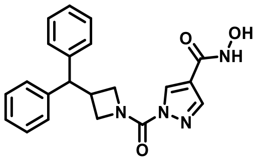	684	285
69j	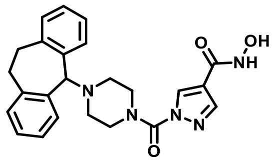	1.86	411

69k	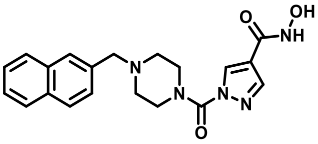	4.23	358
69l	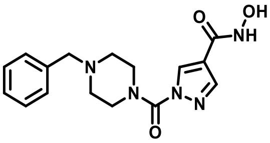	52.1	540
69m	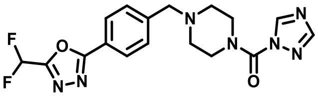	35.4	2856
69n	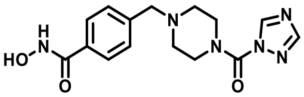	3522	1527
69o	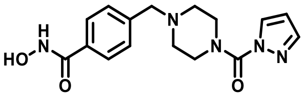	5519	216
69p	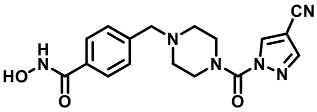	20.7	404
17b[59]	-	11.5	-
68[156]	-	-	41.6

[a] Data are expressed as mean of three independent experiments performed in triplicate. All SDs are within 10%. Data in parentheses indicates inhibition at the 10 μM concentration. Incubation time = 30 min. [b] Data are expressed as mean of three independent experiments performed in triplicate. All SDs are within 10%. Data in parentheses indicates inhibition at the 10 μM concentration. Incubation time = 15 min.

1.11.3 Chemistry

1.11.3.1 Synthesis of Set A compounds (69a-l)

Scheme 3 recapitulates the synthesis of the key synthons useful for the synthesis of the compounds belonging to Set A (**69a-l**).

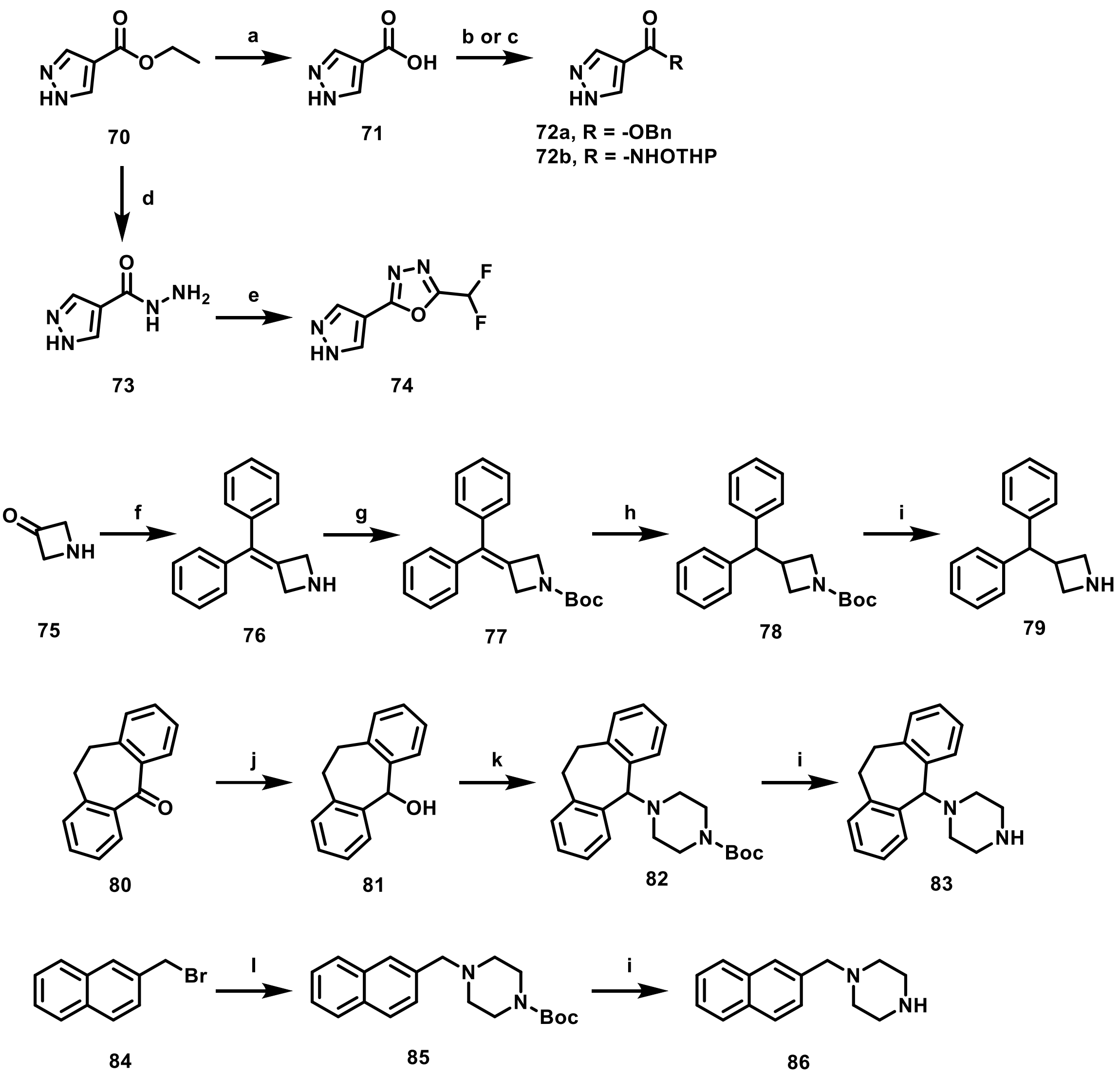

Scheme 3. Reagents and conditions. a) 0.72 N NaOH in H_2O, H_2O 100 °C, 2 h, 99%; b) benzyl alcohol, DCI, dry DMF/DCM, 60 °C, 12 h, 34%; c) NH_2OTHP; EDC·HCl, HOBt, DIPEA, dry DMF, -10 °C to 25 °C, 12 h, 41%; d) NH_2NH_2, EtOH, 82 °C, 12 h, 66%; e) DFAA, dry DMF, -10 °C to 25 °C, 12 h, 45%; f) benzophenone, $TiCl_4$, Zn, dry THF, 0 °C to 60 °C, 12 h, 43%; g) Boc_2O, TEA, dry DCM, 25 °C, 12 h, 70%; h) H_2, Pd/C, MeOH, 25 °C, 12 h, 91%; i) 1 N HCl in MeOH, MeOH, 40 °C, 2 h, 99%; j) $NaBH_4$, MeOH, 25 °C, 1 h, 94%; k) i. $SOCl_2$, Py/PhMe, 25 °C, 3 h; ii. 1-Boc piperazine, K_2CO_3, MeCN, 85 °C, 12 h, 56%; l) 1-Boc piperazine, K_2CO_3, MeCN, 85 °C, 12 h, 69%.

The synthesis of derivatives **72a,b**, and **74** began from a common starting material, the ethyl 1*H*-pyrazole-4-carboxylate (**70**). Basic hydrolysis of **70** furnished the corresponding carboxylic acid **71**. From this latter, two different synthetic strategies were employed to provide intermediates **72a,b**. A Steglich esterification converted **71** into the corresponding benzyl ester **72a**. Alternatively, a coupling reaction with *O*-(tetrahydro-2*H*-pyran-2-yl)hydroxylamine (NH_2OTHP) in the presence of *N*-(3-dimetilaminopropil)-

N′-etilcarbodiimide (EDC·HCl) as coupling agent and 1-hydroxybenzotriazole (HOBt) gave key intermediate **72b**. As for **74**, the carboxylic moiety of compound **70** was converted into the corresponding hydrazide **73**, which was reacted with difluoroacetic anhydride (DFAA) to form the key intermediate **74**. The synthesis of derivative **79** started with the conversion of commercially available 1-Boc-3-azetidinone (**75**) into compound **76** using an asymmetric McMurry reaction in the presence of benzophenone. The following Boc protection of the basic moiety (**77**), and the subsequent reduction of the double bond under H_2 atmosphere led to saturated compound **78**, which was deprotected under acidic conditions, giving key intermediate **79**. Derivative **83** was obtained starting from 10,11-dihydro-5*H*-dibenzo[*a,d*][7]annulen-5-one (**80**), which was reduced by means of $NaBH_4$, furnishing compound **81**. A two steps protocol, involving the interconversion of the hydroxyl group of **81** into the corresponding chloride by means of thionyl chloride, and the subsequent use of this latter as alkylating agent towards 1-Boc piperazine, was employed to form compound **82**. Following Boc deprotection gave key intermediate **83**. The synthesis of derivative **86** began with the alkylation of 1-Boc piperazine by means of 2-(bromomethyl)naphthalene (**84**), providing compound **85**. Boc deprotection under acidic conditions provided key intermediate **86**.

The synthetic strategies affording compound **69a-h** are presented in **Scheme 4**.

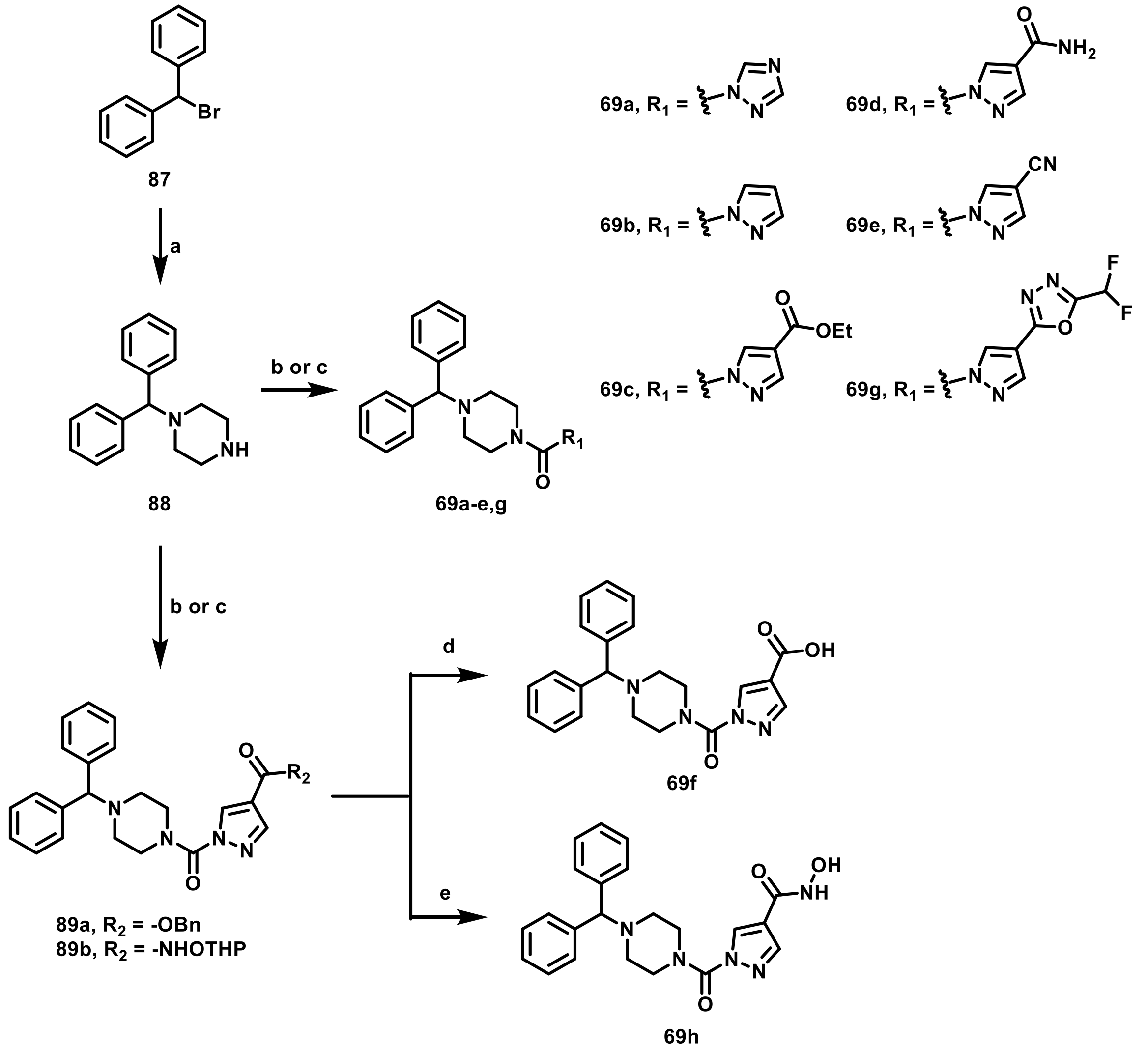

Scheme 4. Reagents and conditions. a) piperazine, K_2CO_3, NaI, MeCN, 85 °C, 12 h, 64%; b) **appropriate azole-based moiety**, 20% w/w $COCl_2$ in PhMe, DMAP, dry DCM, 25 °C, 12 h, 20-90%; c) i. 20% w/w $COCl_2$ in PhMe, saturated solution of $NaHCO_3$ in H_2O/DCM; ii. **appropriate azole-based moiety**, DMAP, dry Py, 30%; d) H_2, Pd/C, EtOAc/MeOH, 25 °C, 12 h, 16%; e) 1 N HCl in MeOH, MeOH, 0 °C, 30 min, 53%.

The piperazine was alkylated by means of bromo derivative **87**, yielding intermediate **88**. In the presence of the appropriate azole-based moieties, this latter was involved in two different protocols for urea formation, affording either compounds **69a-e** and **69g**, or the key intermediates **89a,b**. Intermediate **89a** was deprotected under H_2 atmosphere, providing **69f**. On the other hand, the treatment of **89b** under acidic conditions gave compound **69h**.

The synthetic approaches employed to obtain compound **69i-l** began with a shared starting point, azole-based compound **74** (**Scheme 5**).

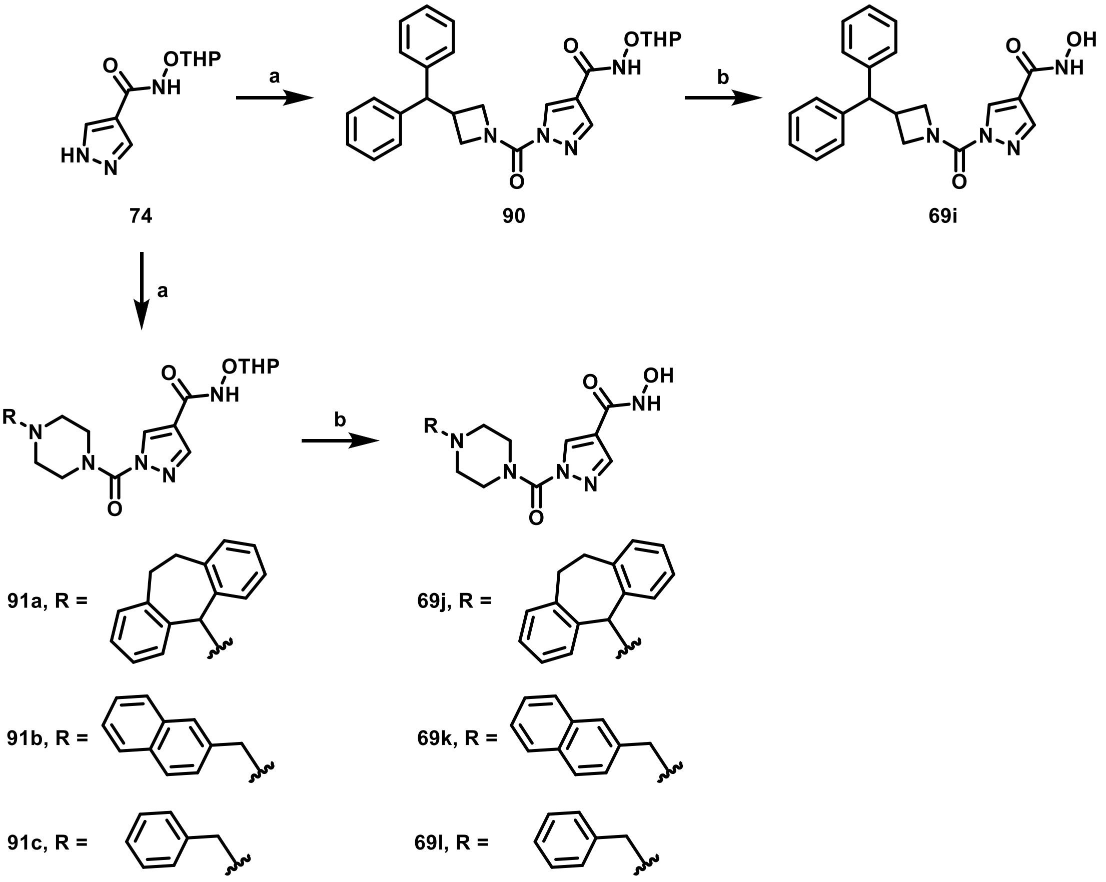

Scheme 5. Reagents and conditions. a) i. (**79** for **90**, **83**, **86**, and 1-Bn piperazine for **91a-c**, respectively), 20% w/w $COCl_2$ in PhMe, $NaHCO_3$ in H_2O/DCM; ii. DMAP, dry Py, 25 °C, 12 h, 26-59%; b) (**90** for **69i**, **91a** for **69j**, **91b** for **69k**, **91c** for **69l**), 1 N HCl in MeOH, MeOH, 0 °C, 30 min, 28-82%.

This latter was coupled with azetidine-based intermediate **79**, giving derivative **90**, which was subsequently deprotected using a 1 N solution of HCl in MeOH. Similarly, a coupling reaction involving **74** in the presence of the appropriate piperazine-based moiety led to compounds **91a-c**, that were deprotected under the same acidic conditions as for **69i**, providing compounds **69j-l**.

1.11.3.2 Synthesis of Set B compounds (69m-p)

Scheme 6 recapitulates the synthesis of the key synthons useful to attain compounds belonging to Set B (**69m-p**).

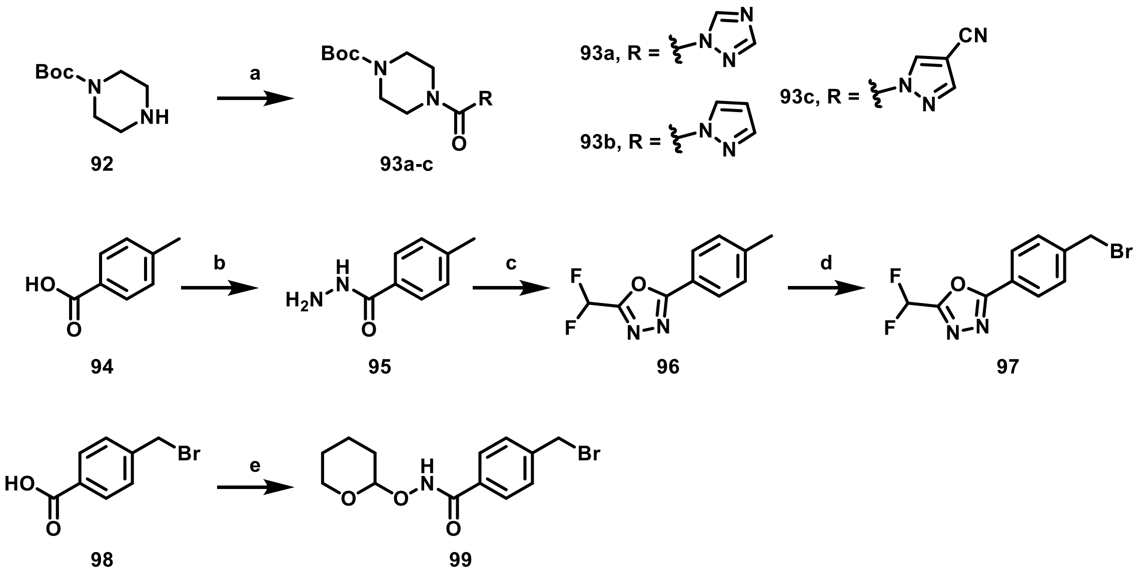

Scheme 6. Reagents and conditions. a) appropriate azole-based moiety, 20% w/w $COCl_2$ in PhMe, DMAP, dry DCM, 25 °C, 12 h, 43-90%; b) i. H_2SO_4, EtOH, 82 °C, 12 h; ii. NH_2NH_2, EtOH, 82 °C, 12 h, 62%; c) DFAA, dry DMF, 25 °C, 12 h, 34%; d) NBS, AIBN, dry MeCN, 85 °C, 12 h, 54%; e) NH_2OTHP, EDC·HCl, dry DCM/DMF, 25 °C, 12 h, 55%.

Derivatives **93a-c** were synthesised starting from 1-Boc piperazine (**92**), which was reacted with the appropriate azole-based moiety in the presence of phosgene to give ureas **93a-c**. The synthetic strategy affording intermediate **97** began with the conversion of the carboxylic function of compound **94** into the corresponding hydrazide **95** via a two steps protocol, involving Fisher esterification in EtOH and subsequent aminolysis in the presence of monohydrate hydrazine. Derivative **95** was treated with DFAA, affording compound **96**. Following radical bromination of **96**'s benzyl position in the presence of *N*-bromosuccinimide (NBS) and 2,2'-azobisisobutyronitrile formed key intermediate **97**. Key intermediate **99** was generated by applying a coupling reaction between compound **98** and NH_2OTHP in the presence of EDC·HCl as coupling agent.

The synthetic strategies affording compound **69m-p** are presented in **Scheme 7**.

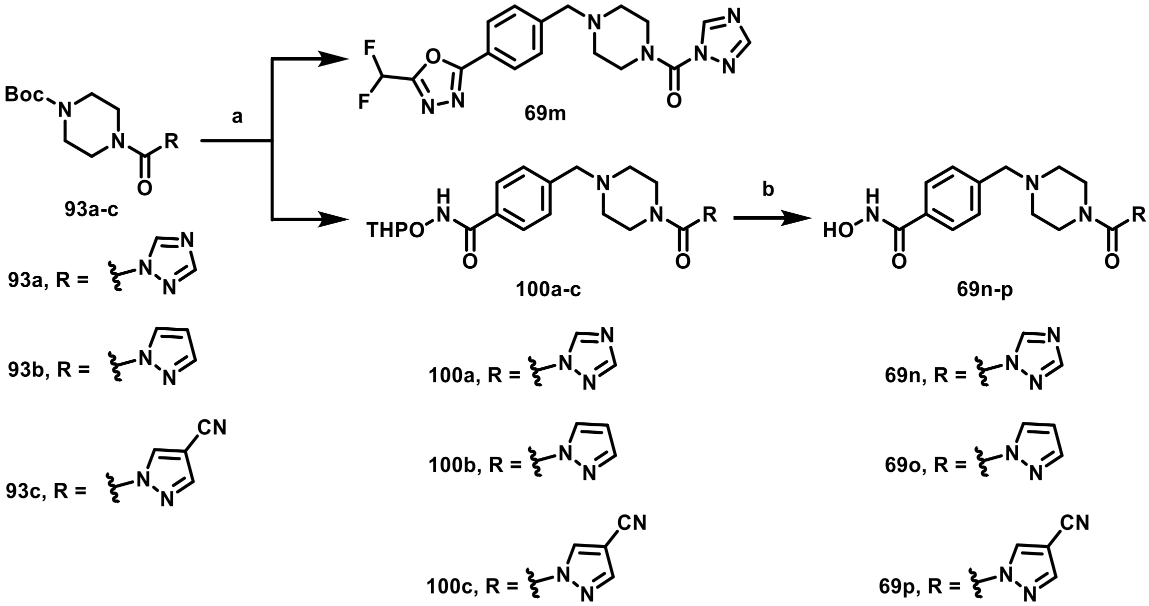

Scheme 7. Reagents and conditions. a) i. (**93a** for **69m** and **100a**, **93b** for **100b**, **93c** for **100c**), 1 N HCl in MeOH, MeOH, 40 °C, 2 h; ii. (**97** for **69m**, **99** for **100a-c**), TEA, MeCN, 85 °C, 12 h, 40-58%; b) (**100a** for **69n**, **100b** for **69o**, **100c** for **69p**), 1 N HCl in MeOH, MeOH, 0 °C, 30 min, 24-53%.

Following Boc deprotection of derivative **93a**, compounds **97** and **99** were used as alkylating agent to give title compound **69m** and intermediate **100a**. Similarly, compound **99** was employed as alkylating agent towards **93b,c**, after Boc deprotection of these latter, providing the key intermediates **100b,c**. The hydroxamate functionalities of **100a-c** was deprotected under acidic conditions, leading to ureas **69n-p**, respectively.

1.11.4 Computational studies

To further investigate the influence of the EWG in position 4 of the pyrazole in driving the inhibitory potency for *h*MGL, quantum mechanics/molecular mechanics (QM/MM) studies were performed. First, the trajectory of the irreversible carbamylation of catalytic Ser122 residue was inquired using reference compound **16**, characterising the free energy profile along the reaction coordinate from reactants to products. The same analyses were conducted for compounds **69a,b,d,e,f,h**, focusing on the activation barrier associated with the transition state.

Analysis of MGL Ser122 carbamylation by reference compound 16

As previously reported, compound **16** is a well-established MGLi carbamylating agent encompassing potent inhibitory activity, and showing high similarity with the MGLis herein described. Hence, it perfectly fits as a suitable candidate to study the mechanism of Ser122 carbamylation. The kinetic of this phenomenon is supposed to occur in four stages, as depicted in **Figure 31**.

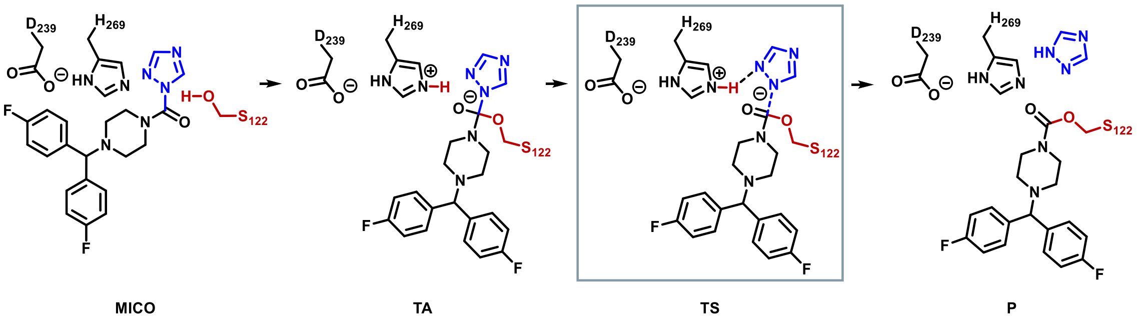

Figure 31. Schematic representation of MGL Ser122 carbamylation by means of compound **16**. First, the ligand reaches MGL binding pocket, forming a non-covalent enzyme-substate complex known as Michaelis complex (MICO). Then, the electrophilic urea centre undergoes a nucleophilic attack from the catalytic Ser122 residue, producing a tetrahedral adduct (TA), in which the negative charge is delocalised on the N_1 of the 1,2,4-triazole ring. This switch allows the TA to evolve into the transition state (TS), where the bond between the N_1 of the leaving group and the carbonyl group is broken. Notably, this feature is not fully displaced, but it remains coordinated to the electrophilic centre, keeping in touch with it. Moreover, the N_2 of the 1,2,4-triazole ring contacts the protonated nitrogen atom of His269. This highly energetic status is extremely unstable; hence it is prone to collapse into the final products (P), in which the leaving group is completely detached from the electrophilic centre, and the catalytic Ser122 residue is carbamylated with the remaining part of the molecule.

This was further confirmed by QM/MM simulations, which also elucidate the binding pose of the ligand within MGL binding pocket (**Figure 32A**). Interestingly, the piperazine ring of **16** seems to undergo a 90° flip in its orientation during the progression from the tetrahedral adduct (TA) to the transition state (TS). This effect needs to be further interrogated with additional studies, but it is presumed to contribute to the elevated energetic nature of the TS. Further, a diagram of the free energy profile for MGL Ser122 carbamylation along the reaction coordinate was calculated, displaying that the TS plays a crucial role in the progression from the reactants to the products (**Figure 32B**).

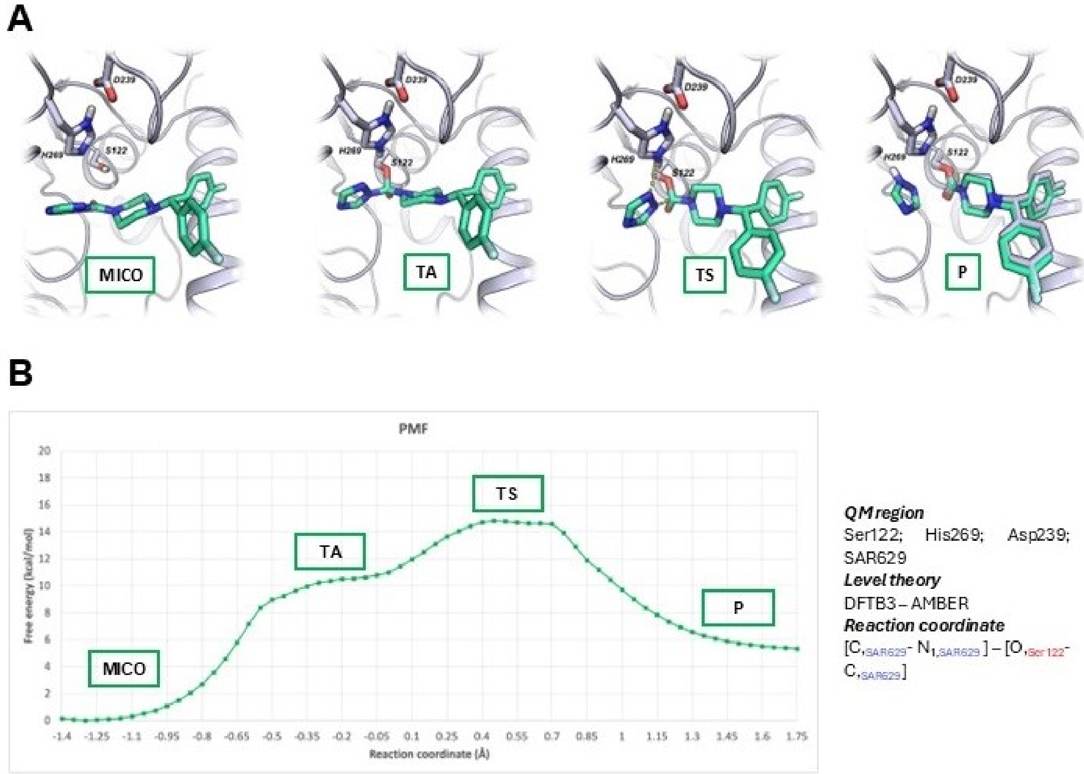

QM region
Ser122; His269; Asp239; SAR629
Level theory
DFTB3 – AMBER
Reaction coordinate
$[C_{,SAR629}-N_{1,SAR629}]-[O_{,Ser122}-C_{,SAR629}]$

Figure 32. Free-energy profile for MGL Ser122 carbamylation by QM/MM simulations. A) Docking models for the main energy states occurring during Ser122 carbamylation. Michael complex (MICO), tetrahedral adduct (TA), transition state (TS), and products (P). B) Graphical trajectory of the free-energy variation along the reactions coordinates from reactants to products.

QM/MM simulations of selected compounds 69a,b,d-f,h

To decipher the influence of the EWG on the activation barrier and the inhibitory potency for the target protein of the newly synthesised MGLis, QM/MM simulations were also performed for compounds **69a,b,d-f,h** (**Table 7**).

Table 7. E_a and IC_{50} values for *h*MGL of selected compounds **69a,b,d-f,h**.

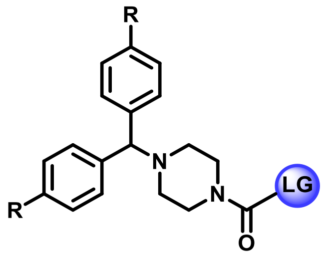

69a,b,d,e,f,h, R = -H
16, R = -F

Cmpd	LG	E_a (kcal/mol)	*h*MGL IC_{50} (nM)
69a (**AKU-005**)	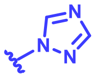	≈14	0.82
69b	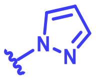	≈20	12.6
69d	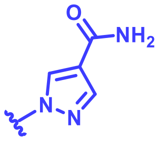	≈15	0.34
69e	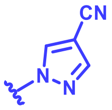	≈14	0.24
69f	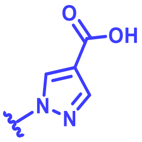	≈25	45.3
69h	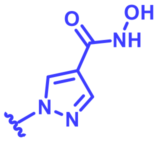	≈16	2.96
16	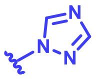	≈14.5	1.1 (*r*MGL)

Compound **69a** (E_a = 14 kcal/mol, *h*MGL IC_{50} = 0.82 nM) perfectly aligns with the data shown for compound **16**. As predicted, removing the nitrogen at position 4 significantly affects both the E_a and the IC_{50}, explaining the lower activity of compound **69b** (E_a = 20 kcal/mol, *h*MGL IC_{50} = 12.6 nM) compared to **69a**. On the other hand, the replacement of the N_4 of the 1,2,4-triazole ring with a pyrazole unit supporting a lipophilic EWG (amide for **69d**, or cyano for **69e**) in the same position improves the inhibitory potency for *h*MGL (IC_{50} values of 0.34 and 0.24 for compound **69d** and **69e**, respectively), lowering the activation barrier (E_a = 15 and 14 kcal/mol, respectively). The addition in position 4 of hydrophilic moieties (carboxylic acid for **69f**, hydroxamate group for **69h**) negatively impacts the activity of these compounds compared to **69a**. Particularly, the carboxylic acid of **69f** substantially augments the E_a while decreasing the *h*MGL IC_{50} values (E_a = 25 kcal/mol, IC_{50} = 45.3 nM), whereas this effect is mitigated in **69h (**E_a = 16 kcal/mol, IC_{50} = 2.96 nM), presenting a hydroxamate group.

Collectively, these studies corroborate the initial hypothesis, underlining that the installation of an EWG in position 4 of a pyrazole scaffold could substitute a 1,2,4-triazole ring for generating a good leaving group making the N1 of the pyrazole moiety better suited for accommodating a negative charge in the TS. Furthermore, stereoelectronic properties of the EWG strongly influenced the activity on *h*MGL. Indeed, it was observed that an EWG supports the delocalisation of the negative charge on the leaving group during the TS, decreasing both the E_a and the IC_{50} values for *h*MGL. An inverse correlation between these two data was found across the tested compound, displaying that the higher the E_a, the lower the IC_{50} value. Of course, these speculations need to be further confirmed by enzymatic studies that are in course.

1.11.5 Pharmacological studies

Selectivity profile for selected compounds 69c,h-l,p

For the most representative compounds, the selectivity profile over relevant off-targets was evaluated *in vitro* (**Table 8**). Therefore, the activity of selected derivatives on *h*HDAC6 (*h*HDAC1,2,3,10) and *h*MGL (*h*FAAH) cognates was evaluated. Compounds **69c** and **69p** do not inhibit *h*HDAC1, whilst **69h** displays low activity on this HDAC isoform. As for other HDAC class I members, compounds **69i** and **69k** exhibit poor affinity for *h*HDAC2, while the other tested derivatives (**69h**, **69j**, and **69p**) are completely selective. On the other hand, only **69p** do not show any activity on *h*HDAC3, whereas **69h, 69i, 69j**, and **69k** inhibit this isoform at micromolar concentrations. Regarding *h*HDAC10, **69h** show little interference towards this class IIB member, while **69p** do not affect it. Lastly, compounds **69h**, **69l**, and **69p** displayed micromolar inhibition of *h*FAAH. Comprehensively, these data highlight that compound **69h** has lower selectivity profile across the HDAC family of enzymes displaying inhibition potency values in the micromolar range, while derivative **69p** only showed some inhibition of *h*FAAH (IC_{50} = 2094 nM). Nonetheless, this effect is elicited at a concentration 100-fold higher than its *h*MGL IC_{50} value, ensuring a suitable selectivity ratio.

Table 8. Selectivity data for selected compounds **69c,h-l,p** for *h*HDAC6-related isoforms (*h*HDAC1,2,3,10) and *h*MGL off-target (*h*FAAH).

Cmpd	***h*HDAC1 IC_{50} (nM)[a]**	***h*HDAC2 IC_{50} (nM)[a]**	***h*HDAC3 IC_{50} (nM)[a]**	***h*HDAC10 IC_{50} (nM)[a]**	***h*FAAH IC_{50}(mM)[b]**
69c	>10000 (21%)	-	-	-	-
69h	1782	>10000 (36%)	4275	2896	4750
69i		7211	1684		
69j		>10000 (22%)	3518		
69k		3770	1077		
69l					1438
69p	>10000 (8%)	>10000 (18%)	>10000 (37%)	>10000 (41%)	2094

[a] Data are expressed as mean of three independent experiments performed in triplicate. All SDs are within 10%. Data in parentheses indicates inhibition at the 10 μM concentration. Incubation time = 15 min. [b] Data are expressed as mean of three independent experiments performed in triplicate. All SDs are within 10%. Incubation time = 30 min.

Toxicity assessment in murine and human in vitro models

Cytotoxicity of the selected derivatives **69h-j,l,p** was evaluated in 3T3 murine fibroblasts, and 1321N1 human astrocytes (**Figure 33A-B**). In murine cells, only **69j** markedly reduced cell viability (<50%), while **69h,I,l,p** did not significantly affect murine fibroblasts vitality (>90%) up to a dose of 30 μM following a 24 h exposure period. On the other hand, only **69l** moderately diminished human astrocytes vitality, whilst **69h-j,p** showed only minimal effects on cell viability (>90%) up to a dose of 30 μM following a 24 h exposure period. Notably, the most interesting derivatives of this series, **69h** and **69p**, did not exert any cytotoxic effects at all the tested concentrations, supporting their safety suitability for *in vivo* studies.

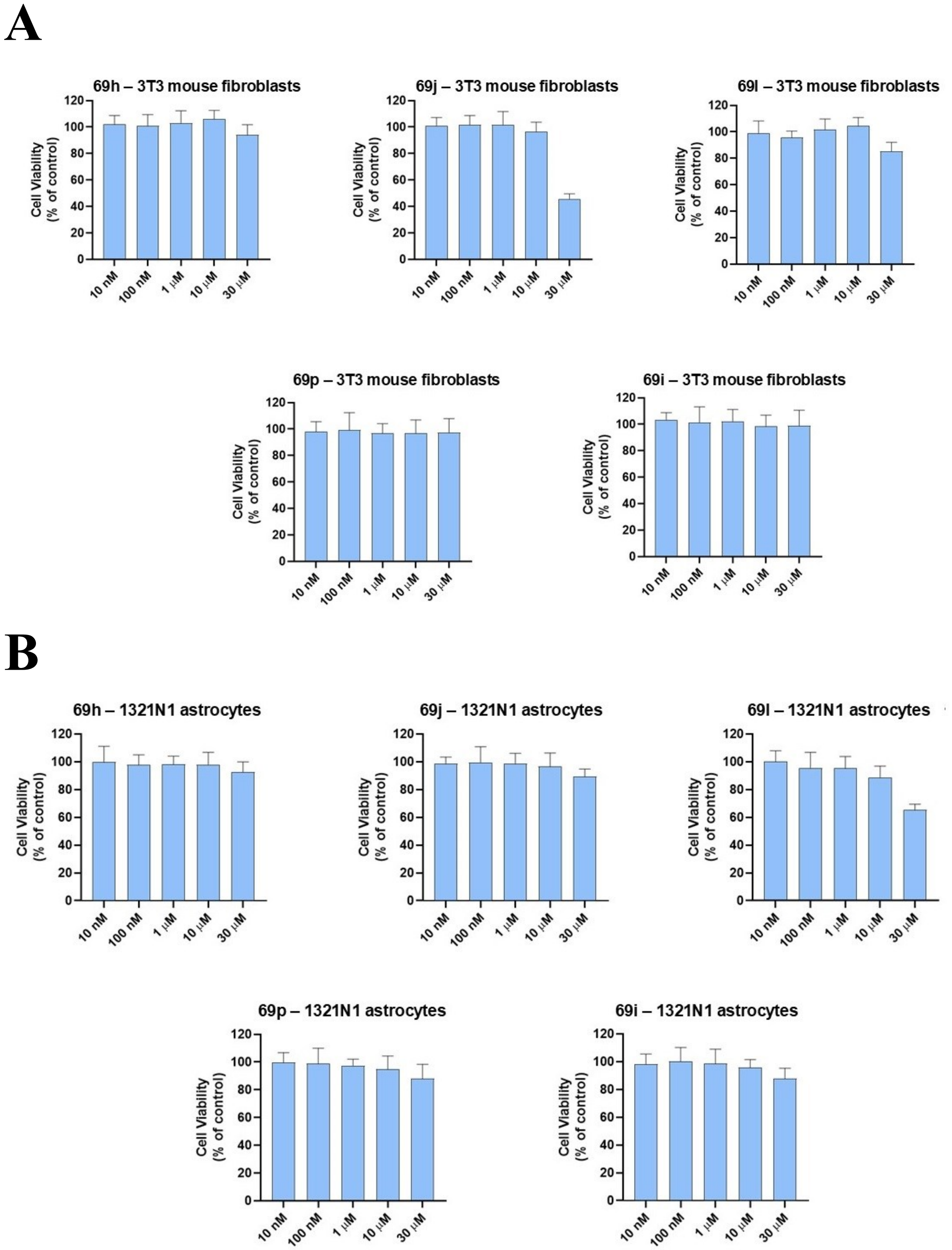

Figure 33. A) Remaining 3T3 mouse fibroblasts cell viability after 24 hours of treatment. B) Remaining 1321N1 human astrocytes cell viability after 24 hours of treatment.

1.12 Novel DGLα/β-FAAH hybrids

1.12.1 Background

Lots of evidence highlight that ECS activation elicited by direct agonists plays a pivotal role in controlling epileptic episodes.[159] The antiseizure properties of these compounds are associated with the neuromodulation of CB_1Rs, that regulates glutamate transmission mitigating synaptic overstimulation and excitotoxicity. In this light, compound **8** previously demonstrated good anticonvulsant efficacy in clinical trials enrolling patients with pharmaco-resistant forms of epilepsy, including Dravet and Lennox-Gastaut syndromes.[160] Since both AEA and 2-AG proved to alleviate epileptic episodes, both FAAH and MGL inhibition or simultaneous blockade of these two have been proposed as promising strategies for tackling these pathological conditions.[161,162] FAAHis, such as **22**, hold strong antiepileptic potential, as they can restore hippocampal physiological synaptic functionality while soothing excitotoxicity.[163] Moreover, **22** demonstrated to revert emotional alterations, acting on amygdala.[164] The research team were I performed my PhD internship recently embarked in the development of a series of selective FAAH carbamylating agents as potential antiseizure tools. Among them, compound **23a,b** stood out for their exceptional activity in pilocarpine-induced murine model of temporal lobe epilepsy (TLE).[88] On the other hand, MGLis, such as **14**, proved to exert beneficial effects in controlling kainic acid-induced seizures.[165] In AE, two clinical features emerged as crucial for promoting antiepileptic effects: drugs should be acutely administrated, as sub- or chronic application might induce pro-convulsant activity; high dosages foster spontaneous seizures, hence low dosage pharmacological treatments are the golden standards.[166,167] Recently, Epidiolex, an oral formulation of the phytocannabinoid **8**, entered in a phase II clinical trial, holding promise as a groundbreaking drug candidate potentially harnessing pharmaco-resistant CAE.[26,168] Nevertheless, the potential short- and long-term side effects associated with chronic administration of direct CB_1R agonist in CAE patients still limits its clinical application. Similarly, FAAHis, like **27**, unequivocally showed promising anti-absence properties.[169,170] However, MGL inhibition might induce CB_1R-related side effects, due to a narrow therapeutic window in epileptic context.[167] Furthermore, increased 2-AG levels have been detected in patients affected by AE.[171] This is further corroborated by the controversial data observed in chronic-stage TLE mouse models, in which the administration of **14** resulted in augmented seizure susceptibility, whereas pharmacological treatment with the DGL inhibitor **28** induced antiepileptic effects.[172]

On this ground, reducing 2-AG levels by inhibiting DLGα/β enzymes represents an innovative strategy for addressing AE. Moreover, the quest for more efficient pharmacological treatments prompted scientists to look for polypharmacological approaches in managing absence episodes. In this frame, the simultaneous block of DGL- and FAAH-mediated signalling might exert synergistic effects, potentiating therapeutic activity.

1.12.2 Rational design

Previous pharmacological studies (unpublished data from our collaborators at University of Malta) highlighted that the fine regulation of AEA and 2-AG levels within the CNS fosters beneficial effects in animal models of AE. Particularly, these positive outcomes stem from concurrently increasing the levels of AEA whilst lowering 2-AG concentration. Giving the complementary roles of FAAH and DGLα/β enzymes in regulating these two endocannabinoids in the CNS, I developed a series of dual DGLα/β and FAAH inhibitors as potential pharmacological tools in AE treatment. The essential features of compounds

23b, **36a**, and **36b**, mandatory to obtain suitable DGLs and FAAH inhibition, were hybridised, constructing a novel molecular architecture, typified by compounds **101a** and **101b** (**Figure 34**, **Table 9**). This scaffold represents a simplified structure compared to the parent derivatives, embedding a phenylhexyl lipophilic chain for FAAH recognition while exploiting an azole-based urea as reactive warhead. Particularly, both *N*1- and *N*2-substituted 1,2,3-triazole unit were used as leaving groups for carbamylating both FAAH and DGLα/β catalytic serine residues. This point modification aimed to evaluate the difference between the two tautomers in the biological activity across the target proteins and relevant off-targets.

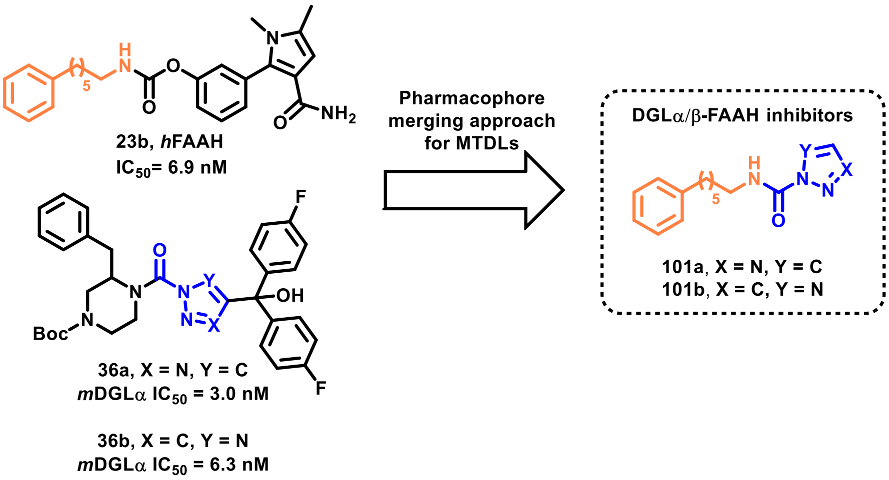

Figure 34. Flow-chart of the rational design for DGLα/β-FAAH hybrids. Different colours highlight the key pharmacophoric elements for the inhibition of both targets, which are incorporated into the structure of the title compounds (**101a,b**).

Table 9. Chemical structures and IC_{50} values of compounds **101a**,**b** for *m*DGLα, *m*DGLβ, and *m*NAPE-PLD.

Cmpd	**101a**	**101b**
Structure	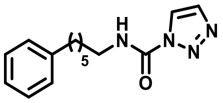	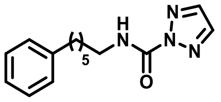
***m*DGLα** **IC_{50} (nM)**[a]	427	240
***m*DGLβ** **IC_{50} (nM)**[a]	63.1	50.1
***m*NAPE-PLD** **IC_{50} (nM)**[a]	>10000	>10000
SI *m*DGLα/*m*DGLβ	≈ 6.8	≈ 4.8
SI *m*NAPE-PLD/ *m*DGLα	69	245
SI *m*NAPE-PLD/ *m*DGLβ	468	1175
***h*FAAH IC_{50} (nM)**[a]	248	18.5
***h*MGL IC_{50} (nM)**[a]	3163	792
SI *h*MGL/*h*FAAH	13	43

[a] Data are expressed as mean of three independent experiments performed in triplicate. All SDs are within 10%.

1.12.3 Chemistry

1.12.3.1 Synthesis of compounds 101a,b

The synthetic approaches leading to compounds **101a,b** is recapitulated in **Scheme 8**.

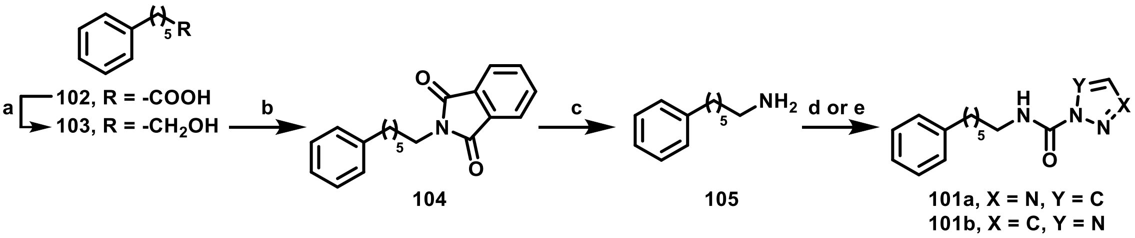

Scheme 8. Reagents and conditions: a) $BH_3{\cdot}S(CH_3)_2$, dry THF, 0 °C, 2 h, 95%; b) phtalimide, PPh_3, DIAD, dry THF, 0 °C to 25 °C, 12 h, 86%; c) $NH_2NH_2{\cdot}H_2O$, EtOH, 82 °C, 2 h, 59%; d) 1,2,3-triazole, 20% solution of $COCl_2$ in PhMe, DMAP, dry DCM, 25 °C, 12 h, 21%; e) i. $(COCl_2)_3$, DIPEA, THF, 0 °C, 30 min; ii. 1,2,3-triazole, DMAP, DIPEA, THF, 0 °C, 30 min, 23%.

The carboxylic acid moiety of compound **102** was reduced by means of borane-dimethylsulfide complex, furnishing compound **103**. This latter was involved in a Mitsunobu protocol in the presence of phthalimide, triphenylphosphine, and diisopropyl azodicarboxylate (DIAD), giving **104**, which was converted into the corresponding primary amine **105** using hydrazide monohydrate. Intermediate **105** was coupled with 1,2,3-triazole to afford compounds **101a,b**. Due to the difference in dipole moment between 1*H*- and 2*H*-1,2,3-triazole tautomers, the correct choice of the reaction parameters, such as the solvent and the temperature, was critical to favour the formation of one isomer over the other.[173,174] The initial formation of a carbamoyl chloride intermediate on the 1,2,3-triazole using phosgene, and subsequent displacement of the chlorine atom by means of **105** led to the formation of title compound **101a**. On the other hand, a two steps protocol afforded **101b** after the conversion of **105** amino function into the corresponding carbamoyl chloride, observed through ESI-MS, that subsequently underwent nucleophilic attack by the NH-group of the 1,2,3-triazole ring.

1.12.4 SARs analysis and selectivity over relevant off-targets

Table 9 summarises the inhibitory potency of **101a** and **101b** for the biological targets. Moreover, **101a,b** were also screened over FAAH and DGLα/β cognates involved in anabolic and catabolic endocannabinoids' pathways. Particularly, their biological activity was also assessed against NAPE-PLD, crucial in AEA biosynthesis, and MGL, the main character in 2-AG degradation, and their selectivity index (SI) were calculated (**Table 9**). As expected, both tested compounds displayed no affinity for *h*NAPE-PLD (IC_{50} values >10 μM). The comparable inhibitory activity in the low nanomolar range of **101a** and **101b** for DGLβ (IC_{50} values of 50.1 and 63.1 nM, respectively) are at least 5-fold greater compared to the potency for *h*DGLα (IC_{50} values of 437 and 240 nM, respectively). This latter data is in line with previous reports, confirming that the different nitrogen position is likely to drive protein recognition establishing additional polar interactions within the binding pocket. The nanomolar affinity for DGL enzymes ensures suitable selectivity ratios over NAPE-PLD. Tested over endocannabinoids' catabolic enzymes, **101b** displayed stronger enzymatic activity for both *h*FAAH (IC_{50} = 18.5 nM), and *h*MGL proteins (IC_{50} = 748 nM) compared to **101a** (IC_{50} values of 248 and 3163 nM, respectively), but also an increased selective profile (SI *h*MGL/*h*FAAH of 43 and 13, respectively).

1.13 Conclusions

The medical treatment of neuroinflammatory-based diseases and neurological disorders is still a paramount challenge. Massive literature reports highlight that polypharmacological approaches exploiting ECS modulation can elicit beneficial effects in treating these pathological conditions. In this context, my PhD work focused on the development of MTLDs, exploiting three different strategies:

1) Concurrent inhibition the endocannabinoids' catabolic enzymes, particularly FAAH and MGL enzymes, while impairing histaminergic system through H_3R antagonism.
2) Simultaneous inhibition of MGL enzyme and the peculiar epigenetic modulator HDAC6.
3) Inhibition of the 2-AG biosynthetic DGLα/β enzymes, while impairing FAAH protein activity.

My first approach led to the development of 2 novel FAAH/H_3R ligands, completing a series of compounds endowed with inhibitory activity over endocannabinoids' catabolic enzyme whilst antagonising H_3Rs. SARs exploration highlighted how subtle modifications of the scaffold significantly impacts the affinity across the target proteins. Among them, compound **46f** emerged as a promising compound for its ability to inhibit both FAAH and MGL enzymes (IC_{50} = 17 nM for *h*FAAH, IC_{50} = 46 nM for *h*MGL), and antagonistic activity on H_3R (K_i = 1.02 nM for *h*H_3R). Therefore, a flow synthetic approach was employed to improve its synthetic route, potentially enabling its large-scale production. **46f** possesses favourable drug-like properties, such as high solubility and chemical stability in water, good log*P* value, satisfactory microsomal stability in mouse. Moreover, though it can interact with some H_3R-related off-targets in the micromolar range, its robust nanomolar affinity for H_3R ensures a suitable selectivity profile.

Compounds **46f**,**g**,**h**,**l** were tested in an *ex-vivo* rat model of neuroinflammation, exhibiting dose-dependent, moderate to high neuroprotective activity, with compound **46l** efficiently reverting neurodegeneration in this model. Further, *h*MO3.13, a cellular model of OPCs, were exposed to the selected molecules **46f**,**h**,**l**, detecting an improvement in the transcription of MBP exerted by all the tested compounds. Notably, **46f**'s impact on MBP transcripts was comparable to the differentiating agent PMA, indicating it can significantly foster oligodendrocyte maturation thus contrasting demyelinating processes. Taking all this data into account, the next steps in this project should be the scaled-up production of compound **46f**, using optimised batch and flow chemistry approaches, as well as more in-depth pharmacological studies interrogating its PK and PD properties *in vivo*.

Regarding the second approach, I developed a first-in-class series of 15 MGLis embedding either a triazole-based or novel pyrazole-based leaving groups. Starting from the previously described **69a** (**AKU-005**), several pyrazole analogues supporting an EWG in position 4 were explored to investigate the influence of the stereoelectronic properties on the inhibitory activity against MGL enzyme. The introduction of a hydroxamic group integrated Zn^{2+} ion chelating ability, affording dual HDAC6/MGL hybrids. Structural modifications of the linker unit and the aromatic region underlined interesting patterns in the biological activity on the targets. In this context, bifurcated compounds were also replaced by linear shaped-molecules, moving the Zn^{2+}-chelating moiety from the leaving group to the aromatic region. The synthetic efforts produced two sets of compounds, titled A and B, displaying different activity across the targets. Among them, compounds **69h** and **69p** show suitable dual HDAC6/MGL inhibition (IC_{50} values of 2.96 and 20.7 nM for *h*MGL, IC_{50} values of 238 and 404 nM for *h*HDAC6) to be further investigated. Furthermore, QM/MM simulations performed on **69a,b,d-f,h** validated the rational design, highlighting that the higher the activation barrier required for the conversion from the transitional states to the products, the higher the IC_{50} values for *h*MGL enzyme. In this light, it was observed that the introduction in position 4 of an EWG on a pyrazole ring significantly lowers the E_a, hence acting as a suitable candidate for replacing 1,2,4-triazole leaving group and exerting effective MGL Ser122 carbamylation. For the most promising compounds, **69h** and **69p**, more in-depth pharmacological evaluations will be performed in order to completely assess their PK and PK profiles. Particularly, since both HDAC6 and MGL are involved in the onset and progression of neuroinflammatory and neurodegenerative diseases, their neuroprotective effects will be interrogated using *in-vitro* and *in-vivo* models of these pathological conditions.

In the third approach, I merged the pharmacophoric elements useful to obtain the concurrent inhibition of both DGL isoforms and FAAH enzymes, constructing a novel scaffold for hybrid activity. These efforts culminating in the synthesis and characterisation of two 1,2,3-triazole based ureas, compounds **101a,b**. Enzymatic assays displayed interesting patterns in the modulation of the target proteins. Further, selectivity over NAPE-PLD and MGL, which are involved in AEA biosynthesis and 2-AG metabolism, respectively, were also assessed. Compound **101b** exhibits improved inhibitory potency compared to **101a** throughout all the screened panel. Both compounds show preferential activity on *h*DGLβ over *h*DGLα, and do not affect *h*NAPE-PLD. Compound **101b** inhibit both *h*FAAH and *h*MGL in the nanomolar range, while **101a** exhibits moderate activity on *h*FAAH and poor inhibition of *h*MGL. These preliminary results validated *2H*-1,2,3-triazole urea as the most suitable warhead for achieving simultaneous DGLα/β and FAAH inhibition, displaying improved enzymatic activity compared to its *1H* tautomer. Future efforts will focus on exploring SARs, introducing bulkier 1,2,3-triazole based leaving groups, as in the parent compounds **101a,b**. This structural modification should improve the selectivity over MGL, which is known to accommodate smaller leaving groups within the binding pocket. In parallel, pharmacological *in vitro* and *in vivo* evaluations will be performed to assess the efficacy and safety profile of **101b** in rodent models of AE.

Chapter 2: leveraging SL-based strategy with novel small peptides and peptidomimetics as PPI disruptors of RAD52 oligomerisation

2.1 Cancer

Cancer is an umbrella term enclosing a plethora of diseases typified by an abnormal growth of mutated cells. Particularly, it is a malignant form of neoplasm, diverging from benign tumour because of its ability to invade surrounding tissue or spreading throughout the body, in a process called metastatization. Several classifications have been proposed so far, based on different principles. Two main categories define the malignancies as blood cancers, affecting cells located in blood and bone marrow, and solid tumours, which are organised into lumps. Among them, the distinct types of cancer could be clustered based on their histological profile (leukaemias, myelomas, lymphomas, sarcomas, carcinomas, blastomas, etc.). the organ where it originates (lung, liver, kidney, breast, etc.), or through the Tumour Node Metastasis (TNM) system, which sized the primary tumour extension, evaluate the regional lymph involvement, and detect the eventual presence of metastasis.[175]

Cancerous cells adopt a specific phenotype characterised by acquired biological features, known as hallmarks, which drives the complex network supporting tumour progression (**Figure 35**).[176]

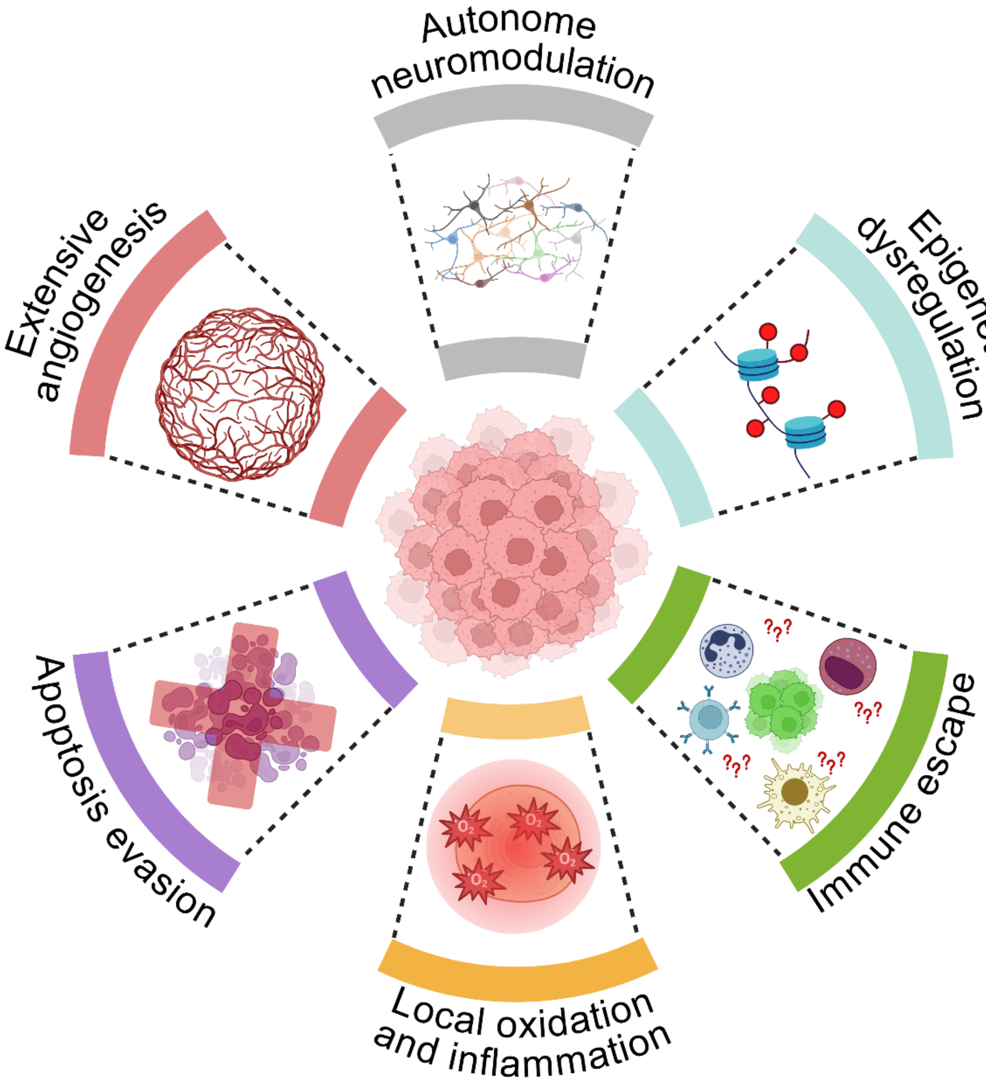

Figure 35. Schematic representation of cancer hallmarks.

The development of an independent neuromodulatory network encourages tumour progression, promotes apoptosis evasion, facilitates the accumulation of non-functional senescent cells, and masks neoplastic cells from the immune host responses controlling cell growth and division. Alongside these features, a robust angiogenesis provides nutrients and oxygen to the highly proliferating cells, reprogramming cellular metabolism. The establishment of a local microenvironment typified by a persistent oxidative and inflammatory states prompts cancer expansion and immune escaping.

Moreover, altered epigenetic pathways contribute to develop unique cancer phenotypes, enabling high plasticity towards the immune checkpoints, and chemotherapeutics.[176]

Despite its low incidence compared to other types of malignant neoplasms, scientific interests in addressing pancreatic cancer are increasing, due to its negative prognosis, and high lethality rates.[177]

2.1.1 Pancreatic cancer

Pancreatic tumours encompass a series of solid and liquid cancer stemming from exocrine or endocrine pancreas. The most representative example is pancreatic ductal adenocarcinoma (PDAC), which accounts for 90% of pancreatic neoplasms, and it affects epithelial ductal cells. In PDAC initial stage, patients do not show significant clinical symptoms, posing serious challenges in early diagnosis. Further, preliminary detection is hindered by low sensitivity of the diagnostic methods currently in use. Indeed, most cases are diagnosed at an advanced stage, when it is impossible to surgical resect the tumour mass, and currently available radio- and chemotherapies offer limited benefits.[177]

In this context, chemotherapeutics are used as adjuvant strategies in patients showing resectable or border line resectable PDAC, limiting negative outcomes pre- or post-surgery intervention. They are also employed in locally advanced and metastatic pancreatic tumours, prolonging patients' lifespan. Though recently FDA-approved nanoliposomal irinotecan combined with 5-fluoroacil/leucovorin and oxaliplatin (NALIRIFOX) showed to be a next-generation intriguing alternative,[178] currently first line chemotherapies rely on the administration of gemcitabine, alone or plus nanoparticle albumin-bound paclitaxel (nab-paclitaxel), and modified 5-fluorouracil plus leucovorin, oxaliplatin and irinotecan (mFOLFIRINOX). Sometimes, these two strategies are combined together or with immunotherapies, to achieve better clinical performances.

Indeed, several immune-based approaches involving humanised and human antibodies, such as pembrolizumab and nivolumab, have been approved by FDA in PDAC treatment.[179]

In parallel, PDAC generally display different genetic isoforms among patients, due to the random genomic alterations occurring during oncogenesis and tumour progression. Therefore, targeted therapies addressing individual gene mutants hold promise in developing candidate drugs specifically customised for each patient. *KRAS* mutations are the most prevalent in PDAC, present in >90% of cases, but no KRAS-targeting direct inhibitor has been developed so far, hence scientific efforts focused on other altered gene isoforms key in tumorigenesis and cancer progress.[180]

On this bases, *Breast cancer gene 1 and 2 (BRCA1/2)* mutations, though expressed with a lower frequency, might determine extended DNA levels. Indeed, these proteins play a pivotal role in homologous recombination (HR), a mechanism involved in DNA double-stand breaks (DSBs) repair machinery. The concurrent inhibition of poly(ADP-ribose) polymerase (PARP), essential to fix DNA single-strand breaks (SSBs), in platinum-sensitive PDAC patients harbouring *BRCA1/2* altered isoforms proved to accumulate DNA lesions, ultimately leading to cell death.[179,180]

Therefore, tackling DNA repair pathways seems to be a suitable approach to develop novel personalised therapeutic strategy, exhibiting more efficacy and less toxic profile.

2.2 DNA repair machinery

DNA is a highly conserved double-helix molecule encompassing all the genetic information of a certain individual. Its integrity is pivotal to build functional biological architectures to sustain life. Nevertheless, DNA is continuously exposed to a plethora of potential exogenous and endogenous threatens, potentially causing spread genetic mutations. The most severe DNA lesions induced by mutagenic agents are breaks through the sugar-phosphate backbones, which generate a discontinuity in one strand (SSBs) or both strands (DSBs) of the DNA molecule, ultimately fragmenting the double-helicoidal structure. To fix these incoming issues, a sophisticated DNA repair machinery, involving different biological pathways and numerous specialised proteins has been evolutionally developed.[181]

SSBs are solved through base-excision repair mechanism, which requires the activity of PPAR1 to temporarily bind the edge of the SSBs, and subsequently promote the recruitment of scaffold proteins and enzymes responsible for DNA repair. Unfixed SSBs produce replication fork collapse, evolving in DSBs.[181]

DSBs can be repaired through non-homologous end joining (NHEJ) and HR, which selective activation depends on the cell cycle. NHEJ predominantly occur during G1 phase, and it directly links two broken DNA ends without the need of a donor DNA molecule. Due to the lack of a DNA templates, during NHEJ cells are prone to undergo genetic alterations.[182]

On the other hand, HR is a low mutagenic DNA repair pathway that requires a broken DNA strand and a homologous DNA template to correctly restore the genetic code. HR is the predominant DNA repair mechanism in cells facing G2 and S phases, thus it is extremely relevant in highly proliferating cancerous cells. HR initial steps (**Figure 36**) need the recruitment of MRE11-RAD50-NBS1 complex (MRN), which engages ATM kinase, a key DNA damage sensor. Together with CtBP-interacting protein (CtIP), this complex operates short-range DNA ends resection, displacing Ku70-Ku80 heterodimer from these sites, hence exposing 3'-single-stranded DNA (ssDNAs) free overhangs. These ssDNA regions represent appropriate anchor points for replication protein A (RPA), which rapidly covered them preventing secondary structure formation and degradation. During this stage, BRCA1 seems to contact CtIP and MRN complex, fine-tuning the extent of DNA end resection. HR proceed via RPA displacement from ssDNA, mediated by a multiprotein complex. In mammals, BRCA2, in concert with BRCA1 and partner and localiser of BRCA2 (PALB2), orchestrates RPA removal from ssDNA regions, allowing RAD51 loading. This process enables the formation of RAD51 nucleoprotein filaments, that conduct the homology research and the strand invasion into a homologous duplex DNA molecule, hence forming three stranded synaptic complexes. Upon successful homology recognition, the non-complementary strand of the invaded DNA duplex is forced out, resulting in the displacement loop (D-loop) generation. Subsequent dissociation of RAD51 from the invading strand enables DNA polymerase δ to extend its 3'-end, thereby endorsing the recovery of missing genetic information from the homologous invaded template.[182]

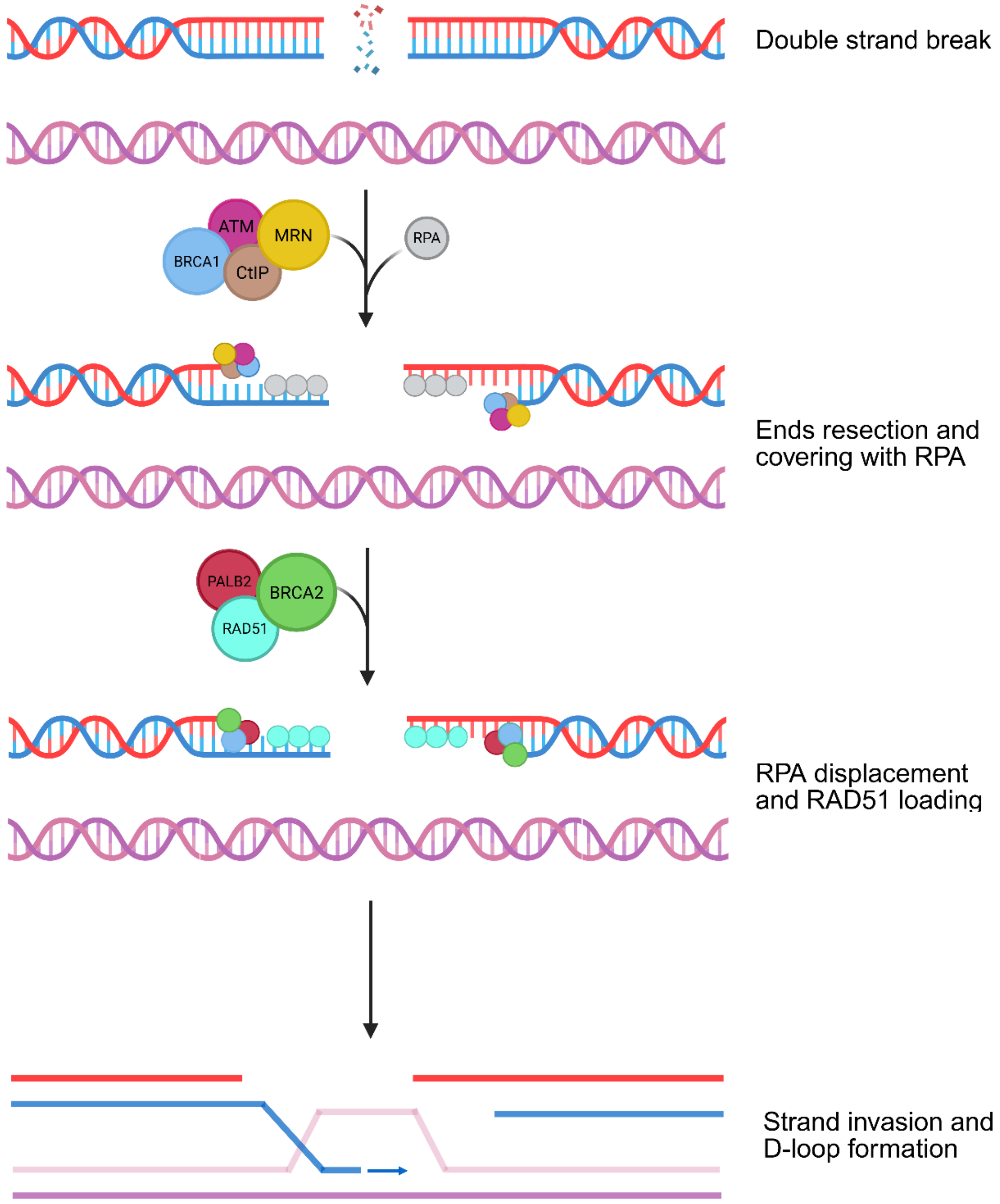

Figure 36. Schematic representation of HR initial steps.

At this crossroad, HR branch in three separate routes (**Figure 37**): double Holliday Junction (dHJ) and synthesis-dependent strand annealing (SDSA), which occurs when double-ended DSBs are exhibited and it induces gene conversion (GC), or break-induced replication (BIR), activated in presence of one end DSBs.

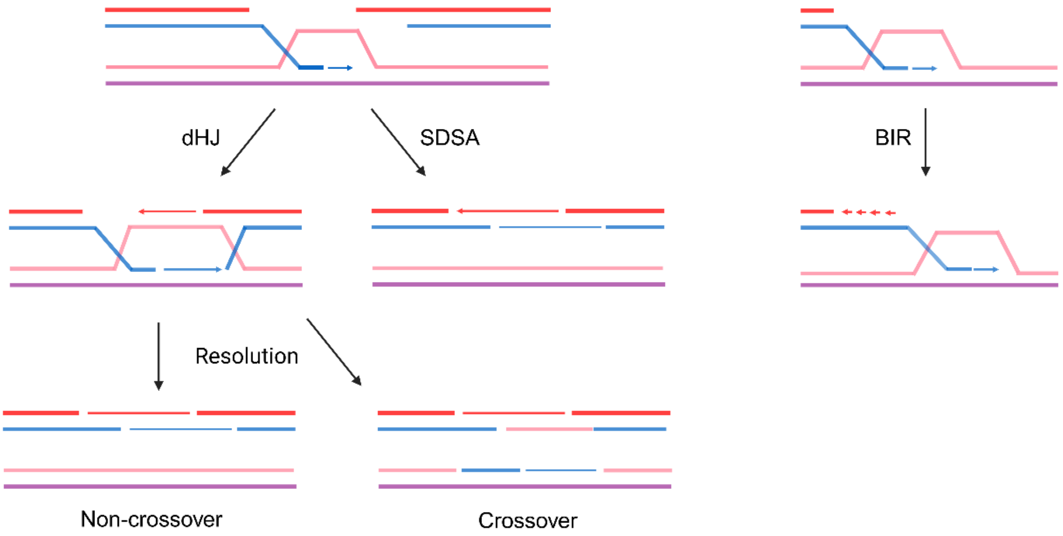

Figure 37. Schematic representation of dHJ, BIR, and SDSA repair mechanisms, including non-crossover and crossover resolutions.

dHJ is the predominant selected mechanism occurring in cells facing meiosis (**Figure 37**). Following this pathway, the newly synthesised D-loop captures the other resected end of the DSB, producing a dHJ. Its final resolution might bring to crossover or non-crossover recombination products. Conversely, mitotic cells preferentially employ the SDSA pathway, which is inherently non-crossover in nature (**Figure 37**). In SDSA, the newly synthesised DNA strand is displaced from its donor template, and it anneals to the complementary sequence at the second resected end of the DSB. Consequently, DNA synthesis and ligation restore the continuity of the DNA double-helix. These pathways are considered error-free, due to their use of a homologous template to maintain genetic integrity.[183]

On the other hand, BIR occurs when only one broken end is available for homologous pairing, as in presence of stalled replication forks or deteriorated telomers (**Figure 37**). Unlike dHJ and SDSA, this pathway is associated with high mutagenic potential. The invading 3'-end strand is extensively elongated till the chromosome end by a DNA polymerase, via Okazaki fragments synthesis. Notably, the multifunctional protein

Radiation sensitive 52 RAD52 is suspected to play a critical role in BIR. Indeed, its annealing activity seems to be essential to recruit RAD51 onto ssDNA, enabling homologous duplex invasion and D-loop formation.[183]

DSBs repair can also proceed through RAD51-indipendent pathways, such as alternative end joining (aEJ) and single-strand annealing (SSA). Both of them need a sufficient homology pairing between two resected ends of opposite DNA termini. While in aEJ the central activity is played by PARP1, that promotes short end-resection of DSB overhangs, the key mediator in SSA is RAD52. Indeed, following extensive end-resection mediated by several nucleases and helicases, RAD52 is essential to remove RPA from ssDNA fragments, and to anneal homologous sequences. Non-paired DNA tails are subsequently excised by some nucleases, whilst DNA polymerase and ligases reconstitute DNA duplex (**Figure 38**). Since one nucleotide sequence is lost, this pathway is more error-prone compared to dHJ and SDSA, hence it holds highly mutagenic potential.[184]

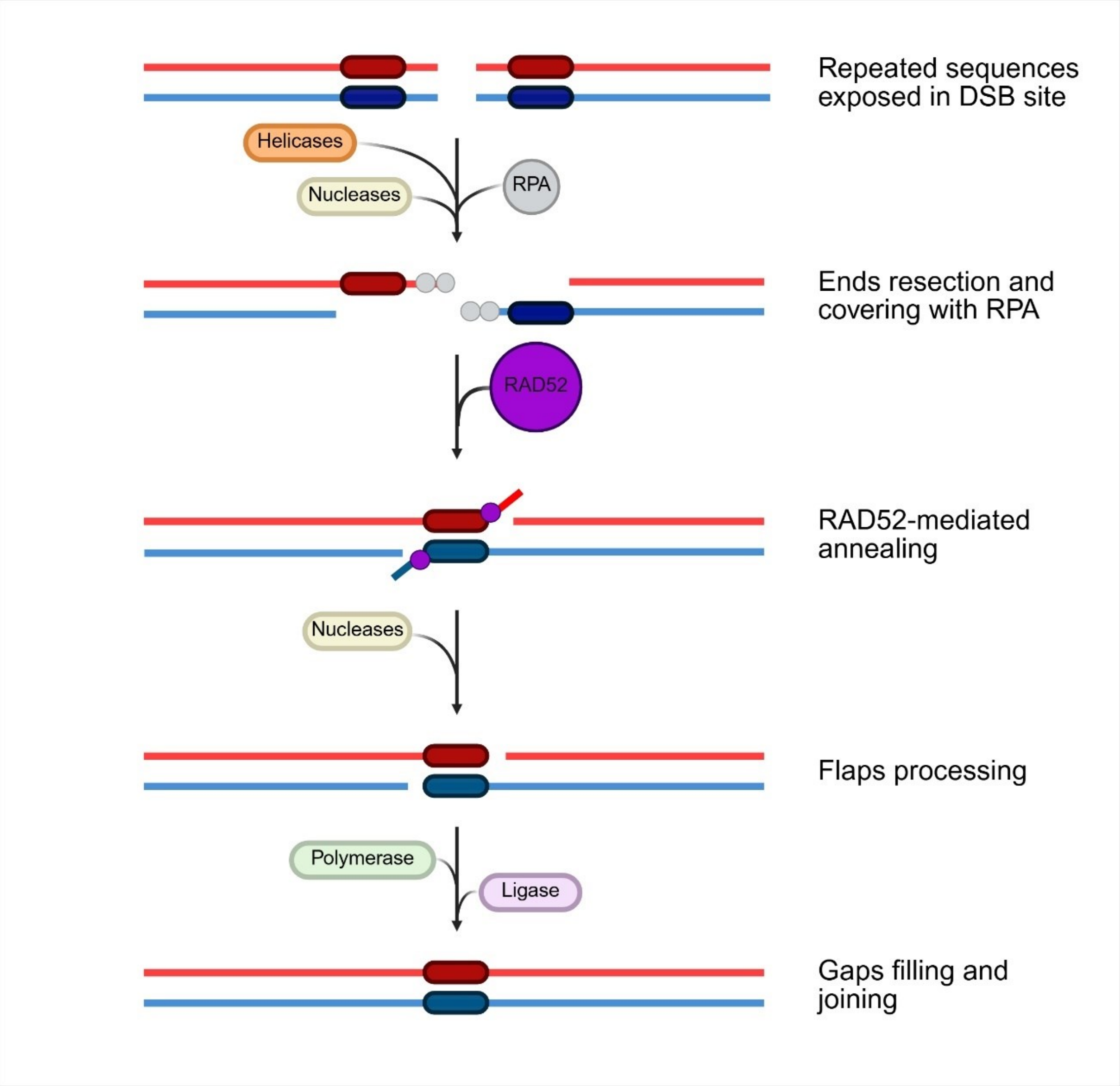

Figure 38. Schematic representation of SSA repair mechanism.

Oncogenesis in several forms of cancer, including PDAC, is significantly influenced by DNA lesions, particularly DSBs, that increase genomic destabilisation. Therefore, encrypting DNA repair pathways could represent a breakthrough discovery in malignant neoplasm treatment. In this framework, synthetic lethality (SL) has gained particular interest as an innovative anticancer strategy able to selectively tackle tumour cells typified inefficient DNA repair pathways.

2.3 Synthetic lethality

Synthetic lethality is a genetic phenomenon, firstly observed in *Drosophila* flies, in which the loss of functionality of two genes induces cell death, while the loss of either gene alone does not.[185] Based on a more recent definition, two genes are considered synthetic lethal partners when an occurring mutation in one of them or the pharmacological inhibition of the corresponding encoded protein provokes death in cells harbouring genetic alterations, while neither the mutation nor the drug alone compromise cell viability. Applied to anticancer therapy, this approach aims to provide new pharmacological tools selectively targeting neoplastic cells expressing specific genetic mutants, sparing normal ones by means of their different genetic profile. This strategy opens the way to tailored precision medicine, significantly enhancing therapeutic efficacy while mitigating potential side effects in healthy tissues. Moreover, any kind of genetic mutation may be addressed, even tumour suppressors and undruggable oncogenes. Despite the recent interest around SL have brought to the identification of several SL partners, only one SL-based therapy has been approved so far, which exploit the SL couple PARP1 and *BRCA1/2* mutated isoforms.[186]

As above mentioned, both BRCA1/2 and PARP1 plays critical role in DNA repair machinery. PARP1 rules BIR, resolving SSBs. At this stage, defection in this mechanism would bring to DSBs, which is predominantly resolved through HR, involving the crucial activity of BRCA1/2. *BRCA1/2* alteration would force cells to rely on alternative options to repair DSBs, like NHEJ, SSA, and aEJ. In this latter, the activity of PARP1 is critical to prompt DSBs resolution. Therefore, neoplastic cells harbouring *BRCA1/2* altered isoforms displayed high sensitivity to PARPis, since most of the DNA repair mechanisms would be extensively blocked. Furthermore, both the remaining functional pathways (NHEJ, and SSA) are considered error-prone, contributing to genomic instability, cell cycle arrest, and cell death. Conversely, normal cells showing a functional HR mediated by BRCA1/2, should not be affected by PARPis treatment.[186,187]

To date, four pan PARPis (**Figure 39**), olaparib (**106**), rucaparib (**107**), niraparib (**108**), talazoparib (**109**), were FDA-approved for a SL-based therapies in ovarian, breast, prostate, and pancreatic tumours carrying *BRCA1* or *BRCA2* mutants.[188]

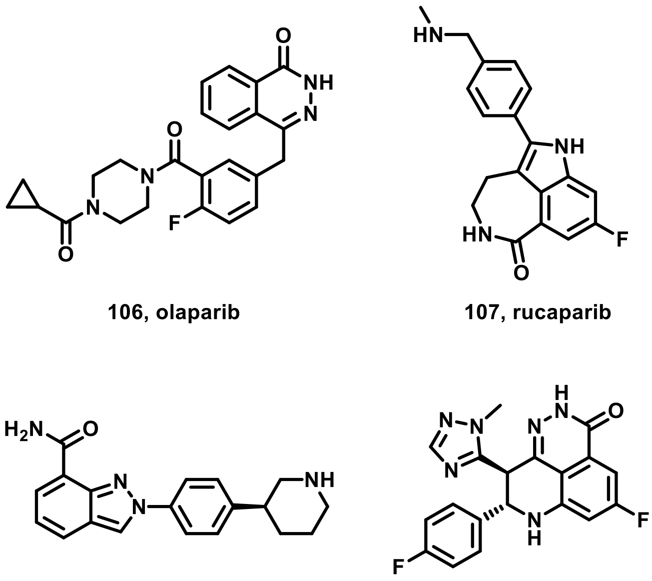
106, olaparib

107, rucaparib

108, niraparib

109, talazoparib

Figure 39. Chemical structures of the FDA-approved pan PARPis for anticancer treatments.

In 2019, **106** was FDA-approved as anticancer pharmacological treatment in treating PDAC patients expressing *BRCA1/2* alterations, representing a significant landmark in cancer treatment. However, several issues started to arise since then. Compound **106** promiscuous activity over PARP isoforms has been associated to potential side effects. Particularly, PARP2 inhibition might induce anaemia, thrombocytopenia, and neutropenia.[189] Furthermore, PARPis efficacy is driven by multiple exogenous and endogenous factors, producing different responsiveness among patients. Lastly, PARPis continuous administration is likely to stimulate tumours adaptability, involving a complex network of intrinsic cellular pathways and interactions with the neoplastic environment. In light of these data, the call for selective PARP1 inhibitors as well as co-administration of immune checkpoints inhibitors, such as pembrolizumab, should mitigate potential toxicological events while reducing acquired chemoresistance.[189,190]

In parallel, the identification of new SL relationships is still ongoing. In 2008, Nomme *et al.* discovered a novel cutting-edge SL strategy, holding promise in anticancer treatment. This approach aims to disrupt protein-protein interactions (PPIs) between RAD51 and BRCA2 by interacting with BRC4-motif. This feature is located in BRCA2 protein, and it represents a crucial hot spot in recruiting RAD51, allowing HR to proceed. Therefore, a small peptide, constituted of 28 amino acids and resembling BRC4 sequence, was subsequently synthesised, proving that it can effectively prevent RAD51 oligomerisation, impairing DNA binding.[191] This evidence represents a solid platform for the development of small molecules able to interfere with BRCA2/RAD51 hetero-oligomerisation processes by perturbating PPIs. These compounds displayed synergistic effects with **106** in PDAC cell lines, suggesting the high relevance in finding innovative SL-based strategy involving new partners and addressing PPIs to achieve improved chemotherapeutics in PDAC treatment.[192–194]

2.4 RAD52

Human RAD52 (*h*RAD52) is a multimeric ring-shaped protein of 418 amino acids, fostering the annealing of complementary DNA strands during HR in mammalian cells, hence it is tightly involved in DNA strands exchange. Its structure is typified by two regions: a C-terminal domain (CTD) and a N-terminal domain (NTD). CTD, a poorly conserved region, includes the binding sites for RPA and RAD51, and the nuclear localisation signal, for the migration of RAD52 into the nucleus. Interestingly, RAD52 monomers are slowly transferred inside the nucleus, whereas its heptameric form is efficiently imported inside its final location, suggesting that the structural conformation is crucial for its biological functions. On the other hand, the NTD encompasses the oligomerisation and the DNA binding domains, critical for its physiological activity. Further, post-translational modification, such as acetylation, SUMOylation, and phosphorylation, largely influenced RAD52 recruitment during DNA repair processes, exerting an important regulatory activity. [195]

The crystal structure of purified *h*RAD52 NTD was resolved in 2002, offering valuable insights into its architecture (**Figure 40**).[196] The NTD is organised as an undecameric circle surrounded by a positively charged furrow, promoting DNA annealing.

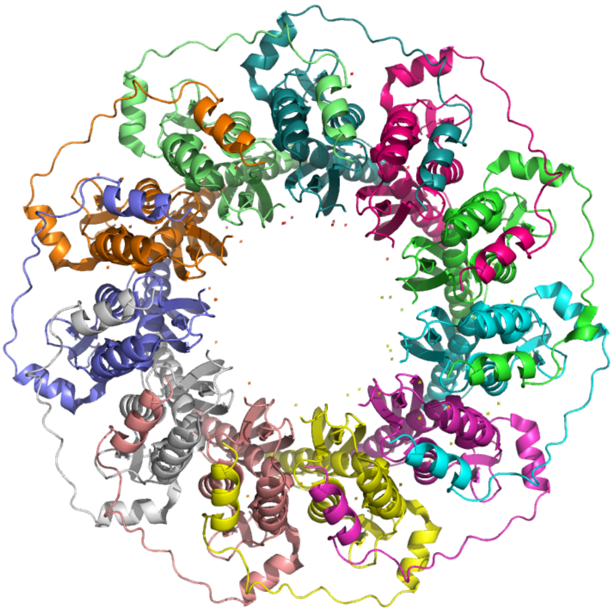

Figure 40. Crystal structure of the undecameric form of *h*RAD52 NTD.

RAD52 is a mediator of various mechanisms involved in DNA repair. In normal cells, *h*RAD52 is a non-essential protein in HR but it becomes central in preserving the viability of mutant cells presenting inactivated or deleted BRCA1/2, PALB2 or RAD51 paralogs. This evidence indicates the existence of an HR backup pathway, in which RAD52 is mandatory required for survival in BRCA-mutated cells, whereas this route is bypassed in BRCA-proficient cells. RAD52 is also responsible for capturing the DSB second end, bearing to the HJ formation. Moreover, it plays pivotal roles in SSA, in which it facilitates the alignment of homologous ssDNA regions, and in BIR pathway, prompting the formation of the D-loop. RAD52 is also involved in RNA-dependent DNA recombination and in lengthening the telomerases.[197]

Since the loss of RAD52 activity was shown to be lethal in the absence of BRCA2, a SL interaction between these two proteins has been proposed. Moreover, normal cells are not affected by RAD52 depletion, as RAD51-dependent HR remains functional in the presence of BRCA2. These findings suggest that RAD52 could represent a promising target for customised anticancer SL-based therapies, particularly in BRCA2-deficient tumours, but also in cells with defective BRCA1, PALB2 and RAD51.[198,199]

2.4.1 RAD52 modulators

Through the years, several small molecules have been identified as RAD52 inhibitors (**Figure 41**): A5MP (**110**), AICAR (**111**), and F779-0434 (**112**) hinder the binding of RAD52 to ssDNA, while C791-0064 (**113**) prevents RAD52 self-association. D-G23 (**114**) and D-103 (**115**) interfere with the D-loop formation., whilst natural products, such as epigallocatechin (**116**) and corilagin (**117**), undermine the wrapping of ssDNA around RAD52. However, their low selective profile as well as their reported side effects raised many concerns about their suitability as clinical candidate drugs, halting further development in the clinical trials.[200–202]

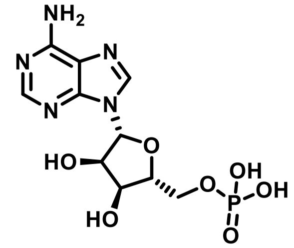

110, A5MP

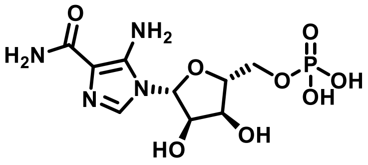

111, AICAR

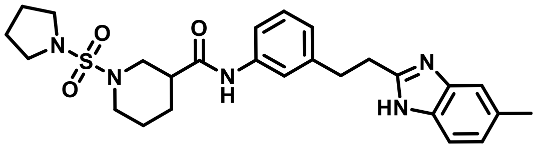

112, F779-0434

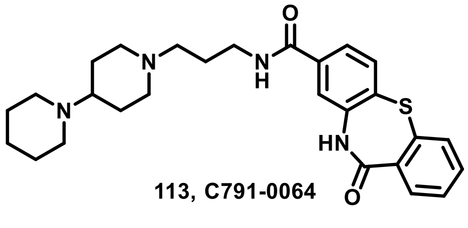

113, C791-0064

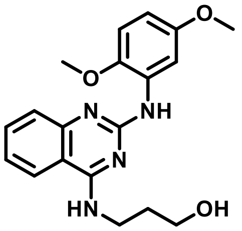

114, D-G23

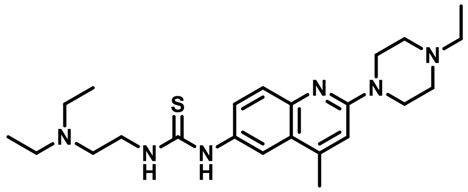

115, D-I03

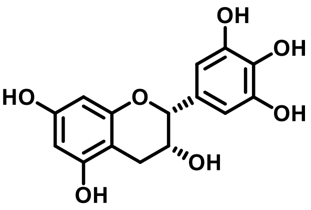

116, (-)-Epigallocatechin

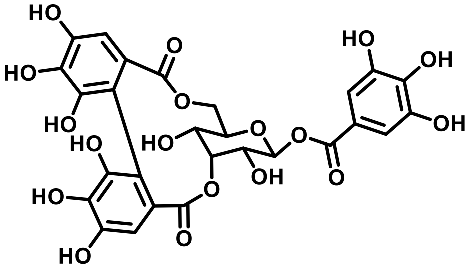

117, Corilagin

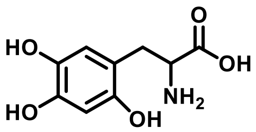

118, 6-OH-DOPA

VINLANEMFGYNG-GGG-YARAAARQARA

119, F79 aptamer sequence

Figure 41. Chemical structures of RAD52 modulators.

In the quest for small-molecule modulating RAD52 activity, 6-OH-DOPA (**118, Figure 41**) emerged as a promising candidate, displaying remarkable dose-dependent regulation of the target.[203] This goal is achieved via allosteric modulation of the 3-D structure of RAD52, converting the undecamers into dimers, thus preventing the binding of ssDNA. Further, it showed high specificity for RAD52, robust downregulation of SSA with minimal impact on RAD51, as well as reduced HR in cells harbouring BRCA mutations, in which it decreases cell survival by accumulating DNA damages and fostering apoptosis, sparing BRCA-proficient cells throughout the pharmacological treatment. These findings demonstrated that addressing RAD52 activity could potentially represent an innovative strategy in anticancer therapies. Particularly, interfering with RAD52 architecture may be a promising approach in treating BRCA-deficient tumours, like PDAC. Nonetheless, chronic administration of 6-OH-DOPA is associated with extrapyramidal side effects, potentially leading to Parkinson's disease, limiting its use in clinic.[204]

More recently, a step forward in targeting RAD52 has been made by Cramer-Morales *et al* with the design of a small peptide aptamer, namely F79 aptamer (**119, Figure 41**), that interferes with the assembly of RAD52 multimers. Its amino acidic backbone encompasses F79 residue and its surrounding sequence of 13 amino acids (residues 71-83), as well as a linker of three glycine and a transductor domain, facilitating the crossing through membranes. Following the identification of the key role of F79 residue in binding RAD52 to ssDNA, this molecule was rationally designed to disrupt PPIs at the interface between two monomers. The DNA binding domain forms a groove accommodating the ssDNA, with the F79 residue protruding into this area, contacting a neighbour RAD52 protomer via hydrophobic interactions. Compound **119** inserts itself into this space, mimicking the PPIs between two adjacent monomers, hence preventing their association. Consequently, **119** blocks RAD52 oligomerisation, impairing its biological activity. Though **119** displayed low target specificity due the presence of similar DNA binding domains present in other relevant off-targets, it also proved to inhibit HR in leukaemia cells and in mice models carrying altered *BRCA1/2* isoforms, corroborating the SL interaction.[205]

This approach demonstrated that RAD52 modulator interfering with the oligomerisation process can be incorporated in novel SL-based strategies. Particularly, the coadministration of a RAD52 modulator and a PARPi in BRCA-deficient cells may decrease the chemoresistance associated with a single drug strategy based on PARPi, since neoplastic cells could not perform HR neither through RAD51-pathway, neither via RAD52 backup route. This combination therapy would reduce the dosages of each drug, thus limiting the side effects while ameliorating clinical efficacy. Moreover, this dual SL-based strategy might spare normal cells, as they possess competent activity of *BRCA* genes and subsequently undergo an efficient RAD51-mediated HR pathway.[206,207]

Therefore, developing new RAD52 modulators able to disrupt PPIs between the protomers appears as an intriguing approach to integrate in PARPi-based therapies for PDAC treatment, concurrently enhancing selectivity, reducing incoming drug resistance, and improving therapeutic efficacy in *BRCA*-mutant cancers.

2.5 Aim of the PhD work

Given the rising scientific interests in targeting neoplastic diseases exploiting the peculiar tumour genetic profile, SL-based approach has recently gained increased attention in this field. To date, only one SL-couple, involving RAD51 protein and *BRCA* genes has been identified and targeted with FDA approved drugs. Identifying new SL-partners will be essential for overcoming the acquired chemoresistance observed in PDAC patients harbouring *BRCA* mutated isoforms and treated with PARPi. Therefore, part of my PhD project focused on the developing of novel small peptides and peptidomimetics acting as potential SL-based anticancer pharmacological tools tackling RAD52, a new partner in PARP-BRCA2 lethal interaction.

2.6 Rational design

Considering the growing scientific interest in SL-based strategy, part of my PhD project was dedicated to the development of a series of small peptides conceived as potential RAD52 modulators. Compared to small molecules, therapeutic peptides may benefit of a higher specificity for the biological target and a larger molecular size, ameliorating their ability to disrupt PPIs. Nevertheless, they are endowed with poor membrane permeability and low *in vivo* stability.[208] These issues could be overcome with the development of cyclic peptides characterised by increased molecular rigidity, which favours the assumption of the active conformation while improving metabolic and proteolytic stability, compared to their linear counterparts.[209] The research group where I did my internship has previously contributed to this field describing a series of both linear and cyclic peptides as pro-apoptotic agents.[210]

In the quest for regulating RAD52 activity, the oligomerisation of the multimeric ring structure, pivotal for the biological activity, appears as a captivating process to be targeted. Capitalising on the information obtained from F79 aptamer, the small peptides herein reported are rationally designed to hamper RAD52 assembly by targeting a specific area between the surface of two adjacent monomers, ultimately thwarting the proper folding and RAD52 physiological activity.

The oligomerisation domain is located in the NTD, within the 85-159 sequence. Structural analysis of this interface revealed the presence of a region constituted by an α-helix and a β-sheet. Due to its highly folded architecture, the development of small peptides replicating the α-helix conformation is a paramount challenge. Conversely, thanks to its higher surface accessibility and its role in PPIs, the β-sheet region involving the segment Gly118-Ser119-Tyr120-His121-Glu122 seems to be more suitable for the development of potential RAD52 PPIs' disruptors, thus it was chosen as the basis for the rational design of small peptides. Therefore, the amino acid 118-122 sequence (**120a**, **Figure 42**) was replicated in order to evaluate its binding to the surface of a monomer in the oligomerisation domain, preventing PPIs with the corresponding protomer and subsequently hindering RAD52 assembly. In this frame I developed a rationally designed set of small peptides and peptidomimetics (**120a-n**, **Figure 42**), that were obtained either by in solution chemistry or by a solid phase approach.

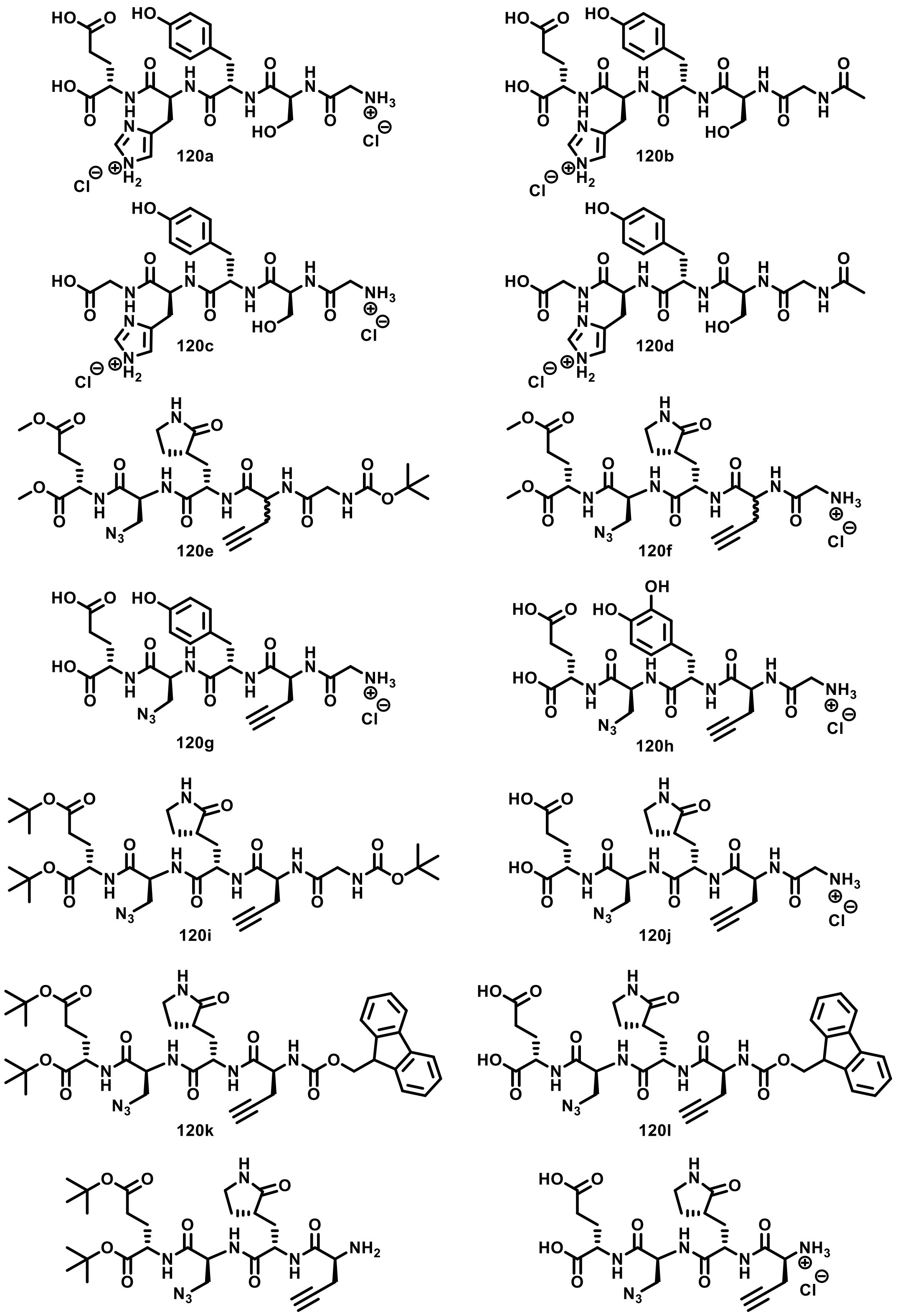

120a 120b 120c 120d 120e 120f 120g 120h 120i 120j 120k 120l 120m 120n

Figure 42. Chemical structures of the developed compounds **120a-n**.

Preliminary computational studies, performed by Prof. Federico Falchi at the University of Bologna, demonstrated that compound **120a** fits well on the surface of the oligomerisation domain. Particularly, the free amino group is positioned within a shallow region, whilst the other residues are engaged in key interactions with the neighbour promoter in the target protein (**Figure 43**). The hydroxyl group of the tyrosine forms hydrogen bonds with both Arg112 and Gln114, while the carboxylic group in the side chain of glutamate interacts with His86. Additionally, the imidazole ring of the histidine concurrently engages His86 in a hydrogen bond and Trp84 in a π-π interaction, hence playing a pivotal role in molecular binding.

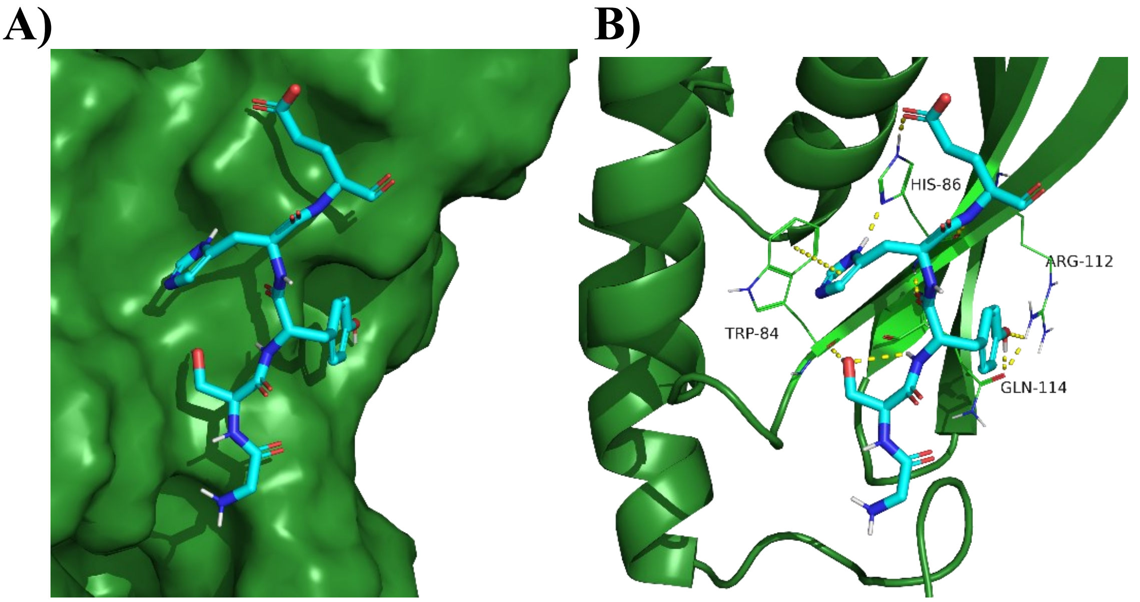

Figure 43. A) Docking model of the pentapeptide **120a** on RAD52 monomer surface. B) Key interactions between the pentapeptide **120a** and the amino acid residues on the surface area of the neighbour monomer in RAD52 oligomerisation domain.

To validate that the presence of a free amino group and two carboxylic acids is pivotal for attaining the proposed binding mode, compounds **120b-d** were synthesised (**Figure 42**) via solid phase peptide synthesis (SPPS), as the parent compound. The amino portion was explored by introducing an acetyl capping motif (**120b**), since it is located inside a shallow pocket. On the other side, one carboxylic acid moiety was removed by substituting the C-terminal Glu residue with a Gly residue (**120c**). Then, both these modifications were incorporated into the scaffold, providing compound **120d**.

Although linear small peptides presenting the same AA 118-122 sequence should efficiently reproduce the PPIs between the protomers, the development of cyclic peptides was also considered during the rational design. Therefore, two non-natural amino acids were introduced in the backbone, bearing an azido and an alkynyl group, respectively. Indeed, these moieties should provide easy and rapid cyclisation of the constructed peptides exploiting a click chemistry strategy. Depending on the metallic catalyst employed during the reaction, a 1,4- or 1,5-disubstituted 1,2,3-triazole can be selectively obtained, mimicking either a trans or cis amide bond, respectively.[211] To investigate the chemical space around the binding region more in-depth, liquid phase peptide synthesis (LPPS) was employed to synthesise compounds showing different C- and N-termini. Moreover, preliminary computational studies also highlighted that different frames could replace the Tyr residue of the parent compound, such as catechol or γ-lactam rings. All these elements were incorporated in compounds **120e,f**, (**Figure 42**) endowed with both methyl ester protection at C-end and a γ-lactam lateral chain in central position of the sequence, whereas the N-terminal was either Boc protected (**120e**) or deprotected (**120f**). Due to synthetic difficulties, these derivatives were obtained as racemic mixtures, hence lots of efforts were focused on finding another synthetic strategy to overcome this issue. The newly developed methodology was introduced both in SPPS and LPPS to obtain enantiomerically pure linear non-natural AA sequences. As a first approach, SPPS was utilised to generate compounds **120g,h** (**Figure 42**), harbouring either Tyr or *L*-DOPA residues in central position of the AA sequence. Nonetheless, the corresponding γ-lactam-based peptide was not afforded employing the same process. Consequently, I switched back to the LPPS, simultaneously exploring structural variations of both C- and N-ends

(**Figure 42**). Compound **120i** was conceived by replacing the methyl ester on the carboxylic acids, displayed in **120e,f**, with *tert*-butyl groups, while **120j** shows unprotected C- and N-terminal functionalities. This would corroborate the different influence on ligand binding exploited by capped and non-capped analogues. Moreover, the importance of the C-end Gly residue was interrogated by constructing truncated tetrapeptidomimetics, lacking this terminal amino acid. Four different tetrapeptidomimetic analogues were synthesised in order to investigate this chemical construct (**Figure 42**). Compound **120k** embeds a *tert*-butyl ester moiety at the C-terminus while the N-terminal is capped with 9*H*-fluoren-9-ylmethoxycarbonyl (Fmoc) group. Compound **120l** encompasses a free carboxylic acid at the C-end, whereas the N-terminus carries a Fmoc residue. In **120m**, the C-terminal is esterified with *tert*-butyl group, while a free amino group is presented at the N-terminal. Compound **120n** bears free amino and carboxylic acid frames at both C- and N-termini, respectively.

2.7 Chemistry

As previously stated, in this this PhD work two methods for the synthesis of small peptides and peptidomimetics were applied: SPPS was applied for compounds **120a-d,g,h**, LPPS was employed to achieve compounds **120e,f,i-n**. Particularly, automated SPPS was performed for obtaining pentapeptides **120a,b,g,h**, utilizing a Syro I peptide synthesiser, whereas the development of compounds **120c,d** exploited manual SPPS under microwave irradiation (MWI), employing a CEM Discovery 2.0 apparatus. Each synthetic approach conducted in automated or manual SPPS included different **General procedures** (**GPs**) for deprotection, coupling, capping, and cleavage steps (see **Table 10** for the list of details, the methods are fully descripted in the Experimental section). For MW-assisted SPPS, the completion of each coupling steps was monitored performing a Kaiser test.[212]

Table 10. Summary of the General procedures employed in automated or manual SPPS for the development of pentapeptides **120a-d,g,h**.

GP	Description	Comments	Reagents	Conditions
A1	Fmoc deprotection	employed in automatic SPPS	piperidine	DMF, 25 °C, (3 + 12) min
A2	Fmoc deprotection	employed in manual SPPS under MWI	piperidine	DMF, 40 W, 40 °C, (30 + 30 + 30) s
B1	Coupling	employed in automatic SPPS	Fmoc-*L*-His-OH, DIC, HOBt, DIPEA,	DMF, 25 °C, (40 + 40) min
B2	Coupling	employed in automatic SPPS	Fmoc-*L*-AA-OH, HBTU, HOBt, DIPEA,	DMF, 25 °C, 40 min
B3	Coupling	employed in manual SPPS under MWI	Fmoc-*L*-His-OH, DIC, HOBt, DIPEA	DMF, 1) 15 W, 50 °C, 2 min, 2) 40 W, 50 °C, 4 min
B4	Coupling	employed in manual SPPS under MWI	Fmoc-*L*-AA-OH, HBTU, HOBt, DIPEA	DMF, 50 W, 40-55 °C, 4 min
B5	Coupling	employed in automatic SPPS	Fmoc-*L*-AA-OH, HATU, oxyma pure, DIPEA	DMF, 25 °C, 40 min
B6	Coupling	employed in automatic SPPS	Fmoc-*L*-AA-OH, HATU, oxyma pure, DIPEA	DMF, 25 °C, (40 + 40) min
C1	Capping	employed in automatic SPPS	Ac_2O, DIPEA	DMF, 25 °C, (10 + 10) min
C2	Capping	employed in manual SPPS under MWI	Ac_2O, DIPEA	DMF, 25 °C, (30 + 30) min
D	Cleavage	-	TIPS, H_2O, TFA	DMF, 25 °C, 3 h
	Precipitation	-	-	Et_2O, 0 °C, 1 h

2.7.1 Synthesis of compounds 120a-d

The SPPS synthetic route affording compounds **120a,b** is recapitulated in **Scheme 9**.

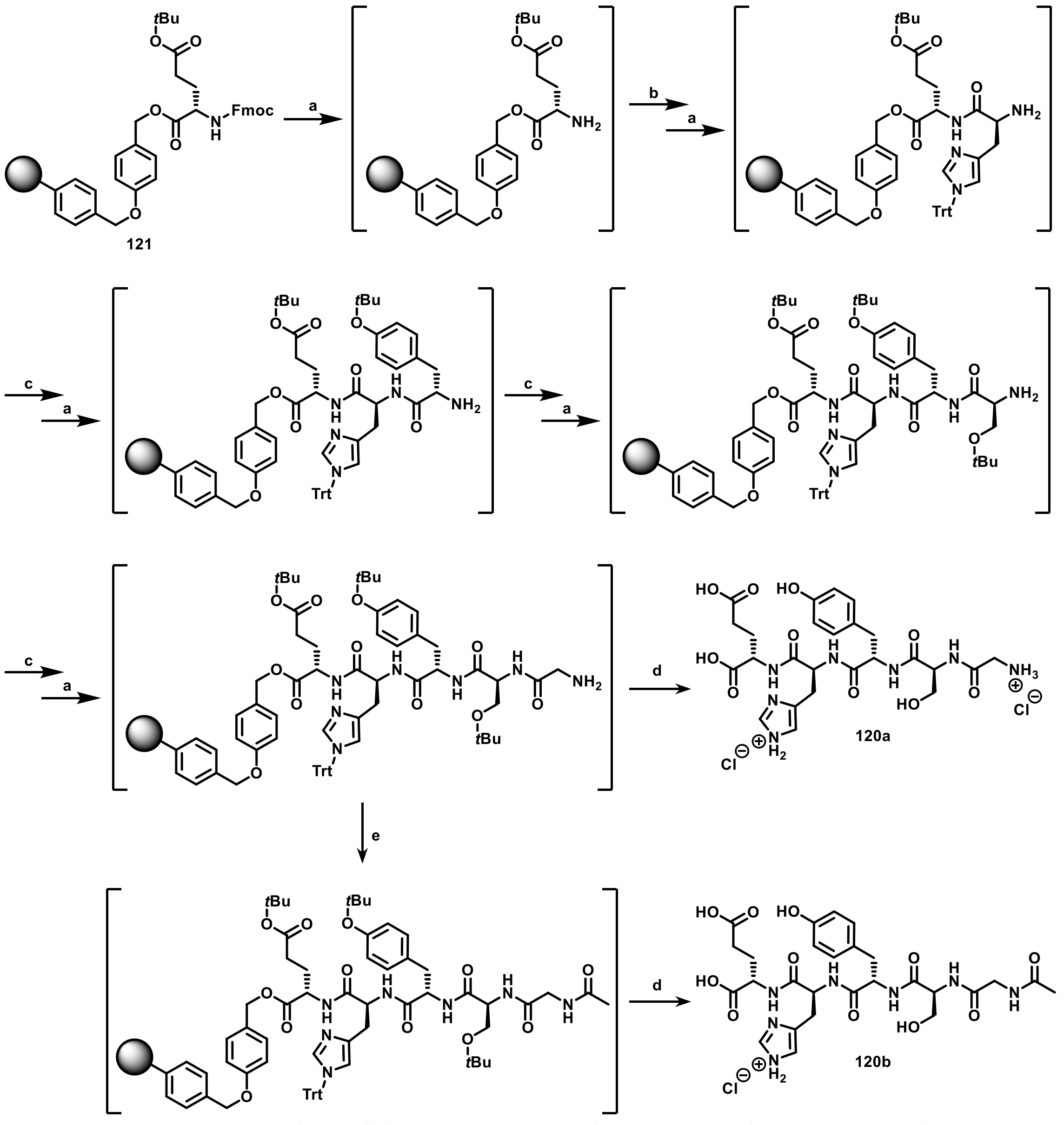

Scheme 9. Reagents and conditions: a) **GP-A1**; b) **GP-B1** using Fmoc-*L*-His(Trt)-OH; then **GP-C1**; c) **GP-B2** using in order Fmoc-*L*-Tyr(*t*Bu)-OH, Fmoc-*L*-Ser(*t*Bu)-OH, Fmoc-Gly-OH; d) **GP-D**, then lyophilisation with 0.1 N HCl, 12 h, 41-71%; e) **GP-C1**.

The synthesis begins with Fmoc-Glu(O*t*Bu)-Wang resin (**121**), which underwent Fmoc removal on N-terminus by adding a 20% solution of piperidine in DMF (**GP-A1)**. The following coupling reaction, involving Fmoc-*L*-His(Trt)-OH residue, appears to be the bottleneck step in this synthetic scheme, due to the steric hindrance introduced by its trityl protecting group and the potential racemisation.[213] Different coupling reagents and synthetic conditions were explored to achieve this goal. The best result was obtained performing **GP-B1** twice in the presence of *N,N'*-diisopropylcarbodiimide (DIC) as coupling agent, HOBt as auxiliary, and diisopropylethylamine (DIPEA) as base. Both HOBt and DIPEA were utilised throughout all the following coupling steps. After that, a capping step was performed according to **GP-C1**, to avoid deleted byproducts. The next residues (Tyr, Ser, Gly) were added following the same deprotection-coupling sequence (**GP-A1** and **GP-B2**), in the presence of hexafluorophosphate benzotriazole tetramethyl hydroxy (HBTU) as coupling agent. Since this approach demonstrated good efficiency in preliminary manual synthesis. The obtained resin loaded with the N-deprotected pentapeptide sequence was subsequently split. A portion of the resin underwent acidic cleavage, followed by filtrate precipitation in cold Et_2O to remove unwanted byproducts, as described in **GP-D**. Then, a 0.1 N solution of HCl in H_2O was added to the resulting white solid and, after lyophilisation, the corresponding hydrochloric salt **120a** was obtained. On the remaining part of the pentapeptide-loaded resin, a capping reaction was performed following **GP-C1**. Then, the same sequence of cleavage, precipitation, dissolution in a 0.1 N solution of HCl in H_2O, and lyophilisation was applied as for **120a**, affording the hydrochloric salt **120b**.

On the other hand, compounds **120c,d** were synthesised using manual SPPS, following **Scheme 10**.

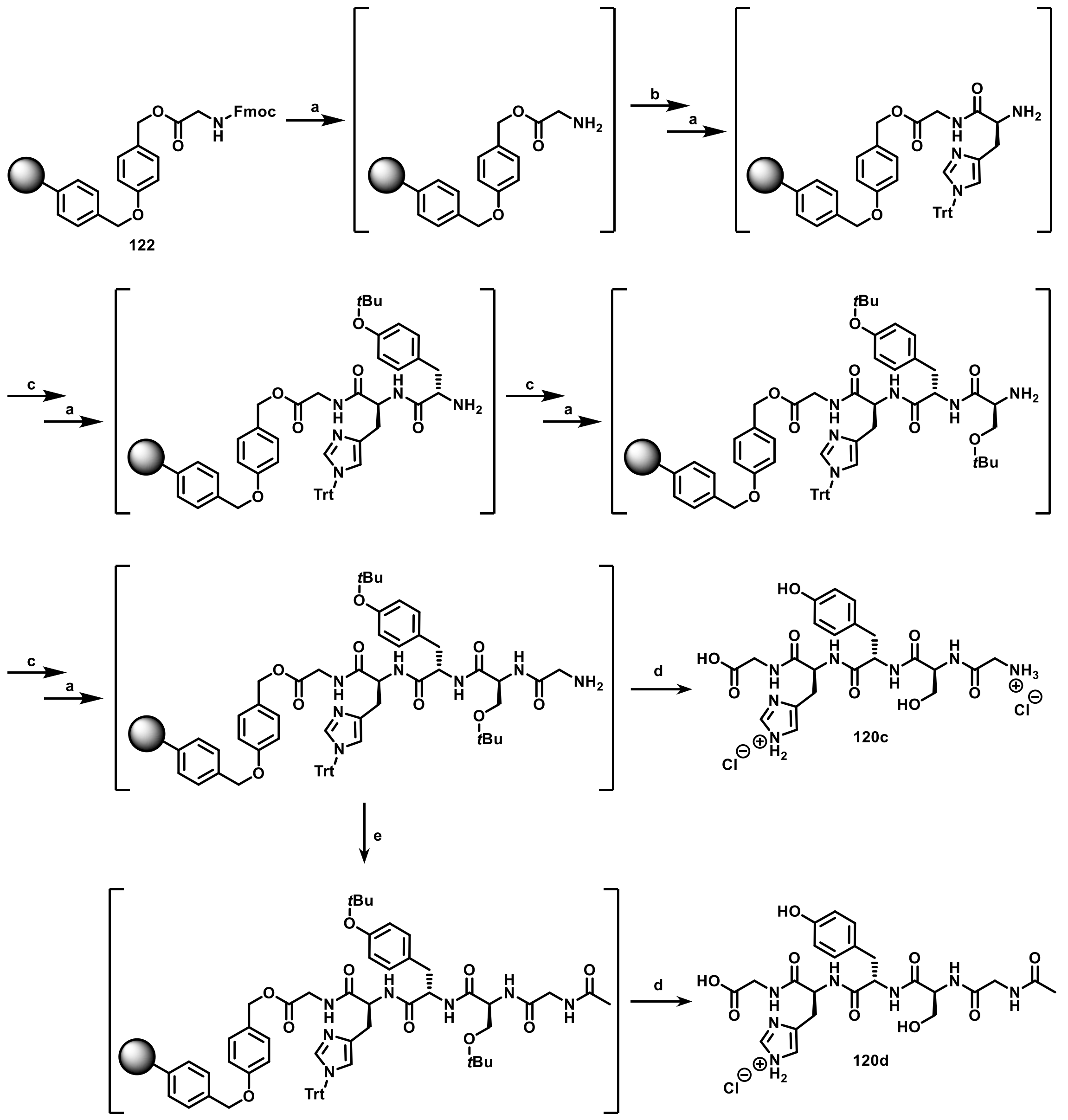

Scheme 10. Reagents and conditions: a) **GP-A2**; b) **GP-B3** using Fmoc-*L*-His(Trt)-OH, repeating the coupling 3 times; c) **GP-B4** using in order Fmoc-*L*-Tyr(*t*Bu)-OH; Fmoc-*L*-Ser(*t*Bu)-OH, Fmoc-Gly-OH, repeating the coupling twice; d) **GP-D**, then lyophilisation with 0.1 N HCl, 12 h, 24-35%; e) **GP-C2**.

The synthesis started with Fmoc-Gly-Wang resin (**122**), which underwent Fmoc deprotection of amino end according to **GP-A2**. Then Fmoc-*L*-His(Trt)-OH was coupled following **GP-B3**, employing MW-aided manual SPPS. The other residues were coupled following the same deprotection-coupling protocols (**GP-A2** and **GP-B4**), choosing HBTU as coupling agent. After deprotecting the N-end of the Gly residue, the pentapeptide-loaded resin was split. A portion of this latter underwent the same sequence of cleavage, precipitation, dissolution in a 0.1 N HCl solution, and lyophilisation applied for **120a**, affording the hydrochloride salt **120c**. On the remaining part of the resin, Gly free amino motif was acetylated according to **GP-C2**. Then, the same sequence of cleavage, precipitation, dissolution in a 0.1 N solution of HCl in H_2O, and lyophilisation was applied as for **120a**, affording the hydrochloride salt **120d**.

2.7.2 Synthesis of compounds 120e,f

The synthetic approach leading to compounds **120e**,**f** is described in **Scheme 11**.

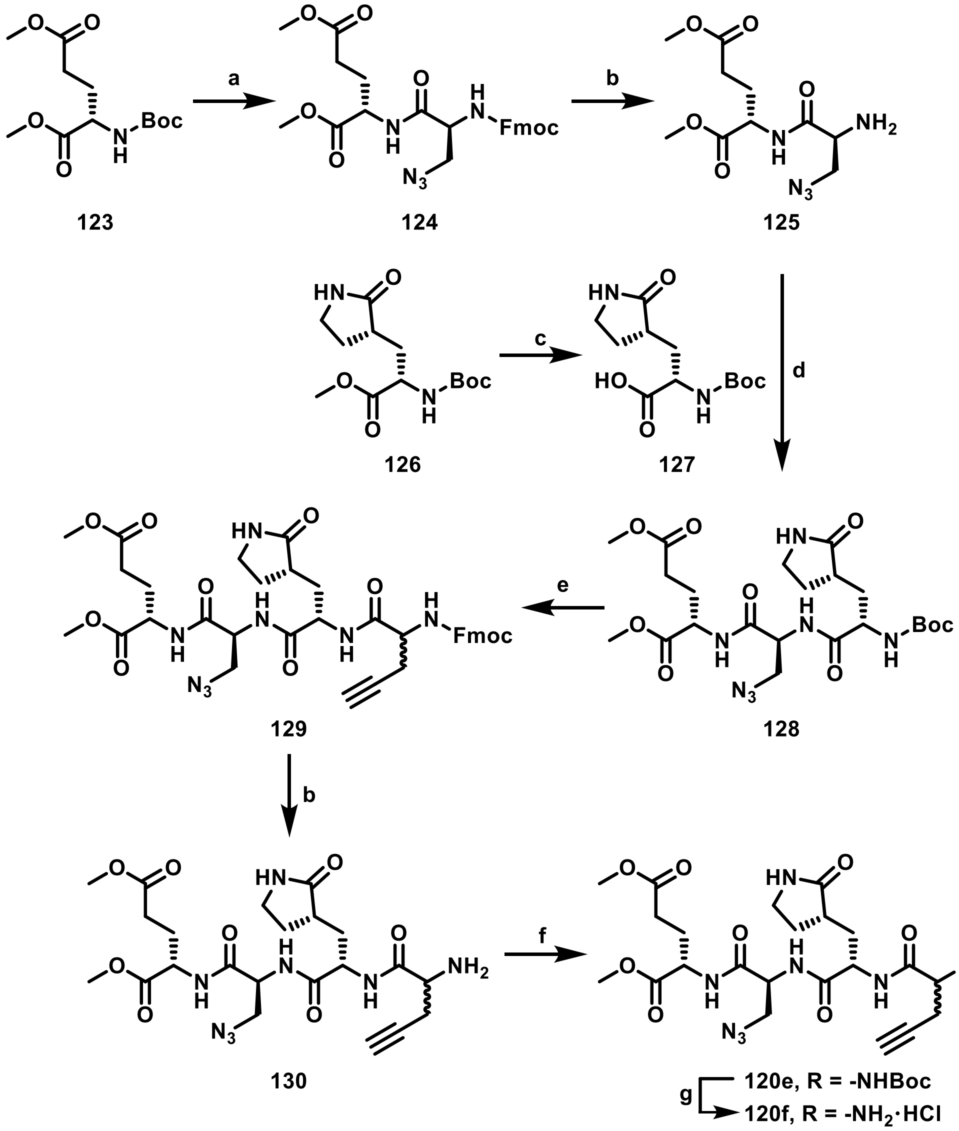

Scheme 11. Reagents and conditions: a) TFA, DCM, 0 °C, 30 min; then Fmoc-*L*-Ala(N_3)-OH, HATU, TEA, dry DCM, 25 °C, 3 h, 81%; b) DBU, EtSH, dry THF, 25 °C, 2 h, 38-90%; c) 1 N LiOH in H_2O, THF, 0 °C, 2 h, 67%; d) DIC/HOBt, TEA, dry DMF, MWI, 40 W, 50 °C, 10 min, 48%; e) TFA, DCM, 0 °C, 30 min; then Fmoc-*L*-Pra-OH, HATU, TEA, dry DMF, MWI, 40 W, 50 °C, (10 + 10 + 30) min, 71%; f) Boc-Gly-OH, HATU, TEA, dry DMF, MWI, 40 W, 40 °C, 5 min, 45%; g) 1 N HCl in MeOH, MeOH, 0 °C, 1 h, 69%.

This synthetic approach stared with acidic deprotection of compound **123**[214] followed by coupling with Fmoc-3-azido-*L*-alanine (Fmoc-*L*-Ala(N_3)-OH); this reaction afforded compounds **124**. The reaction was conducted in batch in the presence of hexafluorophosphate azabenzotriazole tetramethyl hydroxy (HATU) as coupling agent, and TEA as base. This latter was used as the elected base throughout the coupling steps of **Scheme 11**. Intermediate **124** was Fmoc deprotected under basic condition. In this case, the classical procedure, which involves a 20% solution of piperidine in DMF, produced a piperidine-dibenzofulvene (DBF) byproduct posing a serious challenge in the purification step. To overcome this issue, a solution of catalytic amount of 1,5-diazabicyclo(5.4.0)undec-7-ene (DBU) and ethanethiol (EtSH) in THF was employed Indeed, DBU serves as a less nucleophilic, more basic and hindered tertiary amine compared to piperidine, thus accelerating the reaction while decreasing side products formation. On the other hand, EtSH acts as a scavenger, forming a more stable adduct with DBF and liberating DBU in solution, hence allowing to use catalytic amount of the tertiary amine.[215] Therefore, the treatment of **124** with this basic solution efficiently provided the corresponding free amine **125**. This latter was reacted with compound **127**, which was previously obtained following hydrolysis under basic conditions of derivative **126**. The coupling reaction between **125** and **127** occurred under MWI, in the presence of DIC as coupling agent, and HOBt as auxiliary, leading to intermediate **128**. The obtained tripeptidomimetic was Boc deprotected under acidic conditions and subsequently coupled with Fmoc-*L*-2-propargylglycine (Fmoc-*L*-Pra-OH). In **Table 11**, the coupling conditions employed to afford compound **129** are reported. The reaction tests were performed in classical batch conditions (entry **1-3**) or in a MW apparatus (entry **4-10**). A first attempt was conducted using a combination of DIC and HOBt (**entry 1**), but the aimed product was not afforded. Similarly, applying the same procedure in the presence of HATU (**entry 2**) failed to furnish tetrapeptidomimetic **129**, even when the reaction time was extended for 12 h (**entry 3**). MW-aided reactions utilizing DIC/HOBt brought to the same unsuccessful results (**entries 4** and **5**). On the other hand, applying the same protocol in the presence of HATU for 10 min (**entry 6**) succeeded in giving derivative **129**. The best performance in terms of overall yield (71%) was obtained replicating the same conditions as in **entry 6** but extending the reaction time performing 3 cycles (10 +10 +30 min) under MWI (**entry 7**). However, none of the explored conditions prevented the formation of two diastereomers, nor it was possible to separate them by a classical column chromatography.

Table 11. Screening of different coupling conditions used to obtain compound **129**.

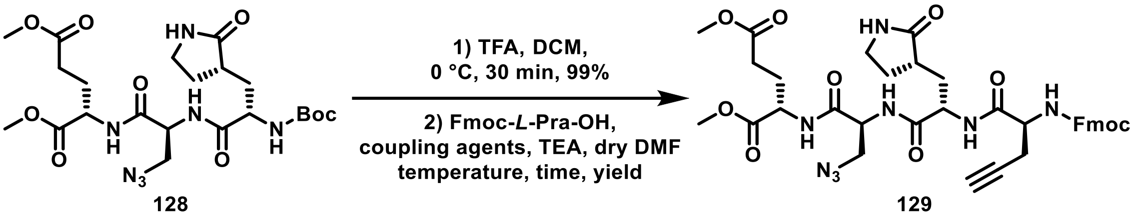

Entry	Coupling agents	Temperature	Time	Yield
1	DIC/HOBt	25 °C	12 h	Fail
2	HATU		4 h	Fail
3			12 h	Fail
4	DIC/HOBt	50 °C	5 min (MWI, 40W)	Fail
5			(10 + 10+ 30) min (MWI, 40W)	Fail
6	HATU		10 min (MWI, 40W)	36%
7			(10 + 10 + 30) min (MWI, 40W)	71%

Intermediate **129** was Fmoc deprotected using the same protocol as reported above (**130**). This latter was reacted with Boc-glycine (Boc-Gly-OH), in the presence of HATU as coupling agent for a short period of time (5 min) under MWI, leading to compound **120e** with satisfactory yield (45%). Following this step, resolution of the epimeric mixture was performed through semipreparative RP-HPLC.[216] After several unfruitful attempts, it was not possible to efficiently separate the two peaks corresponding to the diastereomers through this methodology (**Figure 44**), therefore I proceeded in the synthetic scheme without further purification.

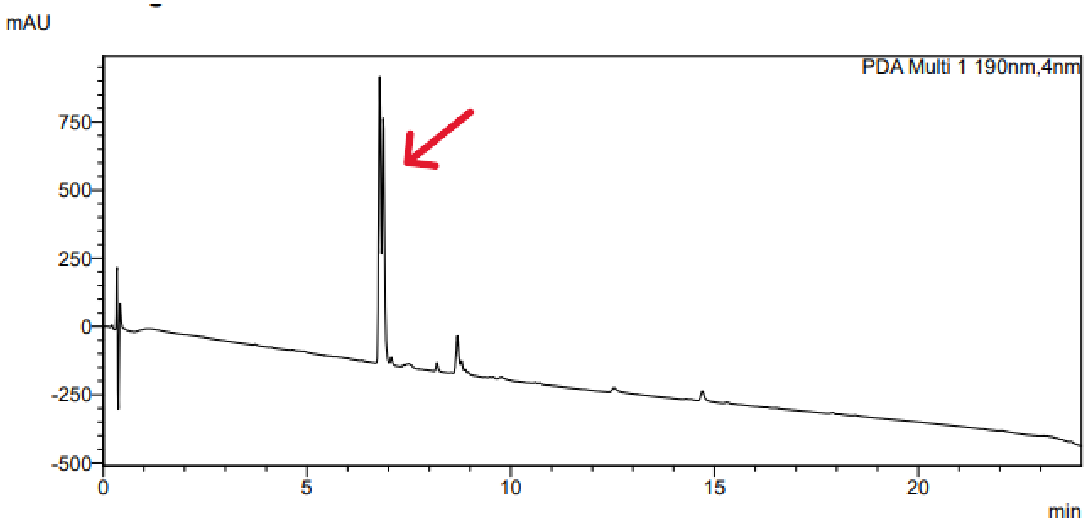

Figure 44. RP-HPLC analysis of epimeric mixture **120e**. Eluent gradient starting from 9:1 H_2O/MeCN to 1:9 MeCN/H_2O.

A portion of **120e** was deprotected at the amino terminus with a 1 N solution of HCl in MeOH, giving the corresponding hydrochloric salt **120f**.

During this synthetic strategy, the epimerisation occurring in the coupling reaction between **128** and Fmoc-*L*-Pra-OH was found to be an extremely challenging issue, since it was not feasible to efficiently isolate the two diastereomers. In order to obtain enantiomerically pure pentapeptidomimetic sequences, literature was deeply delved. From this survey, it emerged that the correct choices of the reaction parameters are crucial to avoid racemisation.[217–219] Taking this information into account, a series of test reactions were performed under MWI to prevent epimerisation (**Table 12**). As a first approach, the same reaction conditions leading to **129** were replicated, reducing the reaction time to 3 min (**entry 1**). However, this attempt failed in giving the aimed product. Consequently, alternative coupling agents/auxiliaries were tested. No product formation was detected when a combination of DIC and *N*-Hydroxy-5-norbornene-2,3-dicarboxylic acid imide (HNOB) was used (**entry 2**), while in the presence of hydroxyamino-1-yloxytripyrrolidinophosphonium hexafluorophosphate (PyBOP) and HOBt the intermediate **129** was obtained but in traces (**entry 3**). Lastly, a protocol between compound **127** and Fmoc-*L*-Pra-OH involving HATU as coupling agent, ethyl cyano(hydroxyamino)acetate (oxyma pure) as auxiliary, and DIPEA as base was applied (**entry 4**). The replacement of DIPEA over TEA stems from its lower tendency to induce racemisation, as reported in literature.[220] Accordingly, oxyma pure is known as an effective racemisation suppressor, as its mild acidity reduces the basic environment derived from the tertiary amine.[221] Performing this optimised approach, enantiomerically pure dipeptidomimetic **131** was afforded with excellent yield (84%). This successful test reaction serves as a proof of concept in the following development of enantiomerically pure peptidomimetic sequences.

Table 12. Screening of different MW-assisted coupling conditions used to obtain enantiomerically pure tetrapeptidomimetic **129**, and dipeptidomimetic **131**.

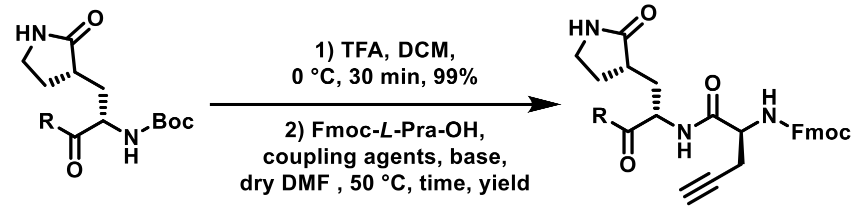

127 R = -OMe
128 R = -NHAla(N_3)-Glu

129 R = -NHAla(N_3)-Glu
131 R = -OMe

Entry	Product	Coupling agents	Base	Time	Yield
1	**129**	HATU	TEA	3 min (MWI, 40W)	Fail
2		DIC/HONB		3 min (MWI, 40W)	Fail
3		PyBOP/HOBt		5 min (MWI, 40W)	Traces
4	**131**	HATU/oxyma pure	DIPEA	(10 + 10) min (MWI, 40W)	84%

2.7.3 Synthesis of compounds 120g,h

The synthetic strategy affording compounds **120g,h** was performed exploiting SPPS as depicted in **Scheme 12**.

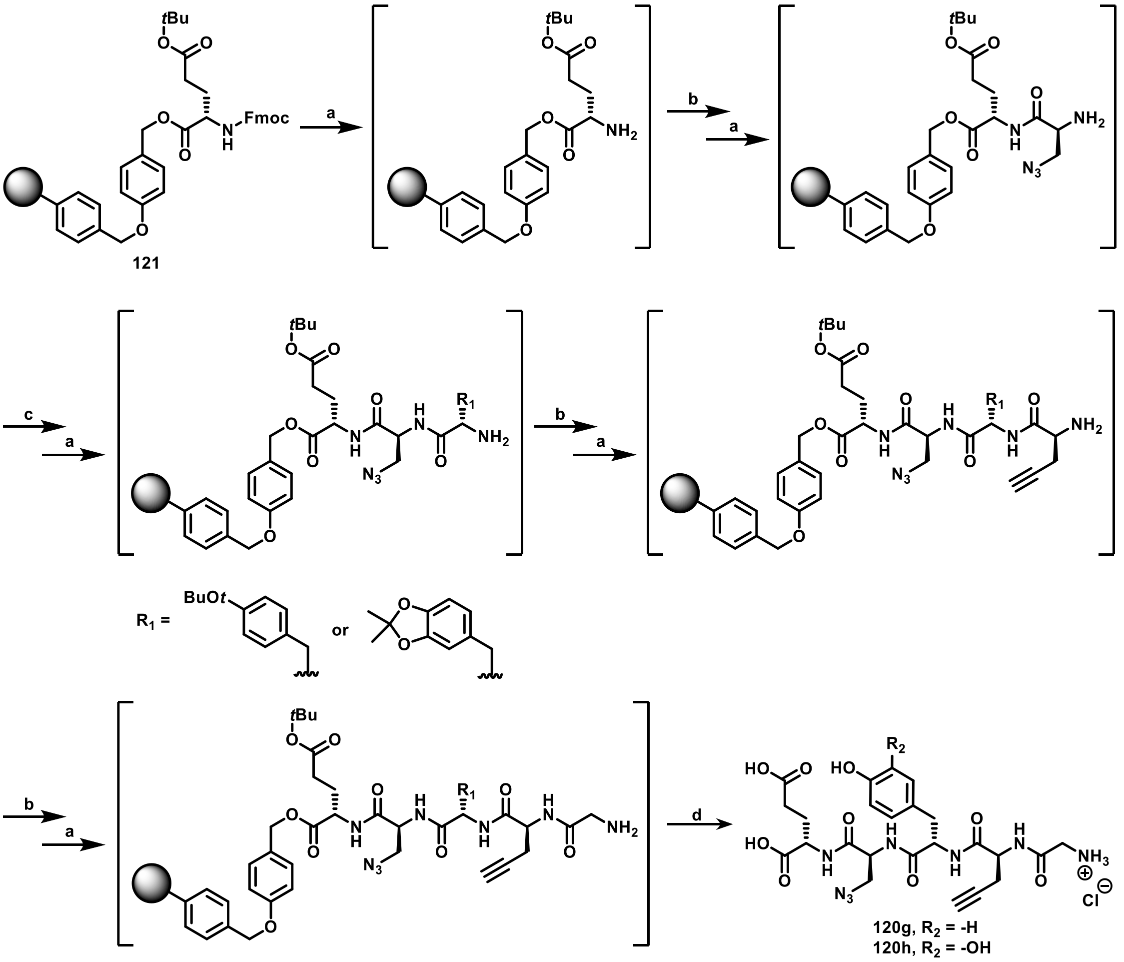

Scheme 12. Reagents and conditions: a) **GP-A1**; b) **GP-B5** using in order Fmoc-*L*-Ala(N_3)-OH, Fmoc-*L*-Pra-OH, Fmoc-Gly-OH; then **GP-C1**; c) **GP-B6** using Fmoc-*L*-Tyr(*t*Bu)-OH or Fmoc-*L*-DOPA(acetonide)-OH; then **GP-C1**; d) **GP-D** and lyophilisation with 0.1 N HCl, 12 h, 21-32%.

The coupling reactions involving Fmoc-*L*-Ala(N_3)-OH, Fmoc-*L*-Pra-OH, and Fmoc-Gly-OH were conducted in the presence of HATU as coupling agent, oxyma pure as auxiliary, and DIPEA as base, following **GP-B5**. On the other hand, **GP-B6** was applied in the coupling steps involving Fmoc-*L*-Tyr(*t*Bu)-OH or Fmoc-*L*-DOPA(acetonide)-OH, providing the total equivalents of the reactants in two steps. The capping steps were performed after the first three coupling reactions, according to **GP-C1**. All the deprotection steps were carried out following **GP-A1**. After completing the pentapeptidomimetic sequences, the obtained resin loaded with the N-deprotected pentapeptidomimetics underwent the same sequence of cleavage, precipitation, dissolution in a 0.1 N solution of HCl in H_2O, and lyophilisation as for **120a**, affording the hydrochloric salt **120g,h**.

The same protocol did not furnish the corresponding γ-lactam based pentapeptide sequence, hence an optimised LPPS approach was employed to afford enantiomerically pure title compound and its tetrapeptidomimetic analogues.

2.7.4 Synthesis of compounds 120i-n

Compounds **120i-n** were synthesised via LPPS. Compound **120k** served as an intermediate for the other title compounds of this section, and it was developed following **Scheme 13**.

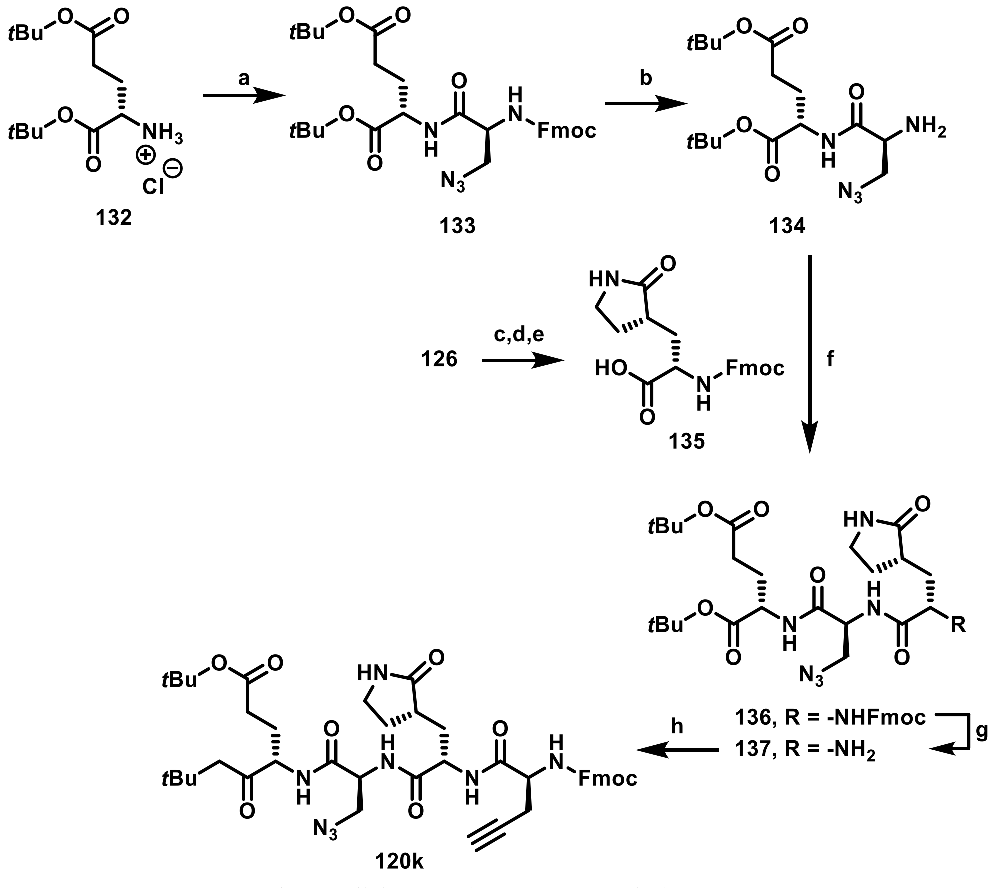

Scheme 13. Reagents and conditions: a) Fmoc-*L*-Ala(N_3)-OH, HATU, oxyma pure, DIPEA, dry DCM, 0 °C to 25 °C, 3 h, 68%; b) DBU, EtSH, THF, 25 °C, 2 h, 99%; c) 1 N LiOH, THF, 25 °C, 2 h; d) TFA, DCM, 0 °C, 30 min; e) Fmoc-Cl, DIPEA, THF, 25 °C, 2 h, (99% over three steps); f) DIC, oxyma pure, DIPEA, dry DMF, MWI, 40 W, 50 °C, (10 + 10) min, 77%; g) piperidine, DMF, 25 °C, 1 h, 99%; h) Fmoc-*L*-Pra-OH, HATU, oxyma pure, DIPEA, dry DMF, MWI, 40 W, 50 °C, (10 + 10) min, 48%.

The synthetic strategy starts with the coupling reaction between **132** and Fmoc-*L*-Ala(N_3)-OH, using HATU as coupling agent, oxyma pure as auxiliary, and DIPEA as base, affording **133**. Subsequent removal of the Fmoc group under basic conditions employing a solution of DBU and EtSH in THF efficiently yielded intermediate **134**. The following step required the synthesis of derivative **135**, since it is not commercially available. Therefore, the target product was obtained via a three steps procedure, involving the hydrolysis of the methyl ester function of compound **126** under basic conditions, Boc deprotection under acidic conditions of its N-terminus, and lastly the alkylation by means of Fmoc-Cl, gave the intermediate compound **135**. The coupling reaction between intermediates **134** and **135** was performed in the presence of DIC, oxyma pure, and DIPEA under MWI, giving **136**. For the subsequent Fmoc deprotection, a 5% solution of piperidine in DMF was used, leading to derivative **137** without any further purification. Lastly, **137** was coupled with Fmoc-*L*-Pra-OH using HATU as coupling agent, oxyma pure as auxiliary, and DIPEA as base under MWI, furnishing compound **120k**.

Starting from **120k**, the other title peptidomimetics were synthesised, as described in **Scheme 14**.

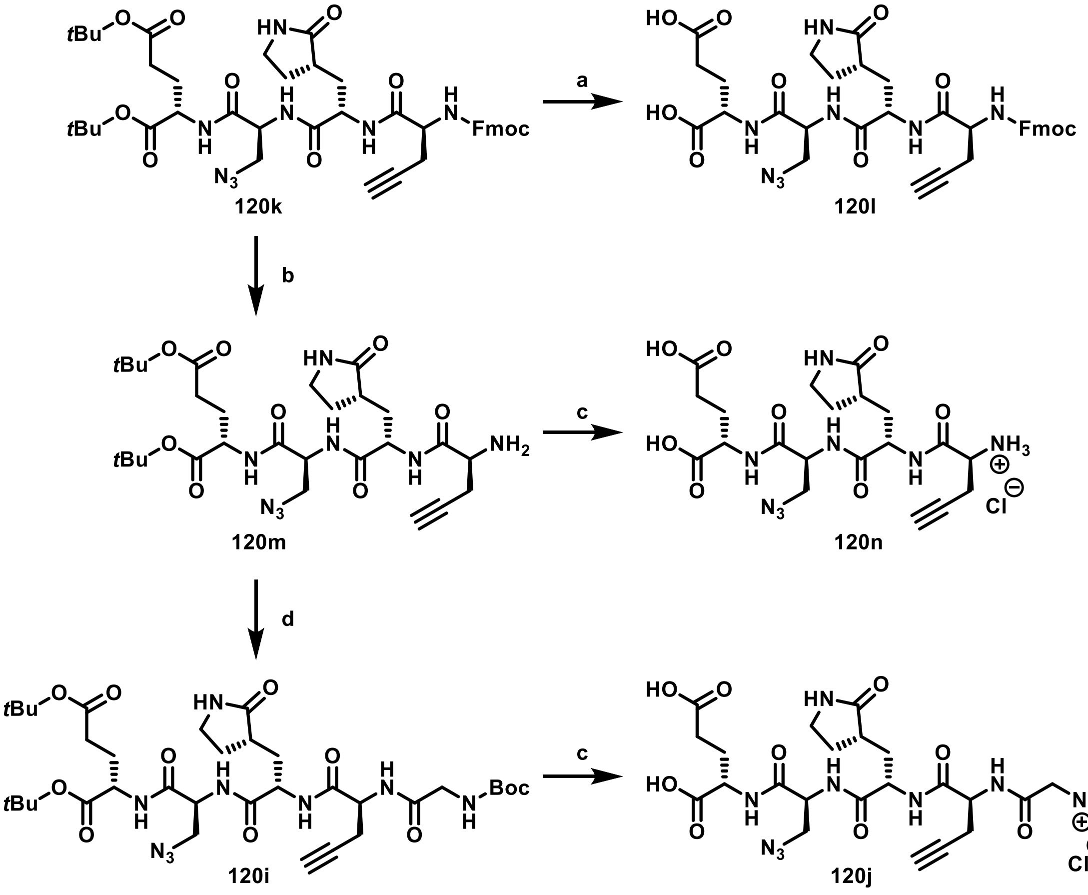

Scheme 14. Reagents and conditions: a) TFA, DCM, 0 °C to 25 °C, 1 h, 69%; b) piperidine, DMF, 25 °C, 2 h, 93%; c) TFA, DCM, 0 °C to 25 °C, 90 min, then lyophilisation with 0.1 N HCl, 12 h, 99%; d) Boc-Gly-OH, HATU, oxyma pure, DIPEA, dry DMF, MWI, 40 W, 50 °C, (10+10) min, 40%.

To obtain compound **120l**, *tert*-butyl ester functionalities of **120k** were hydrolysed using TFA in DCM. On the other hand, the amino terminus of **120k** was deprotected using a 5% solution of piperidine in DMF, affording compound **120m**. On this latter, *tert*-butyl ester groups were removed as for **120l**, providing the corresponding TFA salt. This intermediate was converted into the corresponding hydrochloride salt using the same conditions as for compound **120a-d**, obtaining compound **120n**. Conversely, compound **120m** was involved in a coupling reaction with Boc-Gly-OH under the same conditions as for **137**, giving compound **120i**. This latter was treatment with TFA, simultaneously removing both Glu *tert*-butyl esters and Gly Boc group, hence providing the corresponding TFA salt. This intermediate was converted into the corresponding hydrochloride salt using the same conditions as for compound **120a-d**, affording compound **120j**.

2.8 Preliminary biophysical analysis

Preliminary K_d values determination through microscale thermophoresis

Biomolecular interactions between the developed small peptides or peptidomimetic derivatives and the target protein were evaluated by dr. Stefania Girotto at the Italian Institute of Technologies using a microscale thermophoresis (MST) apparatus (**Figure 45A**). MST is a biophysical analysis based on the directed movement of appropriately labelled molecules in a temperature gradient, which strongly depends on molecular properties such as size, charge, hydration shell, and conformation. In this context, ligand-dependent changes in MST are plotted as normalised fluorescence (ΔF_{norm}) values, which represents the ratio at a specific time point between the fluorescence emission detected after IR laser-induced heating and the one detected before laser-assisted irradiation (**Figure 45B-C**), against ligand concentration, affording dose-response binding curves from which K_d values can be determined (**Figure 45D**). This approach is extremely sensitive in estimating a wide range of binding affinities, typically from picomolar to millimolar, and it allows experiments to be performed in a suitable buffer solution, avoiding immobilisation while reducing sample consumption compared to other traditional techniques, such as surface plasmon resonance, isothermal titration calorimetry, and ELISA assays.[222–224]

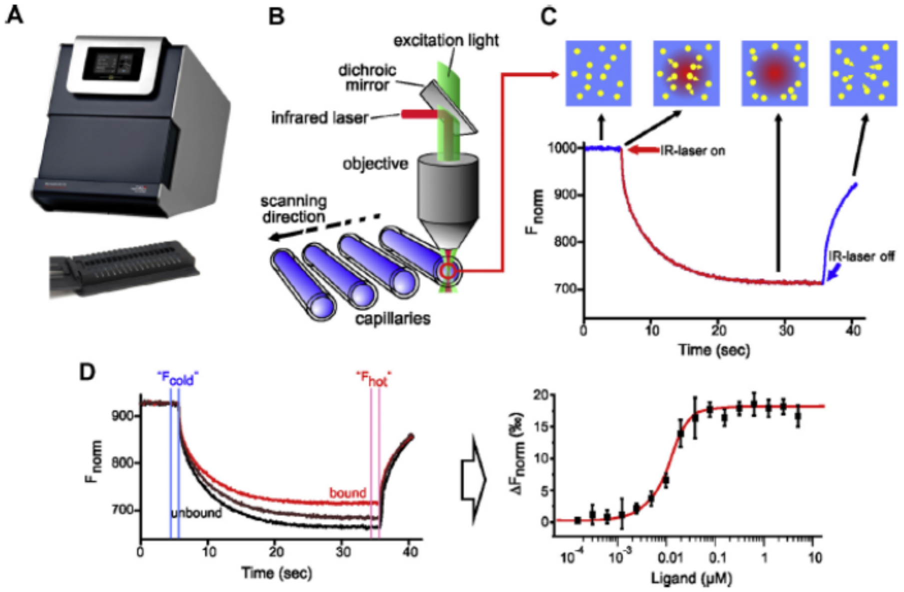

4

Figure 45. Schematic representation of the MST setup and experiment. A) Monolith NT.115 instrument (NanoTemper Technologies GmbH); B) Representation of a typical MST experiment; C) Example of an MST signal: when the IR laser is switched on, a rapid change in fluorophore properties is detected, followed by thermophoretic movement of molecules within the temperature gradient; D) Example of a binding experiment showing differences between the thermophoretic traces of molecules in the bound and unbound states. The fluorescence traces are normalized and plotted as a function of ligand concentration to determine the K_d value. Image adapted from Asmari M. et al., *Methods*, **146**, 107–119, (2018).

The results of these analysis are recapitulated in **Table 13**. At first, binding-check experiments were conducted using 8 capillaries filled with labelled RAD52 either alone or mixed with the presumed ligand at a relatively high selected concentration, generally either 100 or 500 μM. This early screening allows to determine the ligand concentration, reported as "binding concentration" in **Table 13**, at which the binding signal is detected, confirming the presence or absence of the protein-ligand complex in solution. If the signal amplitude is sufficient for further MST analysis, the experiments were followed by classical dose–response MST analysis, as described above, using 16 capillaries, filled with labelled RAD52 either alone or in the presence of increasing ligand concentrations, to determine the K_d values.

Table 13. Labelling methods, binding concentrations, and estimated K_d values for selected small peptides **120a-d** and peptidomimetics **120e,f,i,k-n.**

Cmpd	Protein labelling	Binding concentration (μM)	Estimated K_d values (μM)
120a	NHS Blue	500	<100[a]
120b	NHS Red	100	Ongoing
120c		100	<100[a]
120d	Cys Red	100	<100[b]
120e	NHS Red	150	<10[b]
120f		500	>100[b]
120i		500	Ongoing
120k		500	Ongoing
120l		500	Ongoing
120m		500	Ongoing
120n		500	Ongoing

[a] Data are expressed as mean of three independent experiments performed in triplicate. [b] Data are expressed as mean of three independent experiments performed in quadruplicate.

Compounds **120a** and **120c** showed poor affinity for the target protein, as well as **120f**, whose K_d value is even lower. On the other hand, compound **120e** exhibit good binding affinity for RAD52, therefore its ability to disrupt PPIs between adjacent protomers is currently being investigated. For the other tested compounds, **120b,d,i-n**, the accuracy of the results was likely compromised by the presence of a suspended precipitate, apparently generated within the medium employed during the biophysical assay.

Dynamic light scattering analysis for selected compounds in water media

Dynamic light scattering (DLS) analyses were performed in collaboration with Prof. Claudia Bonechi, to estimate whether the selected compounds might undergo aggregation phenomena in water media. DLS data of the representative compound **120a** is depicted in **Figure 46**, while for the other selected compounds **120b-d,i,j,l** DLS spectra are presented in **Appendix** (**Figure A1-6**).

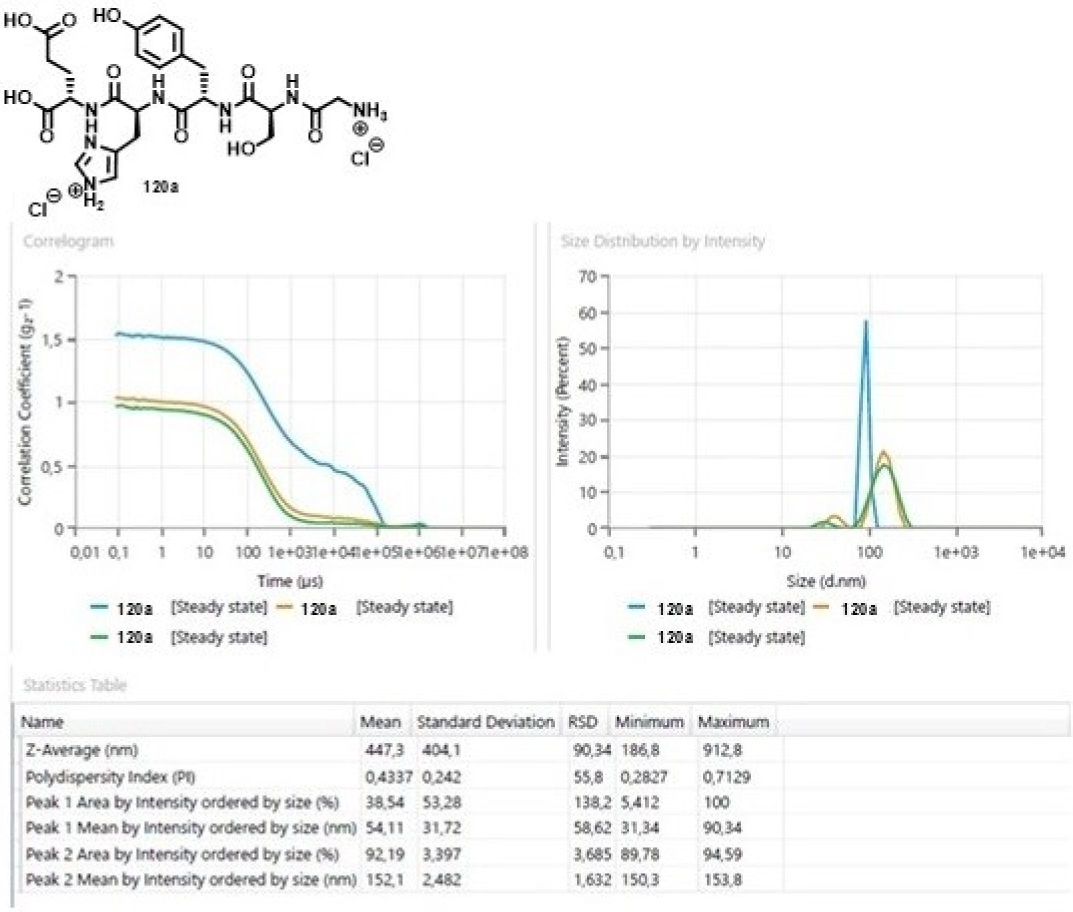

Name	Mean	Standard Deviation	RSD	Minimum	Maximum
Z-Average (nm)	447,3	404,1	90,34	186,8	912,8
Polydispersity Index (PI)	0,4337	0,242	55,8	0,2827	0,7129
Peak 1 Area by Intensity ordered by size (%)	38,54	53,28	138,2	5,412	100
Peak 1 Mean by Intensity ordered by size (nm)	54,11	31,72	58,62	31,34	90,34
Peak 2 Area by Intensity ordered by size (%)	92,19	3,397	3,685	89,78	94,59
Peak 2 Mean by Intensity ordered by size (nm)	152,1	2,482	1,632	150,3	153,8

Figure 46. DLS spectra of compound **120a**.

The DLS spectra displayed Z-average >1 µm in water media. This was a major limitation in the analyses, since above this threshold the measurements are not consistent, meaning that the instrument detects either clearly visible suspended particles in the tested media or no particles at all due to saturation of the signal. Another significant limitation in this assay is represented by the medium in which the analyses were carried out. The measurements were conducted in water and not in the medium used for the binding assay, due the presence of the surfactants in this latter, which may form micelles compromising the accuracy of the data. This difference in the medium could largely impact the aggregation of the constructed compounds, hence alternative biophysical methodologies should be employed in the future to corroborate whether the developed derivatives can aggregate withing the binding assay medium.

2.9 Conclusions

One topic developed during my PhD internship was devoted of the exploitation of a SL-based approach as a suitable strategy potentially furnishing customised anticancer therapy with extremely limited side effects. Building on the success of F79 aptamer, I developed a set of small linear peptides targeting a specific region localised in RAD52 oligomerisation domain. These molecules should disrupt the PPIs established by two adjacent protomers thus interfering with RAD52 assembly, ultimately exerting synergistic lethal effects in *BRCA*-mutated cells in association with PARPis. Exploiting both solid and liquid phases synthesis, 14 peptides and peptidomimetics were synthesised. Starting from previous docking studies identifying the pentapeptide **120a** as a suitable RAD52 modulator, the chemical space around the C- and N-termini was systematically explored introducing different capping groups and replacing the C-terminal Glu residue with a Gly residue. The central Tyr residue was substituted with either a *L*-DOPA or a γ-lactam-based residues. This latter was employed to obtain both pentapeptide sequences, displaying different N-ends, as well as truncated tetrapeptides, further exploring SARs. Non-natural amino acids harbouring an azido and an alkynyl moieties were introduced to develop cyclic peptides via click chemistry. Since this latter offer several benefits over linear counterparts, future efforts will focus on the development of cyclic peptidomimetics encompassing a 1,4- or 1.5-disubstituted 1,2,3-triazole. These cyclic molecules may also be less prone to undergone aggregation phenomena compared to their linear counterparts, overcoming the major limitation during the binding assays. In this context, more in-depth biophysical studies should be performed to understand whether linear compounds **120b,d,i,j,l** undergo aggregation phenomena in the suitable medium or if the detected suspended precipitate might come from different operational procedure (e.g. stirring) during the binding assay.

3.0 Experimental section

Reagents were purchased from Sigma-Aldrich, Fluorochem, and Iris Biotech and used without further purification. All moisture-sensitive reactions were performed under nitrogen atmosphere using oven-dried glassware and anhydrous solvents. Flash column chromatography was carried out on silica gel (Merck: Kieselgel 60, particle size 0.040–0.063 mm). Reactions' progression was monitored by thin-layer chromatography (TLC), carried out using glass- or aluminium backed plates coated with Merck Kieselgel 60 GF254. Plates were visualised under UV light (at 254 nm). ^{1}H NMR, ^{13}C NMR, and ^{19}F NMR spectra were recorded on a Varian 300 MHz or Bruker Avance 400 MHz spectrometers using the residual signal of the deuterated solvent as an internal standard. Coupling constants (J) are given in Hertz (Hz). Splitting patterns are described as singlet (s), doublet (d), triplet (t), quartet (q), and broad (br); the values of chemical shifts (δ) are given in parts per million (ppm). The gradient was optimised based on compound polarity. Electrospray ionisation mass spectrometry (ESI-MS) was performed using a Shimadzu LCMS-2050 apparatus, incorporating a NexeraTM X3 UHPLC system along with a heated dual ion source (DUIS) unit. Microwave irradiation was furnished by means of a CEM Discover 2.0 Microwave Synthesiser, comprising Activent Technology for gas releasing and iWave temperature sensor. Automatic SPPS was performed on a MultiSynTech Syro I, multiple peptide automated synthesiser. Yields refer to purified products and are not optimised. All moisture-sensitive reactions were conducted under a N_2 atmosphere using oven-dried glassware and anhydrous solvents. The purity of final products (>95 %, detection at 254 nm; flow rate = 1.0 mL/min; mobile phase A, 0.01 % TFA (*v*/v) in water; mobile B, acetonitrile; gradient, 90/10–10/90 A/B in 26 min), pseudothermodynamic solubility, and chemical stability were determined by analytical high-performance liquid chromatography, using a Purospher® STAR RP-18 endcapped column (5µm), whereas a Poroshell 120 EC-C18 (2.7 µm) column was utilised to evaluate log*P* values.

3.1 Experimental section of the FAAH/MGL inhibitors and H_3R antagonists

3.1.1 Synthetic procedures and NMR spectra

*tert-Butyl 4-(6-hydroxy-3,4-dihydroisoquinolin-2(1H)-yl)piperidine-1-carboxylate (**48**:* to a solution of **47** (200 mg, 1.34 mmol) in EtOH (4 mL), AcOH (4 µL, 0.07 mmol), and 1-Boc-4-piperidone (534 mg, 2.68 mmol) were added, Temperature was increased to 82 °C, and the reaction mixture was stirred for 2 h. After cooling down to 25 °C, the solvent was removed under vacuum. The residue was diluted with 0 °C cooled MeOH (4 mL), and $NaBH_3CN$ (101 mg, 1.61 mmol) was added portion wise over 20 minutes. Temperature was allowed to reach 25 °C, and the reaction mixture was stirred for 12 h. The solvent was removed under vacuum. The residue was taken up with DCM, a saturated solution of $NaHCO_3$ was added, and the mixture was extracted with DCM (3 x 10 mL). The collected organic layers were dried over $MgSO_4$, filtered, and concentrated under vacuum. The crude was purified by column chromatography on silica gel (DCM/MeOH starting from 40:1 to 20:1) to afford the title compound as a yellow solid (38% yield). **ESI-MS** *m*/*z*: 333 $[M + H]^+$; 355 $[M + Na]^+$.**^{1}H NMR** (300 MHz, $(CD_3)_2CO$) δ 6.89 – 6.81 (m, 1H), 6.61 – 6.51 (m, 2H), 4.16 – 4.02 (m, 2H), 3.68 – 3.60 (m, 2H), 2.84 – 2.71 (m, 6H), 2.65 – 2.51 (m, 1H), 1.89 – 1.78 (m, 2H), 1.52 – 1.36 (m, 11H).

*tert-Butyl 4-(6-(3-(piperidin-1-yl)propoxy)-3,4-dihydroisoquinolin-2(1H)-yl)piperidine-1-carboxylate (**49**):* to a solution of compound **48** (170 mg, 0.51 mmol) in MeCN (3 mL), K_2CO_3 (107 mg, 0.76 mmol), and 1-(3-chloropropyl)piperidin-1-ium (67 mg, 0.34 mmol) were added. Temperature was increased to 75 °C, and the reaction mixture was stirred for 12 h under N_2 atmosphere. A saturated solution of $NaHCO_3$ was added, and the mixture was extracted with EtOAc (3 x 10 mL). The collected organic layers were dried over Na_2SO_4, filtered, and concentrated under vacuum. The crude was purified by column chromatography on silica gel (DCM/MeOH/NH_4OH starting from 20:1:0.1 to 10:1:0.1) to afford the title compound as a yellow oil (38% yield). **ESI-MS** *m*/*z*: 458 $[M + H]^+$. **^{1}H NMR** (300 MHz, $(CD_3)_2CO$) δ 6.96 – 6.90 (m, 1H), 6.71 – 6.61 (m, 2H), 4.15 – 4.05 (m, 2H), 3.99 (t, *J* = 6.4 Hz, 2H), 3.70 – 3.63 (m, 2H), 3.17 – 2.99 (m, 4H), 2.66 – 2.54 (m, 1H), 2.50 – 2.37 (m, 6H), 1.97 – 1.78 (m, 4H), 1.62 – 1.50 (m, 4H), 1.49 – 1.37 (m, 15H).

*6-(3-(Piperidin-1-yl)propoxy)-2-(piperidin-4-yl)-1,2,3,4-tetrahydroisoquinoline (**50**)*: to a solution of compound **49** (61 mg, 0.13 mmol) in MeOH (5 mL), a 1 N solution of HCl in MeOH (130 µL, 0.13 mmol) was added. Temperature was increased to 40 °C, and the reaction mixture was stirred for 1 h. The solvent was removed under vacuum. The solid residue was taken up with DCM, neutralised with a saturated solution of $NaHCO_3$, and extracted with DCM (3 x 10 mL). The collected organic layers were dried over Na_2SO_4, filtered, and concentrated under vacuum. The crude was used in the following step without any further purification (yellow solid) (99% yield). **ESI-MS** *m*/*z*: 358 $[M + H]^+$; 179 $[M/2 + H]^+$. **^{1}H NMR** (300 MHz, $(CD_3)_2CO$) δ 6.97 – 6.89 (m, 1H), 6.71 – 6.60 (m, 2H), 3.98 (t, *J* = 6.4 Hz, 2H), 3.69 – 3.65 (m, 2H), 3.20 – 3.12 (m, 3H), 2.81 – 2.75 (m, 4H), 2.72 – 2.61 (m, 2H), 2.46 – 2.32 (m, 8H), 1.95 – 1.81 (m, 4H), 1.59 – 1.48 (m, 6H), 1.43 – 1.37 (m, 2H).

tert-Butyl 4-((6-hydroxy-3,4-dihydroisoquinolin-2(1H)-yl)methyl)piperidine-1-carboxylate (51): compound **51** was prepared according to procedure used for **48**, starting from **47** (300 mg, 2.01 mmol), AcOH (6 µL, 0.10 mmol), and 1-Boc-piperidine-4-carboxaldehyde (857 mg, 4.02 mmol) in EtOH (6 mL) in the first step, then $NaBH_3CN$ (151 mg, 2.41 mmol) in MeOH (6 mL). The crude was purified by column chromatography on silica gel (DCM/MeOH starting from 60:1 to 20:1) to afford the title compound as a yellow solid (55% yield). **ESI-MS** *m*/*z*: 347 $[M + H]^+$; 369 $[M + Na]^+$. **^{1}H NMR** (300 MHz, $(CD_3)_2CO$) δ 7.99 (s, 1H), 6.88 – 6.83 (m, 1H), 6.62 – 6.54 (m, 2H), 4.10 – 4.01 (m, 2H), 3.50 – 3.45 (m, 2H), 3.34 – 3.28 (m, 2H), 2.81 – 2.73 (m, 4H), 2.66 – 2.58 (m, 2H), 2.34 – 2.29 (m, 2H), 1.91 – 1.71 (m, 1H), 1.43 (s, 9H), 1.02 (td, J = 12.6, 12.1, 4.2 Hz, 2H).

tert-Butyl 4-((6-(3-bromopropoxy)-3,4-dihydroisoquinolin-2(1H)-yl)methyl)piperidine-1-carboxylate (52): compound **52** was prepared according to procedure used for **49**, starting from **51** (911 mg, 2.63 mmol), K_2CO_3 (545 mg, 3.94 mmol), and 1,3-dibromopropane (534 µL, 5.26 mmol) in MeCN (14 mL). The crude was purified by column chromatography on silica gel (DCM/MeOH starting from 100:1 to 80:1) to afford the title compound as a yellow oil (20% yield). **ESI-MS** *m*/*z*: 468 $[M + H]^+$. **^{1}H NMR** (300 MHz, $(CD_3)_2SO$) δ 6.96 – 6.90 (m, 1H), 6.73 – 6.65 (m, 2H), 4.02 (t, J = 6.0 Hz, 2H), 3.96 – 3.86 (m, 2H), 3.65 (t, J = 6.5 Hz, 2H), 3.45 – 3.40 (m, 2H), 2.81 – 2.65 (m, 4H), 2.63 – 2.54 (m, 2H), 2.30 – 2.15 (m, 4H), 1.80 – 1.62 (m, 2H), 1.38 (s, 9H), 1.23 (s, 1H), 1.03 – 0.83 (m, 2H).

tert-Butyl 4-((6-(3-(piperidin-1-yl)propoxy)-3,4-dihydroisoquinolin-2(1H)-yl)methyl)piperidine-1-carboxylate (53): compound **53** was prepared according to procedure used for **49**, starting from **52** (320 mg, 0.68 mmol), K_2CO_3 (141 mg, 1.02 mmol), and piperidine (140 µL, 1.36 mmol) in MeCN (3 mL). The crude was purified by column chromatography on silica gel (DCM/MeOH starting from 50:1 to 10:1) to afford the title compound as a yellow oil (47% yield). **ESI-MS** *m*/*z*: 472 $[M + H]^+$. **^{1}H NMR** (300 MHz, $CDCl_3$) δ 6.93 – 6.87 (m, 1H), 6.70 – 6.60 (m, 2H), 4.13 – 4.02 (m, 2H), 3.96 (t, J = 6.4 Hz, 2H), 3.55 – 3.46 (m, 2H), 2.88 – 2.79 (m, 2H), 2.76 – 2.62 (m, 4H), 2.51 – 2.36 (m, 6H), 2.35 – 2.27 (m, 2H), 2.02 – 1.87 (m, 4H), 1.77 (d, J = 12.8 Hz, 2H), 1.59 (p, J = 5.5 Hz, 4H), 1.45 (s, 9H), 1.25 (s, 1H), 1.19 – 1.02 (m, 2H).

6-(3-(Piperidin-1-yl)propoxy)-2-(piperidin-4-ylmethyl)-1,2,3,4-tetrahydroisoquinoline (54): compound **54** was prepared according to procedure used for **50**, starting from **53** (151 mg, 0.32 mmol), and a 1 N solution of HCl in MeOH (320 µL, 0.32 mmol) in MeOH (10 mL). The crude was used in the following step without any further purification (yellow solid) (99% yield). **ESI-MS** *m*/*z*: 372$[M + H]^+$. **^{1}H NMR** (300 MHz, CD_3OD) δ 7.18 – 7.11 (m, 1H), 6.88 – 6.81 (m, 2H), 5.47 (s, 1H), 4.67 – 4.54 (m, 1H), 4.27 (d, J = 14.7 Hz, 1H), 4.07 (t, J = 5.7 Hz, 2H), 3.56 (d, J = 12.1 Hz, 2H), 3.46 – 3.36 (m, 4H), 3.34 – 3.22 (m, 6H), 3.17 – 3.03 (m, 2H), 2.96 (t, J = 12.1 Hz, 2H), 2.30 – 2.18 (m, 2H), 2.17 – 2.02 (m, 2H), 1.97 – 1.73 (m, 6H), 1.68 – 1.44 (m, 3H).

*3-(Piperidin-1-yl)propan-1-ol (**56**)*: to a solution of **55** (23 mL, 235 mmol) in acetone (200 mL), K_2CO_3 (3200 mg, 235 mmol), KI (2600 mg, 157 mmol), and 3-chloropropan-1-ol (13 mL, 157 mmol) were added. Temperature was increased to 65 °C, and the reaction mixture was stirred for 96 h. After cooling down to 25 °C, the suspension was filtered, and the filtrate was concentrated under vacuum. The crude was purified by means of distillation under reduced pressure (T_b = 65-80°C at 5 mmbar) to afford the title compound as a white solid (64% yield). **^{1}H NMR** (300 MHz, $CDCl_3$) δ 3.80 – 3.76 (m, 2H), 2.57 – 2.51 (m, 2H), 2.48 – 2.29 (m, 4H), 1.72 – 1.64 (m, 2H), 1.60 – 1.51 (m, 4H), 1.47 – 1.36 (m, 2H).

*4-(3-(Piperidin-1-yl)propoxy)benzaldehyde (**57**)*: compound **56** (798 mg, 5.57 mmol), 4-hydroxybenzaldehyde (1013 mg, 8.30 mmol), and PPh_3 (2175 mg, 8.30 mmol) were dissolved in THF (10 mL) and injected via line A (50 µL/min). A solution of DEAD (40% toluene solution, 3253 µL, 8.30 mmol) in THF (10 mL) was injected via line B (50 µL/min). The reaction was conducted at 60 °C with a total flow rate of 100 µL/min, (τ = 1 min). The reactor output was collected, and the solvent was removed under vacuum. The residue was dissolved in EtOAc, and extracted with a 2 N solution of HCl in H_2O (3 x 10 mL). The collected aqueous layers were extracted with EtOAc (2 x 10 mL), then basified till pH = 10 using 2 N solution of NaOH, and subsequently extracted with EtOAc (3 x 10 mL). The collected organic layers were washed with H_2O (3 x 10 mL), and a saturated solution of NaCl (1 x 10 mL), dried over $MgSO_4$, filtered, and concentrated under vacuum. The crude product was used in the following step without further purification (orange oil) (72% LC-MS determined yield).

*Tert-Butyl 4-(benzylamino)piperidine-1-carboxylate (**60**)*: compound **60** was prepared according to procedure used for **48**, starting from **58** (502 mg, 2.52 mmol), and **59** (550 µL, 5.04 mmol) in EtOH (21 mL) for the first step, then $NaBH_4$ (96 mg, 2.55 mmol) in MeOH (42 mL). The crude was purified by column chromatography on silica gel (DCM/MeOH/NH_3 starting from 99:1 to 97:3) to afford the title compound as a yellowish oil (85% yield). **^{1}H NMR** (300 MHz, $CDCl_3$) δ 7.37 – 7.28 (m, 5H), 4.02 (d, J = 12.3 Hz, 2H), 3.82 (s, 2H), 2.80 (t, J = 11.5 Hz, 2H), 2.70 – 2.61 (m, 1H), 1.86 (d, J = 10.5 Hz, 2H), 1.45 (s, 9H), 1.38 – 1.21 (m, 2H).

*tert-Butyl 4-(benzyl(4-(3-(piperidin-1-yl)propoxy)benzyl)amino)piperidine-1-carboxylate (**61**)*: compound **57** (909 mg, 3.68 mmol), and ethyl orthoformate (1231 µL, 7.40 mmol) were dissolved in EtOH (8 mL) and subsequently injected via line A (20 µL/min). A solution of AcOH (430 µL, 7.40 mmol), $NaBH_3CN$ (350 mg, 5.57 mmol), and **60** (1068 mg, 3.68 mmol) in EtOH (8 mL) was injected via line B (20 µL/min). The reaction was conducted at 75 °C with a total flow rate of 40 µL/min (τ = 2.5 min). The reactor output was collected, and the solvent was removed under vacuum. The residue was dissolved in EtOAc, and washed with 2 N solution of NaOH (2 x 10 mL), a saturated solution of NaCl (2 x 10 mL), dried over $MgSO_4$, filtered, and concentrated under vacuum. The crude product was used without further purification (yellowish oil) (33% LC-MS determined yield).

*N-Benzyl-N-(4-(3-(piperidin-1-yl)propoxy)benzyl)piperidin-4-amine (**62**)*: compound **62** was prepared according to procedure used for **50**, starting from **60** (94 mg, 0.18 mmol), and a 1 N solution of HCl in MeOH (940 µL, 0.18 mmol) in MeOH (11 mL). The crude was used in the following step without any further purification (yellow oil) (83% yield). **^{1}H NMR** (300 MHz, $CDCl_3$) δ 7.31 – 7.05 (m, 7H), 6.74 (d, J = 8.5 Hz, 2H), 3.90 (t, J = 6.4 Hz, 2H), 3.55 (s, 2H), 3.49 (s, 2H), 3.13 – 3.02 (m, 2H), 2.58 – 2.28 (m, 9H), 1.94 – 1.83 (m, 2H), 1.79 – 1.70 (m, 2H), 1.59 – 1.47 (m, 6H), 1.41 – 1.32 (m, 2H).

*(4-(Benzyl(4-(3-(piperidin-1-yl)propoxy)benzyl)amino)piperidin-1-yl)(1H-1,2,4-triazol-1-yl)methanone (**46f**)*: compound **61** (336 mg, 0.65 mmol) was dissolved in THF (5 mL) and injected via line A (20 µL/min). A solution of CDT (298 mg, 1.82 mmol) in THF (5 mL) was injected via line B (20 µL/min). The reaction was conducted at 40 °C with a total flow rate of 40 µL/min (τ = 2.5 min). The reactor output was collected, and the solvent was removed under vacuum. The residue was purified by reverse phase flash chromatography (H_2O/MeCN starting from 100:0 to 0:100) to afford the title compound as a yellowish oil. (59% yield). **ESI-MS** *m/z*: 517 $[M + H]^+$. **^{1}H NMR** (300 MHz, $CDCl_3$) δ 8.69 (s, 1H), 7.93 (s, 1H), 7.33 – 7.09 (m, 7H), 6.74 (d, J = 9.1 Hz, 2H), 4.55 – 4.49 (m, 2H), 3.91 (t, J = 6.3 Hz, 2H), 3.56 (s, 2H), 3.51 (s, 2H), 2.89 – 2.68 (m, 3H), 2.53 – 2.32 (m, 6H), 2.00 – 1.77 (m, 4H), 1.78 – 1.60 (m, 2H), 1.60 – 1.26 (m, 6H). **^{13}C NMR** (75 MHz, $CDCl_3$) δ 158.0, 151.9, 148.4, 146.5, 140.3, 131.9, 129.4, 128.3, 128.2, 126.8, 114.3, 66.5, 56.0, 55.6, 54.6, 53.6, 53.2, 27.7, 26.9, 26.0, 24.4.

*(4-(6-(3-(Piperidin-1-yl)propoxy)-3,4-dihydroisoquinolin-2(1H)-yl)piperidin-1-yl)(1H-1,2,4-triazol-1-yl)methanone (**46k**)*: to a solution of compound **50** (43 mg, 0.12 mmol) in dry DCM (10 mL), CDT (20 mg, 0.12 mmol) was added, and the reaction mixture was stirred for 12 h at 25 °C under N_2 atmosphere. H_2O was added, and the mixture was extracted with EtOAc (3 x 10 mL). The collected organic layers were dried over Na_2SO_4, filtered, and concentrated under vacuum. The crude was purified by column chromatography on silica gel (Et_2O/IPA/TEA starting from 30:1:0.1 to 10:1:0.1) to afford the title compound as a yellow oil (77 mg, 58% yield) **ESI-MS** *m/z*: 531 $[M + H]^+$. **^{1}H NMR** (300 MHz, $CDCl_3$) δ 8.78 (s, 1H), 8.09 (s, 1H), 6.91 (d, J = 8.4 Hz, 1H), 6.72 – 6.66 (m, 1H), 6.62 (d, J = 2.6 Hz, 1H), 4.69 – 4.52 (m, 2H), 3.95 (t, J = 6.3 Hz, 2H), 3.74 (s, 2H), 3.11 (t, J = 12.8 Hz, 2H), 2.90 – 2.73 (m, 5H), 2.52 – 2.37 (m, 6H), 2.10 – 1.91 (m, 4H), 1.77 (qd, J = 12.1, 4.1 Hz, 2H), 1.60 (p, J = 5.5 Hz, 4H), 1.45 (q, J = 6.3 Hz, 2H). **^{13}C NMR** (75 MHz, $CDCl_3$) δ 157.4, 152.0, 146.5, 135.4, 127.6, 126.8, 114.0, 112.8, 66.4, 60.8, 56.0, 54.5, 51.4, 46.7, 29.7, 28.3, 26.6, 25.7, 24.3.

*(4-((6-(3-(Piperidin-1-yl)propoxy)-3,4-dihydroisoquinolin-2(1H)-yl)methyl)piperidin-1-yl)(1H-1,2,4-triazol-1-yl)methanone (**46l**)*: compound **46l** was prepared according to procedure used for **46k**, starting from **54** (119 mg, 0.32 mmol), and CDT (164 mg, 0.32 mmol) in dry DCM (26 mL). The crude was purified column chromatography on silica gel (Et_2O/IPA/TEA starting from 30:1 to 15:1), to afford the title compound as a yellow oil (61% yield). **ESI-MS** *m/z* 467$[M + H]^+$ **^{1}H NMR** (300 MHz, $CDCl_3$) δ 8.74 (s, 1H), 7.98 (s, 1H), 6.94 – 6.84 (m, 1H), 6.72 – 6.58 (m, 2H), 4.60 – 4.42 (m, 2H), 3.95 (t, J = 6.3 Hz, 2H), 3.52 (m, 2H), 3.04 (t, J = 12.7 Hz, 2H), 2.87 – 2.78 (m, 2H), 2.72 – 2.61 (m, 2H), 2.54 – 2.33 (m, 8H), 2.03 – 1.84 (m, 4H), 1.66 – 1.55 (m, 4H), 1.50 – 1.20 (m, 5H). **^{13}C NMR** (75 MHz, $CDCl_3$) δ 157.5, 152.0, 148.7, 146.5, 135.5, 127.5, 127.0, 114.1, 112.8, 66.7, 64.1, 56.3, 56.1, 54.8, 53.5, 51.5, 34.0, 30.9, 29.5, 27.0, 26.1, 24.6.

3.1.2 HPLC procedures for determining pseudothermodynamic solubility, chemical stability, and log*P* value

Pseudothermodynamic solubility assessment

The HPLC procedure used for determining pseudothermodynamic solubility was adapted from previous literature work.[88] Gradient elution was performed, starting from 10% MeCN (with 0.1% TFA as a phase modifier) in H_2O (0.1% TFA) and progressing to 90% MeCN (0.1% TFA) in H_2O (0.1% TFA) over 20 minutes. The flow rate was set at 1.0 mL/min, with a column temperature maintained at 25 °C. Sample injection volume was 50 µL, and detection was carried out at a wavelength of 215 nm. The retention times for the analysed compounds were as follows: **46f** at 8.89 min, **46g** at 11.21 min, **46h** at 11.06 min, and **46l** at 7.13 min.

A 10 mM stock solution of each tested compound was prepared by dissolving the compound in DMSO. From this stock solution, three samples were prepared; one serving as the reference solution, and the other two as test solutions adjusted to pH = 3.0 and pH = 7.4. Each sample was adjusted to a final concentration of 250 µM, with 2.5% (v/v) DMSO. The reference solution was prepared by diluting the stock solution with a 70:30 (v/v) water/acetonitrile mixture. The two test solutions were prepared by diluting the stock solution with 50 mM of either acetic acid (pH = 3.0) or PBS buffer (pH = 7.4), respectively. The prepared suspensions/solutions were then sealed, and incubated at 25 °C under orbital shaking for 24 hours, to reach pseudothermodynamic equilibrium. After incubation, the samples were filtered through PTFE filters, and injected inside the HPLC apparatus to calculate the AUC. Each sample was analysed in triplicate, and the reported solubility values are given as mean. Pseudothermodynamic solubility was calculated by comparing the peak areas of the sample with those of the standard using the following equation:

$$\text{Solubility} = \frac{\text{AUC (sample) x C (reference)}}{\text{AUC (reference)}}$$

AUC (Sample): area under the curve of the compound peak from the test solution; C (reference): concentration of the reference solution (250 mM); AUC (reference): area under the curve of the compound peak from reference solution.

Chemical stability assessment

The HPLC procedure used for determining chemical stability was adapted from previous literature work.[88] However, the performed gradient elution was shorter, starting from 10% MeCN (0.1% TFA) in H_2O (0.1% TFA) and progressing to 90% MeCN (0.1% TFA) in H_2O (0.1% TFA) over 10 minutes. The corresponding retention time for **46f** was therefore 6.60 minutes.

A 10 mM stock solution of **46f** was prepared using MeCN. From this stock solution, two test solutions at pH = 3.0 and pH = 7.4, each with a concentration of 400 µM, were prepared by dilution with 50 mM of either acetic acid (pH 3.0) or PBS buffer (pH 7.4), respectively. The prepared solutions were incubated at 25 °C under orbital shaking for 24 hours. At t_0, as well as after t_{24h}, samples were withdrawn from the solution, and injected inside the HPLC apparatus to calculate the AUC. Each sample was analysed in triplicate, and the reported stability values are given as mean. Chemical stability was determined by comparing the area AUC of the peak at t_0 with the AUC of the peak of the same sample solution at t_{24h}. The stability percentage was then calculated using the following equation:

$$\%\text{remaining} = \frac{\text{AUC}\ (t_{24h})}{\text{AUC}\ (t_0)}\ \text{x}\ 100$$

AUC (t_{24h}): Area under the curve (AUC) of the compound peak from the test solution after 24 hours; AUC (t_0): area under the curve of the compound peak from test solution at the beginning.

LogP value assessment

For the HPLC log*P* value analysis, a Poroshell 120 EC-C18 (2.7 µm) column was utilised. The mobile phase comprised 50% MeCN and 50% pyrrolidine aqueous buffer (0.25 mM), adjusting pH = 10.75 to ensure the neutral form of the evaluated compounds during chromatographic measurements. Isocratic elution was employed, with a flow rate set at 1.0 ml/min and a column temperature maintained at 25 °C. The sample injection volume was 50 µl, and the detection was performed at a wavelength of 215 nm. Thiourea was used for determining the dead time.

The partition coefficient of compounds was determined following guidelines provided by the Organisation of Economic Co-operation and Development (OECD) for HPLC method.[225] All reference and test compounds were initially prepared as 10 mM stock solutions in MeCN. These samples were then diluted with the mobile phase to achieve a final concentration of 1 mM, which was used for the analysis. Using the dead time determined with thiourea, the capacity factor (k) can be calculated from the retention times of the reference compounds using the following equation:

$$\mathrm{k} = \frac{t_r - t_0}{t_0}$$

k: capacity factor; t_r: retention time of the compound, t_0: retention time of thiourea (deadtime)

By plotting the literature-known log*P* values of the reference compounds against the logarithm of the capacity factor, a calibration curve can be generated, allowing for the determination of the log*P* values of unknown substances. The injected reference compounds cover a wide range of log*P* values, ensuring good accuracy. All measurements were performed in duplicate. To determine the log*P* values of the samples, the capacity factor was calculated from their retention times using the formula. Its logarithmic value can then be substituted into the equation of the calibration curve, allowing for the calculation of the respective log*P* value.

3.2 Experimental section of the HDAC6/MGL inhibitors

*1H-Pyrazole-4-carboxylic acid (**71**)*: compound **70** (1000 mg, 7.14 mmol) was dissolved in a solution of NaOH (286 mg, 7.14 mmol) in H_2O (5 mL). The temperature was increased to 100 °C, and the reaction mixture was stirred for 2 h. Temperature was cooled down to 0 °C, and concentrated HCl (595 µL, 7.14 mmol) was added. The suspension was decanted, and the solid residue was washed with H_2O (2 x 2 mL). The residual washing solvent was removed under vacuum. Et_2O (2 x 20 mL) was added, and the solvent was removed under vacuum. The crude was used in the following step without any further purification (white solid) (99% yield). **ESI-MS** *m*/*z*: 111 $[M-\mathrm{H}]^-$; 147 $[M+\mathrm{Cl}]^-$. ^{1}**H NMR** (300 MHz, CD_3OD) δ 8.04 (s, 2H). ^{13}**C NMR** (75 MHz, CD_3OD) δ 168.1, 137.5, 117.7, 30.9.

*Benzyl 1H-pyrazole-4-carboxylate (72**a**)*: to a solution of compound **71** (100 mg, 0.82 mmol) in a mixture of dry DCM (1 mL) and dry DMF (1 mL), DMAP (11 mg, 0.10 mmol), DIC (168 µL, 1.07 mmol), and benzyl alcohol (168 µL, 1.07 mmol) were added. Temperature was increased to 60 °C, and the reaction mixture was stirred for 12 h under N_2 atmosphere. The solvent was removed under N_2 stream. A saturated solution of NH_4Cl was added, and the mixture was extracted with EtOAc (3 x 10 mL). The collected organic layers were washed with a saturated solution of NH_4Cl (2 x 10 mL), dried over Na_2SO_4, filtered, and concentrated under vacuum. The crude was purified by column chromatography on silica gel (Ep/EtOAc starting from 6:1 to 2:1) to afford the title compound as a colourless oil (34%). ^{1}**H NMR** (300 MHz, $CDCl_3$) δ 8.10 (s, 2H), 7.45 – 7.31 (m, 5H), 5.31 (s, 2H).

*N-((Tetrahydro-2H-pyran-2-yl)oxy)-1H-pyrazole-4-carboxamide (72**b**)*: to a -10 °C cooled solution of compound **71** (46 mg, 0.41 mmol) in dry DMF (0.4 mL), HOBt (72 mg, 0.53 mmol), DIPEA (162 µL, 0.94 mmol), and EDC·HCl (102 mg, 0.53 mmol) were added. The reaction mixture was stirred for 30 minutes under N_2 atmosphere. After that, *O*-(tetrahydro-2*H*-pyran-2-yl)hydroxylamine (48 mg, 0.41 mmol) was added. Temperature was allowed to reach 25 °C, and the reaction mixture was stirred for 12 h under N_2 atmosphere. A saturated solution of NH_4Cl was added, and the mixture was extracted with EtOAc (3 x 10 mL). The collected organic layers were washed with a saturated solution of $NaHCO_3$ (1 x 10 mL), H_2O (1 x 10 mL), and a saturated solution of NaCl (1 x 10 mL), dried over Na_2SO_4, filtered, and concentrated under vacuum. The crude was purified by column chromatography on silica gel (DCM/MeOH starting from 20:1 to 10:1) to afford the title compound as a white solid (41% yield). ^{1}**H NMR** (300 MHz, CD_3OD) δ 8.05 (s, 2H), 5.00 (t, J = 3.0 Hz, 1H), 4.15 – 4.00 (m, 1H), 3.67 – 3.58 (m, 1H), 1.96 – 1.77 (m, 3H), 1.75 – 1.51 (m, 3H).

1H-Pyrazole-4-carbohydrazide (73): to a solution of compound **70** (200 mg, 1.43 mmol) in EtOH (8 mL), hydrazine monohydrate (444 µL, 14.27 mmol) was added. Temperature was increased to 82 °C, and the reaction mixture was stirred for 12 h. The solvent was removed under vacuum. Et_2O (3 x 10 mL) was added, and the solvent was removed under vacuum. The crude was used in the following step without any further purification (white solid) (66% yield). **ESI-MS** *m/z*: 127 $[M + H]^+$. **^{1}H NMR** (300 MHz, $(CD_3)_2SO$) δ 13.00 (s, 1H), 9.27 (s, 1H), 7.98 (s, 2H), 4.30 (s, 2H).

2-(Difluoromethyl)-5-(1H-pyrazol-4-yl)-1,3,4-oxadiazole (74): to a -10 °C cooled solution of compound **73** (106 mg, 0.84 mmol) in dry DMF (2 mL), DFAA (313 µL, 2.52 mmol) was added. Temperature was allowed to reach 25 °C, and the reaction mixture was stirred for 12 h under N_2 atmosphere. A saturated solution of $NaHCO_3$ was added, and the mixture was extracted with EtOAc (3 x 10 mL). The collected organic layers were washed with a saturated solution of NH_4Cl (2 x 10 mL), and a saturated solution of NaCl (1 x 10 mL), dried over Na_2SO_4, filtered, and concentrated under vacuum. The crude was used in the following step without any further purification (white solid) (45% yield). **^{1}H NMR** (300 MHz, $(CD_3)_2CO$) δ 8.36 (s, 1H), 7.32 (t, J = 51.7 Hz, 1H). **^{19}F NMR** (282 MHz, $(CD_3)_2CO$) δ -121.1, -121.3.

3-(Diphenylmethylene)azetidine (76): to a 0 °C cooled solution of **75** (1000 mg, 5.84 mmol) in dry THF (30 mL), benzophenone (1700 mg, 9.35 mmol), and Zn powder (1910 mg, 29.21 mmol) were added, and the reaction mixture was stirred for 15 minutes under N_2 atmosphere. After that, $TiCl_4$ (1.63 mL, 14.60 mmol) was added. Temperature was increase to 60 °C, and the reaction mixture was stirred for 12 h under N_2 atmosphere. A 1 N solution of HCl in H_2O was added, and the mixture was extracted with EtOAc (3 x 10 mL). The collected organic layers were dried over Na_2SO_4, filtered, and concentrated under vacuum. The crude was purified by column chromatography on silica gel ($DCM/MeOH/NH_4OH$ from 40:1:0.1 to 10:1:0.1) to afford the title compound as a yellowish solid (43% yield). **ESI-MS** *m/z*: 222 $[M + H]^+$. **^{1}H NMR** (400 MHz, $CDCl_3$) δ 7.37 – 7.32 (m, 4H), 7.31 – 7.23 (m, 2H), 7.21 – 7.11 (m, 4H), 4.57 (s, 4H).

tert-Butyl 3-(diphenylmethylene)azetidine-1-carboxylate (77): to a solution of **76** (558 mg, 2.52 mmol) in dry DCM (12 mL), TEA (703 µL, 5.04 mmol), and Boc_2O (605 mg, 2.77 mmol) were added, and the reaction mixture was stirred at 25 °C for 12 h under N_2 atmosphere. A saturated solution of $NaHCO_3$ was added, and the mixture was extracted with DCM (3 x 10 mL). The collected organic layers were dried over Na_2SO_4, filtered, and concentrated under vacuum. The crude was purified by column chromatography on silica gel (Ep/EtOAc starting from 30:1 to 10:1) to afford the title compound as a white solid (70% yield). **ESI-MS** *m/z*: 344 $[M + Na]^+$; 360 $[M + K]^+$. **^{1}H NMR** (400 MHz, $CDCl_3$) δ 7.40 – 7.34 (m, 4H), 7.33 – 7.27 (m, 2H), 7.23 – 7.15 (m, 4H), 4.75 (s, 5H), 1.51 (s, 9H).

tert-Butyl 3-benzhydrylazetidine-1-carboxylate (78): to a solution of **77** (874 mg, 2.72 mmol) in MeOH (55 mL), Pd/C (10% w/w) was added, and the reaction mixture was stirred at 25 °C for 12 h under H_2 atmosphere. The suspension was filtered, and the collected organic solution was concentrated in vacuum The crude was used in the following step without any further purification (91%) (white solid). **ESI-MS** *m/z*: $[M + Na]^+$ 344; $[M + K]^+$ 360. **^{1}H NMR** (400 MHz, $CDCl_3$) δ 7.34 – 7.26 (m, 5H), 7.25 – 7.17 (m, 5H), 4.13 (d, J = 11.8 Hz, 1H), 4.00 (dd, J = 8.9, 8.1 Hz, 2H), 3.65 (dd, J = 8.9, 5.6 Hz, 2H), 3.40 – 3.26 (m, 1H), 1.44 (s, 9H).

*3-Benzhydrylazetidine (**79**)*: to a solution of compound **78** (200 mg, 0.62 mmol) in MeOH (10 mL), a 1 N solution of HCl in MeOH (620 µL, 0.62 mmol) was added. Temperature was increased to 40 °C, and the reaction mixture was stirred for 2 h. Solvent was removed under vacuum. The crude was used in the following step without any further purification (99%) (white solid). **ESI-MS** *m*/*z*: 224 $[M - H]^+$.

*10,11-Dihydro-5H-dibenzo[a,d][7]annulen-5-ol (**81**)*: to a solution of **80** (300 mg, 1.44 mmol) in MeOH (10 mL), $NaBH_4$ (218 mg, 5.76 mmol) was added, and the reaction mixture was stirred at 25 °C for 1 h. The solvent was removed under vacuum. A saturated solution of $NaHCO_3$ was added, and the mixture was extracted with DCM (3 x 10 mL). The crude was used in the following step without any further purification (white solid) (94%). **^{1}H NMR** (400 MHz, $CDCl_3$) δ 7.53 – 7.43 (m, 2H), 7.34 – 7.09 (m, 6H), 5.98 (s, 1H), 3.53 – 3.40 (m, 2H), 3.21 – 3.08 (m, 2H), 2.32 (s, 1H).

*tert-Butyl 4-(10,11-dihydro-5H-dibenzo[a,d][7]annulen-5-yl)piperazine-1-carboxylate (**82**)*: to a solution of compound **81** (200 mg, 0.95 mmol) in a :mixture of pyridine (2 mL) and toluene (2 mL), $SOCl_2$ (972 µL, 13.32 mmol) was added, and the reaction mixture was stirred at 25 °C for 3 h. The solvent was removed under vacuum. The solid residue was dissolved in MeCN (6 mL), K_2CO_3 (197 mg, 1.42 mmol), and 1-Boc piperazine (265 mg, 1.42 mmol) were added. Temperature was increased to 85 °C, and the reaction mixture was stirred for 12 h. The solvent was removed under vacuum. A saturated solution of $NaHCO_3$ was added, and the mixture was extracted with EtOAc (3 x 10 mL). The crude was purified by column chromatography on silica gel (Ep/EtOAc starting from 50:1 to 10:1) to afford the title compound as a white solid (56% yield). **ESI-MS** *m*/*z*: 379 $[M + H]^+$; 401 $[M + Na]^+$. **^{1}H NMR** (400 MHz, $CDCl_3$) δ 7.22 – 7.00 (m, 8H), 4.09 – 3.94 (m, 3H), 3.35 (t, $J = 5.1$ Hz, 4H), 2.26 (t, $J = 4.9$ Hz, 4H), 1.46 (s, 8H).

*1-(10,11-Dihydro-5H-dibenzo[a,d][7]annulen-5-yl)piperazine (**83**)*: compound **83** was prepared according to procedure used for compound **79**, starting from compound **82** (300 mg, 0.79 mmol), and a 1 N solution of HCl in MeOH (790 µL, 0.79 mmol) in MeOH (18 mL). The crude was used in the following step without any further purification (yellow oil) (99% yield). **ESI-MS** *m*/*z*: 279 $[M + H]^+$. **^{1}H NMR** (400 MHz, $CDCl_3$) δ 7.21 – 7.02 (m, 8H), 4.07 – 3.98 (m, 2H), 3.96 (s, 1H), 2.86 – 2.74 (m, 6H), 2.29 (d, $J = 11.9$ Hz, 4H), 2.05 (s, 1H).

*tert-Butyl 4-(naphthalen-2-ylmethyl)piperazine-1-carboxylate (**85**)*: to a solution of **84** (200 mg, 0.90 mmol) in MeCN (7 mL), K_2CO_3 (250 mg, 1.81 mmol), and 1-Boc piperazine (337 mg, 1.81 mmol) were added. Temperature was increased to 85 °C, and the reaction mixture was stirred for 12 h. The solvent was removed under vacuum. A saturated solution of $NaHCO_3$ was added, and the mixture was extracted with DCM (3 x 10 mL). The crude was purified by column chromatography on silica gel (Ep/EtOAc starting from 10:1 to 3:1) to afford the title compound as a yellow oil (69%). **ESI-MS** m/z: 337 $[M + H]^+$; 349 $[M + Na]^+$.**^{1}H NMR** (400 MHz, $CDCl_3$) δ 7.86 – 7.77 (m, 3H), 7.73 (s, 1H), 7.53 – 7.41 (m, 3H), 3.66 (s, 2H), 3.45 (t, $J = 5.0$ Hz, 4H), 2.43 (t, $J = 5.0$ Hz, 4H), 1.46 (s, 9H).

*1-(Naphthalen-2-ylmethyl)piperazine(**86**)*: compound **86** was prepared according to procedure used for compound **79**, starting from compound **85** (203 mg, 0.90 mmol), and a 1 N solution of HCl in MeOH (900 µL, 0.90 mmol) in MeOH (20 mL). The crude was used in the following step without any further purification (white solid) (99% yield). **^{1}H NMR** (400 MHz, $CDCl_3$) δ 7.85 – 7.76 (m, 2H), 7.73 (s, 1H), 7.53 – 7.40 (m, 2H), 3.64 (s, 2H), 2.89 (t, J = 4.9 Hz, 4H), 2.49 – 2.42 (m, 4H), 1.96 (s, 1H).

*1-Benzhydrylpiperazine (**88**)*: to a solution of piperazine (700 mg, 8.13 mmol) in MeCN (15 mL), K_2CO_3 (560 mg, 4.05 mmol) and NaI (120 mg, 0.80 mmol) were added. Temperature was increased to 85 °C, and the reaction mixture was stirred until all the solids were dissolved. After that, compound **87** (1000 mg, 4.05 mmol) was added, and the reaction mixture was stirred for 12 hours. H_2O was added, and the mixture was extracted with DCM (3 x 10 mL). The collected organic layers were dried over Na_2SO_4, filtered, and concentrated under vacuum. The crude was purified by column chromatography on silica gel (DCM/MeOH isocratic 10:1) to afford the title compound as a yellow solid (64% yield). **^{1}H NMR** (300 MHz, $CDCl_3$) δ 7.44 – 7.36 (m, 4H), 7.31 – 7.22 (m, 4H), 7.20 – 7.13 (m, 2H), 4.21 (s, 1H), 2.90 (t, J = 4.9 Hz, 4H), 2.43 – 2.31 (m, 4H).

*Benzyl 1-(4-benzhydrylpiperazine-1-carbonyl)-1H-pyrazole-4-carboxylate (**89a**)*: to a solution of 1*H*-1,2,4-triazole (401 mg, 1.98 mmol) in dry DCM (3.4 mL), DMAP (68 mg, 0.56 mmol), and a 20% w/w solution of phosgene in toluene (1.05 mL, 1.98 mmol) were added. The reaction mixture was stirred at 25 °C for 30 minutes under N_2 atmosphere. After that, compound **72a** (250 mg, 0.99 mmol) was added, and the reaction mixture was stirred at 25 °C for 12 h under N_2 atmosphere. H_2O was added, and the mixture was extracted with DCM (3 x 10 mL). The collected organic layers were dried over Na_2SO_4, filtered, and concentrated under vacuum. The crude was purified by flash chromatography on silica gel (Ep-EtOAc 0-30%) to afford the title compound as colourless oil (44% yield). **ESI-MS** *m*/*z*: 481 $[M + H]^+$. **^{1}H NMR** (300 MHz, $CDCl_3$) δ 8.58 (s, 1H), 7.98 (s, 1H), 7.47 – 7.33 (m, 9H), 7.29 (t, J = 7.7 Hz, 4H), 7.24 – 7.16 (m, 2H), 5.30 (s, 2H), 4.29 (s, 1H), 3.85 (s, 4H), 2.50 (t, J = 4.9 Hz, 4H).

*1-(4-Benzhydrylpiperazine-1-carbonyl)-N-((tetrahydro-2H-pyran-2-yl)oxy)-1H-pyrazole-4-carboxamide (**89b**)*: compound **87** was dissolved (86 mg, 0.34 mmol) in a mixture of DCM (6 mL) and a saturated solution of $NaHCO_3$ (2 mL). Temperature was cooled to 0 °C, a 20% w/w solution of phosgene in toluene (358 µL, 0.68 mmol) was added inside the organic phase, and the reaction mixture was stirred for 30 minutes. After collecting the organic phase, the aqueous phase was extracted with DCM (3 x 10 mL). The collected organic layers were dried over Na_2SO_4, filtered, and concentrated under vacuum. The crude was dissolved in dry Py (1 mL) and added to a preformed solution of compound **72b** (50 mg, 0.23 mmol), and DMAP (3 mg, 0.02 mmol) in dry Py (1 mL). The reaction mixture was stirred at 25 °C for 12 h under N_2 atmosphere. The solvent was removed under N_2 stream. The oily residue was taken up with toluene (2 x 5 mL), and the solvent was removed under N_2 stream. The crude was purified by column chromatography on silica gel (DMC/MeOH starting from 100:1 to 50:1) to afford the title compound as a white solid (30% yield). **ESI-MS** *m*/*z*: 490 $[M + H]^+$, 512 $[M + Na]^+$. **^{1}H NMR** (400 MHz, $CDCl_3$) δ 8.70 (s, 1H), 8.51 (s, 1H), 7.93 (s, 1H), 7.43 – 7.35 (m, 4H), 7.31 – 7.22 (m, 4H), 7.21 – 7.13 (m, 2H), 4.96 (s, 1H), 4.25 (s, 1H), 3.93 (t, J = 10.3 Hz, 1H), 3.85 – 3.81 (m, 4H), 3.67 – 3.58 (m, 1H), 2.48 (t, J = 5.2 Hz, 4H), 1.81 (s, 3H), 1.60 – 1.55 (m, 3H).

*1-(3-Benzhydrylazetidine-1-carbonyl)-N-((tetrahydro-2H-pyran-2-yl)oxy)-1H-pyrazole-4-carboxamide (**90**)*: compound **90** was prepared according to a two steps procedure used for compound **89b**, starting from compound **79** (140 mg, 0.62 mmol), and a 20% w/w solution of phosgene in toluene (663 µL, 1.25 mmol) in a mixture of DCM (11 mL) and a saturated solution of $NaHCO_3$ (3 mL) in the first step, then compound **72b** (88 mg, 0.42 mmol), and DMAP (5 mg, 0.04 mmol) in dry Py (5 mL). The crude was purified by column chromatography on silica gel (Ep/EtOAc starting from 5:1 to 1:1) to afford the title compound as a colourless oil (26% yield). **ESI-MS** *m*/*z*: 461 $[M + H]^+$; 483 $[M + Na]^+$. **^{1}H NMR** (400 MHz, $CDCl_3$) δ 8.74 (s, 1H), 7.98 (s, 1H), 7.36 – 7.27 (m, 7H), 7.27 – 7.15 (m, 7H), 5.01 (s, 1H), 4.76 (t, *J* = 9.5 Hz, 1H), 4.38 (dd, *J* = 10.8, 5.9 Hz, 1H), 4.30 (t, *J* = 9.3 Hz, 1H), 4.20 (d, *J* = 11.8 Hz, 1H), 4.03 – 3.92 (m, 2H), 3.68 – 3.60 (m, 1H), 3.53 (dtt, *J* = 11.6, 8.3, 5.8 Hz, 1H), 1.81 (s, 3H), 1.71 – 1.52 (m, 7H).

*1-(4-(10,11-Dihydro-5H-dibenzo[a,d][7]annulen-5-yl)piperazine-1-carbonyl)-N-((tetrahydro-2H-pyran-2-yl)oxy)-1H-pyrazole-4-carboxamide (**91a**)*: compound **91a** was prepared according to a two steps procedure used for compound **89b**, starting from compound **83** (224 mg, 0.80 mmol), and a 20% w/w solution of phosgene in toluene (851 µL, 1.61 mmol) in a mixture of DCM (14 mL) and a saturated solution of $NaHCO_3$ (3.5 mL) in the first step, then compound **72b** (115 mg, 0.54 mmol), and DMAP (7 mg, 0.05 mmol) in dry Py (4 mL). The crude was purified by column chromatography on silica gel (Ep/EtOAc starting from 7:1 to 1:1) to afford the title compound as a colourless oil (24% yield). **ESI-MS** *m*/*z*: 538 $[M + Na]^+$. **^{1}H NMR** (400 MHz, $CDCl_3$) δ 8.59 (s, 1H), 7.99 (s, 1H), 7.21 – 7.03 (m, 8H), 5.29 (s, 1H), 4.99 (s, 1H), 4.05 – 3.91 (m, 3H), 3.75 (s, 4H), 3.66 – 3.56 (m, 1H), 2.89 – 2.75 (m, 2H), 2.40 (t, *J* = 4.9 Hz, 4H), 1.89 – 1.77 (m, 3H), 1.68 – 1.51 (m, 3H).

*1-(4-(Naphthalen-2-ylmethyl)piperazine-1-carbonyl)-N-((tetrahydro-2H-pyran-2-yl)oxy)-1H-pyrazole-4-carboxamide (**91b**)*: compound **91b** was prepared according to a two steps procedure used for compound **89b**, starting from compound **84** (137 mg, 0.61 mmol), and a 20% w/w solution of phosgene in toluene (640 µL, 1.21 mmol) in a mixture of DCM (11 mL) and a saturated solution of $NaHCO_3$ (3 mL) in the first step, then compound **72b** (85 mg, 0.40 mmol), and DMAP (5 mg, 0.04 mmol) in dry Py (3 mL). The crude was purified by column chromatography on silica gel (DMC/MeOH starting from 100:1 to 50:1) to afford the title compound as a colourless oil (28 % yield). **ESI-MS** *m*/*z*: 464 $[M + H]^+$. ^{1}H NMR (400 MHz, $CDCl_3$) δ 8.60 (s, 1H), 8.02 (s, 1H), 7.84 – 7.79 (m, 3H), 7.73 (s, 1H), 7.51 – 7.42 (m, 3H), 5.00 (s, 1H), 4.03 – 3.93 (m, 1H), 3.90 – 3.77 (m, 5H), 3.66 – 3.58 (m, 1H), 2.59 (t, *J* = 5.0 Hz, 4H), 1.60 (qd, *J* = 9.6, 6.1, 4.5 Hz, 3H), 1.35 – 1.21 (m, 3H).

*1-(4-benzylpiperazine-1-carbonyl)-N-((tetrahydro-2H-pyran-2-yl)oxy)-1H-pyrazole-4-carboxamide (**91c**)*: compound **91c** was prepared according to a two steps procedure used for compound **89b**, starting from 1-benzylpiperazine (116 mg, 0.66 mmol), and a 20% w/w solution of phosgene in toluene (696 µL, 1.32 mmol) in a mixture of DCM (13 mL) and a saturated solution of $NaHCO_3$ (3 mL) in the first step, then compound **72b** (93 mg, 0.44 mmol), and DMAP (5 mg, 0.04 mmol) in dry Py (3 mL). The crude was purified by column chromatography on silica gel (DCM/MeOH starting from 20:1 to 10:1) to afford the title compound as a white solid (59% yield). **ESI-MS** *m*/*z*: 414 $[M + H]^+$. **^{1}H NMR** (300 MHz, $CDCl_3$) δ 8.98 (s, 1H), 8.57 (s, 1H), 8.01 (s, 1H), 7.38 – 7.22 (m, 5H), 5.06 – 4.93 (m, 1H), 4.03 – 3.92 (m, 1H), 3.91 – 3.76 (m, 4H), 3.70 – 3.60 (m, 1H), 3.55 (s, 2H), 2.55 (t, *J* = 5.0 Hz, 4H), 1.89 – 1.78 (m, 3H), 1.71 – 1.53 (m, 3H).

*tert-Butyl 4-(1H-1,2,4-triazole-1-carbonyl)piperazine-1-carboxylate (**93a**)*: compound **93a** was prepared according to procedure used for compound **89a**, starting from compound 1*H*-1,2,4-triazole (100 mg, 1.45 mmol), DMAP (354 mg, 2.90 mmol), a 20% w/w solution of phosgene in toluene (765 µL, 1.45 mmol), and 1-Boc-piperazine (135 mg, 0.73 mmol) in dry DCM (5 mL). The crude was purified by column chromatography on silica gel ($CHCl_3$/MeOH 20:1) to afford the title compound as a white solid (90% yield). **ESI-MS** *m*/*z*: 282 $[M + H]^+$. **^{1}H NMR** (300 MHz, $CDCl_3$) δ 8.80 (s, 1H), 8.00 (s, 1H), 3.98 – 3.73 (m, 4H), 3.61 – 3.52 (m, 5H), 1.48 (s, 9H).

*tert-Butyl 4-(1H-pyrazole-1-carbonyl)piperazine-1-carboxylate (**93b**)*: compound **93b** was prepared according to procedure used for compound **89a**, starting from pyrazole (219 mg, 3.22 mmol), DMAP (787 mg, 6.44 mmol), a 20% w/w solution of phosgene in toluene (1.70 mL, 3.22 mmol), and 1-Boc-piperazine (300 mg, 1.61 mmol). The crude was purified by column chromatography on silica gel (Hex/EtOAc starting from 8:1 to 4:1) to afford the title compound as white solid (77% yield). **ESI-MS** *m*/*z*: 281 $[M + H]^+$. **^{1}H NMR** (300 MHz, $CDCl_3$) δ 8.15 – 8.11 (m, 1H), 7.66 – 7.62 (m, 1H), 6.38 – 6.34 (m, 1H), 3.92 – 3.74 (m, 4H), 3.63 – 3.47 (m, 4H), 1.47 (s, 9H).

*tert-Butyl 4-(4-cyano-1H-pyrazole-1-carbonyl)piperazine-1-carboxylate (**93c**)*: compound **93c** was prepared according to procedure used for compound **89a**, starting from 1-Boc piperazine (600 mg, 3.22 mmol), DMAP (787 mg, 6.45 mmol), a 20% w/w solution of phosgene in toluene (1.70 mL, 3,22 mmol), and 1*H*-pyrazole-4-carbonitrile (150 mg, 1.61 mmol). The crude was purified by column chromatography on silica gel (Hex/EtOAc starting from 10:1 to 3:1) to afford the title compound as white solid (43% yield). **ESI-MS** *m*/*z*: 328 $[M + Na]^+$. **^{1}H NMR** (300 MHz, $CDCl_3$) δ 8.54 (s, 1H), 7.88 (s, 1H), 3.94 – 3.67 (m, 4H), 3.60 – 3.51 (m, 4H), 1.47 (s, 9H).

*4-Methylbenzohydrazide (**95**)*: to a solution of **94** (300 mg, 2.20 mmol) in EtOH (13 mL), concentrated H_2SO_4 (118 µL, 2.20 mmol) was added. Temperature was increased to 82°C, and the reaction mixture was stirred for 12 h. After cooling down to 25 °C, solid $NaHCO_3$ was added, and the solvent was removed under vacuum. The solid residue was taken up with DCM, a saturated solution of $NaHCO_3$ was added, and the mixture was extracted with DCM (3 x 10 mL). The collected organic layers were dried over Na_2SO_4, filtered, and concentrated under vacuum. The resulting oil was diluted in EtOH (13 mL), and hydrazine monohydrate (1.07 mL, 22 mmol) was added. Temperature was increased to 82 °C, and the reaction mixture was stirred for 12 h. After cooling down to 25 °C, the solvent was removed under vacuum. A saturated solution of $NaHCO_3$ was added, and the mixture was extracted with DCM (3 x 10 mL). The collected organic layers were dried over Na_2SO_4, filtered, and concentrated under vacuum. The crude was purified by column chromatography on silica gel (DCM/MeOH starting from 100:1 to 20:1) to afford the title compound as a white solid (62% yield). **ESI-MS** *m*/*z*: 151 $[M + H]^+$. **^{1}H NMR** (300 MHz, $(CD_3)_2CO$) δ 9.67 (s, 1H), 7.78 (d, J = 8.2 Hz, 2H), 7.25 (d, J = 7.8 Hz, 2H), 2.93 (s, 2H), 2.37 (s, 3H).

*2-(Difluoromethyl)-5-(p-tolyl)-1,3,4-oxadiazole (**96**)*: compound **96** was prepared according to procedure used for compound **74**, starting from **84** (413 mg, 2.75 mmol), and DFAA (1.03 mL, 8.25 mmol) in dry DMF (5 mL). The crude was purified by column chromatography on silica gel (Hex/EtOAc 100:1 to 30:1) to afford the title compound as a white solid (34% yield). **ESI-MS** *m*/*z*: 211 $[M + \mathrm{H}]^+$. **^{1}H NMR** (300 MHz, $CDCl_3$) δ 7.99 (d, J = 8.2 Hz, 2H), 7.34 (d, J = 7.9 Hz, 2H), 6.90 (t, J = 51.8 Hz, 1H), 2.44 (s, 3H). **^{19}F NMR** (282 MHz, $CDCl_3$) δ -119.1, -119.3.

*2-(4-(Bromomethyl)phenyl)-5-(difluoromethyl)-1,3,4-oxadiazole (**97**)*: to a solution of compound **96** (276 mg, 1.31 mmol) in dry MeCN (2 mL), AIBN (22 mg, 0.13 mmol), and NBS (257 mg,1.44 mmol) were added. Temperature was increased to 85°C, and the reaction mixture was stirred for 12 h under N_2 atmosphere. A saturated solution of $NaHCO_3$ was added, and the mixture was extracted with DCM (3 x 10 mL). The collected organic layers were dried over Na_2SO_4, filtered, and concentrated under vacuum. The crude was purified by column chromatography on silica gel (Ep/EtOAc starting from 80:1 to 20:1) to afford the title compound as a white solid (54% yield). **^{1}H NMR** (300 MHz, $CDCl_3$) δ 8.10 (d, J = 8.3 Hz, 2H), 7.57 (d, J = 8.4 Hz, 2H), 6.92 (t, J = 51.7 Hz, 1H), 4.53 (s, 2H). **^{19}F NMR** (282 MHz, $CDCl_3$) δ -119.1, -119.3.

*4-(Bromomethyl)-N-((tetrahydro-2H-pyran-2-yl)oxy)benzamide (**99**)*: to a solution of 4-(bromomethyl)benzoic acid **98** (200 mg, 0.93 mmol) in a mixture of dry DCM (6 mL) and dry DMF (700 µL), EDC·HCl (215 mg, 1.12 mmol), and *O*-(tetrahydro-2*H*-pyran-2-yl)hydroxylamine (109 mg, 0.93 mmol) were added. The reaction mixture was stirred at 25 °C for 12 h under N_2 atmosphere. The solvent was removed under vacuum. A saturated solution of NH_4Cl was added, and the mixture was extracted with EtOAc (3 x 10 mL). The collected organic layers were washed with H_2O (1 x 10 mL), and a saturated solution of NaCl (1 x 10 mL), dried over Na_2SO_4, filtered, and concentrated under vacuum. The crude was purified by column chromatography on silica gel (Ep/EtOAc starting from 3:1 to 2:1) to afford the title compound as a white solid (55% yield). **^{1}H NMR** (300 MHz, $CDCl_3$) δ 8.77 (s, 1H), 7.75 (d, J = 8.3 Hz, 2H), 7.46 (d, J = 8.3 Hz, 2H), 5.07 (t, J = 3.3 Hz, 1H), 4.06 – 3.93 (m, 1H), 3.72 – 3.61 (m, 1H), 1.96 – 1.80 (m, 3H), 1.72 – 1.60 (m, 3H).

*4-(4-(1H-1,2,4-Triazole-1-carbonyl)piperazine-1-carbonyl)-N-((tetrahydro-2H-pyran-2-yl)oxy)benzamide (**100a**)*: to a solution of compound **93a** (149 mg, 0.53 mmol) in MeOH (10 mL), a 1 N solution of HCl in MeOH (530 µL, 0.53 mmol) was added. Temperature was increased to 40 °C, and the reaction mixture was stirred for 2 h. The solvent was removed under vacuum. After suspending the crude in MeCN (5 mL), TEA (251 µL, 1.80 mmol), and compound **99** (116 mg, 0.36 mmol) were added. The temperature was increased to 85 °C, and the reaction mixture was stirred for 12 h. A saturated solution of $NaHCO_3$ was added, and the mixture was extracted with DCM (3 x 10 mL). The collected organic layers were dried over Na_2SO_4, filtered, and concentrated under vacuum. The crude was purified by column chromatography on silica gel ($CHCl_3$/MeOH starting from 80:1 to 60:1) to afford the title compound as a colourless oil (58% yield). **ESI-MS** *m*/*z*: 437 $[M + \mathrm{Na}]^+$. **^{1}H NMR** (300 MHz, $CDCl_3$) δ 9.15 (s, 1H), 8.76 (s, 1H), 7.96 (s, 1H), 7.72 (d, J = 8.0 Hz, 2H), 7.38 (d, J = 7.9 Hz, 2H), 5.06 (t, J = 2.9 Hz, 1H), 4.05 – 3.93 (m, 1H), 3.92 – 3.72 (m, 4H), 3.67 – 3.59 (m, 1H), 3.57 (s, 2H), 2.53 (t, J = 5.1 Hz, 4H), 1.91 – 1.76 (m, 3H), 1.68 – 1.53 (m, 3H).

*4-((4-(1H-Pyrazole-1-carbonyl)piperazin-1-yl)methyl)-N-((tetrahydro-2H-pyran-2-yl)oxy)benzamide (**100b**)*: compound **100b** was prepared according to a two steps procedure used for compound **100a**, starting from **93b** (263 mg, 0.94 mmol), and a 1 N solution of HCl in MeOH (940 µL, 0.94 mmol) in MeOH (18 mL) in the first step, then TEA (446 µL, 3.20 mmol), and compound **99** (200 mg, 0.64 mmol) in MeCN (4.80 mL). The crude was purified by column chromatography on silica gel (DCM/ MEOH starting from 70:1 to 50:1) to afford the title compound as a white solid (56% yield). **ESI-MS** *m*/*z*: 414 $[M + H]^+$. **^{1}H NMR** (300 MHz, $CDCl_3$) δ 9.13 (s, 1H), 8.11 – 8.07 (m, 1H), 7.71 (d, J = 7.9 Hz, 2H), 7.64 – 7.59 (m, 1H), 7.38 (d, J = 7.9 Hz, 2H), 6.37 – 6.30 (m, 1H), 5.11 – 5.01 (m, 1H), 4.07 – 3.94 (m, 1H), 3.92 – 3.78 (m, 4H), 3.69 – 3.59 (m, 1H), 3.56 (s, 2H), 2.51 (t, J = 5.0 Hz, 4H), 1.90 – 1.78 (m, 3H), 1.60 (h, J = 6.0, 5.1 Hz, 3H).

*4-((4-(4-Cyano-1H-pyrazole-1-carbonyl)piperazin-1-yl)methyl)-N-((tetrahydro-2H-pyran-2-yl)oxy)benzamide (**100c**)*: compound **100c** was prepared according to a two steps procedure used for compound **100a**, starting from **93c** (721 mg, 2.36 mmol), and a 1 N solution of HCl in MeOH (2.36 mL, 2.36 mmol) in MeOH (45 mL) in the first step, then TEA (1.11 mL, 7.96 mmol), and compound **99** (500 mg, 1.59 mmol) in MeCN (12 mL). The crude was purified by column chromatography on silica gel (DCM/MeOH starting from 80:1 to 50:1) to afford the title compound as a white solid (45% yield). **ESI-MS** *m*/*z*: 439 $[M + H]^+$; 461 $[M + Na]^+$. **^{1}H NMR** (300 MHz, $CDCl_3$) δ 9.18 (s, 1H), 8.51 (s, 1H), 7.85 (s, 1H), 7.72 (d, J = 8.0 Hz, 2H), 7.37 (d, J = 8.0 Hz, 2H), 5.05 (t, J = 2.7 Hz, 1H), 4.03 – 3.94 (m, 1H), 3.82 (s, 4H), 3.66 – 3.59 (m, 1H), 3.57 (s, 2H), 2.52 (t, J = 5.0 Hz, 4H), 1.90 – 1.76 (m, 3H), 1.59 (p, J = 7.8, 5.9 Hz, 3H).

*(4-Benzhydrylpiperazin-1-yl)(1H-1,2,4-triazol-1-yl)methanone (**69a, AKU-005**)*: compound **69b** was prepared according to procedure used for compound **89a**, starting from 1*H*-1,2,4-triazole (19 mg, 0.28 mmol), DMAP (68 mg, 0.56 mmol), a 20% w/w solution of phosgene in toluene (147 µL, 0.28 mmol), and compound **77** (35 mg, 0.14 mmol) in dry DCM (1 mL). The crude was purified by column chromatography on silica gel ($CHCl_3$/MeOH 20:1) to afford the title compound as a white solid (90% yield). **ESI-MS** *m*/*z*: 348 $[M + H]^+$. Spectroscopic data are in line with those reported in literature.[57]

*(4-Benzhydrylpiperazin-1-yl)(1H-pyrazol-1-yl)methanone (**69b**)*: compound **69b** was prepared according to procedure used for compound **89a**, starting from pyrazole (14 mg, 0.20 mmol), DMAP (50 mg, 0.40 mmol), a 20% w/w solution of phosgene in toluene (109 µL, 0.20 mmol) and compound **77** (26 mg, 0.10 mmol) in dry DCM (1 mL). The crude was purified by column chromatography on silica gel (Ep/EtOAc starting from 8:1 to 6:1) to afford the title compound as a colourless oil (40% yield). **ESI-MS** *m*/*z*: 347 $[M + H]^+$; 369 $[M + Na]^+$. **^{1}H NMR** (400 MHz, $CDCl_3$) δ 8.10 – 8.05 (m, 1H), 7.60 – 7.55 (m, 1H), 7.44 – 7.37 (m, 5H), 7.31 – 7.23 (m, 5H), 7.23 – 7.13 (m, 2H), 6.31 – 6.31 (m, 1H), 4.26 (s, 1H), 3.88 – 3.84 (m, 5H), 2.49 (t, J = 5.0 Hz, 5H). **^{13}C NMR** (101 MHz, $CDCl_3$) δ 151.0, 142.1, 141.7, 131.8, 128.6, 127.9, 127.9, 127.2, 107.1, 76.0, 51.8.

Ethyl 1-(4-benzhydrylpiperazine-1-carbonyl)-1H-pyrazole-4-carboxylate (***69c***): compound **69c** was prepared according to procedure used for compound **89a**, starting from compound **70** (28 mg, 0.20 mmol), DMAP (49 mg, 0.40 mmol), a 20% w/w solution of phosgene in toluene (105 µL, 0.20 mmol), and compound **77** (25 mg, 0.10 mmol) in dry DCM (3 mL). The crude was purified by column chromatography on silica gel ($CHCl_3$/MeOH isocratic 100:1) to afford the title compound as a white solid (41% yield). **ESI-MS** *m*/*z*: 419 [*M* + H]$^+$. **^{1}H NMR** (300 MHz, $CDCl_3$) δ 8.53 (s, 1H), 7.93 (s, 1H), 7.45 – 7.36 (m, 4H), 7.32 – 7.24 (m, 4H), 7.22 – 7.14 (m, 2H), 4.38 – 4.23 (m, 3H), 3.93 – 3.75 (m, 4H), 2.49 (t, *J* = 5.0 Hz, 4H), 1.33 (t, *J* = 7.1 Hz, 3H). **^{13}C NMR** (75 MHz, $CDCl_3$) δ 162.4, 150.1, 142.1, 135.4, 128.8, 128.0, 127.4, 116.6, 60.8, 51.8, 14.4.

1-(4-Benzhydrylpiperazine-1-carbonyl)-1H-pyrazole-4-carboxamide (***69d***): compound **69d** was prepared according to procedure used for compound **89a**, starting from 1*H*-pyrazole-4-carboxamide (44 mg, 0.40 mmol), DMAP (98 mg, 0.80 mmol), a 20% w/w solution of phosgene in toluene (203 µL, 0.40 mmol), and compound **77** (50 mg, 0.20 mmol) in dry DCM (6 mL). The crude was purified by column chromatography on silica gel (Ep/EtOAc starting from 8:1 to 7:1) to afford the title compound as a colourless oil (20% yield). **ESI-MS** *m*/*z*: 390 [*M* + H]$^+$. **^{1}H NMR** (300 MHz, $(CD_3)_2CO$) δ 8.80 (s, 1H), 8.12 (s, 1H), 7.55 – 7.46 (m, 4H), 7.31 (t, *J* = 7.5 Hz, 4H), 7.23 – 7.17 (m, 2H), 4.40 (s, 1H), 3.87 – 3.72 (m, 4H), 2.50 (t, *J* = 5.0 Hz, 4H). **^{13}C NMR** (75 MHz, $(CD_3)_2CO$) δ 150.0, 143.75, 143.5, 138.9, 129.5, 128.8, 128.0, 113.3, 94.9, 76.5, 52.5.

1-(4-Benzhydrylpiperazine-1-carbonyl)-1H-pyrazole-4-carbonitrile (***69e***): compound **69e** was prepared according to procedure used for compound **89b**, starting from compound **77** (50 mg, 0.20 mmol), and a 20% w/w solution of phosgene in toluene (214 µL, 0.40 mmol) in a mixture of DCM (4 mL) and a saturated solution of $NaHCO_3$ (1 mL) in the first step, then 1*H*-pyrazole-4-carbonitrile (16 mg, 0.17 mmol), and DMAP (2 mg, 0.02 mmol) in dry Py (2 mL). The crude was purified by column chromatography on silica gel (Ep/EtOAc starting from 8:1 to 6:1) to afford the title compound as a white solid (30% yield). **ESI-MS** *m*/*z*: 372 [*M* + H]$^+$. **^{1}H NMR** (300 MHz, $CDCl_3$) δ 8.50 (s, 1H), 7.82 (s, 1H), 7.46 – 7.39 (m, 4H), 7.29 (dd, *J* = 8.2, 6.5 Hz, 4H), 7.24 – 7.16 (m, 2H), 4.29 (s, 1H), 3.96 – 3.73 (m, 4H), 2.51 (t, *J* = 5.0 Hz, 4H). **^{13}C NMR** (75 MHz, $CDCl_3$) δ 149.0, 142.8, 141.9, 137.6, 128.8, 128.0, 127.4, 112.4, 94.5, 76.0, 51.7, 31.0.

1-(4-Benzhydrylpiperazine-1-carbonyl)-1H-pyrazole-4-carboxylic acid (***69f***): compound **69f** was prepared according to procedure used for compound **78**, starting from compound **89a** (208 mg, 0.43 mmol) in a mixture of MeOH (12 mL) and EtOAc (6 mL). The crude was purified by column chromatography on silica gel (DCM/MeOH starting from 30:1 to 10:1) to afford the title compound as white solid (16% yield)). **ESI-MS** m/z: 391 [*M* + H]$^+$; 413 [*M* + Na]$^+$; 389 [*M* – H]$^-$; 391 [*M* + Cl$^-$]; **^{1}H NMR** (400 MHz, $CDCl_3$) δ 8.60 (s, 1H), 7.97 (s, 1H), 7.45 – 7.36 (m, 4H), 7.32 – 7.23 (m, 4H), 7.22 – 7.14 (m, 2H), 4.27 (s, 1H), 3.91 – 3.79 (m, 4H), 2.50 (t, *J* = 4.9 Hz, 4H). **^{13}C NMR** (101 MHz, $CDCl_3$) δ 167.1, 149.8, 142.5, 141.8, 136.2, 128.7, 127.9, 127.3, 76.0, 51.7, 29.7.

*(4-benzhydrylpiperazin-1-yl)(4-(5-(difluoromethyl)-1,3,4-oxadiazol-2-yl)-1H-pyrazol-1-yl)methanone (**69g**)*: compound **69g** was prepared according to procedure used for compound **89a**, starting from compound **73** (35 mg, 0.19 mmol), DMAP (46 mg, 0.38 mmol), a 20% w/w solution of phosgene in toluene (100 µL, 0.19 mmol), and compound **77** (24 mg, 0.06 mmol). The crude was purified by column chromatography on silica gel (Ep/EtOAc starting from 10:1 to 5:1) to afford the title compound as colourless oil (60% yield). **ESI-MS** *m*/*z*: 465 $[M + H]^+$. **^{1}H NMR** (300 MHz, $CDCl_3$) δ 8.74 (s, 1H), 8.14 (s, 1H), 7.46 – 7.40 (m, 4H), 7.33 – 7.25 (m, 4H), 7.24 – 7.16 (m, 2H), 6.88 (t, J = 51.7 Hz, 1H), 4.30 (s, 1H), 4.00 – 3.77 (m, 4H), 2.53 (t, J = 5.0 Hz, 4H). **^{13}C NMR** (101 MHz, $CDCl_3$) δ 160.6, 157.6, 149.4, 141.9, 140.0, 132.9, 128.7, 127.8, 127.3, 107.3, 105.7, 76.0, 51.7. **^{19}F NMR** (282 MHz, $CDCl_3$) δ -119.1, -119.3.

*1-(4-Benzhydrylpiperazine-1-carbonyl)-N-hydroxy-1H-pyrazole-4-carboxamide (**69h**)*: to a 0 °C cooled solution of compound **69b** (168 mg, 0.34 mmol) in MeOH (13.6 mL) a 1 N solution of HCl in MeOH (13.6 mL, 13.6 mmol) was added, and the reaction mixture was stirred for 30 minutes. A solution 0.1 N of KOH in MeOH was added to adjust pH = 7, and the solvent was removed under vacuum. The crude was purified by column chromatography on silica gel (DCM/MeOH starting from 30:1 to 10:1, then DCM/MeOH/NH_4OH 10:1:0.1) to afford the title compound as an orange solid (53% yield). **ESI-MS** *m*/*z*: 406 $[M + H]^+$; 428 $[M + Na]^+$; 404 $[M – H]^-$; 440 $[M + Cl]^-$. **^{1}H NMR** (400 MHz, $(CD_3)_2SO$) δ 8.51 (s, 1H), 7.99 (s, 1H), 7.44 (d, J = 7.1 Hz, 4H), 7.31 (t, J = 7.5 Hz, 4H), 7.21 (t, J = 7.3 Hz, 2H), 4.40 (s, 1H), 3.71 (s, 4H), 2.41 (t, J = 4.8 Hz, 4H). **^{13}C NMR** (400 MHz, $(CD_3)_2SO$) δ 159.3, 150.2, 142.7, 141.0, 132.3, 129.0, 128.1, 127.4, 117.7, 75.0, 51.6.

*1-(3-Benzhydrylazetidine-1-carbonyl)-N-hydroxy-1H-pyrazole-4-carboxamide (**69i**)*: compound **69i** was prepared according to procedure used for compound **69h**, starting from compound **90** (49 mg, 0.11 mmol), and 1 N solution of HCl in MeOH (4.4 mL, 4.4 mmol) in MeOH (4.4 mL). The crude was purified by column chromatography on silica gel (DCM/MeOH starting from 40:1 to 10:1) to afford the title compound as white solid (82% yield). **ESI-MS** *m*/*z*: 376 $[M + H]^+$; 399 $[M + Na^+]^+$; 414 $[M + K^+]^+$; 374 $[M + H^-]^-$; 411 $[M + Cl^-]^-$. **^{1}H NMR** (400 MHz, $(CD_3)_2SO$) δ 11.04 (s, 1H), 9.08 (s, 1H), 8.64 (s, 1H), 8.01 (s, 1H), 7.38 – 7.26 (m, 8H), 7.24 – 7.14 (m, 2H), 4.57 (t, J = 9.0 Hz, 1H), 4.34 (d, J = 11.8 Hz, 1H), 4.19 – 4.09 (m, 2H), 3.78 – 3.70 (m, 1H), 3.68 – 3.53 (m, 1H). **^{13}C NMR** (101 MHz, $(CD_3)_2SO$) δ 159.4, 149.1, 143.1, 142.2, 129.9, 129.0, 128.2, 126.9, 117.6, 59.5, 55.3, 53.7, 33.6.

*1-(4-(10,11-Dihydro-5H-dibenzo[a,d][7]annulen-5-yl)piperazine-1-carbonyl)-N-hydroxy-1H-pyrazole-4-carboxamide (**69j**)*: compound **69j** was prepared according to procedure used for compound **69h**, starting from compound **91a** (65 mg, 0.13 mmol), and 1 N solution of HCl in MeOH (5.2 mL, 5.2 mmol) in MeOH (5.2 mL). The crude was purified by column chromatography on silica gel (DCM/MeOH starting from 40:1 to 10:1) to afford the title compound as white solid (54% yield). **ESI-MS** *m*/*z*: 454 $[M + Na]^+$; 430 $[M + H]^-$; 466 $[M + Cl]^-$.**^{1}H NMR** (400 MHz, $CD_3)_2SO$) δ 11.04 (s, 1H), 9.07 (s, 1H), 8.54 (s, 1H), 8.02 (s, 1H), 7.30 – 7.05 (m, 8H), 4.09 (s, 1H), 3.92 (q, J = 7.4 Hz, 2H), 3.62 – 3.58 (m, 4H), 2.76 (q, J = 8.1 Hz, 1H), 2.33 – 2.26 (m, 4H).**^{13}C NMR** (101 MHz, $(CD_3)_2SO$) δ 159.0, 149.7, 140.6, 139.1, 138.6, 131.9, 130.7, 130.6, 127.8, 125.6, 117.2, 77.3, 51.2, 31.0.

*N-Hydroxy-1-(4-(naphthalen-2-ylmethyl)piperazine-1-carbonyl)-1H-pyrazole-4-carboxamide **(69k)***: compound **69k** was prepared according to procedure used for compound **69h**, starting from compound **91b** (49 mg, 0.13 mmol), and a 1 N solution of HCl in MeOH (5.2 mL, 5.2 mmol) in MeOH (5.2 mL). The crude was purified by column chromatography on silica gel (DCM/MeOH starting from 40:1 to 10:1) to afford the title compound as white solid (28% yield). **ESI-MS** *m*/*z*: 380 [*M* + H]$^+$.^{1}**H NMR** (400 MHz, $(CD_3)_2SO$) δ 10.99 (s, 1H), 9.02 (s, 1H), 8.51 (s, 1H), 8.00 (s, 1H), 7.90 – 7.81 (m, 3H), 7.77 (s, 1H), 7.54 – 7.39 (m, 3H), 3.77 – 3.53 (m, 6H), 2.51 – 2.41 (m, 4H). ^{13}**C NMR** (101 MHz, $(CD_3)_2SO$) δ 158.9, 149.8, 140.6, 135.4, 132.9, 132.3, 131.9, 127.8, 127.6, 127.5, 127.3, 126.1, 125.7, 117.2, 61.8, 52.3.

*1-(4-benzylpiperazine-1-carbonyl)-N-hydroxy-1H-pyrazole-4-carboxamide **(69l)***: compound **69l** was prepared according to procedure used for compound **69h**, starting from compound **91c** (83 mg, 0.20 mmol), and a 1 N solution of HCl in MeOH (8 mL, 8.00 mmol) in MeOH (8 mL). The crude was purified by column chromatography on silica gel (DCM/MeOH starting from 30:1 to 10:1, then DCM/MeOH/NH_4OH 10:1:0.1) to afford the title compound as a white solid (44% yield). **ESI-MS** *m*/*z*: 330 [*M* + H]$^+$; 352 [*M* + Na]$^+$; 328 [*M* – H]$^-$; 364 [*M* + Cl]$^-$. ^{1}**H NMR** (400 MHz, $(CD_3)_2SO$) δ 11.02 (s, 1H), 9.06 (s, 1H), 8.54 (s, 1H), 8.04 (s, 1H), 7.38 – 7.30 (m, 4H), 7.29 – 7.23 (m, 1H), 3.72 – 3.64 (m, 4H), 3.53 (s, 2H), 2.46 (t, *J* = 5.0 Hz, 4H). ^{13}**C NMR** (101 MHz, $(CD_3)_2SO$) δ 159.4, 150.2, 141.0, 138.1, 132.3, 129.4, 128.7, 127.5, 117.6, 62.2, 52.6.

*(4-(4-(5-(Difluoromethyl)-1,3,4-oxadiazol-2-yl)benzyl)piperazin-1-yl)(1H-1,2,4-triazol-1-yl)methanone **(69m)***: compound **69m** was prepared according to two steps procedure used for compound **100a**, starting from **93a** (138 mg, 0.49 mmol), and a 1 N solution of HCl in MeOH (19.6 mL, 19.6 mmol) in MeOH (19.6 mL) in the first step, then TEA (229 µL, 1,64 mmol), and compound **97** (95 mg, 0,33 mmol) in MeCN (2,50 mmol). The crude was purified by column chromatography on silica gel (DCM/ MEOH starting from 100:1 to 70:1) to afford the title compound as a yellowish oil (40% yield). **ESI-MS** *m*/*z*: 390 [*M* + H]$^+$. ^{1}**H NMR** (300 MHz, $CDCl_3$) δ 8.78 (s, 1H), 8.08 (d, *J* = 8.3 Hz, 2H), 7.98 (s, 1H), 7.53 (d, *J* = 8.3 Hz, 2H), 6.91 (t, *J* = 51.7 Hz, 1H), 4.02 – 3.79 (m, 4H), 3.63 (s, 2H), 2.58 (t, *J* = 5.1 Hz, 4H). ^{13}**C NMR** (75 MHz, $CDCl_3$) δ 166.0, 158.1, 152.0, 148.4, 146.6, 143.0, 129.7, 127.6, 121.7, 105.8, 62.2, 52.7. ^{19}**F NMR** (282 MHz, $CDCl_3$) δ -119.1, -119.3.

*4-((4-(1H-1,2,4-Triazole-1-carbonyl)piperazin-1-yl)methyl)-N-hydroxybenzamide **(69n)***: compound **69n** was prepared according to procedure used for compound **69h**, starting from compound **100a** (101 mg, 0.31 mmol), and a 1 N solution of HCl in MeOH (12.4 µL, 12,4 mmol) in MeOH (12.4 mL). The crude was purified by column chromatography on silica gel (DCM/MeOH starting from 30:1 to 10:1) to afford the title compound as a white solid (21% yield). **ESI-MS** *m*/*z*: 331 [*M* + H$^+$]$^+$, 329 [*M* – H]$^-$. ^{1}**H NMR** (300 MHz, CD_3OD) δ 8.94 (s, 1H), 8.10 (s, 1H), 7.72 (d, *J* = 8.1 Hz, 2H), 7.46 (d, *J* = 7.9 Hz, 2H), 3.85 – 3.77 (m, 4H), 3.63 (s, 2H), 2.57 (t, *J* = 5.1 Hz, 4H). ^{13}**C NMR** (101 MHz, CD_3OD) δ 156.2, 151.1, 141.8, 141.4, 129.3, 129.1, 128.8, 126.7, 61.8, 52.3, 51.8.

4-((4-(1H-Pyrazole-1-carbonyl)piperazin-1-yl)methyl)-N-hydroxybenzamide ***(69o)***: compound **69o** was prepared according to procedure used for compound **69h**, starting from compound **100b** (147 mg, 0.41 mmol), and a 1 N solution of HCl in MeOH (16.4 mL, 16.40 mmol) in MeOH (16.4 mL). The crude was purified by column chromatography on silica gel (DCM/MeOH/NH_4OH starting from 30:1:0,1 to 10:1:0,1) to afford the title compound as a white solid (27% yield). **ESI-MS** *m*/*z*: 330 $[M + H]^+$; 328 $[M - H]^-$. **^{1}H NMR** (300 MHz, CD_3OD) δ 8.12 (d, J = 2.7 Hz, 1H), 7.76 – 7.68 (m, 3H), 7.47 (d, J = 7.9 Hz, 2H), 6.47 – 6.43 (m, 1H), 3.82 (t, J = 5.0 Hz, 4H), 3.63 (s, 2H), 2.56 (t, J = 5.0 Hz, 4H). **^{13}C NMR** (101 MHz, $(CD_3)_2SO$) δ 164.5, 150.9, 142.2, 141.5, 132.5, 132.1, 129.2, 127.3, 107.8, 61.7, 52.8.

4-((4-(4-Cyano-1H-pyrazole-1-carbonyl)piperazin-1-yl)methyl)-N-hydroxybenzamide ***(69p)***: compound **69p** was prepared according to procedure used for compound **69h**, starting from compound **100c** (265 mg, 0.60 mmol), and a 1 N solution of HCl in MeOH (24 mL, 24 mmol) in MeOH (24 mL). The crude was purified by column chromatography on silica gel (DCM/MeOH/NH_4OH starting from 40:1:0,1 to 10:1:0,1) to afford the title compound as white solid (53% yield). **ESI-MS** *m*/*z*: 355 $[M + H]^+$; 377 $[M + Na]^+$; 353 $[M - H]^-$. **^{1}H NMR** (400 MHz, $(CD_3)2SO$) δ 11.13 (s, 1H), 9.02 (d, J = 0.7 Hz, 1H), 8.96 (s, 1H), 8.28 (d, J = 0.7 Hz, 1H), 7.68 (d, J = 8.3 Hz, 2H), 7.35 (d, J = 8.2 Hz, 2H), 3.59 (t, J = 4.9 Hz, 4H), 3.53 (s, 2H), 2.43 (t, J = 5.0 Hz, 4H). **^{13}C NMR** (101 MHz, $(CD_3)_2SO$) δ 164.6, 149.4, 143.7, 141.4, 139.2, 132.1, 129.2, 127.3, 113.5, 93.6, 61.6, 52.5.

3.3 Experimental section of the DGLα/β-FAAH inhibitors

*6-Phenylhexan-1-ol (**103**)*: to a 0 °C cooled solution of compound **102** (485 µL, 2.60 mmol) in dry THF (2 mL), a 2 N solution of borane dimethyl sulphide complex in THF (3380 µL; 2.60 mmol) was added. The reaction mixture was stirred for 2 h under N_2 atmosphere. A saturated solution of $NaHCO_3$ was added, and the mixture was extracted with EtOAc (3 x 10 mL). The collected organic layers were dried with Na_2SO_4, filtered, and concentrated under vacuum. The crude was purified by column chromatography on silica gel (Ep/EtOAc starting from 7:1 to 4:1) to afford the title compound as a colourless oil (95% yield). **^{1}H NMR** (300 MHz, $CDCl_3$) *δ* 7.34 – 7.24 (m, 2H), 7.22 – 7.14 (m, 3H), 3.64 (t, J = 6.6 Hz, 2H), 2.61 (t, J = 8.7, 6.7 Hz, 2H), 1.72 – 1.51 (m, 4H), 1.44 – 1.30 (m, 4H).

*2-(6-Phenylhexyl)isoindoline-1,3-dione (**104**)*: to a 0 °C cooled solution of **103** (430 mg, 2.41 mmol) in dry THF (22 mL), PPh_3 (947 mg, 3.61 mmol), and DIAD (706 µL, 3.86 mmol) were added. The reaction mixture was stirred for 30 minutes under N_2 atmosphere. After that, phthalimide (390 mg, 2.65 mmol) was added. Temperature was allowed to reach 25 °C, and the reaction mixture was stirred for 12 h under N_2 atmosphere. The solvent was removed under vacuum. The crude was purified by column chromatography on silica gel (Ep/EtOAc starting from 8:1 to 7:1) to afford the title compound as a white solid (86% yield). **^{1}H NMR** (300 MHz, $CDCl_3$) *δ* 7.92 – 7.81 (m, 2H), 7.79 – 7.67 (m, 2H), 7.33 – 7.24 (m, 2H), 7.22 – 7.14 (m, 3H), 3.70 (t, *J* = 7.3 Hz, 2H), 2.62 (t, *J* = 7.7 Hz, 2H), 1.78 – 1.58 (m, 4H), 1.43 – 1.37 (m, 4H).

*6-phenylhexan-1-amine (**105**)*: to a solution of **104** (203 mg, 0.66 mmol) in EtOH (8 mL), hydrazine monohydrate (130 µL, 2.64 mmol) was added. Temperature was increased to 82 °C, and the reaction mixture was stirred for 2 h. After cooling down to 25 °C, the reaction mixture was filtered, and the solvent was removed under vacuum. The solid residue was taken up with DCM, and extracted with a 2 N solution of HCl in H_2O (2 x 10 mL). Solid $NaHCO_3$ was added to the aqueous phase to adjust pH ≈ 7. The obtained solution was extracted with DCM (3 x 10 mL). The crude was used in the following step without any further purification (yellow oil) (59% yield). **ESI-MS** *m/z*: 178 $[M + H]^+$, 200 $[M + Na]^+$.**^{1}H NMR** (300 MHz, $CDCl_3$) δ 7.33 – 7.22 (m, 2H), 7.22 – 7.12 (m, 3H), 2.68 (t, J = 6.8 Hz, 2H), 2.64 – 2.56 (m, 2H), 1.80 – 1.70 (m, 2H), 1.67 – 1.55 (m, 2H), 1.50 – 1.40 (m, 2H), 1.39 – 1.30 (m, 4H).

*N-(6-Phenylhexyl)-1H-1,2,3-triazole-1-carboxamide (**101a**)*: to a solution of 1*H*-1,2,3-triazole (81 mg, 0.68 mmol) in dry DCM (8 mL), DMAP (166 mg, 1.36 mmol), and a 20% w/w solution of phosgene in toluene (350 µL, 0.68 mmol) were added. The reaction mixture was stirred at 25 °C for 30 minutes under N_2 atmosphere. After that, compound **105** (61 mg, 0.34 mmol) was added. The reaction mixture was stirred for 12 h under N_2 atmosphere. H_2O was added, and the mixture was extracted with DCM (3 x 10 mL). The collected organic layers were dried with Na_2SO_4, filtered, and concentrated under vacuum. The crude was purified by column chromatography on silica gel (Ep/EtOAc starting from 6:1 to 2:1) to afford the title compound as a white solid (21% yield). **ESI-MS** *m/z*: 295 $[M + Na]^+$, **^{1}H NMR** (300 MHz, $CDCl_3$) δ 8.28 (s, 1H), 7.76 (s, 1H), 7.34 – 7.23 (m, 2H), 7.21 – 7.12 (m, 3H), 3.48 (q, J = 7.2 Hz, 2H), 2.61 (t, J = 6.7 Hz, 2H), 1.72 – 1.57 (m, 4H), 1.48 – 1.34 (m, 4H). **^{13}C NMR** (75 MHz, $CDCl_3$) δ 147.2, 142.5, 134.4, 128.4, 128.3, 125.7, 122.3, 40.7, 35.8, 31.3, 29.3, 28.8, 26.6.

*N-(6-Phenylhexyl)-2H-1,2,3-triazole-2-carboxamide (**101b**)*: to a 0 °C cooled solution of compound **105** (93 mg, 0.52 mmol) in dry THF (7 mL), DIPEA (450 µL, 2.60 mmol), and triphosgene (77 mg, 0.26 mmol) were added. The reaction mixture was stirred for 30 minutes under N_2 atmosphere. Then, H_2O was added, and the mixture was extracted with EtOAc (3 x 10 mL). The collected organic layers were washed with H_2O (1 x 10 mL), and a saturated solution of NaCl (1 x 10 mL). dried with Na_2SO_4, filtered, and concentrated under vacuum. The residue was dissolved in dry THF (14 mL), and DIPEA (450 µL, 2.60 mmol), DMAP (64 mg, 0.52 mmol), and 1*H*-1,2,3-triazole (62 mg, 0.52 mmol) were added. The temperature was increased to 66 °C, and the reaction mixture was stirred for 2 h under N_2 atmosphere. A saturated solution of NH_4Cl was added, and the mixture was extracted with EtOAc (3 x 10 mL). The collected organic layers were washed with H_2O (1 x 10 mL) and a saturated solution of NaCl (1 x 10 mL), dried with Na_2SO_4, filtered, and concentrated under vacuum. The crude was purified by column chromatography on silica gel (Ep/EtOAc starting from 6:1 to 3:1) to afford the title compound as a white solid (23% yield). **ESI-MS** *m/z*: 295 $[M + Na]^+$. **^{1}H NMR** (300 MHz, $CDCl_3$) δ 7.81 (s, 2H), 7.33 – 7.22 (m, 2H), 7.17 (td, J = 4.9, 2.7 Hz, 3H), 3.48 (q, J = 6.8 Hz, 2H), 2.61 (t, J = 7.7 Hz, 2H), 1.74 – 1.57 (m, 4H), 1.51 – 1.34 (m, 4H). **^{13}C NMR** (75 MHz, $CDCl_3$) δ 147.4, 142.7, 136.7, 128.3, 128.2, 125.8, 40.8, 35.9, 31.3, 29.4, 28.8, 26.6

3.4 Experimental section of the RAD52 peptide and peptide-mimetic modulators

3.4.1 Experimental section for SPPS

General procedure A1: Fmoc deprotection employed in automatic SPPS
To the resin in a plastic fritted syringe, a solution of piperidine in DMF (40% V/V, 1.2 mL) was added. The reaction was conducted at 25 °C for 3 min, alternating cycles of 10 seconds of shaking and 1 minute of rest. The resin was filtered, and a solution of piperidine in DMF (20% V/V, 1.2 mL) was added. The reaction was conducted at 25 °C for 12 min, carrying out cycles of 10 seconds of shaking every 2 min. The resin was filtered and washed with DMF (6 x 1.3 mL).

General procedure A2: Fmoc deprotection employed in manual SPPS under MWI
To the resin in a pyrex MW tube, a solution of piperidine in DMF (30% V/V) was added, considering a resin/deprotecting solution ratio of 200 mg/3 mL. The reaction was conducted under MWI, with a fixed power of 40 W at 40 °C for 30 seconds. The deprotecting protocol was repeated 3 times, allowing the mixture to cool between each cycle to avoid byproducts formation. After that, the deprotection mixture was decanted from the suspension of the resin. The resin was washed with DCM (3 x 10 mL), MeOH (3 x 10 mL), and DMF (3 x 10 mL) on a Gooch crucible connected to a Schlenk line to filter off the washing solvents.

General procedure B1: coupling protocol employed in automatic SPPS
To the resin in a plastic fritted syringe, a solution of Fmoc-*L*-His-OH in DMF (800 µL, 0.25 M, 0.2 mmol), a solution of DIC and HOBt in DMF (800 µL, 0.25 M, 0.2 mmol), and a solution of DIPEA in DMF (800 µL, 0.625 M, 0.5 mmol) were added. The reaction was conducted at 25 °C for 40 min, carrying out cycles of 15 seconds of shaking every 2 min. After that, the resin was filtered, and the coupling procedure was repeated. The resin was filtered and washed with DMF (3 x 2.4 mL).

General procedure B2: coupling protocol employed in automatic SPPS
To the resin in a plastic fritted syringe, a solution of the appropriate Fmoc-*L*-amino acid-OH in DMF (800 µL, 0.5 M, 0.4 mmol), a solution of HBTU and HOBt in DMF (800 µL, 0.5 M, 0.4 mmol), and a solution of DIPEA in DMF (800 µL, 0.625 M, 0.5 mmol) were added. The reaction was conducted at 25 °C for 40 min, carrying out cycles of 15 seconds of shaking every 2 min. The resin was filtered and washed with DMF (3 x 2.4 mL).

General procedure B3: coupling protocol employed in manual SPPS under MWI
To a solution of Fmoc-*L*-His-OH in DMF in a round bottom flask, a solution of DIC, HOBt, and DIPEA in DMF was added. The reaction was conducted at 25 °C for 10 min. The resulting solution was added to the loaded Wang resin in a pyrex MW tube. The reaction was carried out under MWI for two cycles: the first one was performed with a fixed power of 15 W at 50 °C for 2 min; the second one was performed with a fixed power of 40 W at 50 °C for 4 min. The coupling mixture was decanted from the suspension of the resin. The resin was washed with DCM (3 x 10 mL), MeOH (3 x 10 mL), and DMF (3 x 10 mL) on a Gooch crucible connected to a Schlenk line to filter off the washing solvents.

General procedure B4: coupling protocol employed in manual SPPS under MWI
To a solution of the appropriate Fmoc-*L*-amino acid-OH in DMF in a round bottom flask, a solution of HBTU, HOBt, and DIPEA in DMF was added. The reaction was conducted at 25 °C for 10 min. The resulting solution was added to the loaded resin in a pyrex MW tube, and the reaction was carried out under MWI, with a cycling power of 50 W at a temperature ranging from 40-55 °C for 4 min. If another coupling reaction had to be performed, the coupling mixture was decanted from the suspension of the resin, and the procedure was repeated under the same conditions. The resin was washed with DCM (3 x 10 mL), MeOH (3 x 10 mL), and DMF (3 x 10 mL) on a Gooch crucible connected to a Schlenk line to filter off the washing solvents.

General procedure B5: coupling protocol employed in automatic SPPS
To the resin, a solution of the appropriate Fmoc-*L*-amino acid-OH in DMF (800 μL, 0.31 M, 0.248 mmol), a solution of oxyma pure in DMF (800 μL, 0.31 M, 0.248 mmol), a solution of DIPEA in DMF (800 μL, 0.39 M, 0.312 mmol), and a solution of HATU in DMF (800 μL, 0.31 M, 0.248 mmol) were added. The reaction was conducted at 25 °C for 40 min, carrying out cycles of 15 seconds of shaking every 2 min. The resin was filtered and washed with DMF (3 x 3.2 mL).

General procedure B6: coupling protocol employed in automatic SPPS
To the resin, a solution of Fmoc-*L*-amino acid-OH in DMF (800 μL, 0.155 M, 0.124 mmol), a solution of oxyma pure in DMF (800 μL, 0.31 M, 0.248 mmol), a solution of DIPEA in DMF (800 μL, 0.39 M, 0.312 mmol), and a solution of HATU in DMF (800 μL, 0.31 M, 0.248 mmol) were added. The reaction was conducted at 25 °C for 40 min, carrying out cycles of 15 seconds of shaking every 2 min. After that, the resin was filtered and the reaction repeated. The resin was filtered and washed with DMF (3 x 3.2 mL).

General procedure C1: capping protocol employed in automatic SPPS
To the resin, a solution of acetic anhydride (Ac_2O) and DIPEA in DMF (10/2.5/87.5% V/V respectively, 800 μL) was added. The reaction was conducted at 25 °C for 10 min, carrying out cycles of 20 seconds of shaking every 1 min. The resin was filtered, and the procedure was repeated under the same conditions. The resin was filtered and washed with DMF (3 x 2.4 mL).

General procedure C2: capping protocol employed in manual SPPS under MWI
To the resin, a solution of acetic anhydride (Ac_2O) and DIPEA in DMF (10/2.5/87.5% V/V respectively) was added considering a resin/capping solution ratio of 200 mg/5 mL. The suspension was shaken on an orbital shaker at 25 °C for 30 min. The capping solution was decanted from the suspension of the resin, and the procedure was repeated under the same conditions. The resin was washed with DCM (3 x 10 mL), MeOH (3 x 10 mL), and DMF (3 x 10 mL) on a Gooch crucible connected to a Schlenk line to filter off the washing solvents.

General procedure D: cleavage and precipitation
To a sealed vial containing the resin, a solution of triisopropylsilane (TIPS) and H_2O in TFA (2.5/2.5/95% V/V respectively) was added considering a resin/cleavage solution ratio of 250 mg/5 mL. The reaction was shaken on an orbital shaker at 25 °C for 3 h. The resin was filtered, and the filtrate was concentrated by removing solvents under N_2 flow. After that, 0 °C cooled Et_2O was added. Following centrifugation, the supernatant was removed, and the precipitate was washed twice with cold Et_2O.

*4-((S)-2-((S)-2-((S)-2-(2-Ammonioacetamido)-3-hydroxypropanamido)-3-(4-hydroxyphenyl)propanamido)-3-(((S)-1,3-dicarboxypropyl)amino)-3-oxopropyl)-1H-imidazol-1-ium chloride (**120a**)*: Fmoc-*L*-Glu(*t*Bu)-Wang resin (0.62 mmol/g, 161 mg, 0.10 mmol) was swollen in DMF (2 mL) for 40 min. Fmoc group was removed following **GP-A1**. To the swollen Wang resin, Fmoc-*L*-His(Trt)-OH, DIC, HOBt, and DIPEA were added in two steps, and the reaction was carried out according to **GP-B1**. Unreacted amino groups were acetylated as described in **GP-C1**. Fmoc group was removed following **GP-A1**. To the resin, Fmoc-*L*-Tyr(*t*Bu)-OH, HBTU, HOBt, and DIPEA were added, and the reaction was carried out according to **GP-B2**. Fmoc group was removed following **GP-A1**. To the resin, Fmoc-*L*-Ser(*t*Bu)-OH, HBTU, HOBt, and DIPEA were added, and the reaction was carried out according to **GP-B2**. Fmoc group was removed following **GP-A1**. To the resin, Fmoc-Gly-OH, HBTU, HOBt, and DIPEA were added, and the reaction was carried out according to **GP-B2**. Fmoc group was removed following **GP-A1**. After that, the peptide was cleaved from the resin and precipitated in cold Et_2O, as described in **GP-D**. No further purification steps were needed. A 0.1 N solution of HCl in H_2O was added considering a peptide/HCl solution ratio of 3 mg/mL. The resulting solution was lyophilised to afford the title compound as a white solid (41% yield). **ESI-MS** *m/z*: 592 $[M + H]^+$; 590 $[M - H]^-$. **^{1}H NMR** (400 MHz, $(CD_3)_2SO$) δ 14.39 (m , 2H), 9.02 (s, 1H), 8.58 (d, J = 7.4 Hz, 1H), 8.33 (t, J = 8.5 Hz, 2H), 8.28 (d, J = 7.5 Hz, 1H), 8.20 – 8.03 (m, 3H), 7.41 (s, 1H), 7.02 (d, J = 8.4 Hz, 2H), 6.63 (d, J = 8.2 Hz, 2H), 4.62 (td, J = 8.5, 5.0 Hz, 1H), 4.37 (q, J = 6.1 Hz, 2H), 4.22 (td, J = 8.4, 4.8 Hz, 2H), 3.60 (d, J = 11.6 Hz, 3H), 3.53 (q, J = 5.8, 5.3 Hz, 2H), 3.16 (dd, J = 15.4, 4.9 Hz, 1H), 3.02 – 2.84 (m, 2H), 2.72 (dd, J = 14.3, 9.8 Hz, 1H), 2.37 – 2.23 (m, 2H), 2.06 – 1.94 (m, 1H), 1.88 – 1.75 (m, 1H). **^{13}C NMR** (101 MHz, $(CD_3)_2SO$) δ 173.7, 173.0, 171.2, 169.9, 169.6, 166.1, 155.8, 133.4, 130.0, 129.2, 127.9, 116.8, 114.9, 61.8, 55.2, 54.8, 51.6, 51.4, 35.9, 30.0, 26.9, 26.2. 1D and 2D spectra, as well as tentative peak assignments, are provided in the **Appendix** (**Figure A7-11 and Table A1-2**).

*4-((2S,5S,8S)-2-(((S)-1,3-Dicarboxypropyl)carbamoyl)-5-(4-hydroxybenzyl)-8-(hydroxymethyl)-4,7,10,13-tetraoxo-3,6,9,12-tetraazatetradecyl)-1H-imidazol-1-ium chloride (**120b**)*: compound **120b** was prepared according to procedure used for compound **120a**, starting from compound Fmoc-*L*-Glu(*t*Bu)-Wang resin (0.62 mmol/g, 161 mg, 0.10 mmol), Fmoc-*L*-His(Trt)-OH, Fmoc-*L*-Tyr(*t*Bu)-OH, Fmoc-*L*-Ser(*t*Bu)-OH, Fmoc-Gly-OH. The free N-terminus of the loaded pentapeptide sequence was acetylated following **GP-C1**. After that, the peptide was cleaved from the resin and precipitated in cold Et$_2$O, as described in **GP-D**. The crude was purified on RP column chromatography (H$_2$O + 0.1% TFA). A 0.1 N solution of HCl in H$_2$O was added, considering a peptide/HCl solution ratio of 3 mg/mL. The resulting solution was lyophilised to afford the title compound (71% yield). **ESI-MS** *m/z*: 634 $[M + \mathrm{H}]^+$; 632 $[M - \mathrm{H}]^-$. **^{1}H NMR** (400 MHz, CD$_3$OD) δ 7.29 (s, 1H), 6.99 (d, *J* = 8.0 Hz, 2H), 6.64 (d, *J* = 7.7 Hz, 2H), 4.68 – 4.60 (m, 1H), 4.40 (dt, *J* = 13.6, 5.6 Hz, 2H), 4.31 (t, *J* = 4.9 Hz, 1H), 3.84 (q, *J* = 16.8 Hz, 2H), 3.76 – 3.58 (m, 2H), 3.30 – 3.17 (m, 1H), 3.10 – 2.94 (m, 2H), 2.87 – 2.76 (m, 1H), 2.46 – 2.32 (m, 2H), 2.15 (m, 1H) 1.97 (s, 3H), 1.95 – 1.85 (m, 2H). **^{13}C NMR** (101 MHz, (CD$_3$)$_2$SO) δ 173.7, 172.9, 171.1, 169.9, 169.5, 155.2, 133.4, 130.0, 129.2, 127.8, 116.8, 114.9, 61.4, 55.3, 54.1, 51.6, 51.4, 35.8, 29.7, 29.0, 26.0, 22.4.

*4-((S)-2-((S)-2-((S)-2-(2-Ammonioacetamido)-3-hydroxypropanamido)-3-(4-hydroxyphenyl)propanamido)-3-((carboxymethyl)amino)-3-oxopropyl)-1H-imidazol-1-ium chloride (**120c**)*: Fmoc-Gly-Wang resin (0.85 mmol/g, 200 mg, 0.17 mmol) was swollen in DMF for 40 min. Fmoc group was removed following **GP-A2**. To the swollen Wang resin, a preformed solution of Fmoc-*L*-His(Trt)-OH (316 mg, 0.51 mmol), DIC (80 µL, 0.51 mmol), HOBt (69 mg, 0.51 mmol), and DIPEA (118 µl, 0.68 mmol) in DMF (1.5 mL) was added, and the reaction was carried out according to **GP-B3**, performing a total of 3 coupling reactions. Fmoc group was removed following **GP-A2**. To the resin, a preformed solution of Fmoc-*L*-Tyr(*t*Bu)-OH (234 mg, 0.51 mmol), HBTU (193 mg, 0.51 mmol), HOBt (69 mg, 0.51 mmol), and DIPEA (118 µL, 0.68 mmol) in DMF (1.5 mL) was added, and the reaction was carried out according to **GP-B4**. Fmoc group was removed following **GP-A2**. To the resin, a preformed solution of Fmoc-*L*-Ser(*t*Bu)-OH (196 mg, 0.51 mmol), HBTU (193 mg, 0.51 mmol), HOBt (69 mg, 0.51 mmol), and DIPEA (118 µL, 0.68 mmol) in DMF (1.5 mL) was added, and the reaction was carried out according to **GP-B4**, performing a total of 2 coupling reactions. Fmoc group was removed following **GP-A2**. To the resin, a preformed solution of Fmoc-Gly-OH (152 mg, 0.51 mmol), HBTU (193 mg, 0.51 mmol), HOBt (69 mg, 0.51 mmol), and DIPEA (118 µL, 0.68 mmol) in DMF (1.5 mL) was added, and the reaction was carried out according to **GP-B4**, performing a total of 2 coupling reactions. Fmoc group was removed following **GP-A2**. After that, the peptide was cleaved from the resin and precipitated in cold Et$_2$O, as described in **GP-D**. The crude was purified on RP column chromatography (H$_2$O + 0.1% TFA). A 0.1 N solution of HCl in H$_2$O was added, considering a peptide/HCl solution ratio of 3 mg/mL. The resulting solution was lyophilised to afford the title compound as a white solid (35% yield). **ESI-MS** *m/z*: 520 $[M + \mathrm{H}]^+$; 518 $[M - \mathrm{H}]^-$. **^{1}H NMR** (400 MHz, CD$_3$OD) δ 7.52 (dd, *J* = 6.0, 1.7 Hz, 1H), 7.07 (dt, *J* = 8.6, 1.1 Hz, 2H), 6.98 (dd, *J* = 4.9, 1.7 Hz, 1H), 6.76 – 6.70 (m, 2H), 4.57 (dt, *J* = 9.3, 5.9 Hz, 1H), 4.44 (dt, *J* = 8.6, 6.0 Hz, 1H), 4.20 (dt, *J* = 8.5, 4.3 Hz, 1H), 3.90 – 3.83 (m, 2H), 3.80 (m, 2H), 3.73 (dd, *J* = 5.7, 4.2 Hz, 2H), 3.18 (m, 1H), 3.08 – 2.93 (m, 2H), 2.72 – 2.64 (m, 1H). **^{13}C NMR** (101 MHz, (CD$_3$)$_2$SO) δ 172.1, 171.5, 170.9, 170.5, 170.1, 169.6, 167.0, 156.1, 134.2, 131.1, 129.9, 128.7, 117.1, 116.0, 62.4, 56.1, 55.2, 52.8, 52.3, 35.0.

4-((2S,5S,8S)-2-((Carboxymethyl)carbamoyl)-5-(4-hydroxybenzyl)-8-(hydroxymethyl)-4,7,10,13-tetraoxo-3,6,9,12-tetraazatetradecyl)-1H-imidazol-1-ium chloride ***(120d)***: compound **120d** was prepared according to procedure used for compound **120c**, starting from compound Fmoc-Gly-Wang resin (0.85 mmol/g, 200 mg, 0.17 mmol), Fmoc-*L*-His(Trt)-OH (316 mg, 0.51 mmol), Fmoc-*L*-Tyr(*t*Bu)-OH (234 mg, 0.51 mmol), Fmoc-*L*-Ser(*t*Bu)-OH (196 mg, 0.51 mmol), Fmoc-Gly-OH (152 mg, 0.51 mmol). The free N-terminus of the loaded pentapeptide sequence was acetylated following **GP-C1**. After that, the peptide was cleaved from the resin and precipitated in cold Et_2O, as described in **GP-D**. The crude was purified on RP column chromatography (H_2O + 0.1% TFA). A 0.1 N solution of HCl was added, considering a peptide/HCl solution ratio of 3 mg/mL solution. The resulting solution was lyophilised to afford the title compound as a white solid (24% yield). **ESI-MS** *m/z*: 562 $[M + H]^+$; 560 $[M - H]^-$. **^{1}H NMR** (400 MHz, CD_3OD) δ 7.52 (dd, J = 6.0, 1.7 Hz, 1H), 7.07 (m, 2H), 6.98 (dd, J = 4.8, 1.7 Hz, 1H), 6.76 – 6.70 (m, 2H), 4.57 (m, 1H), 4.44 (m, 1H), 4.18 (m, 1H), 3.94 – 3.86 (m, 1H), 3.90 – 3.82 (m, 1H), 3.80 (dd, J = 6.4, 1.8 Hz, 2H), 3.73 (dd, J = 5.6, 4.3 Hz, 2H), 3.18 (m, 1H), 3.08 – 2.93 (m, 2H), 2.71 – 2.64 (m, 1H), 2.06 (s, 3H). **^{13}C NMR** (101 MHz, $(CD_3)_2SO$) δ 171.7, 171.4 (2C), 170.8, 170.6, 170.1, 169.4, 166.6, 156.3, 133.9, 130.5, 129.6, 128.2, 117.4, 115.4, 62.2, 55.7, 55.5, 52.4, 52.1, 35.7, 27.4.

(4S,7S,10S,13S)-10-(Azidomethyl)-13,15-dicarboxy-7-(4-hydroxybenzyl)-2,5,8,11-tetraoxo-4-(prop-2-yn-1-yl)-3,6,9,12-tetraazapentadecan-1-aminium chloride ***(120g)***: Fmoc-*L*-Glu(*t*Bu)-Wang resin (0.62 mmol/g, 100 mg, 0.06 mmol) was swollen in DMF (2 mL) for 40 min. Fmoc group was removed following **GP-A1**. To the swollen Wang resin, Fmoc-*L*-Ala(N_3)-OH, HATU, HOBt, and DIPEA were added, and the reaction was carried out according to **GP-B5**. Unreacted amino group was acetylated following **GP-C1**. Fmoc group was removed following **GP-A1**. To the resin, Fmoc-*L*-Tyr(*t*Bu)-OH, HATU, HOBt, and DIPEA were added, and the reaction was carried out according to **GP-B6**. Unreacted amino group was acetylated following **GP-C1**. Fmoc group was removed following **GP-A1**. To the resin, Fmoc-*L*-Pra-OH, HATU, HOBt, and DIPEA were added, and the reaction was carried out according to **GP-B5**. Unreacted amino group was acetylated following **GP-C1**. Fmoc group was removed following **GP-A1**. To the resin, Fmoc-Gly-OH, HATU, HOBt, and DIPEA were added, and the reaction was carried out according to **GP-B5**. Fmoc group was removed following **GP-A1**. After that, the peptide was cleaved from the resin and precipitated in cold Et_2O, as described in **GP-D**. The crude was purified on RP column chromatography (H_2O/ACN/TFA 9:1:0.1). A 0.1 N solution of HCl was added, considering a peptide/HCl solution ratio of 3 mg/mL solution. The resulting solution was lyophilised to afford the title compound as a white solid (32% yield). **ESI-MS** *m/z*: 575 $[M + H]^+$; 573 $[M - H]^-$. **^{1}H NMR** (400 MHz, CD_3OD) δ 7.01 – 6.93 (m, 2H), 6.63 – 6.56 (m, 2H), 4.52 – 4.32 (m, 4H), 3.64 (d, J = 1.7 Hz, 2H), 3.61 – 3.47 (m, 2H), 3.00 (dd, J = 14.1, 5.5 Hz, 1H), 2.80 (dd, J = 14.1, 9.0 Hz, 1H), 2.61 – 2.51 (m, 1H), 2.45 (ddd, J = 17.0, 8.1, 2.7 Hz, 1H), 2.33 (t, J = 7.6 Hz, 2H), 2.28 (t, J = 2.6 Hz, 1H), 2.17 – 2.05 (m, 1H), 1.88 (ddt, J = 14.2, 8.9, 7.2 Hz, 1H). **^{13}C NMR** (101 MHz, CD_3OD) δ 177.7, 173.4, 171.9, 170.3, 167.0, 158.9, 132.6, 128.9, 116.3, 78.9, 71.7, 56.5, 54.2, 53.9, 53.1, 52.5, 41.9, 37.6, 30.6, 28.6, 23.1.

(4S,7S,10S,13S)-10-(Azidomethyl)-13,15-dicarboxy-7-(3,4-dihydroxybenzyl)-2,5,8,11-tetraoxo-4-(prop-2-yn-1-yl)-3,6,9,12-tetraazapentadecan-1-aminium chloride ***(120h)***: compound **120h** was prepared according to procedure used for compound **120g**, starting from compound Fmoc-*L*-Glu(*t*Bu)-Wang resin (0.62 mmol/g, 100 mg, 0.06 mmol), Fmoc-*L*-Ala(N$_3$)-OH, Fmoc-*L*-DOPA(acetonide)-OH, Fmoc-*L*-Pra-OH, and Fmoc-Gly-OH. A 0.1 N solution of HCl was added, considering a peptide/HCl solution ratio of 3 mg/mL solution. The resulting solution was lyophilised to afford the title compound as a white solid (21% yield). **ESI-MS** *m/z*: 591 $[M + H]^+$; 589 $[M - H]^-$. ^{1}**H NMR** (400 MHz, CD$_3$OD) δ 6.71 – 6.64 (m, 2H), 6.56 (dd, J = 8.2, 2.1 Hz, 1H), 4.60 – 4.38 (m, 4H), 3.74 (d, J = 5.4 Hz, 2H), 3.71 – 3.54 (m, 2H), 3.05 (dd, J = 14.0, 5.3 Hz, 1H), 2.88 – 2.79 (m, 1H), 2.70 – 2.50 (m, 2H), 2.42 (dd, J = 8.8, 6.4 Hz, 2H), 2.38 – 2.32 (m, 1H), 2.19 (dtd, J = 16.2, 8.5, 7.9, 5.3 Hz, 1H), 1.97 (tdd, J = 16.7, 8.6, 3.5 Hz, 1H). ^{13}**C NMR** (101 MHz, CD$_3$OD) δ 175.0, 174.4, 173.4, 171.9, 171.2, 167.6, 146.1, 145.2, 129.7, 121.8, 117.6, 116.4, 80.0, 72.7, 56.5, 54.2, 53.9, 53.0, 52.8, 41.5, 37.8, 31.0, 27.7, 22.5.

3.4.2 Experimental section for LPPS

Dimethyl ((S)-2-((((9H-fluoren-9-yl)methoxy)carbonyl)amino)-3-azidopropanoyl)-L-glutamate ***(124)***: to a 0 °C cooled solution of **123** (945 mg, 3.43 mmol) in dry DCM (2.3 mL), TFA (10.5 mL, 137.30 mmol) was added, and the reaction mixture was stirred for 30 min under N$_2$ atmosphere. The solvent was removed under N$_2$ stream. To a solution of the resulting crude in dry DCM (6 mL), TEA (655 µL, 4.67 mmol), and HATU (1310 mg, 3.43 mmol) were added, and the reaction mixture was stirred for 15 min under N$_2$ atmosphere. Then, a preformed solution of Fmoc-*L*-Ala(N$_3$)-OH (1100 mg, 3.12 mmol), and TEA (655 µL, 4.67 mmol) in dry DCM (6 mL) was added. The temperature was allowed to reach 25 °C, and the reaction mixture was stirred for 4 h under N$_2$ atmosphere. A saturated solution of NH$_4$Cl was added, and the reaction mixture was extracted with DCM (3 x 10 mL). The collected organic layers were dried over Na$_2$SO$_4$, filtered, and concentrated under vacuum. The crude was purified by column chromatography on silica gel (Ep/EtOAc starting from 5:1 to 1:1) to afford the title compound as a white solid (81% yield). ^{1}**H NMR** (400 MHz, CD$_3$OD) δ 7.83 – 7.76 (m, 2H), 7.71 – 7.63 (m, 2H), 7.43 – 7.35 (m, 2H), 7.35 – 7.27 (m, 3H), 4.49 (dd, J = 9.2, 5.0 Hz, 1H), 4.42 – 4.33 (m, 3H), 4.24 (t, J = 6.9 Hz, 1H), 3.71 (s, 3H), 3.62 – 3.52 (m, 5H), 2.42 (t, J = 7.4 Hz, 2H), 2.19 (dq, J = 13.5, 7.3 Hz, 1H), 1.94 (ddd, J = 16.3, 14.1, 7.4 Hz, 1H).

Dimethyl ((S)-2-amino-3-azidopropanoyl)-L-glutamate ***(125)***: to a solution of **124** (133 mg, 0.26 mmol) in dry THF (4 mL), EtSH (290 µL, 3.92 mmol), and DBU (1.3 µL, 0.01 mmol) were added. The reaction mixture was stirred at 25 °C for the 2 h under N$_2$ atmosphere. After that, the solvent was removed under N$_2$ stream. The solid residue was taken up with DCM, neutralised with a saturated solution of NaHCO$_3$, and extracted with DCM (3 x 10 mL). The collected organic layers were dried over Na$_2$SO$_4$, filtered, and concentrated under vacuum. The crude was purified by column chromatography on silica gel (DCM/MeOH starting from 50:1 to 40:1) to afford the title compound as a yellowish oil (90 % yield). ^{1}**H NMR** (400 MHz, CD$_3$OD) δ 4.51 (dd, J = 9.0, 5.2 Hz, 1H), 3.73 (s, 3H), 3.67 (s, 3H), 3.57 – 3.54 (m, 2H), 3.53 – 3.48 (m, 1H), 2.45 (t, J = 7.6 Hz, 2H), 2.25 – 2.15 (m, 1H), 2.04 – 1.92 (m, 1H).

(S)-2-((tert-Butoxycarbonyl)amino)-3-((S)-2-oxopyrrolidin-3-yl)propanoic acid (**127**): to a 0 °C cooled solution of compound **126** (250 mg, 0.87 mmol) in THF (11 mL), LiOH (8.7 mL, 8.70 mmol) was added, and the reaction mixture was stirred for 2 h. After that, a 1 N solution of HCl in H_2O was added to adjust the pH ≈ 3. THF was removed under vacuum, and the mixture was extracted with EtOAc (3 x 10 mL). The collected organic layers were washed with a saturated solution of NaCl (1 x 10 mL), dried over Na_2SO_4, filtered, and concentrated under vacuum. The crude was used in the following step without any further purification (white solid) (67% yield). **^{1}H NMR** (400 MHz, CD_3OD) δ 3.96−4.28 (m,1H), 3.25−3.42 (m, 2H), 2.44−2.57 (m, 1H), 2.29−2.40 (m, 1H), 2.03−2.14 (m, 1H), 1.73−1.91 (m, 2H), 1.44 (s, 9H).

*Dimethyl ((S)-3-azido-2-((S)-2-((tert-butoxycarbonyl)amino)-3-((S)-2-oxopyrrolidin-3-yl)propanamido)propanoyl)-L-glutamate (**128**)*: to a solution of compound **127** (230 mg, 0.85 mmol) in dry DMF (3.5 mL) in a pyrex MW tube, HOBt (114 mg, 0.85 mmol), TEA (110 µL, 0.79 mmol), DIC (132 µL, 0.85 mmol), and a preformed solution of **125** (152 mg, 0.53 mmol) in dry DMF (3.5 mL) were added. The reaction was conducted under MWI, with a fixed power of 40 W at 50 °C for one cycle (10 min) under N_2 atmosphere. A saturated solution of NH_4Cl was added, and the mixture was extracted with EtOAc (3 x 10 mL). The collected organic layers were washed with a saturated solution of NH_4Cl (2 x 10 mL), a saturated solution of NaCl (1 x 10 mL), dried over Na_2SO_4, filtered, and concentrated under vacuum. The crude was purified by column chromatography on silica gel (DCM/MeOH starting from 50:1 to 30:1) to afford the title compound as a colourless oil (48% yield). **^{1}H NMR** (400 MHz, CD_3OD) δ 5.49 (s, 1H), 4.56 (t, J = 6.0 Hz, 1H), 4.48 (dd, J = 9.3, 5.1 Hz, 1H), 4.18 (dd, J = 10.2, 5.1 Hz, 1H), 3.72 (s, 3H), 3.68 – 3.64 (m, 5H), 3.37 – 3.32 (m, 2H), 2.59 – 2.50 (m, 1H), 2.43 (t, J = 7.4 Hz, 2H), 2.40 – 2.31 (m, 1H), 2.25 – 2.14 (m, 1H), 2.07 – 1.74 (m, 4H), 1.45 (s, 9H).

*Dimethyl ((S)-2-((S)-2-((S)-2-((((9H-fluoren-9-yl)methoxy)carbonyl)amino)pent-4-ynamido)-3-((S)-2-oxopyrrolidin-3-yl)propanamido)-3-azidopropanoyl)-L-glutamate (**129**)*: to a 0 °C cooled solution of **128** (308 mg, 0.57 mmol) in DCM (8 mL), TFA (1.74 mL, 22.75 mmol) was added, and the reaction mixture was stirred for 30 min. The solvent was removed under N_2 stream. The resulting crude was dissolved in DCM (4 mL) and added to a preformed solution Fmoc-*L*-2-propargylglycine (305 mg, 0.91 mmol), TEA (240 µL, 1.71 mmol), and HATU (346 mg, 0.91 mmol), in dry DMF (2 mL) in a pyrex MW tube. The reaction was conducted under MWI, with a fixed power of 40 W at 50 °C for three cycles (10 + 10 + 30 min) under N_2 atmosphere. A saturated solution of NH_4Cl was added, and the mixture was extracted with EtOAc (3 x 10 mL). The collected organic layers were washed with a saturated solution of NH_4Cl (2 x 10 mL) and a saturated solution of NaCl (1 x 10 mL), dried over Na_2SO_4, filtered, and concentrated under vacuum. The crude was purified by column chromatography on silica gel (DCM/MeOH starting from 100:1 to 70:1) to afford the title compound as a white solid (71% yield). **^{1}H NMR** (400 MHz, $(CD_3)_2SO$) δ 8.48 (d, J = 7.7 Hz, 1H), 8.32 (d, J = 8.0 Hz, 1H), 8.27 (d, J = 8.1 Hz, 1H), 7.90 (d, J = 7.5 Hz, 2H), 7.74 (dd, J = 15.0, 7.9 Hz, 3H), 7.63 (s, 1H), 7.42 (t, J = 7.4 Hz, 2H), 7.33 (t, J = 7.4 Hz, 2H), 4.49 (td, J = 7.6, 5.0 Hz, 1H), 4.41 – 4.17 (m, 7H), 3.61 (s, 3H), 3.57 (s, 4H), 3.55 (d, J = 5.0 Hz, 1H), 3.50 – 3.43 (m, 1H), 3.14 – 3.07 (m, 1H), 3.02 (q, J = 8.5 Hz, 1H), 2.87 – 2.83 (m, 1H), 2.48 – 2.41 (m, 0H), 2.37 (t, J = 7.5 Hz, 2H), 2.33 – 2.24 (m, 1H), 2.14 – 1.90 (m, 2H), 1.83 (dd, J = 14.7, 7.5 Hz, 1H), 1.70 – 1.59 (m, 1H), 1.58 – 1.48 (m, 1H), 1.38 (d, J = 6.6 Hz, 1H).

Dimethyl ((2S)-2-((S)-2-((S)-2-aminopent-4-ynamido)-3-((S)-2-oxopyrrolidin-3-yl)propanamido)-3-azidopropanoyl)-L-glutamate ***(130)***: compound **130** was prepared according to procedure used for **125**, starting from compound **129** (150 mg, 0.20 mmol), EtSH (220 µL, 2.97 mmol), and DBU (885 µL, 0.01 mol) in dry THF (3 mL). The crude was purified by column chromatography on silica gel ($CHCl_3$/MeOH starting from 100:1 to 30:1) to afford the title compound as a white solid (38% yield). **^{1}H NMR** (400 MHz, CD_3OD) *δ* 4.53 (ddt, *J* = 26.9, 9.0, 5.6 Hz, 3H), 3.72 (s, 3H), 3.66 (s, 4H), 3.52 (t, *J* = 5.5 Hz, 1H), 3.35 – 3.28 (m, 3H), 2.63 – 2.53 (m, 3H), 2.47 – 2.40 (m, 3H), 2.40 – 2.32 (m, 1H), 2.26 – 2.07 (m, 2H), 2.02 – 1.80 (m, 3H).

Methyl (S)-2-((S)-2-((((9H-fluoren-9-yl)methoxy)carbonyl)amino)pent-4-ynamido)-3-((S)-2-oxopyrrolidin-3-yl)propanoate ***(131)***: compound **131** was prepared according to two-steps procedure used for **128**, starting from compound **126** (25 mg, 0.09 mmol), and TFA (267 µL, 3.49 mmol) in DCM (1 mL). The resulting crude was dissolved in dry DMF (1 mL) and added to a preformed solution of DIPEA (60 µL, 0.35 mmol), oxyma pure (20 mg, 0.14 mmol), HATU (52 mg, 0.14 mmol), Fmoc-*L*-Pra-OH (46 mg, 0.14 mmol) in dry DMF (1 mL) in a pyrex MW tube. The reaction was conducted under MWI for two cycles (10 + 10 min). The crude was purified by column chromatography on silica gel (DCM/MeOH starting from 70:1 to 20:1) to afford the title compound as a white solid (84% yield). **ESI-MS** *m/z*: 504 [M + H]$^+$; 526 [M + Na]$^+$. **^{1}H NMR** (400 MHz, CD_3OD) *δ* 7.80 (d, *J* = 7.5 Hz, 2H), 7.68 (d, *J* = 7.5 Hz, 2H), 7.39 (t, *J* = 7.5 Hz, 2H), 7.31 (t, *J* = 7.5 Hz, 2H), 4.59 – 4.49 (m, 1H), 4.36 (d, *J* = 7.1 Hz, 2H), 4.33 – 4.28 (m, 1H), 4.24 (t, *J* = 7.0 Hz, 1H), 3.71 (s, 3H), 3.27 – 3.12 (m, 2H), 2.71 – 2.59 (m, 2H), 2.55 – 2.47 (m, 1H), 2.38 (t, *J* = 2.7 Hz, 1H), 2.33 – 2.22 (m, 1H), 2.22 – 2.10 (m, 1H), 1.86 – 1.68 (m, 2H).

Di-tert-butyl ((S)-2-((((9H-fluoren-9-yl)methoxy)carbonyl)amino)-3-azidopropanoyl)-L-glutamate ***(133)***: compound **133** was prepared according to procedure used for **124**, starting from a solution of Fmoc-*L*-Ala(N_3)-OH (1000 mg, 2.84 mmol), oxyma pure (645 mg, 4.54 mmol), DIPEA (1.48 mL, 8.52 mmol), and HATU (2160 mg, 5.68 mmol) in dry DCM (20 mL). A saturated solution of NH_4Cl was added, and the mixture was extracted with EtOAc (3 x 10 mL). The collected organic layers were washed with a saturated solution of NH_4Cl (1 x 10 mL), a 1 N solution of LiOH (2 x 10 mL), and a saturated solution of NaCl (1 x 10 mL), dried over anhydrous $MgSO_4$, filtered, and concentrated under vacuum. The crude was purified via column chromatography on silica gel (PE/EtOAc starting from 8:1 to 2:1) to afford the title compound as a yellow solid (68% yield). **ESI-MS** *m/z*: 594 [M + H]$^+$; 616 [M + Na]$^+$. **^{1}H NMR** (400 MHz, CD_3OD) *δ* 7.80 (d, *J* = 7.5 Hz, 2H), 7.68 (t, *J* = 6.2 Hz, 2H), 7.39 (t, *J* = 7.5 Hz, 2H), 7.31 (t, *J* = 7.4 Hz, 2H), 4.43 – 4.30 (m, 4H), 4.25 (t, *J* = 7.0 Hz, 1H), 3.64 – 3.57 (m, 2H), 2.32 (t, *J* = 7.5 Hz, 2H), 2.17 – 2.04 (m, 1H), 1.87 (dt, *J* = 14.6, 7.4 Hz, 1H), 1.46 (s, 9H), 1.41 (s, 9H).

Di-tert-butyl ((S)-2-amino-3-azidopropanoyl)-L-glutamate ***(134)***: compound **134** was prepared following the procedure used for **125**, starting from a (480 mg, 0.81 mmol), EtSH (900 µL, 12.13 mmol), and DBU (4 µL, 0.02 mmol) in dry THF (17 mL). The crude was purified via column chromatography on silica gel (DCM/MeOH starting from 50:1 to 10:1), to afford the title compound as a yellow oil (99% yield). **ESI-MS** *m/z*: 372 [M + H]$^+$. **^{1}H NMR** (400 MHz, CD_3OD) *δ* 4.36 (dd, *J* = 8.8, 5.1 Hz, 1H), 3.56 (d, *J* = 5.2 Hz, 2H), 3.50 (dd, *J* = 5.9, 4.5 Hz, 1H), 2.34 (t, *J* = 7.6 Hz, 2H), 2.17 – 2.05 (m, 1H), 1.95 – 1.82 (m, 1H), 1.48 (s, 9H), 1.45 (s, 9H).

*(S)-2-((((9H-Fluoren-9-yl)methoxy)carbonyl)amino)-3-((S)-2-oxopyrrolidin-3-yl)propanoic acid (**135**)*: to a solution of compound **126** (2000 mg, 6.98 mmol) in THF (70 mL), a solution 1 N solution of LiOH in H_2O (69.85 mL, 69.85 mmol) was added. The reaction mixture was stirred at 25 °C for 2 h. The solvent was removed under N_2 stream. The resulting crude was dissolved in 0 °C cooled DCM (70 mL), TFA (21.36 mL, 279.10 mmol) was added, and the reaction mixture was stirred for 30 min. The solvent was removed under N_2 stream. To a solution of the crude in THF (70 mL), DIPEA (6.07 mL, 34.85 mmol) was added. The reaction mixture was stirred at 25 °C for 10 min. Then, a preformed solution of Fmoc-Cl (1800 mg, 6.98 mmol) in THF (70 mL) was added. The reaction mixture was stirred at 25 °C for 2 h. After that, ice was added, and the mixture was extracted three times with EtOAc (3 x 10 mL). Then, a 1 N solution of HCl in H_2O was added to the collected aqueous layers to adjust pH ≈ 4-5, and the mixture was extracted with EtOAc (3 x 10 mL). The collected organic layers were dried over Na_2SO_4, filtered, and concentrated under vacuum. The crude was used in the following step without any further purification (99% yield) (colourless oil). **ESI-MS** *m/z*: 395 $[M + H]^+$; 393 $[M - H]^-$. **^{1}H NMR** (400 MHz, CD_3OD) δ 7.77 (d, J = 7.5 Hz, 2H), 7.66 (t, J = 8.1 Hz, 2H), 7.37 (t, J = 7.5 Hz, 2H), 7.29 (t, J = 7.4 Hz, 2H), 4.43 – 4.34 (m, 2H), 4.25 – 4.15 (m, 2H), 3.76 – 3.61 (m, 1H), 3.19 (q, J = 7.4 Hz, 1H), 2.47 – 2.37 (m, 1H), 2.35 – 2.25 (m, 1H), 2.18 – 2.08 (m, 1H), 1.80 (m, 2H), 1.44 (s, 1H).

*Di-tert-butyl ((S)-2-((S)-2-((((9H-fluoren-9-yl)methoxy)carbonyl)amino)-3-((S)-2-oxopyrrolidin-3-yl)propanamido)-3-azidopropanoyl)-L-glutamate (**136**)*: compound **136** was prepared according to procedure used for **128**, starting from a solution of compound **135** (411 mg, 1.11 mmol), oxyma pure (252 mg, 1.77 mmol), DIPEA (770 µL, 4.43 mmol), DIC (277 µL, 1.77 mmol), and compound **134** (524 mg, 1.33 mmol) in dry DMF (12 mL). The reaction was conducted under MWI for two cycles (10 + 10 min). The crude was purified via column chromatography on silica gel (DCM/MeOH starting from 40:1 to 25:1) to afford the title compound as a white solid (77% yield). **ESI-MS** *m/z*: 748 $[M + H]^+$. **^{1}H NMR** (400 MHz, CD_3OD) δ 7.81 (d, J = 7.5 Hz, 2H), 7.69 (t, J = 7.1 Hz, 2H), 7.40 (t, J = 7.5 Hz, 2H), 7.32 (t, J = 7.4 Hz, 2H), 4.60 (t, J = 5.6 Hz, 1H), 4.47 (dd, J = 10.4, 7.1 Hz, 1H), 4.40 (t, J = 5.3 Hz, 1H), 4.38 – 4.30 (m, 1H), 4.25 (q, J = 6.3 Hz, 2H), 3.80 (m, 2H), 3.68 (d, J = 4.9 Hz, 1H), 3.36 (s, 1H), 2.56 – 2.43 (m, 1H), 2.31 (t, J = 7.5 Hz, 3H), 2.15 – 2.01 (m, 2H), 1.85 (m, 3H), 1.47 (s, 9H), 1.44 (s, 9H).

*Di-tert-butyl ((S)-2-((S)-2-amino-3-((S)-2-oxopyrrolidin-3-yl)propanamido)-3-azidopropanoyl)-L-glutamate (**137**)*: to a solution of **136** (132 mg, 0.18 mmol) in DMF (1.8 mL), piperidine (87 µL, 0.88 mmol) was added. The reaction mixture was stirred at 25 °C for 1 h. The mixture was cooled in ice bath, a saturated solution of $NaHCO_3$ and EtOAc were added, and the mixture was extracted with EtOAc (3 x 10 mL). The collected organic layers were washed with a saturated solution of NaCl (2 x 10 mL), dried over Na_2SO_4, filtered, and concentrated under vacuum. The crude was used in the following step without any further purification (99% yield) (colourless oil). **ESI-MS** *m/z*: 526 $[M + H]^+$.

Dimethyl ((2S)-3-azido-2-((2S)-2-(-2-(2-((tert-butoxycarbonyl)amino)acetamido)pent-4-ynamido)-3-((S)-2-oxopyrrolidin-3-yl)propanamido)propanoyl)-L-glutamate ***(120e)***: compound **120e** was prepared according to procedure used for compound **128**, starting from compound **130** (150 mg, 0.28 mmol), Boc-*L*-glycine (78 mg, 0.45 mmol), TEA (117 µL, 0.84 mmol), and HATU (170 mg, 0.45 mmol) in dry DMF (3.8 mL). The reaction was conducted under MWI for one cycle (5 min). The crude was purified by column chromatography on silica gel (DCM/MeOH starting from 60:1 to 10:1) to afford the title compound as a colourless oil (45% yield). **ESI-MS** *m/z*: 694 [*M* + H]$^+$; 716 [*M* + Na]$^+$. **^{1}H NMR** (400 MHz, CD_3OD) δ 4.57 (q, *J* = 6.0 Hz, 1H), 4.53 – 4.41 (m, 3H), 3.80 (d, *J* = 9.3 Hz, 2H), 3.72 (s, 3H), 3.70 – 3.62 (m, 5H), 3.35 (s, 4H), 2.74 – 2.67 (m, 2H), 2.65 – 2.52 (m, 1H), 2.49 – 2.40 (m, 3H), 2.39 – 2.29 (m, 1H), 2.26 – 2.06 (m, 1H), 2.05 – 1.79 (m, 1H), 1.45 (s, 9H).

(6S,9S,12S)-9-(Azidomethyl)-6-(methoxycarbonyl)-3,8,11,14,17-pentaoxo-12-(((S)-2-oxopyrrolidin-3-yl)methyl)-15-(prop-2-yn-1-yl)-2-oxa-7,10,13,1-tetraazaoctadecan-18-aminium chloride ***(120f)***: to a 0 °C cooled solution of compound **120f** (32 mg, 0.05 mmol) in MeOH (2 mL), a 1 N solution of HCl in MeOH (2 mL, 2.00 mmol) was added, and the reaction mixture was stirred for 1 h. The solvent was removed under N_2 stream. The crude was purified by column chromatography on silica gel (DCM/MeOH/NH_4OH starting from 10:1:0.1 to 9:1:0.1) to afford the title compound as a white solid (69% yield). **ESI-MS** *m/z:* 594 [*M* + H]$^+$; 616 [*M* + Na]$^+$. **^{1}H NMR** (400 MHz, CD_3OD) δ 4.43 – 4.37 (m, 1H), 4.36 – 4.19 (m, 4H), 3.64 – 3.59 (m, 1H), 3.58 – 3.53 (m, 1H), 3.51 (s, 3H), 3.49 – 3.43 (m, 4H), 3.10 (p, *J* = 1.7 Hz, 2H), 2.60 – 2.54 (m, 1H), 2.53 – 2.49 (m, 1H), 2.49 – 2.41 (m, 1H), 2.30 – 2.25 (m, 1H), 2.25 – 2.20 (m, 2H), 2.20 – 2.10 (m, 1H), 2.04 – 1.86 (m, 2H), 1.85 – 1.61 (m, 3H).

Di-tert-butyl ((S)-2-((S)-2-((S)-2-((((9H-fluoren-9-yl)methoxy)carbonyl)amino)pent-4-ynamido)-3-((S)-2-oxopyrrolidin-3-yl)propanamido)-3-azidopropanoyl)-L-glutamate ***(120k)***: compound **120k** was prepared according to procedure used for compound **128**, starting from Fmoc-*L*-Pra-OH (285 mg, 0.85 mmol), oxyma pure (161 mg, 1.13 mmol), DIPEA (0.37 mL, 2.12 mmol), HATU (431 mg, 1.13 mmol), and compound **137** (372 mg, 0.71 mmol) in dry DMF (7 mL). The reaction was conducted under MWI for two cycles (10 + 10 min). The crude was purified by column chromatography on silica gel (DCM/MeOH 20:1) to afford the title compound as a white solid (48% yield). **ESI-MS** *m/z*: 843 [*M* + H]$^+$. **^{1}H NMR** (400 MHz, CD_3OD) δ 7.81 (d, *J* = 7.5 Hz, 2H), 7.71 (dd, *J* = 7.3, 2.9 Hz, 2H), 7.41 (t, *J* = 7.5 Hz, 2H), 7.33 (t, *J* = 7.4 Hz, 2H), 4.65 – 4.59 (m, 1H), 4.51 (dd, *J* = 11.4, 4.9 Hz, 1H), 4.40 (d, *J* = 6.9 Hz, 2H), 4.36 (dd, *J* = 9.3, 4.8 Hz, 1H), 4.28 (dt, *J* = 13.4, 6.9 Hz, 2H), 3.68 (d, *J* = 5.8 Hz, 2H), 3.35 – 3.32 (m, 1H), 3.32 – 3.21 (m, 2H), 2.71 (t, *J* = 5.9 Hz, 1H), 2.66 – 2.54 (m, 1H), 2.45 (t, *J* = 2.6 Hz, 1H), 2.35 (t, *J* = 7.5 Hz, 3H), 2.13 (m, 2H), 1.99 – 1.75 (m, 3H), 1.46 (d, *J* = 14.9 Hz, 18H). **^{13}C NMR** (101 MHz, CD_3OD) δ 182.0, 173.7, 172.0, 171.0, 158.6, 145.2, 145.2, 142.6, 128.8, 128.2, 126.3, 126.3, 120.9, 83.1, 81.8, 80.4, 72.7, 68.3, 66.9, 55.9, 54.1, 53.9, 53.8, 52.8, 41.6, 39.7, 34.0, 32.5, 29.0, 28.4, 28.2, 27.8, 23.5, 22.4, 15.4.

((S)-2-((S)-2-((S)-2-(((9H-Fluoren-9-yl)methoxy)carbonyl)amino)pent-4-ynamido)-3-((S)-2-oxopyrrolidin-3-yl)propanamido)-3-azidopropanoyl)-L-glutamic acid ***(120l)***: to a 0 °C cooled solution of **120k** (20 mg, 0.02 mmol) in DCM (2 mL), TFA (2 mL, 26 mmol) was added. After 40 min, temperature was allowed to reach 25 °C, and the reaction mixture was stirred for 20 min. The solvent was removed under vacuum. The crude was purified by column chromatography on silica gel (DCM/MeOH/HCOOH starting from 40:1:0.1 to 10:1:0.1) to afford the title compound as a white solid (35% yield). **ESI-MS** *m/z*: 731 $[M + H]^+$, 753 $[M + Na]^+$, 729 $[M - H]^-$. **^{1}H NMR** (400 MHz, CD_3OD) δ 7.80 (d, J = 7.5 Hz, 2H), 7.69 (d, J = 7.5 Hz, 2H), 7.40 (t, J = 7.5 Hz, 2H), 7.32 (t, J = 7.4 Hz, 2H), 4.60 (t, J = 5.9 Hz, 1H), 4.52 (dd, J = 10.9, 4.6 Hz, 1H), 4.45 (dt, J = 8.1, 3.9 Hz, 1H), 4.42 – 4.34 (m, 2H), 4.27 (dt, J = 13.8, 6.8 Hz, 2H), 3.69 – 3.63 (m, 2H), 3.29 – 3.18 (m, 2H), 2.72 – 2.66 (m, 2H), 2.62 – 2.53 (m, 1H), 2.47 – 2.38 (m, 3H), 2.29 (dd, J = 12.2, 8.6 Hz, 1H), 2.26 – 2.07 (m, 2H), 1.98 (dq, J = 15.0, 7.8 Hz, 1H), 1.91 – 1.76 (m, 2H). **^{13}C NMR** (101 MHz, CD_3OD) δ 182.1, 176.4, 173.8, 173.6, 171.1, 158.6, 145.2, 142.6, 128.8, 128.2, 126.3, 126.3, 120.9, 80.4, 72.6, 68.3, 55.8, 54.2, 53.6, 53.2, 52.8, 41.6, 39.7, 34.1, 31.1, 30.8, 28.9, 27.8, 22.4.

Di-tert-butyl ((S)-2-((S)-2-((S)-2-aminopent-4-ynamido)-3-((S)-2-oxopyrrolidin-3-yl)propanamido)-3-azidopropanoyl)-L-glutamate ***(120m)***: compound **120m** was prepared according to procedure used for compound **137**, starting from **120k** (25 mg, 0.03 mmol), and piperidine (15 μL, 0.15 mmol) in DMF (300 μL). The solvent was removed under vacuum. The crude was purified via column chromatography on silica gel ($DCM/MeOH/NH_4OH$ starting from 30:1:0.1 to 10:1:0.1) to afford the title compound as a white solid (92% yield). **ESI-MS** *m/z*: 621 $[M + H]^+$. **^{1}H NMR** (400 MHz, CD_3OD) δ 4.64 – 4.53 (m, 2H), 4.36 (dd, J = 8.7, 5.6 Hz, 1H), 3.74 – 3.63 (m, 2H), 3.58 – 3.48 (m, 2H), 3.41 – 3.34 (m, 2H), 2.61 (tt, J = 8.8, 5.8 Hz, 3H), 2.44 (td, J = 2.7, 1.1 Hz, 1H), 2.35 (t, J = 7.5 Hz, 2H), 2.20 – 2.07 (m, 2H), 1.96 – 1.82 (m, 3H), 1.48 (d, J = 7.5 Hz, 18H). **^{13}C NMR** (101 MHz, CD_3OD) δ 182.0, 176.0, 173.7, 173.6, 172.1, 171.1, 83.1, 81.8, 80.8, 72.8, 72.6, 66.9, 54.9, 54.1, 53.8, 53.4, 52.9, 41.6, 39.7, 34.6, 32.5, 29.0, 28.4, 28.2, 27.9, 25.8.

(S)-1-(((S)-1-(((S)-3-Azido-1-(((S)-1,3-dicarboxypropyl)amino)-1-oxopropan-2-yl)amino)-1-oxo-3-((S)-2-oxopyrrolidin-3-yl)propan-2-yl)amino)-1-oxopent-4-yn-2-aminium chloride ***(120n)***:compound **120n** was prepared according to procedure used for compound **120l**, starting from **120m** (17 mg, 0.03 mmol), and TFA (1 mL, 13 mmol) in DCM (1 mL). The solvent was removed under vacuum, and a 0.1 N solution of HCl in H_2O (3 mg/mL solution) was added. The solution was lyophilised to afford the title compound as a white salt (99% yield). **ESI-MS** *m/z*: 509 $[M + H]^+$, 531 $[M + Na]^+$, 507 $[M - H]^-$. **^{1}H NMR** (400 MHz, CD_3OD) δ 4.58 (m, 2H), 4.44 (td, J = 10.3, 9.2, 4.9 Hz, 1H), 4.05 (dd, J = 7.6, 5.4 Hz, 1H), 3.69 – 3.56 (m, 2H), 3.37 – 3.30 (m, 2H), 2.95 – 2.74 (m, 2H), 2.64 (d, J = 2.6 Hz, 1H), 2.53 (dt, J = 14.5, 7.4 Hz, 1H), 2.46 – 2.31 (m, 3H), 2.19 (m, 1H), 2.08 (m, 1H), 1.93 (m, 1H), 1.88 – 1.80 (m, 2H). **^{13}C NMR** (101 MHz, CD_3OD) δ 181.9, 174.8, 174.3, 173.1, 171.2, 171.1, 168.6, 77.4, 75.2, 54.2, 53.4, 53.0, 52.9, 41.7, 39.6, 34.8, 31.0, 30.9, 28.9, 27.8, 27.6, 22.4.

*Di-tert-butyl ((S)-3-azido-2-((S)-2-((S)-2-(2-((tert-butoxycarbonyl)amino)acetamido)pent-4-ynamido)-3-((S)-2-oxopyrrolidin-3-yl)propanamido)propanoyl)-L-glutamate (**120i**)*: compound **100i** was prepared according to procedure used for compound **108**, starting from Boc-Gly-OH (17 mg, 0.10 mmol), oxyma pure (14 mg, 0.10 mmol), DIPEA (32 µL, 0.18 mmol), and HATU (37 mg, 0.10 mmol), and **100n** (38 mg, 0.06 mmol) in DMF (3 mL) was added. The reaction was conducted under MWI for two cycles (10 + 10 min). The crude was purified via column chromatography on silica gel (DCM/MeOH starting from 60:1 to 50:1), to afford the title compound as a white solid (40% yield). **ESI-MS** *m/z*: 778 $[M + H]^+$, 800 $[M + Na]^+$, 776 $[M - H]^-$. **^{1}H NMR** (400 MHz, CD_3OD) δ 4.58 (t, J = 5.9 Hz, 1H), 4.49 – 4.39 (m, 2H), 4.33 (dd, J = 9.3, 5.0 Hz, 1H), 3.81 (s, 2H), 3.69 (d, J = 5.8 Hz, 2H), 3.34 (d, J = 2.7 Hz, 2H), 2.72 (dd, J = 6.3, 2.6 Hz, 2H), 2.59 (m, 1H), 2.44 (t, J = 2.7 Hz, 1H), 2.34 (t, J = 7.6 Hz, 3H), 2.18 – 2.03 (m, 2H), 1.88 (m, 3H), 1.55 – 1.39 (m, 27H). **^{13}C NMR** (101 MHz, CD_3OD) δ 182.0, 173.7 (2C), 173.1, 173.0, 172.0, 171.0, 158.4, 83.1, 81.8, 80.8, 80.1, 73.0, 54.2, 54.1, 53.8, 52.8, 44.7, 41.6, 39.9, 33.8, 32.5, 22.2.

*(4S,7S,10S,13S)-10-(Azidomethyl)-13,15-dicarboxy-2,5,8,11-tetraoxo-7-(((S)-2-oxopyrrolidin-3-yl)methyl)-4-(prop-2-yn-1-yl)-3,6,9,12-tetraazapentadecan-1-aminium chloride (**120j**)*: compound **120j** was prepared according to procedure used for compound **120l**, starting from **120i** (18 mg, 0.02 mmol), TFA was added (1 mL, 13 mmol) in DCM (1 mL). The solvent was removed under vacuum, and 0.1 N solution of HCl in H_2O (3 mg/mL solution) was added. The solution was lyophilised to afford the title compound as a white salt (99% yield). **ESI-MS** *m/z*: 567 $[M + H]^+$; 564 $[M - H]^-$. **^{1}H NMR** (400 MHz, CD_3OD) δ 4.60 – 4.50 (m, 2H), 4.50 – 4.42 (m, 2H), 3.82 (q, J = 16.1 Hz, 2H), 3.71 – 3.64 (m, 2H), 3.42 – 3.33 (m, 2H), 2.80 – 2.65 (m, 2H), 2.64 – 2.52 (m, 1H), 2.49 – 2.31 (m, 4H), 2.28 – 2.15 (m, 1H), 2.12 – 1.95 (m, 2H), 1.94 – 1.79 (m, 2H). **^{13}C NMR** (101 MHz, CD_3OD) δ 182.3, 174.8, 173.8, 173.2, 172.6, 171.2, 168.1, 80.1, 72.9, 54.4, 54.3, 53.1, 52.9, 52.6, 49.6, 49.4, 49.2, 49.0, 48.8, 48.6, 48.4, 41.8, 41.7, 40.1, 34.0, 30.9, 29.2, 27.5, 22.2.

4. **Appendix**

DLS spectra for compounds 120b-d,i,j,l

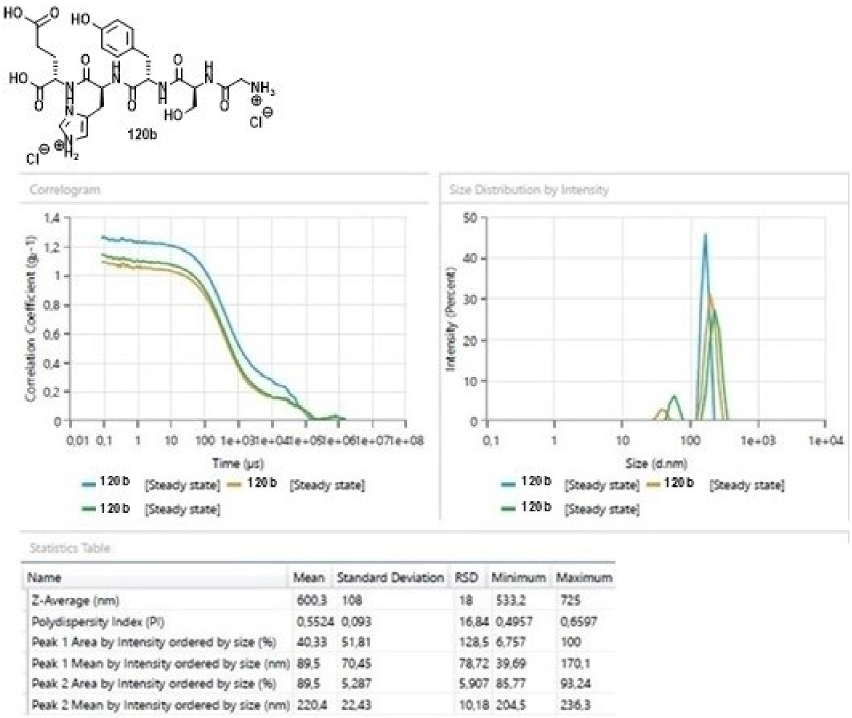

Name	Mean	Standard Deviation	RSD	Minimum	Maximum
Z-Average (nm)	600,3	108	18	533,2	725
Polydispersity Index (PI)	0,5524	0,093	16,84	0,4957	0,6597
Peak 1 Area by Intensity ordered by size (%)	40,33	51,81	128,5	6,757	100
Peak 1 Mean by Intensity ordered by size (nm)	89,5	70,45	78,72	39,69	170,1
Peak 2 Area by Intensity ordered by size (%)	89,5	5,287	5,907	85,77	93,24
Peak 2 Mean by Intensity ordered by size (nm)	220,4	22,43	10,18	204,5	236,3

Figure A1. DLS spectra of small peptide **120b**.

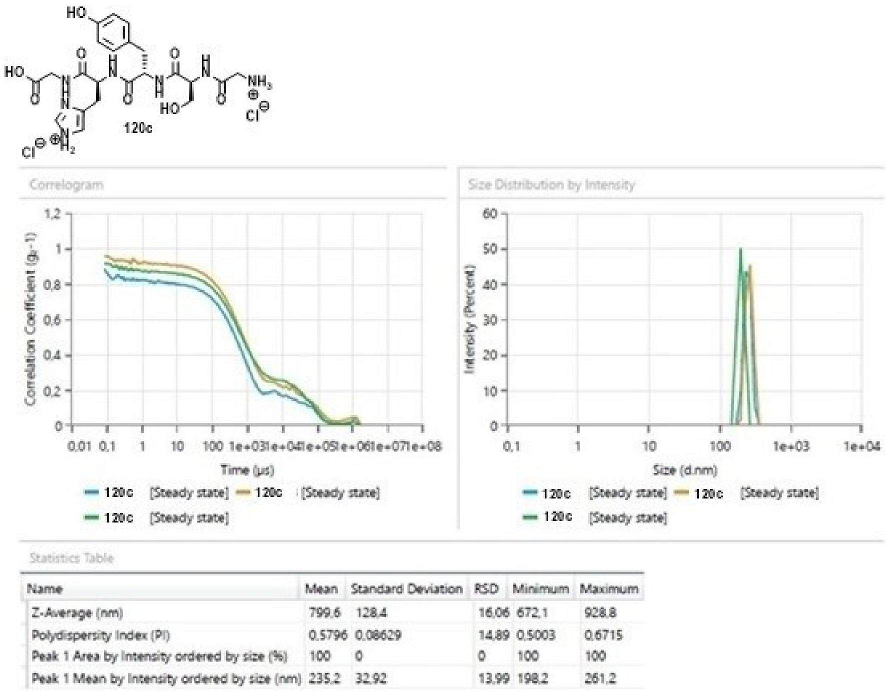

Name	Mean	Standard Deviation	RSD	Minimum	Maximum
Z-Average (nm)	799,6	128,4	16,06	672,1	928,8
Polydispersity Index (PI)	0,5796	0,08629	14,89	0,5003	0,6715
Peak 1 Area by Intensity ordered by size (%)	100	0	0	100	100
Peak 1 Mean by Intensity ordered by size (nm)	235,2	32,92	13,99	198,2	261,2

Figure A2. DLS spectra of small peptide **120c**.

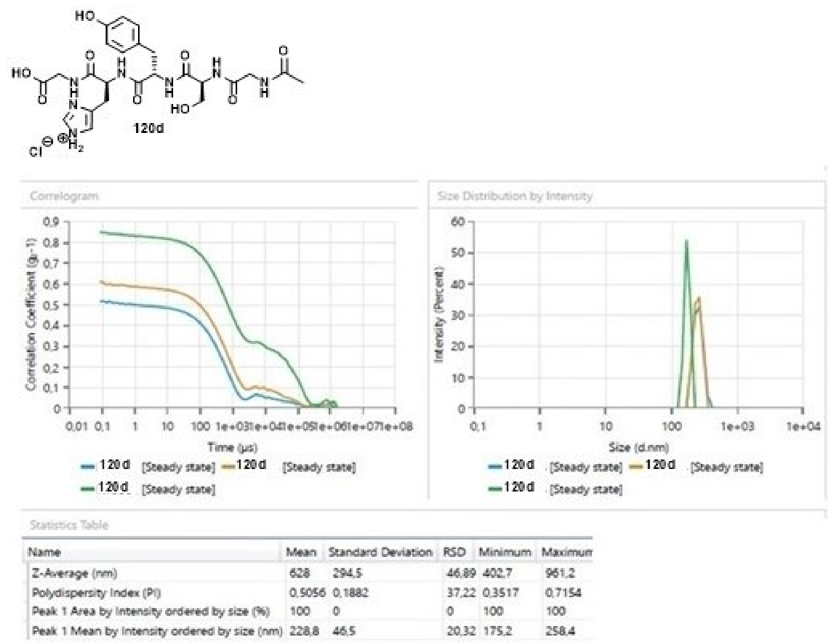

Name	Mean	Standard Deviation	RSD	Minimum	Maximum
Z-Average (nm)	628	294,5	46,89	402,7	961,2
Polydispersity Index (PI)	0,5056	0,1882	37,22	0,3517	0,7154
Peak 1 Area by Intensity ordered by size (%)	100	0	0	100	100
Peak 1 Mean by Intensity ordered by size (nm)	228,8	46,5	20,32	175,2	258,4

Figure A3. DLS spectra of small peptide **120d.**

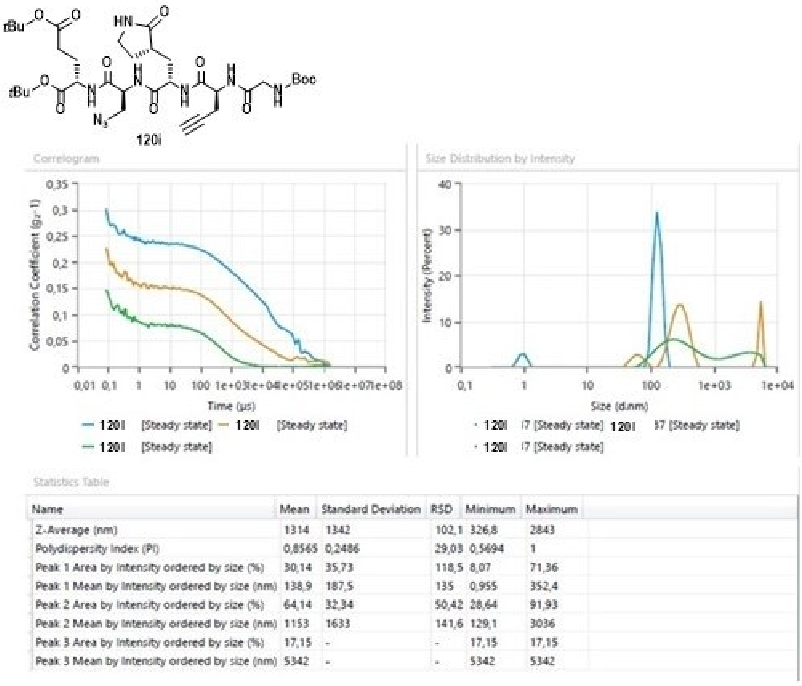

Name	Mean	Standard Deviation	RSD	Minimum	Maximum
Z-Average (nm)	1314	1342	102,1	326,8	2843
Polydispersity Index (PI)	0,8565	0,2486	29,03	0,5694	1
Peak 1 Area by Intensity ordered by size (%)	30,14	35,73	118,5	8,07	71,36
Peak 1 Mean by Intensity ordered by size (nm)	138,9	187,5	135	0,955	352,4
Peak 2 Area by Intensity ordered by size (%)	64,14	32,34	50,42	28,64	91,93
Peak 2 Mean by Intensity ordered by size (nm)	1153	1633	141,6	129,1	3036
Peak 3 Area by Intensity ordered by size (%)	17,15	-	-	17,15	17,15
Peak 3 Mean by Intensity ordered by size (nm)	5342	-	-	5342	5342

Figure A4. DLS spectra of peptidomimetic **120i.**

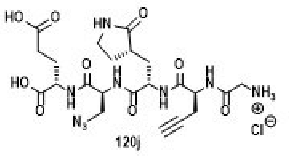

120j

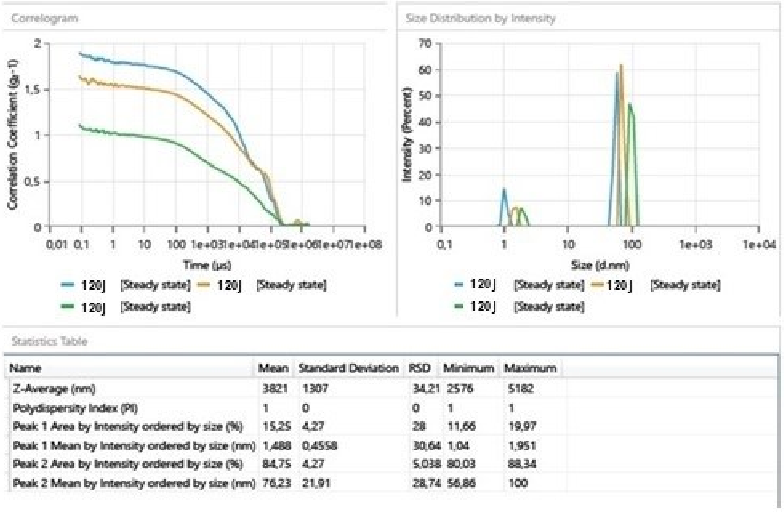

Name	Mean	Standard Deviation	RSD	Minimum	Maximum
Z-Average (nm)	3821	1307	34,21	2576	5182
Polydispersity Index (PI)	1	0	0	1	1
Peak 1 Area by Intensity ordered by size (%)	15,25	4,27	28	11,66	19,97
Peak 1 Mean by Intensity ordered by size (nm)	1,488	0,4558	30,64	1,04	1,951
Peak 2 Area by Intensity ordered by size (%)	84,75	4,27	5,038	80,03	88,34
Peak 2 Mean by Intensity ordered by size (nm)	76,23	21,91	28,74	56,86	100

Figure A5. DLS spectra of peptidomimetic **120j.**

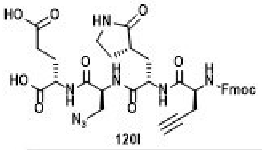

120l

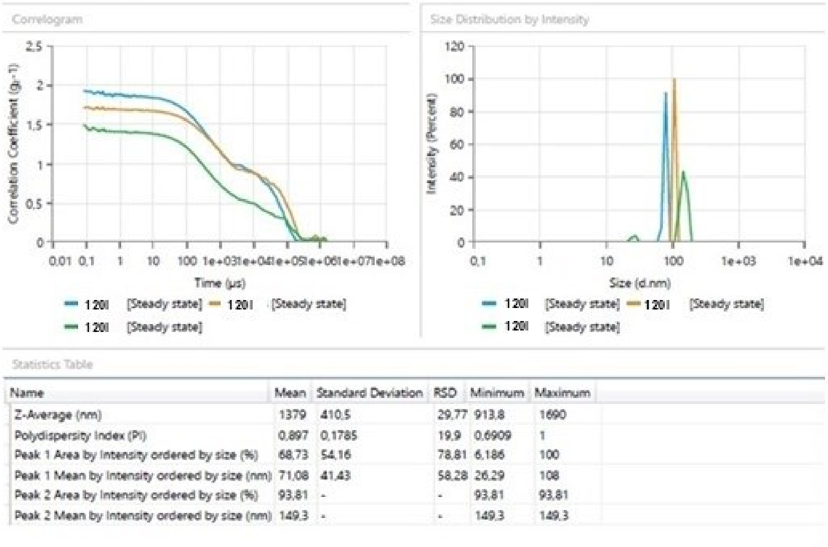

Name	Mean	Standard Deviation	RSD	Minimum	Maximum
Z-Average (nm)	1379	410,5	29,77	913,8	1690
Polydispersity Index (PI)	0,897	0,1785	19,9	0,6909	1
Peak 1 Area by Intensity ordered by size (%)	68,73	54,16	78,81	6,186	100
Peak 1 Mean by Intensity ordered by size (nm)	71,08	41,43	58,28	26,29	108
Peak 2 Area by Intensity ordered by size (%)	93,81	-	-	93,81	93,81
Peak 2 Mean by Intensity ordered by size (nm)	149,3	-	-	149,3	149,3

Figure A6. DLS spectra of peptidomimetic **120l.**

NMR characterisation of compound 120a

1D NMR spectra (^{1}H NMR and ^{13}C NMR) and 2D NMR spectra (COSY and NOESY) were recorded on a Bruker 400 MHz spectrometer, with TMS as the internal standard. 2D NMR spectra were acquired as reported: for DQF-COSY, relaxation delay 1.5 s, recorded in phase sensitive mode; for NOESY, relaxation delay 2 s, mixing time 0.35 s, recorded in phase sensitive with gradients mode.

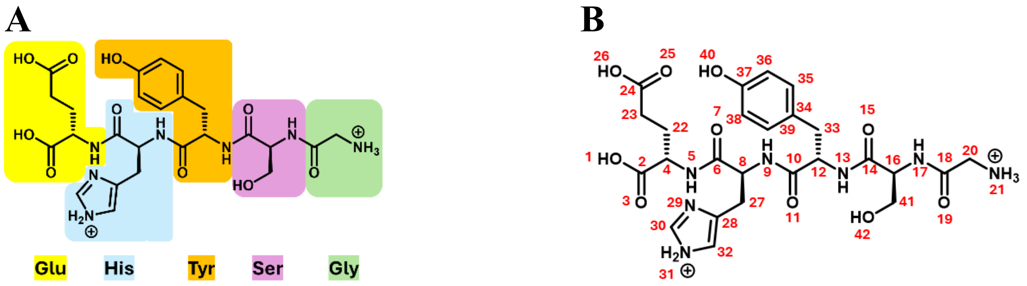

Figure A7. A) Amino acid residues of compound **120a** identified by colour. B) Chemical structure of compound **120a**, with numbered structural features.

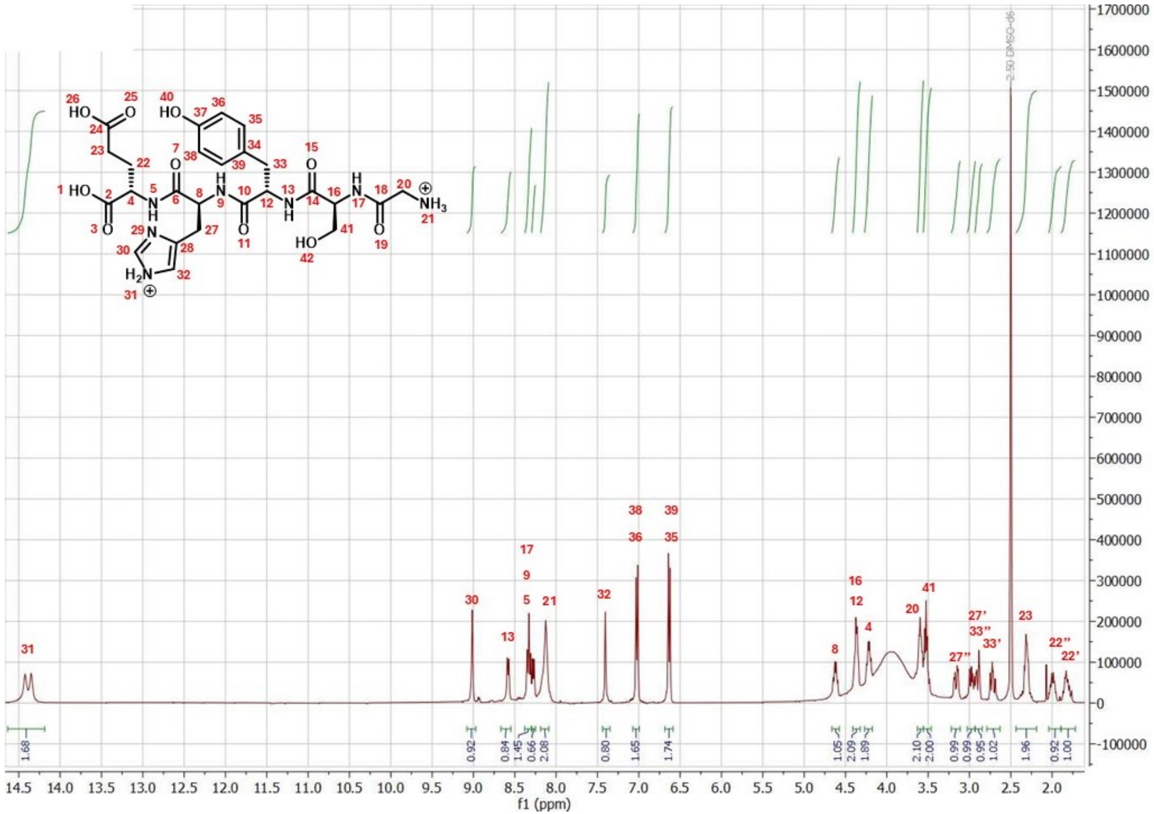

Figure A8. ^{1}H NMR spectrum of compound **120a** and proposed peak assignments.

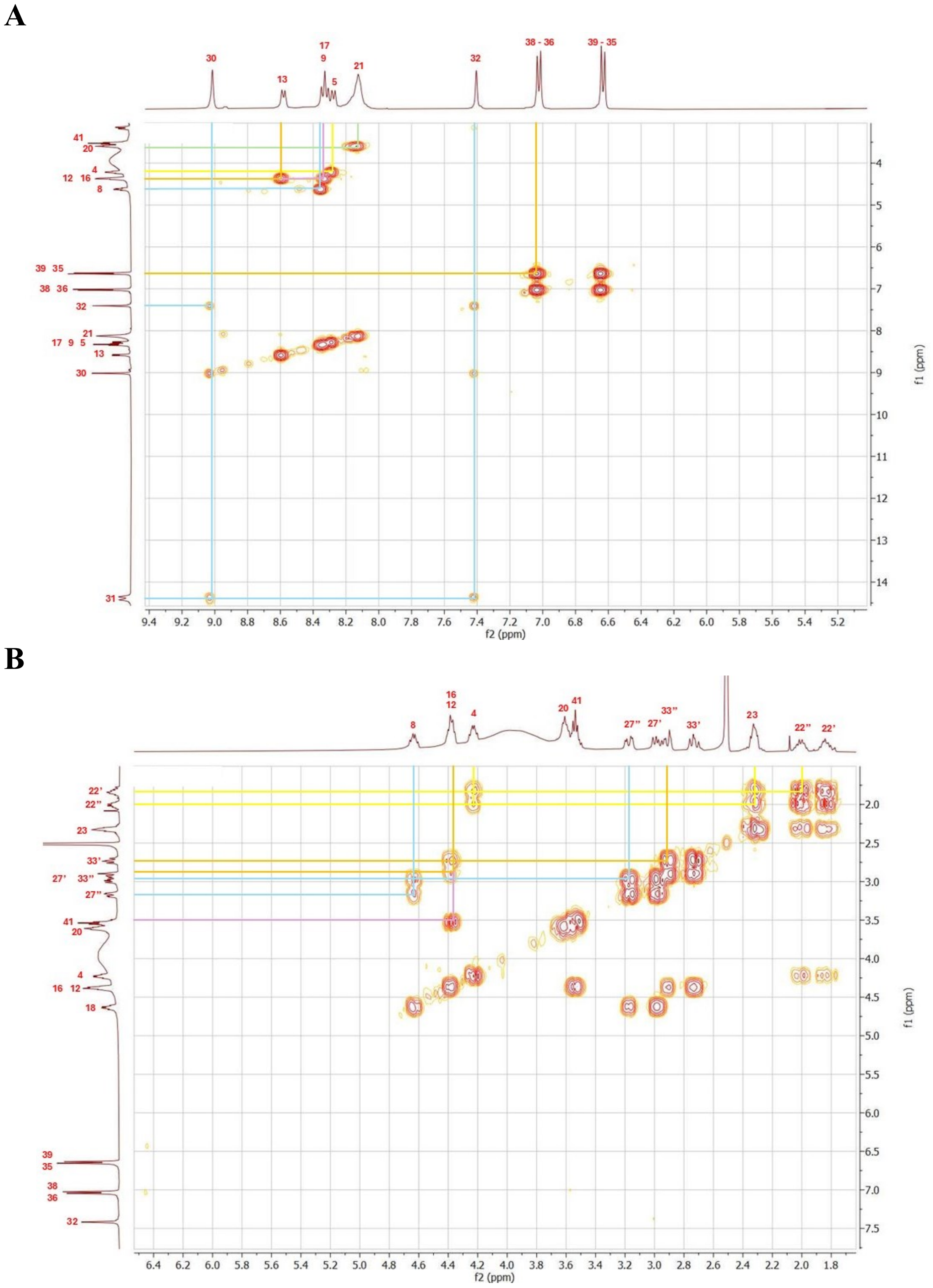

Figure A9. Focused views of regions A (9.4 – 5.0 ppm horizontal; 3.0 – 14.5 ppm vertical) and B (6.5 – 1.7 ppm horizontal; 1.0 – 7.7 ppm vertical) of COSY spectrum of compound **120a**.

Table A1. Summary of COSY experiment data and proposed peak assignments.

Assignment	δ (ppm)	δ (ppm)	Assignment
31	14.35	9	**30**
		7.43	**32**
30	9	14.35	**31**
		7.43	**32**
13	8.59	4.38	**12**
9 – 17	8.32	4.38	**16**
		4.62	**8**
5	8.29	4.24	**4**
21	8.13	3.59	**20**
32	7.43	14.35	**31**
		9	**30**
36 – 38	7.02	6.63	**35 – 39**
35 – 39	6.63	7.02	**36 – 38**
8	4.62	8.32	**9**
		3.17	**27”**
		2.98	**27’**
12 - 16	4.38	8.59	**13**
		8.32	**17**
		3.52	**41**
		2.91	**33”**
		2.73	**33’**
4	4.24	8.29	**5**
		1.99	**22”**
		1.80	**22’**
20	3.59	8.13	**21**
41	3.52	4.38	**16**
27”	3.17	4.62	**8**
		2.98	**27’**
27’	2.98	4.62	**8**
		3.17	**27”**
33”	2.91	4.38	**12**
		2.73	**33’**
33’	2.73	4.38	**12**
		2.91	**33”**
23	2.31	1.99	**22”**
		1.80	**22’**
22”	1.99	4.24	**4**
		2.31	**23**
		1.80	**22’**
22’	1.80	4.24	**4**
		2.31	**23**
		1.99	**22”**

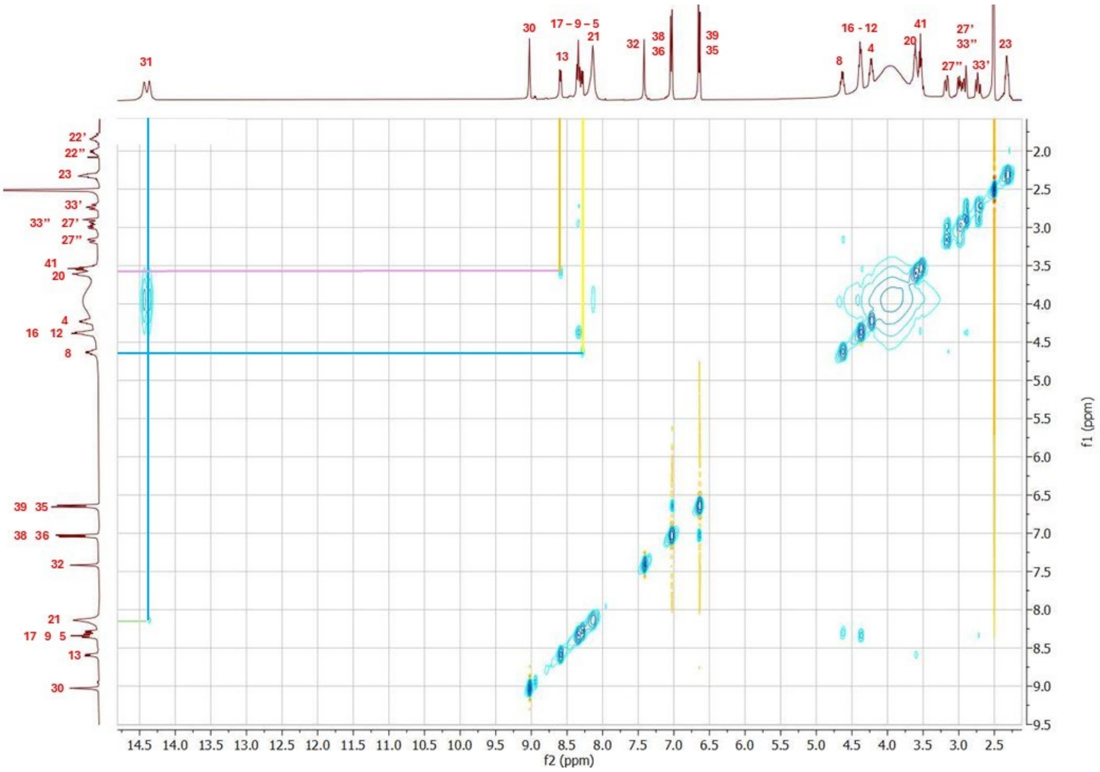

Figure A10. Focused view of NOESY spectrum of compound **120a**.

Table A2. Summary of NOESY experiment data and proposed peak assignments.

Assignment	δ (ppm)	δ (ppm)	Assignment
31	14.35	8.13	**21**
13	8.59	3.59	**20**
5	8.29	4.62	**8**
21	8.13	14.35	**31**
8	4.62	8.29	**5**
20	3.59	8.59	**13**

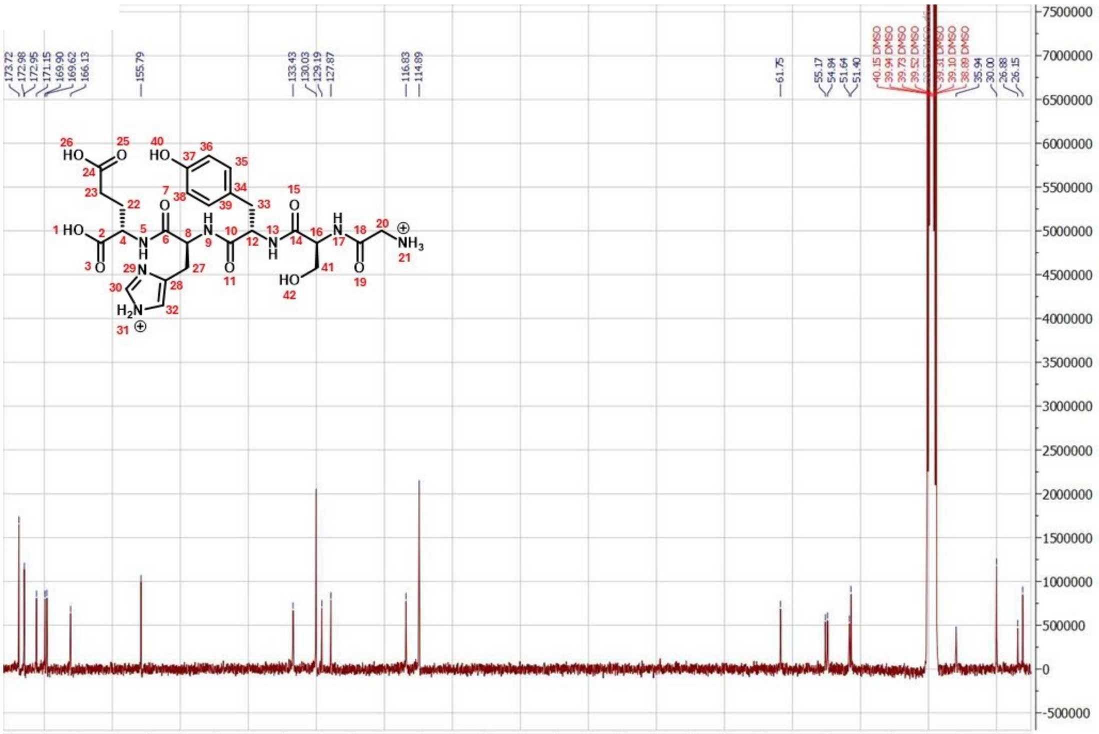

Figure A11. ^{13}C NMR spectrum of compound **120a**.

5. Bibliography

1. Hardy, K. Paleomedicine and the Evolutionary Context of Medicinal Plant Use. *Rev. Bras. Farmacogn.* **1**, 1–15 (2021).
2. Crane-Kramer, G. & Buckberry, J. Changes in health with the rise of industry. *Int. J. Paleopathol.* **40**, 99–102 (2023).
3. The top 10 causes of death. *World Health Organization* https://www.who.int/news-room/fact-sheets/detail/the-top-10-causes-of-death (2024).
4. Cancer. *World Health Organization* https://www.who.int/news-room/fact-sheets/detail/cancer (2025).
5. Rojas, N. G. *et al.* Neurodegenerative diseases and cancer: Sharing common mechanisms in complex interactions. *J. Integr. Neurosci*. **19**, 187–199 (202
6. Driver, J. A. Understanding the link between cancer and neurodegeneration. *J. Geriatr. Oncol.* **3**, 58–67 (2012).
7. Steinmetz, J. D. *et al.* Global, regional, and national burden of disorders affecting the nervous system, 1990–2021: a systematic analysis for the Global Burden of Disease Study 2021. *Lancet Neurol.* **23**, 344–381 (2024).
8. Gadhave, D. G. *et al.* Neurodegenerative disorders: Mechanisms of degeneration and therapeutic approaches with their clinical relevance. *Ageing Res. Rev.* **99**, 102357 (2024).
9. Bloomingdale, P. *et al.* Hallmarks of neurodegenerative disease: A systems pharmacology perspective. *CPT: Pharmacomet. Syst. Pharmacol.* **11**, 1399–1429 (2022).
10. Lardenoije, R. *et al.* The epigenetics of aging and neurodegeneration. *Prog. Neurobiol.* **131**, 21–64 (2015).
11. Hwang, J. Y., *et al.* The emerging field of epigenetics in neurodegeneration and neuroprotection. *Nat. Rev. Neurosci.* **18**, 347–361 (2017).
12. Klineova, S. & Lublin, F. D. Clinical course of multiple sclerosis. *Cold Spring Harb. Perspect. Med.* **8** (2018).
13. Olsson, T., *et al.* Interactions between genetic, lifestyle and environmental risk factors for multiple sclerosis. *Nat. Rev. Neurol.* **13**, 26–36 (2016).
14. Murúa, S. R., *et al.* The Immune Response in Multiple Sclerosis. *Annu. Rev. Pathol. Mech. Dis.* **17**, 121–139 (2022).
15. Tepavčević, V. & Lubetzki, C. Oligodendrocyte progenitor cell recruitment and remyelination in multiple sclerosis: the more, the merrier? *Brain* **145**, 4178–4192 (2022).
16. Wang, Q. *et al.* Oligodendroglial precursor cells modulate immune response and early demyelination in a murine model of multiple sclerosis. *Sci. Transl. Med.* **17**, (2025).
17. Hauser, S. L. & Cree, B. A. C. Treatment of Multiple Sclerosis: A Review. *Am. J. Med.* **133**, 1380-1390 (2020).
18. Dobson, R. & Giovannoni, G. Multiple sclerosis – a review. *Eur J Neurol.* **26**, 27–40 (2019).
19. Jalkh, G., *et al.* Safety of newer disease modifying therapies in multiple sclerosis. *Vaccines* **9** 1–30 (2021).
20. Rudick, R. A. *et al.* Natalizumab plus Interferon Beta-1a for Relapsing Multiple Sclerosis. *N. Engl. J. Med.* **354**, 911–923 (2006).
21. Papa, A. *et al.* Polypharmacological Approaches for CNS Diseases: Focus on Endocannabinoid Degradation Inhibition. *Cells* **11**, (2022).

22. Albertini, C., *et al.* From combinations to multitarget-directed ligands: A continuum in Alzheimer's disease polypharmacology. *Med. Res. Rev.* **41** 2606–2633 (2021).
23. Epilepsy. *World Health Organization* https://www.who.int/news-room/fact-sheets/detail/epilepsy (2024).
24. Beniczky, S. *et al.* Updated classification of epileptic seizures: Position paper of the International League Against Epilepsy. *Epilepsia* **66**, 1804–1823 (2025).
25. Barone, V., *et al.* Absence epilepsy: Characteristics, pathophysiology, attention impairments, and the related risk of accidents. A narrative review. *Epilepsy Behav.* **112** 107342 (2020).
26. Crunelli, V. *et al.* Clinical and experimental insight into pathophysiology, comorbidity and therapy of absence seizures. *Brain* **143** 2341–2368 (2020).
27. Sarkisova, K. & van Luijtelaar, G. The impact of early-life environment on absence epilepsy and neuropsychiatric comorbidities. *IBRO Neurosci. Rep.* **13** 436–468 (2022).
28. Leitch, B. Molecular Mechanisms Underlying the Generation of Absence Seizures: Identification of Potential Targets for Therapeutic Intervention. *Int. J. Mol. Sci.* **25**, 9821 (2024).
29. Auvin, S. *et al.* Systematic review of the screening, diagnosis, and management of ADHD in children with epilepsy. Consensus paper of the Task Force on Comorbidities of the ILAE Pediatric Commission. *Epilepsia* **59**, 1867–1880 (2018).
30. Menon, R. N. & Helen Cross, J. Childhood epilepsy. *The Lancet* **406**, 636–649 (2025).
31. Anighoro, A., *et al.* Polypharmacology: Challenges and Opportunities in Drug Discovery. *J. Med. Chem* **57**, 7874–7887 (2014).
32. Kabir, A. & Muth, A. Polypharmacology: The science of multi-targeting molecules. *Pharmacol. Res.* **176**, 106055 (2022).
33. Proschak, E., *et al.* Polypharmacology by Design: A Medicinal Chemist's Perspective on Multitargeting Compounds. *J. Med. Chem.* **62**, 420–444 (2019).
34. Zhou, J. *et al.* Rational Design of Multitarget-Directed Ligands: Strategies and Emerging Paradigms. *J. Med. Chem.* **62**, 8881–8914 (2019).
35. Kogan, N. M. & Mechoulam, R. Cannabinoids in health and disease. *Dialogues Clin. Neurosci.* **9**, 413–430 (2007).
36. Bonini, S. A. *et al.* Cannabis sativa: A comprehensive ethnopharmacological review of a medicinal plant with a long history. *J. Ethnopharmacol.* **227**, 300–315 (2018).
37. Mackie, K. Cannabinoid receptors: Where they are and what they do. *J. Neuroendocrinol.* **20**, 10–14 (2008).
38. Cascio, M. G. & Marini, P. Biosynthesis and fate of endocannabinoids. *Handb. Exp. Pharmacol.* **231**, 39–58 (2015).
39. Mechaoulam, R. *et al.* Identification of an endogenous 2-monoglyceride, present in canine gut, that binds to cannabinoid receptors. *Biochem. Pharmacol.* **50**, 83–90 (1995).
40. Pertwee, R. G. *et al.* International Union of Basic and Clinical Pharmacology. LXXIX. Cannabinoid receptors and their ligands: Beyond CB1 and CB2. *Pharmacol. Rev.* **62**, 588–631 (2010).
41. Muccioli, G. G. Endocannabinoid biosynthesis and inactivation, from simple to complex. *Drug Discov. Today* **15**, 474–483 (2010).

42. Brunt, T. M. & Bossong, M. G. The neuropharmacology of cannabinoid receptor ligands in central signaling pathways. *Eur. J. Neurosci* **55**, 909–921 (2022).
43. Manning, J. J., *et al.* Pharmacological selection of cannabinoid receptor effectors: Signalling, allosteric modulation and bias. *Neuropharmacology* **193**, 108611 (2021).
44. Ibsen, M. S., *et al.* Cannabinoid CB1 and CB2 Receptor Signaling and Bias. *Cannabis Cannabinoid Res.* **2**, 48–60 (2017).
45. Urquhart, P., *et al.* Endocannabinoids and their oxygenation by cyclo-oxygenases, lipoxygenases and other oxygenases. *Biochim. Biophys. Acta Mol. Cell Biol. Lipids* **1851**, 366–376 (2015).
46. Van Egmond, N., *et al.* Targeting Endocannabinoid Signaling: FAAH and MAG Lipase Inhibitors. *Annu. Rev. Pharmacol. Toxicol.* **61**, 441–461 (2021).
47. Ahn, K., *et al.* Enzymatic pathways that regulate endocannabinoid signaling in the nervous system. *Chem- Rev.* **108**, 1687–1707 (2008).
48. Labar, G. *et al.* Crystal structure of the human monoacylglycerol lipase, a key actor in endocannabinoid signaling. *ChemBioChem* **11**, 218–227 (2010).
49. Tuo, W. *et al.* Therapeutic Potential of Fatty Acid Amide Hydrolase, Monoacylglycerol Lipase, and N-Acylethanolamine Acid Amidase Inhibitors. *J. Med. Chem.* **60**, 4–46 (2017).
50. Palermo, G. *et al.* Keys to Lipid Selection in Fatty Acid Amide Hydrolase Catalysis: Structural Flexibility, Gating Residues and Multiple Binding Pockets. *PLoS Comput. Biol.* **11**, 4-46 (2015).
51. King, A. R. *et al.* A critical cysteine residue in monoacylglycerol lipase is targeted by a new class of isothiazolinone-based enzyme inhibitors. *Br. J. Pharmacol.* **157**, 974–983 (2009).
52. Gil-Ordóñez, A., Martín-Fontecha, M., Ortega-Gutiérrez, S. & López-Rodríguez, M. L. Monoacylglycerol lipase (MAGL) as a promising therapeutic target. *Biochem. Pharmacol.* **157**, 18–32 (2018).
53. Kapanda, C. N. *et al.* Synthesis and pharmacological evaluation of 2,4-dinitroaryldithiocarbamate derivatives as novel monoacylglycerol lipase inhibitors. *J. Med. Chem.* **55**, 5774–5783 (2012).
54. Cisar, J. S. *et al.* Identification of ABX-1431, a Selective Inhibitor of Monoacylglycerol Lipase and Clinical Candidate for Treatment of Neurological Disorders. *J. Med. Chem.* **61**, 9062–9084 (2018).
55. Müller-Vahl, K. R. *et al.* Monoacylglycerol Lipase Inhibition in Tourette Syndrome: A 12-Week, Randomized, Controlled Study. *Movement Disorders* **36**, 2413–2418 (2021).
56. Bertrand, T. *et al.* Structural Basis for Human Monoglyceride Lipase Inhibition. *J. Mol. Biol.* **396**, 663–673 (2010).
57. Aaltonen, N. *et al.* Piperazine and piperidine triazole ureas as ultrapotent and highly selective inhibitors of monoacylglycerol lipase. *Chem. Biol.* **20**, 379–390 (2013).
58. Brindisi, M. *et al.* Development and Pharmacological Characterization of Selective Blockers of 2-Arachidonoyl Glycerol Degradation with Efficacy in Rodent Models of Multiple Sclerosis and Pain. *J. Med. Chem.* **59**, 2612–2632 (2016).
59. Butini, S. *et al.* Development of Potent and Selective Monoacylglycerol Lipase Inhibitors. SARs, Structural Analysis, and Biological Characterization. *J. Med. Chem.* **67**, 1758–1782 (2024).

60. Deng, H. & Li, W. Monoacylglycerol lipase inhibitors: modulators for lipid metabolism in cancer malignancy, neurological and metabolic disorders. *Acta Pharm. Sin. B.* **10**, 582–602 (2020).
61. Farrell, E. K. & Merkler, D. J. Biosynthesis, degradation and pharmacological importance of the fatty acid amides. *Drug Discov. Today* **13**, 558–568 (2008).
62. Wei, B. Q., *et al.* second fatty acid amide hydrolase with variable distribution among placental mammals. *J. Biol. Chem.* **281**, 36569–36578 (2006).
63. Egertová, M., *et al.* Comparative analysis of fatty acid amide hydrolase and CB1 cannabinoid receptor expression in the mouse brain: Evidence of a widespread role for fatty acid amide hydrolase in regulation of endocannabinoid signaling. *Neuroscience* **119**, 481–496 (2003).
64. Mauro, M. *et al.* Structure-guided inhibitor design for human FAAH by interspecies active site conversion. *Proc Natl Acad Sci U S A* **105**, 12820–12824 (2008).
65. Mileni, M. *et al.* Binding and inactivation mechanism of a humanized fatty acid amide hydrolase by α-ketoheterocycle inhibitors revealed from cocrystal structures. *J. Am. Chem. Soc.* **131**, 10497–10506 (2009).
66. Tripathi, R. K. P. A perspective review on fatty acid amide hydrolase (FAAH) inhibitors as potential therapeutic agents. *Eur. J. Med. Chem.* **188**, 111953 (2020).
67. Otrubova, K., *et al.* The discovery and development of inhibitors of fatty acid amide hydrolase (FAAH). *Bioorg. Med. Chem. Lett.* **21**, 4674–4685 (2011).
68. Tarzia, G. *et al.* Design, synthesis, and structure - Activity relationships of alkylcarbamic acid aryl esters, a new class of fatty acid amide hydrolase inhibitors. *J. Med. Chem.* **46**, 2352–2360 (2003).
69. Alexander, J. P. & Cravatt, B. F. Mechanism of carbamate inactivation of FAAH: Implications for the design of covalent inhibitors and in vivo functional probes for enzymes. *Chem. Biol.* **12**, 1179–1187 (2005).
70. Butini, S. *et al.* Discovery of potent inhibitors of human and mouse fatty acid amide hydrolases. *J. Med. Chem.* **55**, 6898–6915 (2012).
71. Grillo, A. *et al.* Selective Fatty Acid Amide Hydrolase Inhibitors as Potential Novel Antiepileptic Agents. *ACS Chem. Neurosci.* **12**, 1716–1736 (2021).
72. Papa, A. *et al.* Development of potent and selective FAAH inhibitors with improved drug-like properties as potential tools to treat neuroinflammatory conditions. *Eur. J. Med. Chem.* **246**,114952 (2023).
73. Ahn, K. *et al.* Novel mechanistic class of fatty acid amide hydrolase inhibitors with remarkable selectivity. *Biochemistry* **46**, 13019–13030 (2007).
74. Ahn, K. *et al.* Discovery and Characterization of a Highly Selective FAAH Inhibitor that Reduces Inflammatory Pain. *Chem. Biol.* **16**, 411–420 (2009).
75. Maccarrone, M. *et al.* Goods and Bads of the Endocannabinoid System as a Therapeutic Target: Lessons Learned after 30 Years. *Pharmacol. Rev.* **75**, 885–958 (2023).
76. Vasincu, A. *et al.* Endocannabinoid Modulation in Neurodegenerative Diseases: In Pursuit of Certainty. *Biology* **11**, 440 (2022).
77. Chen, R. *et al.* Monoacylglycerol Lipase Is a Therapeutic Target for Alzheimer's Disease. *Cell Rep.* **2**, 1329–1339 (2012).
78. Pihlaja, R. *et al.* Monoacylglycerol lipase inhibitor JZL184 reduces neuroinflammatory response in APdE9 mice and in adult mouse glial cells. *J. Neuroinflammation* **12**, 81 (2015).

79. Hashem, J., *et al.* Inhibition of 2-Arachidonoylglycerol Metabolism Alleviates Neuropathology and Improves Cognitive Function in a Tau Mouse Model of Alzheimer's Disease. *Mol. Neurobiol.* **58**, 4122–4133 (2021).
80. Fernández-Suárez, D. *et al.* The monoacylglycerol lipase inhibitor JZL184 is neuroprotective and alters glial cell phenotype in the chronic MPTP mouse model. *Neurobiol. Aging* **35**, 2603–2616 (2014).
81. Mounsey, R. B. *et al.* Increasing levels of the endocannabinoid 2-AG is neuroprotective in the 1-methyl-4-phenyl-1,2,3,6-tetrahydropyridine mouse model of Parkinson's disease. *Exp. Neurol.* **273**, 36–44 (2015).
82. Aymerich, M. S. *et al.* Neuroprotective Effect of JZL184 in MPP+-Treated SH-SY5Y Cells Through CB2 Receptors. *Mol. Neurobiol.* **53**, 2312–2319 (2016).
83. Bernal-Chico, A. *et al.* Blockade of monoacylglycerol lipase inhibits oligodendrocyte excitotoxicity and prevents demyelination in vivo. *Glia* **63**, 163–176 (2015).
84. Johnston, T. H. *et al.* Fatty Acid Amide Hydrolase (FAAH) inhibition reduces L-3,4- dihydroxyphenylalanine-induced hyperactivity in the 1-methyl-4-phenyl-1,2,3,6- tetrahydropyridine-lesioned non-human primate model of Parkinson's disease. *J. Pharmacol. Exp. Ther.* **336**, 423–430 (2011).
85. Escamilla-Ramírez, A. *et al.* URB597 and the Cannabinoid WIN55,212-2 Reduce Behavioral and Neurochemical Deficits Induced by MPTP in Mice: Possible Role of Redox Modulation and NMDA Receptors. *Neurotox. Res.* **31**, 532–544 (2017).
86. Grieco, M. *et al.* Fatty acid amide hydrolase (Faah) inhibition modulates amyloid-beta-induced microglia polarization. *Int. J. Mol. Sci.* **22**, 7711 (2021).
87. Armeli, F. *et al.* FAAH Inhibition Counteracts Neuroinflammation via Autophagy Recovery in AD Models. *Int. J. Mol. Sci.* **25**, 12044 (2024).
88. Grillo, A. *et al.* Development of novel multipotent compounds modulating endocannabinoid and dopaminergic systems. *Eur. J. Med. Chem.* **183**, 111674 (2019).
89. Papa, A. *et al.* Pioneering first-in-class FAAH-HDAC inhibitors as potential multitarget neuroprotective agents. *Arch. Pharm. (Weinheim).* **356**, e2300410 (2023).
90. Yuan, D., *et al.* Evolution of the diacylglycerol lipases. *Prog. Lipid Res.* **64**, 85–97 (2016).
91. Reisenberg, M., *et al.* The diacylglycerol lipases: Structure, regulation and roles in and beyond endocannabinoid signalling. *Philos. Trans. R. Soc. B.* **367**, 3264–3275 (2012).
92. Matheson, J., *et al.* Potential of Fatty Acid Amide Hydrolase (FAAH), Monoacylglycerol Lipase (MAGL), and Diacylglycerol Lipase (DAGL) Enzymes as Targets for Obesity Treatment: A Narrative Review. *Pharmaceuticals* **14**,1316 (2021).
93. Winters, N. D. *et al.* Targeting diacylglycerol lipase reduces alcohol consumption in preclinical models. *J Clin Invest.* **131**, e146861 (2021).
94. Wilkerson, J. L. *et al.* Diacylglycerol lipase β inhibition reverses nociceptive behaviour in mouse models of inflammatory and neuropathic pain. *Br. J. Pharmacol.* **173**, 1678–1692 (2016).
95. Wilkerson, J. L. *et al.* Investigation of diacylglycerol lipase alpha inhibition in the mouse lipopolysaccharide inflammatory pain model[s]. *J. Pharmacol. Exp. Ther.* **363**, 394–401 (2017).

96. Janssen, F. J. & van der Stelt, M. Inhibitors of diacylglycerol lipases in neurodegenerative and metabolic disorders. *Bioorg. Med. Chem. Lett.* **26**, 3831–3837 (2016).
97. Hsu, K. L. *et al.* DAGLβ inhibition perturbs a lipid network involved in macrophage inflammatory responses. *Nat. Chem. Biol.* **8**, 999–1007 (2012).
98. Ogasawara, D. *et al.* Rapid and profound rewiring of brain lipid signaling networks by acute diacylglycerol lipase inhibition. *Proc. Natl. Acad. Sci. U. S. A.* **113**, 26–33 (2016).
99. Deng, H. *et al.* Triazole Ureas Act as Diacylglycerol Lipase Inhibitors and Prevent Fasting-Induced Refeeding. *J. Med. Chem.* **60**, 428–440 (2017).
100. Janssen, A. P. A. *et al.* Structure Kinetics Relationships and Molecular Dynamics Show Crucial Role for Heterocycle Leaving Group in Irreversible Diacylglycerol Lipase Inhibitors. *J. Med. Chem.* **62**, 7910–7922 (2019).
101. Deng, H. *et al.* Chiral disubstituted piperidinyl ureas: A class of dual diacylglycerol lipase-α and ABHD6 inhibitors. *Medchemcomm* **8**, 982–988 (2017).
102. Niphakis, M. J., *et al.* O-hydroxyacetamide carbamates as a highly potent and selective class of endocannabinoid hydrolase inhibitors. in *ACS Chem. Neurosci.* **3**, 418–426 (2012).
103. Jaiswal, S., *et al.* Synthesis and evaluation of dual fatty acid amide hydrolase-monoacylglycerol lipase inhibition and antinociceptive activities of 4-methylsulfonylaniline-derived semicarbazones. *Bioorg. Med. Chem.* **60**, (2022).
104. Barth, M. *et al.* Hexafluoroisopropyl Carbamates as Selective MAGL and Dual MAGL/FAAH Inhibitors: Biochemical and Physicochemical Properties. *ChemMedChem* **17**, e202100757 (2022).
105. Bajaj, S., *et al.* Effect of the MAGL/FAAH Dual Inhibitor JZL-195 on Streptozotocin-Induced Alzheimer's Disease-like Sporadic Dementia in Mice with an Emphasis on Aβ, HSP-70, Neuroinflammation, and Oxidative Stress. *ACS Chem. Neurosci.* **13**, 920–932 (2022).
106. Adamson Barnes, N. S., *et al.* Actions of the dual FAAH/MAGL inhibitor JZL195 in a murine neuropathic pain model. *Br. J. Pharmacol.* **173**, 77–87 (2016).
107. Brindisi, M. *et al.* Harnessing the pyrroloquinoxaline scaffold for FAAH and MAGL interaction: Definition of the structural determinants for enzyme inhibition. *RSC Adv.* **6**, 64651–64664 (2016).
108. Matuszak, N. *et al.* Dual inhibition of MAGL and type II topoisomerase by N-phenylmaleimides as a potential strategy to reduce neuroblastoma cell growth. *European Journal of Pharmaceutical Sciences* **45**, 263–271 (2012).
109. Peng, X. *et al.* Structural basis for recognition of antihistamine drug by human histamine receptor. *Nat. Commun.* **13**, 6105 (2022).
110. Chen, Y. *et al.* Histamine receptor 3 negatively regulates oligodendrocyte differentiation and remyelination. *PLoS One* **12**, e0189380 (2017).
111. Esbenshade, T. A. *et al.* The histamine H 3 receptor: An attractive target for the treatment of cognitive disorders. *Br. J. Pharmacol.* **154** 1166–1181 (2008).
112. Szczepanska, K., *et al.* Histamine H3 Receptor Ligands in the Group of (Homo)piperazine Derivatives. *Curr. Med. Chem.* **25**, 1609–1626 (2017).
113. Singh, M. & Jadhav, H. R. Histamine H3 Receptor Function and Ligands: Recent Developments. *Mini Rev. Med. Chem.* **13**, 47–57 (2013).
114. Schwartz, J.-C. The histamine H3 receptor: from discovery to clinical trials with pitolisant *Br. J. Pharmacol.* **163**, 713–721 (2011).

115. Wang, J. *et al.* Histamine H3R antagonist counteracts the impaired hippocampal neurogenesis in Lipopolysaccharide-induced neuroinflammation. *Int. Immunopharmacol.* **110**, 109045 (2022).
116. Zhou, Z. *et al.* Histamine and receptors in neuroinflammation: Their roles on neurodegenerative diseases. *Behav. Brain Res.* **465**, 114964 (2024).
117. Thomas, S. D. *et al.* Targeting Microglia in Neuroinflammation: H3 Receptor Antagonists as a Novel Therapeutic Approach for Alzheimer's Disease, Parkinson's Disease, and Autism Spectrum Disorder. *Pharmaceuticals* **17**, 831 (2024).
118. Khanfar, M. A. *et al.* Multiple targeting approaches on histamine H3 receptor antagonists. *Front. Neurosci.* **10**, 201 (2016).
119. Hagenow, S. *et al.* Adenosine A2AR/A1R Antagonists Enabling Additional H3R Antagonism for the Treatment of Parkinson's Disease. *J. Med. Chem.* **64**, 8246–8262 (2021).
120. Łażewska, D. *et al.* Multitargeting Histamine H3 Receptor Ligands among Acetyl- and Propionyl-Phenoxyalkyl Derivatives. *Molecules* **28**, 2349 (2023).
121. Rangon, C. M. *et al.* Myelination induction by a histamine H3 receptor antagonist in a mouse model of preterm white matter injury. *Brain Behav. Immun.* **74**, 265–276 (2018).
122. Schwartzbach, C. J. *et al.* Lesion remyelinating activity of GSK239512 versus placebo in patients with relapsing-remitting multiple sclerosis: a randomised, single-blind, phase II study. *J. Neurol.* **264**, 304–315 (2017).
123. Imeri, F. *et al.* Novel compounds with dual S1P receptor agonist and histamine H3 receptor antagonist activities act protective in a mouse model of multiple sclerosis. *Neuropharmacology* **186**, 108464 (2021).
124. Bonaventure, P. *et al.* Histamine H3 receptor antagonists: From target identification to drug leads. *Biochem. Pharmacol.* **73**, 1084–1096 (2007).
125. Falkenstein, M. *et al.* Histamine H3 receptor antagonists with peptidomimetic (keto)piperazine structures to inhibit Aβ oligomerisation. *Bioorg. Med. Chem.* **50**, (2021).
126. Look, G. *et al.* Trimethylorthoformate: A mild and effective dehydrating reagent for solution and solid phase imine formation. *Tetrahedron Lett.* **36**, 2937–2940 (1995).
127. Zhang, L. J., *et al.* Ytterbium Triflate: A Versatile Catalyst in Organic Synthesis. *Curr. Org. Chem.* **17**, 2906–2920 (2013).
128. Lopez-Suarez, L., *et al.* The SH-SY5Y human neuroblastoma cell line, a relevant in vitro cell model for investigating neurotoxicology in human: Focus on organic pollutants. *Neurotoxicology* **92**, 131–155 (2022).
129. Di Venere, A. *et al.* Rat and human fatty acid amide hydrolases: Overt similarities and hidden differences. *Biochim. Biophys. Acta Mol. Cell Biol. Lipids.* **1821**, 1425–1433 (2012).
130. Scalvini, L., *et al.* Monoglyceride lipase: Structure and inhibitors. *Chem. Phys. Lipids* **197**, 13–24 (2016).
131. Humpel, C. Organotypic brain slice cultures: A review. *Neuroscience* **305**, 86–98 (2015).
132. Croft, C. L., *et al.* Organotypic brain slice cultures to model neurodegenerative proteinopathies. *Mol. Neurodegener.* **14**, 45 (2019).
133. De Kleijn, K. M. A., *et al.* Reappraisal of human hog and MO3.13 cell lines as a model to study oligodendrocyte functioning. *Cells* **8**, (2019).

134. Martinsen, V. & Kursula, P. Multiple sclerosis and myelin basic protein: insights into protein disorder and disease. *Amino Acids* **54**, 99–109 (2022).
135. Hogg, S. J., *et al.* Targeting the epigenetic regulation of antitumour immunity. *Nat. Rev. Drug Discov.* **19**, 776–800 (2020).
136. Ho, T. C. S., *et al.* Thirty Years of HDAC Inhibitors: 2020 Insight and Hindsight. *J. Med. Chem.* **63**, 12460–12484 (2020).
137. Hai, Y. & Christianson, D. W. Histone deacetylase 6 structure and molecular basis of catalysis and inhibition. *Nat. Chem. Biol.* **12**, 741–747 (2016).
138. Brindisi, M. *et al.* Old but Gold: Tracking the New Guise of Histone Deacetylase 6 (HDAC6) Enzyme as a Biomarker and Therapeutic Target in Rare Diseases. *J. Med. Chem.* **63**, 23–39 (2020).
139. Magupalli, V. G. *et al.* HDAC6 mediates an aggresome-like mechanism for NLRP3 and pyrin inflammasome activation. *Science* **369**, eaas8995 (2020).
140. Shukla, S. & Tekwani, B. L. Histone Deacetylases Inhibitors in Neurodegenerative Diseases, Neuroprotection and Neuronal Differentiation. *Front. Pharmacol.* **11**, (2020).
141. Zhang, L. Y, *et al.* Role of histone deacetylases and their inhibitors in neurological diseases. *Pharmacol. Res.* **208**, 107410 (2024).
142. Tavares, M. T., *et al.* Mercaptoacetamide: A promising zinc-binding group for the discovery of selective histone deacetylase 6 inhibitors. *Eur. J. Med. Chem.* **209**,112887 (2021).
143. Raucci, A., *et al.* Advancements in Hydrazide-Based HDAC Inhibitors: A Review of Recent Developments and Therapeutic Potential. *J. Med. Chem.* **68**, 14171-14194 (2025).
144. Banerjee, S., *et al.* Histone deacetylase 8 (HDAC8) and its inhibitors with selectivity to other isoforms: An overview. *Eur. J. Med. Chem.* **164**, 214–240 (2019).
145. Pulya, S. *et al.* HDAC6 as privileged target in drug discovery: A perspective. *Pharmacol. Res.* **163**, 105274 (2021).
146. El Omari, N. *et al.* Clinical efficacy and mechanistic insights of FDA-approved HDAC inhibitors in the treatment of lymphoma. *Eur. J. Pharm. Sci.* **208**, 107057 (2025).
147. Subramanian, S., *et al.* Clinical toxicities of histone deacetylase inhibitors. *Pharmaceuticals* **3**, 2751–2767 (2010).
148. Dang, B. *et al.* Histone deacetylase 6 inhibitors in Alzheimer's disease therapy: structure design and challenges. *Bioorg. Med. Chem. Lett.* **127**, 130318 (2025).
149. Lopresti, P. The selective HDAC6 inhibitor ACY-738 sneaks into memory and disease regulation in an animal model of multiple sclerosis. *Front. Neurol.* **10**, (2019).
150. Bae, D. *et al.* CKD-506: A novel HDAC6-selective inhibitor that exerts therapeutic effects in a rodent model of multiple sclerosis. *Sci. Rep.* **11**, 14466 (2021).
151. Yan, S. *et al.* Pharmacological Inhibition of HDAC6 Attenuates NLRP3 Inflammatory Response and Protects Dopaminergic Neurons in Experimental Models of Parkinson's Disease. *Front. Aging Neurosci.* **12**, 78 (2020).
152. Pham, K. Y. *et al.* HDAC6 inhibitor-loaded brain-targeted nanocarrier-mediated neuroprotection in methamphetamine-driven Parkinson's disease. *Redox Biol.* **79**, 103457 (2025).
153. Guo, W., *et al.* Axonal transport defects and neurodegeneration: Molecular mechanisms and therapeutic implications. *Semin. Cell Dev. Biol.* **99**, 133–150 (2020).

154. Zhang, X. H. *et al.* A Review of Progress in Histone Deacetylase 6 Inhibitors Research: Structural Specificity and Functional Diversity. *J. Med. Chem.* **64**, 1362–1391 (2021).
155. Saraswati, A. P. *et al.* Spiroindoline-Capped Selective HDAC6 Inhibitors: Design, Synthesis, Structural Analysis, and Biological Evaluation. *ACS Med. Chem. Lett.* **11**, 2268–2276 (2020).
156. Campiani, G. *et al.* Harnessing the Role of HDAC6 in Idiopathic Pulmonary Fibrosis: Design, Synthesis, Structural Analysis, and Biological Evaluation of Potent Inhibitors. *J. Med. Chem.* **64**, 9960–9988 (2021).
157. Carullo, G. *et al.* Development of Epigenetic Modifiers with Therapeutic Potential in FMS-Related Tyrosine Kinase 3/Internal Tandem Duplication (FLT3/ITD) Acute Myeloid Leukemia and Other Blood Malignancies. *ACS Pharmacol. Transl. Sci.* **7**, 2125–2142 (2024).
158. Fontana, A. *et al.* Spirotetrahydroisoquinoline-Based Histone Deacetylase Inhibitors as New Antifibrotic Agents: Biological Evaluation in Human Fibroblasts from Bronchoalveolar Lavages of Idiopathic Pulmonary Fibrosis Patients. *ACS Pharmacol. Transl. Sci.* **8**, 380–393 (2025).
159. Stockings, E. *et al.* Evidence for cannabis and cannabinoids for epilepsy: A systematic review of controlled and observational evidence. *J. Neurol. Neurosurg. Psychiatry* **89**, 741–753 (2018).
160. Friedman, D., *et al*. M. Safety, efficacy, and mechanisms of action of cannabinoids in neurological disorders. *Lancet Neurol.* **18** 504–512 (2019).
161. Xue, B., *et al.* Bench to bedside: Multiple facets of cannabinoid control in epilepsy. *Neurochem. Int.* **141**, 104898 (2020).
162. Naidoo, V. *et al.* Equipotent Inhibition of Fatty Acid Amide Hydrolase and Monoacylglycerol Lipase - Dual Targets of the Endocannabinoid System to Protect against Seizure Pathology. *Neurotherapeutics* **9**, 801–813 (2012).
163. Colangeli, R. *et al.* The FAAH inhibitor URB597 suppresses hippocampal maximal dentate afterdischarges and restores seizure-induced impairment of short and long-term synaptic plasticity. *Sci. Rep.* **7**, 4648 (2017).
164. Colangeli, R., *et al.* Anandamide signaling augmentation rescues amygdala synaptic function and comorbid emotional alterations in a model of epilepsy. *J. Neurosci.* **40**, 6068–6081 (2020).
165. Sugaya, Y. *et al.* Crucial Roles of the Endocannabinoid 2-Arachidonoylglycerol in the Suppression of Epileptic Seizures. *Cell Rep.* **16**, 1405–1415 (2016).
166. Zeng, C. & Chen, C. Endocannabinoid signaling in epilepsy. *Neurobiol. Dis.* **215**, 107074 (2025).
167. Anderson, L. L. *et al.* The endocannabinoid system impacts seizures in a mouse model of Dravet syndrome. *Neuropharmacology* **205**, 108897 (2022).
168. Rinaldi, V. E., *et al.* Therapeutic options for childhood absence epilepsy. *Pediatr. Rep.* **13**, 658–667 (2021).
169. Sysoeva, M. V. *et al.* Network analysis reveals a role of the hippocampus in absence seizures: The effects of a cannabinoid agonist. *Epilepsy Res.* **192**, 107135 (2023).
170. Montebello, G. & Di Giovanni, G. Dysregulation of the Cannabinoid System in Childhood Epilepsy: From Mechanisms to Therapy. *Int. J. Mol. Sci.* **26,** 6234 (2025).
171. Roebuck, A. J. *et al.* Positive allosteric modulation of type 1 cannabinoid receptors reduces spike-and-wave discharges in Genetic Absence Epilepsy Rats from Strasbourg. *Neuropharmacology* **190**, 108553 (2021).

172. Ma, L. *et al.* Disease-Modifying Effects of RHC80267 and JZL184 in a Pilocarpine Mouse Model of Temporal Lobe Epilepsy. *CNS Neurosci. Ther.* **20**, 905–915 (2014).
173. Bellagamba, M., *et al.* Tautomerism in liquid 1,2,3-triazole: A combined energy-dispersive X-ray diffraction, molecular dynamics, and FTIR study. *Struct. Chem.* **24**, 933–943 (2013).
174. Zdanovskaia, M. A. *et al.* Precise equilibrium structures of 1 H - And 2 H -1,2,3-triazoles (C2H3N3) by millimeter-wave spectroscopy. *J. Chem. Phys.* **157** (2022).
175. Carbone, A. Cancer classification at the crossroads. *Cancers (Basel).* **12**, 980 (2020).
176. Hanahan, D. Hallmarks of Cancer: New Dimensions. *Cancer Discov.* **12**, 31–46 (2022).
177. Cai, J. *et al.* Advances in the epidemiology of pancreatic cancer: Trends, risk factors, screening, and prognosis. *Cancer Lett.* **520**, 1–11 (2021).
178. Wainberg, Z. A. *et al.* NALIRIFOX versus nab-paclitaxel and gemcitabine in treatment-naive patients with metastatic pancreatic ductal adenocarcinoma (NAPOLI 3): a randomised, open-label, phase 3 trial. *The Lancet* **402**, 1272–1281 (2023).
179. Mizrahi, J. D., *et al.* Pancreatic cancer. *The Lancet* **395**, 2008–2020 (2020).
180. Qian, Y. *et al.* Molecular alterations and targeted therapy in pancreatic ductal adenocarcinoma. *J Hematol Oncol.* **13**, 130 (2020).
181. Carusillo, A. & Mussolino, C. DNA Damage: From Threat to Treatment. *Cells*. **9**, 1665 (2020).
182. Scully, R., *et al.* DNA double-strand break repair-pathway choice in somatic mammalian cells. *Nat. Rev. Mol. Cell Biol.* **20**, 698–714 (2019).
183. Kockler, Z. W., *et al.* Repair of DNA Breaks by Break-Induced Replication. **49**, 47 (2025).
184. Kumari, N., *et al.* Regulation of pathway choice in DNA repair after double-strand breaks. *Curr. Opin. Pharmacol.* **80**, 102496 (2025).
185. Dobwansky, T. H. Genetics of natural popoulations XIII. Recombination and variability in populations of Drosophila Pseudoobscura. *Genetics* **31**, 269–290 (1946).
186. O'Neil, N. J., *et al.* Synthetic lethality and cancer. *Nat. Rev. Genet.* **18**, 613–623 (2017).
187. Myers, S. H., *et al.* Synthetic Lethality through the Lens of Medicinal Chemistry. *J. Med. Chem.* **63**, 14151–14183 (2020).
188. Ragupathi, A., *et al.* Targeting the BRCA1/2 deficient cancer with PARP inhibitors: Clinical outcomes and mechanistic insights. *Front. Cell Dev. Biol.* **11**,1133472 (2023).
189. Previtali, V. *et al.* New Horizons of Synthetic Lethality in Cancer: Current Development and Future Perspectives. *J. Med. Chem.* **67**, 11488–11521 (2024).
190. Dibitetto, D., *et al.* PARPi, BRCA, and gaps: controversies and future research. *Trends in Cancer* **10** 857–869 (2024).
191. Nomme, J. *et al.* Inhibition of filament formation of human Rad51 protein by a small peptide derived from the BRC-motif of the BRCA2 protein. *Genes to Cells* **13**, 471–481 (2008).
192. Roberti, M. *et al.* Rad51/BRCA2 disruptors inhibit homologous recombination and synergize with olaparib in pancreatic cancer cells. *Eur. J. Med. Chem.* **165**, 80–92 (2019).

193. Bagnolini, G. *et al.* Synthetic Lethality in Pancreatic Cancer: Discovery of a New RAD51-BRCA2 Small Molecule Disruptor That Inhibits Homologous Recombination and Synergizes with Olaparib. *J. Med. Chem.* **63**, 2588–2619 (2020).
194. Bagnolini, G. *et al.* Identification of RAD51-BRCA2 Inhibitors Using N-Acylhydrazone-Based Dynamic Combinatorial Chemistry. *ACS Med. Chem. Lett.* **13**, 1262–1269 (2022).
195. Toma, M., *et al.* RAD52 as a potential target for synthetic lethality-based anticancer therapies. *Cancers* **11**, 1561 (2019).
196. Kagawa, W. *et al.* Crystal structure of the homologous-pairing domain from the human Rad52 recombinase in the undecameric form. *Molecular Cell* **10**, 359-371 (2002).
197. Gottifredi, V. & Wiesmüller, L. Current Understanding of RAD52 Functions: Fundamental and Therapeutic Insights. *Cancers (Basel)* **17**, 705 (2020).
198. Ashworth, A. & Lord, C. J. Synthetic lethal therapies for cancer: what's next after PARP inhibitors? *Nat. Rev. Clin. Oncol.* **15** 564–576 (2018).
199. Previtali, V. *et al.* New Horizons of Synthetic Lethality in Cancer: Current Development and Future Perspectives. *J. Med. Chem.* **67**, 11488–11521 (2024).
200. Hengel, S. R., *et al*. Small-Molecule Inhibitors Targeting DNA Repair and DNA Repair Deficiency in Research and Cancer Therapy. *Cell Chem. Biol.* **24**, 1101–1119 (2017).
201. Myers, S. H., *et al*. Synthetic Lethality through the Lens of Medicinal Chemistry. *J. Med. Chem.* **63** 14151–14183 (2020).
202. Balboni, B. *et al.* Novel Insights into RAD52's Structure, Function, and Druggability for Synthetic Lethality and Innovative Anticancer Therapies. *Cancers* **15**, 1817 (2023).
203. Chandramouly, G. *et al.* Small-Molecule Disruption of RAD52 Rings as a Mechanism for Precision Medicine in BRCA-Deficient Cancers. *Chem. Biol.* **22**, 1491–1504 (2015).
204. Olney, J. W. *et al.* Excitotoxicity of L-DOPA and 6-OH-DOPA: Implications for Parkinson's and Huntington's Diseases'. *Exp. Neurolog.* **108**, 269–272 (1990).
205. Cramer-Morales, K. *et al.* Personalized synthetic lethality induced by targeting RAD52 in leukemias identified by gene mutation and expression profile. *Blood* **122**, 1293–1304 (2013).
206. Nogueira, A., *et al.* RAD52 functions in homologous recombination and its importance on genomic integrity maintenance and cancer therapy. *Cancers* **11**, 1622 (2019).
207. Sullivan-Reed, K. *et al.* Simultaneous Targeting of PARP1 and RAD52 Triggers Dual Synthetic Lethality in BRCA-Deficient Tumor Cells. *Cell Rep.* **23**, 3127–3136 (2018).
208. Wang, L. *et al.* Therapeutic peptides: current applications and future directions. *Signal Transduct Target Ther.* **7**, 48 (2022).
209. Ji, X., *et al.* Cyclic Peptides for Drug Development. *Angew. Chem. Int. Ed.* **63** (2024).
210. Brindisi, M. *et al.* Development of novel cyclic peptides as pro-apoptotic agents. *Eur. J. Med. Chem.* **117**, 301–320 (2016).
211. Johansson, J. R., *et al.* Ruthenium-Catalyzed Azide Alkyne Cycloaddition Reaction: Scope, Mechanism, and Applications. *Chem. Rev.* **116**, 14726–14768 (2016).

212. Coin, I., Beyermann, M. & Bienert, M. Solid-phase peptide synthesis: From standard procedures to the synthesis of difficult sequences. *Nat. Protoc.* **2**, 3247–3256 (2007).
213. Behrendt, R., *et al.* Advances in Fmoc solid-phase peptide synthesis. *J. Pept. Sci.* **22**, 4–27 (2016).
214. Chalyavi, F., *et al.* Synthesis of 5-Cyano-Tryptophan as a Two-Dimensional Infrared Spectroscopic Reporter of Structure. *Angew. Chem.* **130**, 7650–7654 (2018).
215. Sheppeck, J. E.,*et al.* A convenient and scaleable procedure for removing the Fmoc group in solution. *Tetrahedron Lett.* **41**, 5329–5333 (2000).
216. Griehl, C. & Merkel, S. Synthesis and separation of protected tripeptide epimers by RP-HPLC. *Int. J. Pept. Protein Res.* **45**, 217–224 (1995).
217. Elsawy, M. A., *et al.* Racemisation of N-Fmoc phenylglycine under mild microwave-SPPS and conventional stepwise SPPS conditions: attempts to develop strategies for overcoming this. *J. Pept. Sci.* **18**, 302–311 (2012).
218. Palasek, S. A., *et al.* Limiting racemization and aspartimide formation in microwave-enhanced Fmoc solid phase peptide synthesis. *J. Pept. Sci.* **13**, 143–148 (2007).
219. Xiao, N., *et al.* Enantioselective synthesis of (2R, 3S)- and (2S, 3R)-4,4,4-trifluoro-N-Fmoc-O-tert-butyl-threonine and their racemization-free incorporation into oligopeptides via solid-phase synthesis. *Biopolymers* **88**, 781–796 (2007).
220. Duengo, S., *et al.* Epimerisation in Peptide Synthesis. *Molecules* **28**, 8017 (2023).
221. Jad, Y. E. *et al.* Oxyma-B, an excellent racemization suppressor for peptide synthesis. *Org. Biomol. Chem.* **12**, 8379–8385 (2014).
222. Seidel, S. A. I. *et al.* Microscale thermophoresis quantifies biomolecular interactions under previously challenging conditions. *Methods* **59**, 301–315 (2013).
223. Magnez, R. *et al.* PD-1/PD-L1 binding studies using microscale thermophoresis. *Sci. Rep.* **7**, 17623 (2017).
224. Asmari, M., *et al.* Thermophoresis for characterizing biomolecular interaction. *Methods* **146**, 107–119 (2018).
225. Test No. 117: Partition Coefficient (n-Octanol/Water)*, HPLC Method*. (OECD, 2022).